DESIGN, CHARACTERIZATION & APPLICATION OF STIMULI RESPONSIVE SELF-FOLDING SOFT MICROSYSTEMS

by
Chang-Kyu Yoon

A dissertation submitted to Johns Hopkins University in conformity with the requirements for the degree of Doctor of Philosophy

Baltimore, Maryland

January, 2017

Abstract

This dissertation demonstrates design, characterization, and application of stimuli responsive self-folding soft microsystem. Stimuli responsive self-folding soft robotics is an emerging attractive field to mimic motions of biological systems by utilizing hydrogels, polymer or hybrid combination of them, which guide three dimensional (3D) shape change. The stimuli responsive soft robotics have numerous distinct advantages such as lightweight, inexpensive, flexible, easy to design, and able to operate in aqueous environments with no aids of complex feedback sensors, wires, tethers or batteries, as different from conventional electrically or pneumatically driven metals or/and ceramic based robotics.

To establish the foundations of collective innovations and integrated intelligent biomimetic stimuli responsive microsystems, a self-folding strategy can be adapted. Self-folding is a new paradigm to manipulate 2D thin film structures transforming to 3D when triggered by external stimuli such as heat, pH, light, ionic strengths, mechanical stress, magnetic or electrical fields etc. In order to broadly implement this strategy, nanoelectromechanical systems (NEMS) and microelectromechanical systems (MEMS) inspired high throughput photolithography can be adapted. Conventional VLSI fabrication such as photolithography, etching, physical vapor deposition (PVD) can provide reliable and reproducible approaches to pattern particular designs of polymer or/and hydrogels in a cost-effective manner.

Finally, this dissertation demonstrates the design principles, materials characterization and high applicability of those reconfigurable stimuli responsive self-folding soft microsystems for a variety of applications such as soft robotic actuators, biological biopsy tools, and reconfigurable opto-electrical sensors etc.

Advisor: David H. Gracias, Ph. D.

Other committees: Thao D. Nguyen, Ph. D.; Sung Hoon Kang, Ph. D;

Kalina Hristova, Ph. D.; Margarita Herrera-Alonso, Ph. D.

Acknowledgements

I could complete Ph. D. dissertation by virtue of big sacrificing of my great people. In particular, I would like to extend my gratitude to Professor David Gracias who transformed me into a creative and thoughtful researcher by his full support during my Ph. D periods. I would also like to thank my graduate board oral exam & thesis committee member Professors Thao (Vicky) Nguyen, Sung Hoon Kang, Kalian Hristova, and Margarita Herrera-Alonso for their help and feedback with the thesis. In addition, I thank all my professors on qualifier examination board in the Department of Materials Science and Engineering. In specific, I fully appreciate Professor Robert Cammarata to help me a lot when I prepared the subjects of structures, thermodynamics, and phase transformation for qualifying examination.

I also appreciate all professors during my studies at Johns Hopkins. In particular, Professors Robert Cammarata (Thermodynamics and Structures) and Todd C. Hufnagel (Structures), Jonah Erlebacher (Phase transformation), Timothy P. Weihs and Kevin Hemker (Mechanical properties, Thin films, and TEM), and Kaliat. T. Ramesh, Jaafar El-Awady and, Thao (Vicky) Nguyen (Solid mechanics 1, 2). I also like to thank Professor Sung Hoon Kang for being my great mentor during my Ph. D period.

Next, I would like to thank Dr. Shivendra Pandey and Dr. Jae-Hyun Park at Gracias lab. I could have a good start because of them when I joined Gracias lab. Also, my special thanks to my previous and current lab mates, specially, Dr. Hye Rin Kwag, Qianru Jin, Seung Hyun Oh, Kunihiko Kobayasi, Dr. Evin Gultepe, Dr. Joyce

Breger, Dr. Tao Deng. In addition, I would like to thank my great collaborators, Dr. Rui Xiao, Professor Thao (Vicky) Nguyen, Federico Ongaro, Dr. Stefano Scheggi, Professor Sarthak Misra, Angelo Cangialosi, and Professor Rebecca Shulman.

In addition, my special gratitude to my undergraduates at Gracias lab, REU and WISE programs colleagues who were inspiring throughout my stay at Johns Hopkins University. My special thanks to Kiwook Kwon, Florencia Velez-Cortes, Sun Joo Lee, Jin Chung, Kayla Boswell, and Jessica Patel. Most importantly, I should thank my wife Jeong Hyun for encouraging me during my Ph. D periods, my parents for being my spiritual mentors, and my three daughters Esther, Eliana, and Eunice for being a joy during my Ph. D. life at the Johns Hopkins University in Baltimore, Maryland.

Finally, I could complete my Ph. D. dissertation by support from Army Research Office (ARO) (W911NF-15-1-0490) and National Institutes of Health (NIH) (R01EB017742) research programs. I thank their support as well.

DEDICATION

To

My parents (Ha-June and Mi-Ae) and parents-in-law (Taek Chun and Hyun Joo)

Lovely wife (Jeong Hyun)

Three daughters (Esther, Eliana and Eunice)

Table of Contents

Abstract ii
Acknowledgements iv
DEDICATION vi
List of Tables x
List of Figures xi
1. Dissertation Outline xv
2. Introduction 1
2.1. Stimuli Responsive Self-folding Microsystems 1
2.1.1. Materials Selection and Synthesis: Stimuli Responsive Materials 2
2.1.2. Fabrication of Stimuli Responsive Systems at Small Scales 4
2.2. Some Deformation Mechanisms of Stimuli Responsive Systems 5
2.2.1. Simulation Methods for Stimuli Responsive Materials 6
2.3. Outlook: Biomedical Applications of Stimuli Responsive Devices 8
2.3.1. Stimuli Responsive Drug Delivery Systems 9
2.3.2. Stimuli Responsive Soft Biopsy Tools 11
3. Stimuli Responsive Materials: Poly (N-isopropylacrylamide) (pNIPAM) 16
3.1. Functional Stimuli Responsive pNIPAM-based Hydrogel Actuators 16
3.2. Materials and Methods 19
3.2.1. Materials 19
3.2.2. Synthesis of pNIPAM-AAc 19
3.2.3. Imaging of pNIPAM-AAc Hydrogel Structures 19
3.3. Fabrication of Crosslink Gradient pNIPAM-AAc Hydrogels 20
3.4. Results and Discussion 22
3.4.1. Characterization of pNIPAM-AAc Hydrogels 22
3.4.2. Thermo-responsive Deformation Mechanism of pNIPAM-AAc Hydrogels 23
3.4.3. Applications of pNIPAM-AAc Hydrogels 28
3.5. Conclusion 30
4. Programmable, High-degree Expansion of Micropatterned DNA Copolymer Hydrogels 43
4.1. Overview 43
4.2. Introduction 44
4.3. Fabrication of DNA Crosslinked Hydrogels 48
4.3.1. DNA-co-Am and BIS-co-Am Solutions Preparation 48
4.3.2. Photolithography Chambers Preparation 49
4.3.3. Self-folding DNA Crosslinked Hydrogel and Imaging 51
4.4. Results and Discussions 53
4.4.1. Fabrication of DNA Crosslinked Hydrogel System 53
4.4.2. Characterization of DNA Crosslinked Hydrogels: Swelling 54
4.4.3. Characterization of DNA and BIS Bilayer Bars 55
4.4.4. Finite Element Analysis: Radius Change of DNA/BIS Bars 56
4.4.5. Multi-state Fabrications of Complex Shaped DNA and BIS Hydrogels 57
4.5. Conclusion 59

5. Programmable Magnetically and Thermally Responsive Self-folding Soft Microgrippers 70
5.1. Overview 70
5.2. Introduction 71
5.3. Materials and Methods 76
5.3.1. Materials 76
5.3.2. Synthesis of Polypropylene Fumarate (PPF) 76
5.3.3. Synthesis of pNIPAM-AAc 76
5.3.4. Thickness Measurement: Profilometry 76
5.4. Experiments 77
5.4.1. Fabrication of Thermo-magnetically Responsive Soft Grippers 77
5.4.2. Modeling of Swelling/Deswelling of Soft Microgrippers 78
5.4.3. Cell Culture 79
5.4.4. Gripping of Tissue 80
5.5. Results and Discussion 80
5.5.1. Design of Soft Grippers 80
5.5.2. Characterization of Gripper Folding 81
5.5.3. Finite Element Analysis of Gripper Folding 84
5.5.4. Applications of Soft Grippers 88
5.6. Conclusion 90
6. Control of Untethered Soft Micro Grippers for Pick-and-place Tasks 100
6.1. Overview 100
6.2. Introduction 101
6.3. Experiments 103
6.3.1. Magnetic and Thermal Systems 103
6.3.2. Fabrication of Soft Grippers 104
6.3.3. Magnetic Characterization of Soft Grippers 105
6.3.4. Thermal Characterization of Soft Grippers 107
6.3.5. Tracking and Control 107
6.4. Results and Discussions 109
6.4.1. Motion Control of Micro Grippers 110
6.4.2. Pick-and-place Tasks 111
6.5. Conclusions 112
7. Autonomous Panning and Control of Soft Untethered Grippers in Unstructured Environments 120
7.1. Overview 120
7.2. Introduction 121
7.3. Experiments 124
7.4. Results and Discussions 125
7.4.1 Detection and Tracking of Grippers 125
7.4.2. Motion Planning 127
7.4.3. FEM Modeling and Validation 129
7.4.4 Temperature Control 130
7.4.5 Experimental Validation 130
7.5. Conclusion 132

8. Stimuli Responsive Self-folding 2D Layered Materials (2DLMs)/Polymer Bilayers 139
8.1. Overview 139
8.2. Introduction 140
8.3. Experiments 144
8.3.1. Fabrication Flow of FLG/SU-8 Bilayer Thin Films 144
8.3.2. Mass Producible FLG/SU-8 Bilayer Thin Films 145
8.4. Results and Discussion 146
8.4.1. Self-folding Mechanism of FLG/SU-8 Thin Films 146
8.4.2. Characterization of FLG/SU-8 Thin Films: Raman Spectroscopy 148
8.4.3. Characterization of FLG/SU-8 Thin Films: Radius of Curvature 149
8.4.4. Characterization of FLG/SU-8 Thin Films: Current vs Voltage 151
8.4.5. Characterization of FLG/SU-8 Thin Films: Photovoltage vs Power 153
8.5. Conclusion 156
9. Patterned Soft Micropolyhedra by Self-folding and Molding 166
9.1. Overview 166
9.2. Introduction 167
9.3. Experiments 168
9.3.1. Fabrication Step: Photolithography, PVD, and Self-folding 168
9.3.2 Fabrication Step: Molding 168
9.4. Results and Discussions 169
9.4.1. Self-folding and Molding 169
9.4.2. Mass-producing 170
9.5. Conclusion 172
10. Rolled-up Nanoporous Membranes by Nanoimprint Lithography and Strain Engineering 178
10.1. Overview 178
10.2. Introduction 179
10.3. Experiments: Nanoporous Si_3N_4/Si Bilayers 181
10.4. Results and Discussions 182
10.4.1. Characterization of Nanoporous Surface 182
10.4.2. Characterization of Nanopores Sizes 182
10.4.3. Characterization of Self-rolled Tubes 183
10.4.4. Applications of Nanoporous Membranes 185
10.5. Conclusion 186
11. Summary and Future Studies 194
References 206
Curriculum Vitae 231

List of Tables

Table 3.1. Parameters determined for the pNIPAM-AAc materials synthesized with different UV intensities. 31

Table 4.1. DNA Sequences. 60

Table 5.1. Parameters of the constitutive model for pNIPAM-AAc and PPF. 92

Table 6.1. Experimental motion control results of soft grippers for point-to-point, circular and square trajectories. 113

Table 7.1. Quality indices for the x- (B*x*) and y- (B*y*) components of the magnetic field for the obtained fitting function. 133

Table 8.1. Simulation parameters and computed radius of curvature for gradient crosslinked and conditioned SU-8. 158

Table 10.1. Elastic properties of each layer. 187

List of Figures

Figure 2.1. Schematic descriptions of self-folding strategies of soft materials. 14

Figure 2.2. Schematic descriptions of precise motion-guided 3D stimuli responsive microsystems. 15

Figure 3.1. Illustration of the key steps utilized in creating 3D self- folding structures using thin, gradient cross-linked hinges and thick, fully cross-linked panels. 32

Figure 3.2. Detailed schematic of the fabrication process to photopattern and actuation of pNIPAM-AAc thin monolayer. 33

Figure 3.3. Characterization of the pNIPAM-AAc hydrogel deposition and patterning process. 34

Figure 3.4. Schematic and optical microscopy images showing thermally responsive self-folding pNIPAM-AAc structures of different shapes. 35

Figure 3.5. Characterization of the effect of UV energy exposure. 36

Figure 3.6. Swelling ratio versus temperature. 37

Figure 3.7. Finite element model of the pyramid specimen. 38

Figure 3.8. Experiments and simulation results of folding angles of pNIPAM-AAc structures according to temperature. 39

Figure 3.9. Parallel self-folding of cubic capsules with thick highly cross-linked panels and thin gradient cross-linked hinges. 40

Figure 3.10. pNIPAM-AAc hydrogel grippers. 41

Figure 3.11. Stimuli responsive thermally steered optoelectronic micro-mirror system. 42

Figure 4.1. Chemomechanical actuation of DNA-crosslinked hydrogels and detailed DNA coupling mechanism in hydrogel net. 61

Figure 4.2. Photopatterning of DNA-crosslinked hydrogels. 62

Figure 4.3. Swelling of DNA-co-Am hydrogels. 63

Figure 4.4. Schematic illustration of photolithographic fabrication steps of DNA/BIS bars. 64

Figure 4.5. Actuation of DNA/BIS bilayer bars and computational estimation of radius changes according to swelling ratio and Young's modulus. 65

Figure 4.6. Schematic illustration of multi-step fabrications of flower shaped DNA/BIS hydrogel system. 66

Figure 4.7. Selective actuation of flower shaped DNA/BIS hydrogel. 67

Figure 4.8. Schematic illustration of multi-domain fabrication steps of a crab shaped DNA/BIS hydrogel system. 68

Figure 4.9. Selective chemomechanical folding of a crab. 69

Figure 5.1. Schematic diagram illustrating the reversible self-folding of soft microgrippers in response to temperature. 93

Figure 5.2. Schematic diagram of the PPF/pNIPAM-AAc microgripper fabrication process flow. 94

Figure 5.3. Optimization of the photopatterning of the microgrippers. 95

Figure 5.4. Experimental and simulation image illustrate reversible thermally responsive self-folding of a representative microgrippers in DI H_20. 96

Figure 5.5. FEM sensitivity analysis exploring the dependence of the microgripper diameter reduction ratio (D/Do). 97

Figure 5.6. Finite element model of gripper specimen. 98

Figure 5.7. Applications of the soft thermoresponsive self-folding grippers. .. 99

Figure 6.1. Photographs of the electromagnetic and thermal systems used to control the soft grippers. 114

Figure 6.2. A schematic of the fabrication process of the soft grippers. 115

Figure 6.3. Schematic of the trajectory of the two-tip dipole during the U-turn experiments for magnetic characterization. 116

Figure 6.4. Results of the opening and closing characterization of the soft grippers. 117

Figure 6.5. Flowchart illustrating the steps in the contour-extraction process for the soft grippers. 118

Figure 6.6. Representative closed-loop motion control experimental results of a gripper. 119

Figure 7.1. Soft grippers. 134

Figure 7.2. Schematic and experimental images of the fabrication and operation of the soft bilayer grippers. 135

Figure 7.3. Flowchart showing the tracking process. 136

Figure 7.4. Biological manipulation of soft grippers. 137

Figure 7.5. Autonomous sorting of soft grippers. 138

Figure 8.1. Schematic of the fabrication and reversible self-folding of FLG/SU-8 bilayers. 159

Figure 8.2. Mass-producible reversibly actuating FLG/SU-8 microstructures in a variety of shapes including rectangular strips, crosses, flowers, and discs. 160

Figure 8.3. Mass production of 3D FLG/SU-8 microstructures. 161

Figure 8.4. Self-folding and reversibly actuating FLG/SU-8 photopatterned bilayer. 162

Figure 8.5. Characterization of thin FLG/SU-8 bilayers and experimental and computational folding degree observation according to UV light exposure energy and strain. 163

Figure 8.6. Schematic and experimental results of a functional self-folded FLG/SU-8 device. 164

Figure 8.7. Sensitivity and selectivity of integrated self-folding FLG/SU-8 tubular optical sensor. 165

Figure 9.1. Schematic showing the comparison of our patterned micropolyhedra as compared toexisting microparticles. 173

Figure 9.2. Schematic of the self-folding and molding process flow. 174

Figure 9.3. Experimental results showing 3D pattern transfer during molding. 175

Figure 9.4. Soft-polyhedra with different polymers and hydrogels with and without loaded chemical dyes. 176

Figure 9.5. Assembly of cell-laden bioblocks for tissue engineering applications. 177

Figure 10.1. Schematic of the process flow that was used to pattern the nanopores in the Si_3N_4/Si bilayer. 188

Figure 10.2. SEM images of nanopores in the Si_3N_4/Si bilayer. 189

Figure 10.3. Reduction in nanopore size by platinum deposition. 190

Figure 10.4. Self-rolling nanoporous films. 191

Figure 10.5. Experiments and FEM results of rolled-up nanoporous membranes with different characteristics. 192

Figure 10.6. Cell culture in nanoporous tubes. 193

1. Dissertation Outline

Stimuli responsive self-folding soft microsystems have many advantages to enlarge schemes of conventional robotics paradigm. Traditional pneumatic, hydraulic, or electrical driven actuation systems are well-developed. However, these reconfigurable systems require tethers or wires connected with an external energy supplier such as batteries. Thus, these actuation systems suffer from limitations to the maneuverability for microsystems such as the difficulty in reaching areas within the human body or complex microfluidic channels in lab-on-a-chip devices. In order to overcome these limitations, alternative strategies are required. As one of the alternatives, innovative stimuli responsive microsystems have been proposed in Chapter 2 with brief reviews of biomedical devices such as drug delivery and biopsy tools.

After reviewing biomedical applications in Chapter 2, stimuli responsive biomimetic untethered microscale actuators are introduced in Chapter 3. In specific, this chapter starts with an innovative methodology that utilizes photolithography to create smart hydrogel based actuators by utilizing stimuli responsive materials such as poly (N-isopropylacrylamide) (pNIPAM). Later in this chapter, potential of multi-functional applications, such as biomedical drug delivery capsules, biopsy tools, multi-scales actuators, and optical mirror systems, are described.

After discussing an initial background of innovative photolithographic approach to fabricate stimuli responsive hydrogel based systems in Chapter 3, sequence-selective and highly swellable intelligent DNA crosslinked soft chemomechanical

actuators have been introduced in Chapter 4. Most of the current chemomechanical systems respond to conventional triggers such as light, heat, or pH; however, in this chapter, DNA hybridized self-folding chemomechanical microsystems are described, which have a high selectivity of folding orders in response to DNA input of particular sequence. These DNAs responsive micro devices could be envisioned to even develop autonomous soft robots and metamorphic materials.

Furthermore, chapter 5 explores an innovative concept of bio-friendly soft micro gripper systems for soft robotics and surgical applications. Untethered small scale reconfigurable soft robots could provide numerous advantages such as micro-assembly, pick-and-place microscale targets for lab-on-a-chip applications, and minimally invasive surgeries. In order to prove the concept of less- or non-invasive biopsy tools, soft micro grippers have been introduced. Especially, materials selection, fabrication design, and characterization of soft grippers have been discussed. In this chapter, thermally and magnetically responsive soft micro grippers have been demonstrated for pick-and-place biological materials in order to prove the concept of less invasive untethered micro surgical tools for biopsy. This chapter analyses the potential of soft micro gripper system as an alternative to the conventional tethered or/and rigid micromanipulators. Finally, self-folding mechanism of these soft grippers are analyzed by using FEM simulation.

In Chapters 6 and 7, autonomous navigation of untethered soft micro grippers has been discussed to validate the possibilities for pick-and-place tasks and to manipulate the biological materials precisely in unstructured environments. In order

to conduct complex tasks remotely in hard-to-reach environments, Chapters 6 and 7 demonstrate the capabilities of navigation and manipulation of soft grippers controlled by a both magnetic field gradient as well as the temperature change in the workspace. Finally, these two chapters describe further innovative untethered soft grippers that are thermally and magnetically responsive, which can be guided by precise haptic and ultrasound feedbacks.

In Chapter 8, in order to design high performance electronic and optical devices, solvent-driven self-folding three dimensional (3D) flexible substrates are incorporated with graphene, which is one of the 2D layered materials (2DLMs). In contrast to planar graphene sensors on rigid substrates, curved and folded sensors can be assembled with smaller form factors due to their 3D geometry and a large surface area from their multiple rolled architectures. Characterization of electrical and optical properties of these devices reveal the effectiveness of the self-folding strategy with 2DLMs. This self-folding 2DLMs approach shows a wide applicability in 3D electronic and optical devices with relevance to sensing, diagnosis, wearables, and energy harvesting.

Chapter 9 describes a highly parallel methodology to create multi-functional complex 3D shapes and multi-scale polymeric or hydrogel particles by self-folding and molding combination. This chapter presets the methodological strategy to combine self-folding and molding, which can be used to design a variety of smart polymer or hydrogel particles and self-assembly building blocks with a precisely patterned surfaces for colloidal science, drug delivery, and tissue engineering.

Chapter 10 describes the concept of nanoporous 3D tubular rolled-up structures that is applicable in controlled drug delivery capsules. In this chapter, a highly parallel strategy that combines nanoimprint lithography (NIL) with thin film bilayer strain engineering have been introduced in order to create the nanoporous self-rolled tubular structures. Further, this NIL with strain engineering processed tubular devices has been highlighted by biocompatibility tasks through the encapsulation of live cells utilizing biomedical therapy.

Finally, Chapter 11 presents the summary of this dissertation and suggests future studies in order to enlarge the applicability of stimuli responsive self-folding soft microsystems for a variety of applications including biomedical non-invasive surgical tools, alternatives of biological organs, and high sensitive and selective flexible actuators and sensors.

2. Introduction*

2.1. Stimuli Responsive Self-folding Microsystems

Stimuli responsive self-folding systems play an important role in multiscale biomimetic, reconfigurable, and multi-functional devices. Stimuli responsive self-folding is a class of self-assembly systems which can fold, curve, or roll in response to external triggers such as heat, pH, light, ionic strength, mechanical stress, electrical, and magnetic fields without the aid of manual control. In order to create stimuli responsive three dimensional (3D) self-folding structures, a number of planar methodologies such as photolithography, micro- and nano-imprinting, or direct contact mode molding are conventionally selected to design two dimensional (2D) thin film structures. Then, the 2D thin film structures can change shapes to 3D in response to selective external stimuli, which change the chemical or/and mechanical properties of the structures. These innovative approaches can create untethered advanced functional 3D structures such as polyhedral drug delivery capsules, biomimetic actuators, valves for lab-on-a-chip applications, optoelectrical sensors, microsurgical devices, and even bioinspired tubulars.

---

* Reprinted with permission from

1. T. Shroff, C. K. Yoon, and D. H. Gracias, "Shape Change Poly (N-isopropylacrylamide) Microstructures for Drug Delivery," Polymeric Drug Delivery Techniques: Translating Polymer Science for Drug Delivery, *Aldrich Materials Science, Sigma-Aldrich*, pages 28-30, 2015.

2. A. Ghosh, C. K. Yoon, F. Ongaro, S. Misra, and D. H. Gracias, "Self-folding polymeric shapes for biomedical applications", In *preparation*, 2017.

2.1.1. Materials Selection and Synthesis: Stimuli Responsive Materials

The new class of soft materials, that respond to their environment by changing their physical or/and chemical properties is referred to as stimuli responsive materials. These stimuli responsive materials can change their shapes in response to various external stimuli like pH,[1] temperature,[2] electric fields,[3] or biomolecules[4–8] and can be programmed to be responsive to more than one stimulus at a time.[9–11] These unique properties of stimuli responsive materials have to be rationalized while considering materials selection and design according to specific application targets and their required properties. Particularly, thermo-responsive soft materials have been extensively used due to their easy to use conventional heat source. Most of the thermo-responsive materials have been synthesized by combining hydrophilic (e.g., amide, carboxyl) and hydrophobic (methyl, ethyl, propyl) groups together in one gel network.[12] These kinds of gel network designs show a sharp critical transition point known as lower critical solution temperature (LCST). The LCST driven stimuli responsive materials have shown unique property changes in a gel system. For example, below LCST, the gel systems change to hydrophilic property because of which they absorb water and above LCST, the hydrophobic property becomes dominant which results in the desorption of water. Amongst many LCST driven thermo-responsive hydrogel systems, the Poly(N-isopropylacrylamide)(pNIPAM)[13] based hydrogel systems have been extensively selected for studies in drug delivery, bio-sensing, artificial muscles, and actuators. This pNIPAM based hydrogel has been traditionally synthesized and fabricated by using photolithography, micro molding, emulsion polymerization or radical polymerization techniques.[14] Recently, Shah *et al.*

have reviewed methods to create monodispersed pNIPAM microgels by using microfluidic devices as well as by manipulation of the conditions required to induce gelation.[15]

Beyond the thermo-responsive hydrogel systems, pH responsive hydrogel systems are also some of the commonly considered strategies while designing stimuli responsive materials and devices. In order to obtain pH sensitive hydrogel systems, weak acid or alkaline groups such as carboxyls or amino can be copolymerized in a gel system.[16] In addition, when these pH sensitive groups are operated together with a thermal responsive monomer, dual thermal and pH responsive hydrogel systems could be designed.[16] A lot of work have been done using pH responsive hydrogels where patterned bilayers of PMMA and poly (EGDMA)[17] or poly (HEMA-co-AA) and poly (HEMA)[18] swell differently under various acidic and basic conditions. In addition, light responsive hydrogel systems respond to an optical stimulus with no requirement of secondary external triggers such as heat, electrical, and magnetic fields. One of the conventional strategies to design light responsive hydrogel system is to employ spiropyrane or its derivatives together with hydrogel network.[19–21] Particularly, Sumaru *et al*. synthesized NIPAM with acrylamide-functionalized spirobenzopyran copolymer hydrogels that respond to light irradiation.[20] Moreoever, it has been reported that incorporation of carbon nanotubes[22] in hydrogel could make it respond to optical or magnetic stimuli.

2.1.2. Fabrication of Stimuli Responsive Systems at Small Scales

Sub-millimeter scale objects are often too small to have an on-board power source like a battery. Sometimes, they are meant to be utilized for in vivo applications where any tethered connection to the outside environment will defeat the purpose. Thus, other innovative power sources have been explored in order to derive the necessity of stimuli responsive self-folding microsystems. In order to manufacture such active microsystems, considerable attention has to be given to the materials selection and fabrication procedure. Conventional fabrication schemes at small length scales are largely two-dimensional in nature, where, by using methods like optical or soft lithography as well as imprint or embossing patterned shapes and surfaces can be produced. Manufacturing three dimensionally structured particles or shapes is challenging. However, recently few 3D fabrication schemes have been proposed, such as laser ablation, stereo lithography, glancing angle deposition, and electrodeposition. However, the problem with these methods are their very low throughput and limited choice of materials. Further, these methods are particularly suitable for creating microstructures using hard materials such as metals or hard dielectrics and plastics. Even though high aspect ratio 3D structures can be produced by lithography, imprint or molding techniques; however, they are either passive or large to actuate devices effectively.[23] Recently, the scope has been improved with the advent of 3D printing which can print a wide variety of materials ranging from plastics[24] to softer gels[25] and even cell-cultured soft materials which have been used for making bionic ears.[26] One promising technique for generating actuation at small length scales is to use stimuli responsive hydrogels and polymers.[27,28] For example,

when two layers of polymers having different swelling behaviors form a bilayer, it can be bent with the more rigid layer inside.[29] In addition, hydrogels are attractive because of their inherent porous nature which can be tuned for controlled drug release applications as well.[30] Further, the advantage of using a layered assembly of stimuli responsive polymers and hydrogels also lies with the ease of creation of different shapes using 2D fabrication schemes like imprint, photo or soft lithography techniques which are very well established. Further, these shapes can self-assemble themselves into various 3D structures after lift-off from the substrate.

2.2. Some Deformation Mechanisms of Stimuli Responsive Systems

Shape change is an emerging concept inspired by robotics and tunable shapes of cells or pathogens. Shape memory polymers and hydrogels are perhaps the most important types of all responsive polymers.[31–33] These systems are often composed of two kinds of molecular moieties, including rigid and flexible chains or hydrophobic and hydrophilic structural units. The paradigm of multilayer and patterned microstructures composed of polymer and hydrogels present an attractive concept for the following reasons: (i) First, the hydrogels have mechanical properties, such as moduli, that are well matched with those of the human tissues and organs. Many are biocompatible and are capable of swelling by several orders of magnitudes in volume in response to different ranges of environmental stimuli.[34,35] In aqueous biological systems, a swelling or a collapse can occur due to absorption or expulsion of water. In addition, gelation can also be triggered in vivo.[36] (ii) Second, due to large changes in volume, swelling and de-swelling can cause large mechanical deformations that can

be used to enable actuation without the need of any external batteries or wires. (iii) Third, multilayers using various combinations of more and less swelling hydrogels or gradient crosslinked hydrogels can be designed so that differential volume change during swelling can be converted to spontaneous curving and folding in order to form a wide range of three-dimensional (3D) shapes and structures (**Figure 2.1.**).[17,28,37,38] (iv) Fourth, with advances in bio-MEMS, a number of techniques have been developed for pattern and structure hydrogels in a wide range of shapes and sizes using mass-producible methods such as photolithography, printing, molding, or layer by layer assembly methods in order to offer a possibility for autonomous, environmentally responsive multi-state functionality.

2.2.1. Simulation Methods for Stimuli Responsive Materials

In order to elucidate the swelling behavior of hydrogel systems and their properties change, many numerical simulation techniques such as macroscopic scale finite element and phase field methods, meshless methods, molecular level Monte Carlo and molecular dynamic approaches have been developed.[39] Initially, Flory and Rehner (FR) developed a statistical thermodynamics model of a swelling polymer network based on entropy changes.[40,41] Recently, many FR model driven statistical approaches have been developed in order to understand polymer networks and predict their shape deformation precisely.[42–44] In general, most macroscopic hydrogel theories that are calculated by minimizing the free energy of the total system are based on the conservation laws and constitutive equations which describe equilibrium state in polymer networks in a given environment.[45–47] In particular,

finite element simulation of hydrogel swelling is one of the most popular methods to solve highly nonlinear cases of monophase theories and phase field method is to solve multiphase systems with interfacial dynamics. Especially, the phase field method allows us to focus on the dynamics of interfaces of multiphase systems related to all physical and chemical driving fields.[48–50] Experimentally, Tanaka *et al.* initially observed the phase transition in hydrogel systems in response to different types of external stimuli such as heat, ionic strength, and light.[51–54] Recently, Suo *et al.* have proposed a thermodynamic theory of phase transition in thermally responsive hydrogels.[55] Furthermore, Toh *et al.* have added a photo-sensitivity parameter in temperature sensitive hydrogels to study the effect of light intensity on the phase transition occurring in these hydrogels.[56]

In addition, meshless methods have been widely used to study stimuli responsive hydrogel systems. Currently, meshfree approaches include a wide spectrum of intelligent parameters to predict the deformation in a gel system such as pH-sensitivity,[57,58] electric sensitivity,[59,60] ionic strength sensitivity[61] or combined electric-pH sensitivity parameters.[62,63] In addition, at micro or nano scale lengths, Monte Carlo, and molecular dynamic simulations can be adapted in order to investigate the properties of polymer networks with molecular level configuration details. Quesada-Perez *et al*. studied steady state swelling behavior of the gels triggered by heat and pH by using coarse grained molecular dynamics,[64] and Jaramillo-Botero *et al.* adopted atomistic level molecular dynamic approach to investigate the hydrogel networks thermodynamically so as to provide insights into

mechanical properties of hydrogel systems at an atomistic level.[65] Finally, in order to understand stimuli responsive soft material networks and their properties, all these simulation approaches have triggered experimental systematic optimizations of stimuli responsive polymer or/and hydrogel systems.

2.3. Outlook: Biomedical Applications of Stimuli Responsive Devices

Biomedical applications such as microsurgery[66] or controlled drug delivery[67] over a prolonged duration require advanced materials and methods to successfully accomplish these tasks in live animals or humans. Present day minimally invasive surgery uses laparoscopic or catheter based technologies, in which a small cut is made on the external tissue to insert the tools such as camera, suction, and cutting tools. Though these methods have reduced patient trauma to a large extent, they still suffer from a compromised dexterity and inaccessibility or risk of injury when they are used to reach very deep locations in the body.[68] For example, in an endovascular intervention in a brain, such as intracranial angioplasty, the maximum diameter of the blood vessel that can be reached is about 2 mm, because of the limitations imposed by the guidewire thickness.[69] In order to reach still smaller regions new technologies have to be developed[70,71] which can enable navigation to a very deep target site,[72] and perform tasks such as stent deployment or drug delivery. Such a system must include ways to scale down the surgical instruments[73] that are used to carry out the procedures. In addition, gripping and cutting tools such as clamps, extractors, and forceps to scissors and rongeurs are ubiquitous in surgical procedures. Miniaturized gripping and cutting tools are particularly attractive because they are

made of soft polymeric materials having a Young's modulus of less than 200 MPa[74] and thus have a rigidity similar to that of the living tissues like skin (≈100 MPa).[75] In addition, these small scales drug delivery and biopsy tools could be controlled in an untethered manner and can be navigated to specific locations. This also ensures compliant movements without causing any injury inside the delicate and tortuous locations of the anatomy.

2.3.1. Stimuli Responsive Drug Delivery Systems

Shape changing self-folding hydrogel microstructures offer many advantages drug delivery systems (DDSs). Therapeutic drugs have evolved from single component formulations such as powders to multi-component DDSs such as capsules, anisotropic particles, or micro fabricated needle patches. An effective DDS must be both smart and multifunctional; it must release a drug at a specific anatomical location within the therapeutic range for a specified period of time and with minimal side effects. DDSs can target cell receptors by using antibodies, ligands, or aptamers for more effective cancer therapeutics[76] or they dissolve and release their cargo in specific anatomical areas such as a stomach, which is highly acidic.[77] Therefore, although polymeric DDSs can bind to specific cells or can be broken apart by biochemical reactions, they are inherently static and do not reconfigure or change shape dynamically. Shape change is an emerging concept in DDSs which is inspired by robotics and the tunable shapes of cells or pathogens. The shape changing feature offers a possibility for autonomous, environmentally responsive multi-state functionality. There are a number of dynamic polymeric DDSs that range in size from

nanometer-sized biomolecular constructs to centimeter-sized implants. These new materials are in different stages of their development, ranging from a laboratory curiosity to clinical trials. Nanometer-sized dynamic shape change structures for DDSs are composed of smart biomolecules, such as DNA, and can be assembled into different shapes such as cubical containers with controllable lids.[78]

In addition, since DDSs are envisioned for in vivo applications, stringent requirements must be met in order to ensure safety and minimize toxicity. These conditions vary depending on the anatomical position and duration of drug release. For example, N-isopropylacrylamide (NIPAM) monomers are potentially toxic in vivo.[79] However, poly (*N*-isopropylacrylamide) (pNIPAM) is widely used in cell culture dishes where no significant cellular toxicity has been observed. Moreover, it can be created with biodegradable crosslinkers thereby offering the possibility of clearance from the body.[80–82] Additionally, ophthalmic formulations of pNIPAM have been reported with no in vitro cytotoxicity.[83] Consequently, these examples of pNIPAM based stimuli responsive microsystems are being used for illustrative purposes and more research is required in order to evaluate their safety. Additional research needs to be conducted to develop such shape changing microstructures by using alternative bio-friendly soft materials such as chitosan,[84] gelatin,[85] cellulose,[86] alginate and hyaluronic acid,[87] PLGA,[88] PVA,[89] PEO, and PEO-PPO-PEO block copolymers like pluronics or poloxamers.[90,91]

Due to significant advances in nanotechnology and bio-fabrication, future DDSs are expected to embody more characteristics of living systems such as self-assembly

and disassembly, energy dissipation and adaptation. They will be dynamic and will be exquisitely structured at various length scales. Much like a complex macro-engineered robotic device, they would likely incorporate feedback, control, logic, and possibly memory that can be manifested through a combination of molecular binding, chemical reaction, and electronic circuits. Embarking again, stimuli responsive microsystems that have curved and folded 3D microstructures, in the absence of any external power sources, could be used to enable a variety of autonomous shape changes and can consequently enable smart behaviors that are a small step toward enabling the grand vision of the ideal therapeutic (**Figure 2.2. (A)**). In future, stimuli responsive micro devices could be utilized widely in biomedical applications such as self-attaching devices for sustained drug release, self-coiling devices for blocking aneurisms, self-expanding drug eluting stents, and self-propelled and miniaturized locomotive devices

2.3.2. Stimuli Responsive Soft Biopsy Tools

Gripping is one of the most fundamental and widely used biomechanical function that finds applications in lifting, grabbing objects, object manipulation etc. (**Figure 2.2. (B)**). With the growing popularity of soft robotic actuators and devices for healthcare related applications, different kinds of gripping tools have been developed. Soft robotic actuators are able to produce extremely compliant omnidirectional movements which were otherwise impossible to achieve using hard robots. For example, macroscale gripping tools replicating a human hand[92] have been used for assisting the limb movements of patients having compromised motor functions due

to stroke or cerebral palsy. These artificial wearable hands are found to accelerate patient recovery and enable them to grasp objects which they were not able to do otherwise without such tools. Different actuation mechanisms have been used, of which electronic and ionic electroactive polymers deserve special mention. Electroactive polymers (EAP)[93] like electrostrictives or piezo-electrics have a sandwiched elastomer in between two metal electrodes. On the application of a large voltage (~ kV to MV), these polymers can be bent by electrostatic interactions. Ionic polymers like IPMC[94] or conjugated polymer[95] on the other hand, can operate with a much lower voltage (~V) and still produce strains as large as the EAP. They operate by the flow of ionic polyelectrolyte and metal ions between the electrodes. Recently, Mc Kibben actuators,[96] which are based on channeling gas/fluid pressure to generate actuation, have been more widely used. As seen in the soft robotic hand,[97] one side of these actuators, which is in contact with the gas, is made up of an extensible material and the other side is made up of a thick inelastic material. Bending of the fingers was achieved by changing air pressure. This robotic hand has been demonstrated to be capable of having widely different movements and was able to grasp various objects like a telephone and a pair of chopsticks. It assists the movements of the hand by using pneumatic actuation and also allows passive movements of the hand when not in use. Another kind of gripping tools have replicated the motion of an octopus arm[98,99] and have been employed to develop advanced catheter designs for minimally invasive surgeries.[100]

One major difference of the miniaturized soft robots from their macroscale counterparts is the power transfer mechanism. In larger scale robots, the power source is mainly electrical, and is either wired,[101] or derived from a battery[102] or is pneumatic[98,103] derived from pumps or fuel sources. As the size of these grippers decreases, power delivery to the tools becomes increasingly difficult due to the reduced available energy storage space. Millimeter scale objects are often too small to have an on-board power source like a battery. In addition, they are meant to be used for in vivo applications where any tethered connection to the outside world will ruin the purpose. Thus, other less bulky sources of power have been explored to derive the necessary gripping forces. Finally, stimuli responsive soft microsystems can provide alternative less-invasive operating power as forms of biopsy tools or drug delivery capsules.

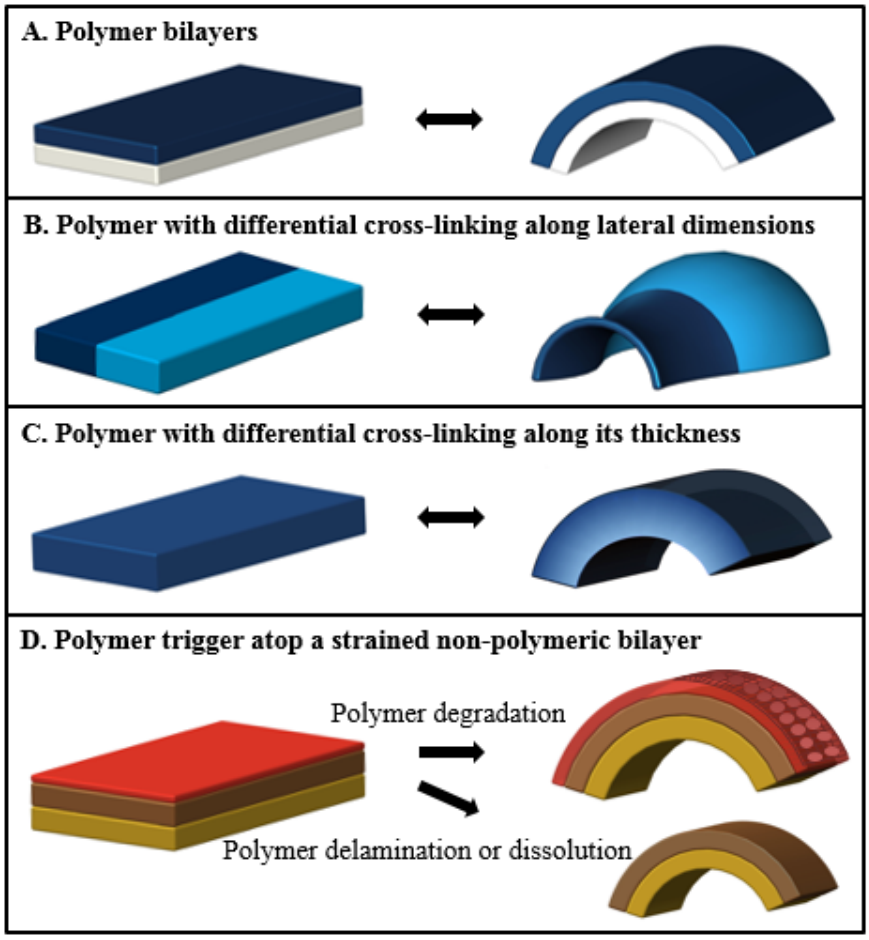

Figure 2.1. Schematic descriptions of self-folding strategies of soft materials. **(A)** Heterogeneous swelling in bilayer **(B)** Bi-strip structures that undergo different swelling in lateral. **(C)** Crosslink gradient along a thickness in monolayer. **(D)** Incorporation with pre-stressed trigger layer that can be eliminated to cause shape changes. Reprinted with permission from Ref. 28 © 2013, *Current Opinion in Chemical Engineering.*

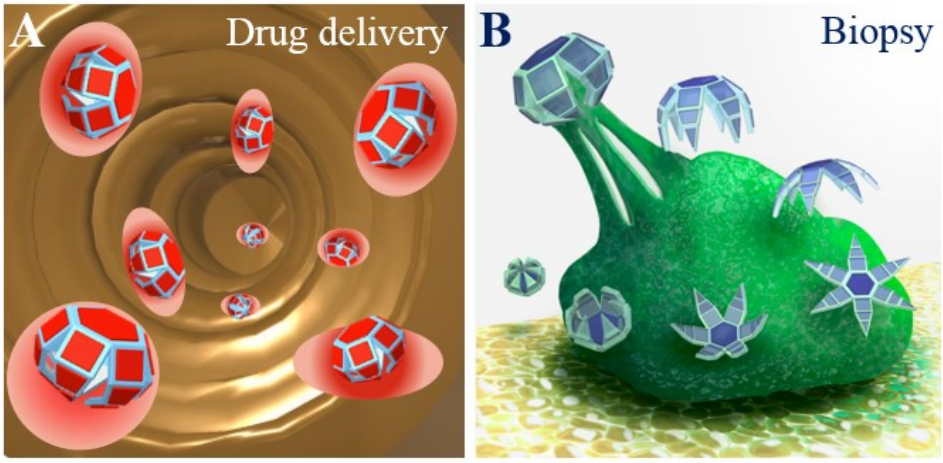

Figure 2.2. Schematic descriptions of precise motion-guided 3D stimuli responsive microsystems. Biomimetic untethered soft grippers for **(A)** drug delivery and **(B)** biopsy applications. (A) Sketch is reprinted with permission from Polymeric Drug Delivery Techniques: Translating Polymer Science for Drug Delivery, T. Shroff, C. K. Yoon, and D. H. Gracias © 2015, *Aldrich Materials Science, Sigma-Aldrich.*

3. Stimuli Responsive Materials: Poly (N-isopropylacrylamide) (pNIPAM)*

3.1. Functional Stimuli Responsive pNIPAM-based Hydrogel Actuators

The development of soft polymeric or hydrogel stimuli responsive actuators and related devices are important from both an intellectual and technological perspective.[28,38,104–109] Stimuli responsive soft-actuators are widely observed in nature, for example in the spontaneous and reversible folding and unfolding movements of plants. Examples include the Rhododendron leaves which respond to temperature[110] or the Dionaea muscipula (Venus flytrap) which responds to mechanical and pH stimulation.[111,112] These actuators enable functions such as defense from predators or consumption of food which are critical to their survival. On the technological front, the development of such bio-inspired synthetic stimuli responsive soft devices could facilitate enhanced functionality for biosensing, robotics and surgery. Specific advantageous traits of these systems include the use of mechanical energy stored within the material, the ability to respond autonomously to enable smart behaviors, and the possibility for extreme miniaturization and untethered operation without the need for wires or batteries or external power sources.

---

* Reprinted with permission from

1. C. K. Yoon, R. Xiao, J. H. Park, J. Cha, T. D. Nguyen and D. H. Gracias, "Functional Stimuli Responsive Hydrogel Devices by Self-Folding," *Smart Materials & Structures*, vol. 23, pp. 094008, 2014.

Poly *N*-isopropylacrylamide (pNIPAM) is an important stimuli responsive hydrogel that undergoes a hydrophilic (swollen in aqueous media) to hydrophobic (deswollen) transition at a temperature just below physiological temperatures (LCST, between 32°C and 36°C).[80,113–116] Further, when combined with other materials either by co- polymerization, blending or layering, these hydrogels can be made responsive to heat,[22,30,37,117–133] pH,[134] light,[22,117,119,121,125] mechanical stress,[126] ionic strength[134,135] and magnetic field.[132,136] Consequently, NIPAM based hydrogels have been used in soft-robotics,[22,118,124,132,134–136] drug delivery[37,121,122,127,129,132,133] and surgery.[126]

Despite these advances, the mass-production and miniaturization of such soft cross-linked hydrogel actuators can be challenging. Further, heterogeneous integration with conventional micro-electro-mechanical systems is often required for functional systems which necessitate the development of processes to pattern these soft materials using high resolution and high throughput techniques such as photolithography, imprinting and molding. Precise structuring of complex three-dimensional (3D) structures is also needed for practical applications. An emerging methodology that overcomes these challenges is the self-folding of precisely patterned hydrogel thin films.[22,28,30,37,38,108,128–132,135] In these methods, existing planar lithographic approaches can be leveraged to create well defined patterns with high resolution and reproducibility. In contrast to previously described relatively higher temperature self-folding approaches for metallic or polymer patterns,[137–139] self-folding of hydrogels can be accomplished at physiologically relevant

temperatures in aqueous media. 3D actuation with large strains can be enabled by incorporating differential swelling of bilayers or films with compositional or cross-link gradients. For example, Klein *et al.* showed how compositionally heterogeneous pNIPAM films could be used to create buckling sheets.[123] Ionov *et al*. described thermo-responsive microcapsules based on pNIPAM-ABP/PCL bilayers.[37,129] Kim *et al.* demonstrated buckled gel surfaces using differential swelling of pNIPAM hydrogels using half-tone lithography.[130,131] Bassik *et al.* showed how pNIPAM-AAc/PEODA bilayers could be used to create flytrap like actuators.[134]

A new approach to create pNIPAM based self-folding systems is described as schematically represented in **Figure 3.1.** Specifically, we utilized co-polymerized pNIPAM-AAc hydrogels which reduces the response time as compared to single component pNIPAM hydrogels due to increased hydrophilicity[140,141] and the AAc component also makes the hydrogel pH responsive.[142] Our approach utilizes the fact that bending of hydrogel thin films depends on three important factors namely their thickness, modulus, and swelling ratio. We create two distinct regions within the hydrogel films; flexible hinges and rigid panels. In addition to being thinner, the flexible hinge also has a cross-link gradient[27] while the interconnecting panels are fully cross-linked and thicker. There are several advantages of our approach. As compared to many previous demonstrations of self-folding hydrogel actuators with bilayers, we use a single material that facilitates easy characterization and modelling for the homogeneous material. In addition, use of a single layer eliminates any risk of delamination that can be a concern in bilayer actuators. We demonstrate feasibility

of our approach and discuss a finite element model that can be used to predict fold angle. As compared to previous methods such as halftone lithography,[130] the thinner gradient hinge provides increased flexibility and larger fold angles, as illustrated in the model. Finally, we highlight several applications to illustrate practical applicability of the approach.

3.2. Materials and Methods

3.2.1. Materials

N-isopropylacrylamide monomer (NIPAM, Scientific Polymer Products Inc.), poly-N-isopropylacrylamide (PNIPAM, 300k MW, Scientific Polymer Products Inc.), N, N-Methylenebis-Acrylamide (BIS-Acrylamide, Aldrich), n-butanol (Sigma), irgacure 2100 (Ciba), acrylic acid (AAc, Aldrich), APS copper etchant 100 (Transene company, INC), Rhodamine 6G (Sigma Aldrich)

3.2.2. Synthesis of pNIPAM-AAc

The PNIPAM-AAc solution was prepared by dissolving 3g NIPAM monomer, 0.4g poly-N-isopropylacrylamide (pNIPAM) and 0.18g cross linking agent BIS-acrylamide in 7.5ml of n-butanol organic solvent. In addition, 100 μm photoinitiator Irgacure 2100 and 0.31 ml pH responsive monomer of acrylic acid (AAc) were added in pNIPAM base. Finally, this pNIPAM-AAc solution was stirred using a magnetic bar for at least 6 hours to dissolve completely.

3.2.3. Imaging of pNIPAM-AAc Hydrogel Structures

The pNIPAM-AAc hydrogel still images and videos were predominantly captured using a NIKON AZ100 multi-zoom microscope with an intensilight UV lamp and a

motorized stage for Z-stack image layers. A KEYENCE VK-X100K color 3D confocal laser microscope was used to take images of photopatterned 2D hydrogel images for thickness measurements. In addition, a Zeiss LSM 510 META confocal microscope was used for Z-directional sectioning images to investigate photo-crosslinking gradients along the thickness of thin pNIPAM-AAc hydrogel.

3.3. Fabrication of Crosslink Gradient pNIPAM-AAc Hydrogels

As illustrated briefly in **Figure 3.1.** and in a more detailed manner in **Figure 3.2.**, two spincoating and two photopatterning steps were utilized; (a) low energy UV light exposure on thin hinges and (b) high energy UV light exposure on thick panels. Different types and combinations of patterns can be created by the appropriate design of photomasks for thick panels and hinges. Details of the process are as follows.

Cr adhesion promoter (20 nm) and Cu sacrificial layer (200 nm) were thermally evaporated on commercial silicon wafer substrates. Then, the pNIPAM-AAc solution was spin-coated (Specialty Coating Systems, G3P-8 model) at 600 rpm to deposit the thick panels which were cross-linked by a high energy (500 mJ cm^{-2}) UV exposure, through a mask that was appropriately designed using AutoCAD. The pNIPAM-AAc solution was UV exposed in non-contact mode by separating the mask from the substrate by thin spacers. A commercial mask aligner (ultra μline series: Quintel) with a 350 W mercury vapor lamp was utilized. Specifically, UV exposure energy was measured by multiplying the exposure time with the UV exposure intensity measured using a UV power meter (Vari-Wave II, 365 nm sensor; Quintel). After UV exposure, the thick panels were developed by immersion in acetone for around 7 s, rinsing with

IPA and then drying using nitrogen gas. Then, thin hinges were patterned using a similar process except that the film were deposited at a higher spin speed to create a thinner film. Also, a second low energy (50 mJ cm^{-2}) UV exposure was selected to photopattern a cross-link gradient along the thickness of the hinges. Then, the hinges were developed as before. The patterned panel and hinge structures were released by dissolving the Cu sacrificial layer in a commercial Cu etchant (APS 100; pH = 2). The samples could be stored and remained unfolded up to a year in APS 100. Self-folding was trigged only on exposure to the correct thermal or pH conditions.

In order to accurately target folding angles of actuable pNIPAM-AAc structures, post-cross-link thickness of rectangular test structures versus spin speed were optimized at the same UV exposure (500 mJ cm^{-2}). We dispensed the pNIPAM-AAc hydrogel solution at six different spin speeds ranging from 600 rpm to 1200 rpm onto flat Si wafer substrates. Specifically, a color 3D pinhole confocal optical microscope (KEYENCE VK-X100K) was used to image and measure the thicknesses of photopatterned pNIPAM-AAc test structures. The thickness versus spin speed data is plotted in **Figure 3.3. (A)**. It demonstrates that the thickness could be reproducibly controlled between thin 1.6μm panels at the high spin speeds of 1200 rpm and thick 6.5μm panels at low spin speeds of 600 rpm. These films are thinner than the previously utilized pNIPAM self-folding structures which typically had thickness between 10 μm[130] and 225 μm.[134] Further, the resolution of our photopatterning process was measured using a ruler mask and the smallest feature that could be reproducibly patterned was 8 μm (**Figures 3.3. (B, C)**). Color images in **Figures 3.3.**

(D-F) show that different hinge and panel thickness could be implemented and also that the thickness within the fully cross-linked panels was relatively uniform.

3.4. Results and Discussion

3.4.1. Characterization of pNIPAM-AAc Hydrogels

By varying the patterns of thick fully cross-linked panels and thin gradient cross-linked hinges using AutoCAD designed photomasks, we were able to create a variety of structures. After fabrication and release from the substrate, the planar photopatterned structures were heated up to 60 °C in the copper etchant APS 100 solution (pH 2). Illustrative examples of a self-folded pyramidal and cubic shaped capsule are shown in **Figure 3.4.** The second and third columns in **Figures 3.4 (A, B)** shows the intermediate and final self-folding steps. We observed that the yield was approximately 60 % for well folded structures with no discernible defects when visualized by optical microscopy.

A key element of our approach is the creation of crosslink gradients on low UV exposure of 50 mJ cm^{-2}. The influence of such low and high exposure energy is evident in the patterning of hole sheets shown in **Figures 3.5. (A, B)**. Such sheets of identical thickness but exposed to low and high energy showed different self-folding characteristics. While sheets exposed to 500 mJ cm^{-2} buckle, they do not roll up due to the absence of a cross-link gradient (**Figure 3.5. (C)**). In contrast, identically shaped sheets patterned with a lower energy of 50 mJ cm^{-2} roll up due to a cross-link gradient along the thickness of the film (**Figure 3.5. (D)**). We characterized the cross-link gradients by adding a fluorescent dye (rhodamine 6G) into the pNIPAM-AAc

solution which was then sonicated for 30 min to form a well-mixed solution. The gradients in the films patterned with low UV exposure could then be visualized using confocal fluorescence microscopy (LSM 510 META, Zeiss). Specifically, we measured the relative pixel intensities from the top to bottom confocal images by depth discriminations and an intensity gradient was observed (**Figure 3.5. (E)**). This experimental data validates our approach of creating hinges with cross-link gradients for self-folding.

3.4.2. Thermo-responsive Deformation Mechanism of pNIPAM-AAc Hydrogels

In addition to experiments, we investigated the thermo-responsive deformation mechanism of the pNIPAM-AAc hydrogel via a 3D constitutive finite deformation model. The model assumes that the free energy change of the hydrogel system is caused by the mechanical stretching of polymer chains based on the classical Gaussian statistics and the polymer and solvent mixing based on Flory-Huggins model. Parameters of this model included the shear modulus and temperature-dependent Flory–Huggins interaction parameter. To determine the interaction parameter, the swelling mass ratio of cross-linked hydrogels was experimentally measured (**Figure 3.6.**). These measurements were carried out by spreading 500 µl pNIPAM-AAc solutions on a glass substrate, exposing the films to UV light with the relevant energies of 50 and 500 mJ cm^{-2} and soaking in DI water. We ensured that the samples reached equilibrium swelling by placing them on a hot plate at each temperature for at least 12 h.

The weight of the gel at this stage represents that of the swelling ratio $\Omega = \frac{Wt.of\ swollen\ gel}{Wt.of\ deswollen\ gel}$ was calculated by dividing the measured weight of the swollen gel at each temperature to that of the deswollen gel (dehydrated gel).

In addition to swelling ratios, the shear modulus of the swollen pNIPAM-AAc hydrogels was measured using a dynamic mechanical analyzer (Q800 DMA; TA instruments). The fully swollen samples exposed at high and low energies were both measured at room temperature in the dynamic mode, with a frequency sweep from 1 Hz to 10 Hz, and a 0.5 % applied strain. The storage modulus was independent of the frequency and is equivalent to the equilibrium Young's modulus. The shear modulus G is related with Young's modulus E as $G = \frac{E}{3}/\Omega_0{}^{1/3}$ where Ω_0 is the swelling ratio at the room temperature.

The constitutive model for the mechanical and swelling behavior of hydrogels is described below. Consider the deformation gradient, defined as $\mathbf{F} = \partial\mathbf{x}/\partial\mathbf{X}$, which describes the stretch and rotation of material lines from the dry stress- free body to the swollen and stressed body. The deformation gradient is decomposed into a mechanical part $\mathbf{F}_e$ and an isotropic swelling part $\mathbf{F}_s$ as $\mathbf{F_s} = \varphi^{\mathbf{-1/3}}\mathbf{F}_e$, where φ is the polymer volume fraction of the polymer-solute system at the swollen, stressed state. Since the gel is initially swollen, we define the initial swollen state as the stress-free reference state, and a deformation gradient **f** mapping the points from the stress free reference state to the final spatial points:

$$\mathbf{f} = \varphi_0^{\mathbf{1/3}}\mathbf{F} \tag{1}$$

where φ_0 is the polymer volume fraction of the polymer-solute system at the reference state. The polymer volume fraction is represented as $\varphi = 1/(1 + vc)$,[143] where v is the volume per solute molecule and c is the number of solute molecules per reference volume. We define the left Cauchy-Green tensor as $\mathbf{b} = \mathbf{F}\mathbf{F}^T$ and express it in terms of its eigenvalues (principal stretches) and eigenvectors (principal directions):

$$\boldsymbol{b} = \sum_{a=1}^{3} \boldsymbol{\lambda}_a^2 \ \boldsymbol{n}_a \otimes \boldsymbol{n}_a \tag{2}$$

where $\lambda_a = \varphi_0^{-1/3}\bar{\lambda}_a$ and $\bar{\lambda}_a$ are the corresponding principal stretches of **f**. We assume that free energy density of the total system is caused by the stretching of polymer chains and the mixing of polymer and solvent, and is represented as:

$$\Psi = \Psi_e(\mathbf{F}, \varphi) + \Psi_m(\varphi) \tag{3}$$

We adopt a quasi-incompressible model for the free energy density associated with stretching polymer chains[41]

$$\Psi_e = \frac{G}{2}\{\lambda_1^2 + \lambda_2^2 + \lambda_3^2 - 3 - 2\ln(\lambda_1\lambda_2\lambda_3)\} + \frac{\kappa}{4}\{(\varphi\lambda_1\lambda_2\lambda_3)^2 - 2ln(\varphi\lambda_1\lambda_2\lambda_3) - 1\} \tag{4}$$

where G and κ is shear modulus and bulk modulus respectively. We assumed the bulk modulus is 1000 times of the shear modulus to achieve the volumetric incompressibility of mechanical deformation.

The mixing component of the free-energy density is represented as[144,145]

$$\Psi_m = \frac{RT}{v\varphi}\{(1-\varphi)ln(1-\varphi) + \chi\varphi(1-\varphi)\} \tag{5}$$

where R is gas constant and χ is Flory-Huggins interaction parameter. The Cauchy stresses tensor $\boldsymbol{\sigma}$ and the chemical potential μ can be obtained from the free energy,[143,146] as

$$\boldsymbol{\sigma} = \sum_{a=1}^{3} \frac{1}{\lambda_1\lambda_2\lambda_3} \lambda_a \frac{\partial \Psi}{\partial \lambda_a} \boldsymbol{n_a} \otimes \boldsymbol{n_a} \tag{6}$$

$$\mu = \frac{\partial \Psi}{\partial \mathbf{c}} \tag{7}$$

Substituting equations (3) - (5) into equations (6) and (7) yields

$$\boldsymbol{\sigma} = \sum_{a=1}^{3} \left\{ \frac{G\varphi_0}{\bar{\lambda}_1\bar{\lambda}_2\bar{\lambda}_3} \left(\varphi_0^{-2/3} \bar{\lambda}_a^2 - 1 \right) + \frac{\kappa\varphi_0}{2\,\bar{\lambda}_1\bar{\lambda}_2\bar{\lambda}_3} \left[\left(\varphi\varphi_0^{-1} \bar{\lambda}_1\bar{\lambda}_2\bar{\lambda}_3 \right)^2 - 1 \right] \right\} \boldsymbol{n_a} \otimes \boldsymbol{n_a} \tag{8}$$

$$\mu = RT\{ln(1-\varphi) + \varphi + \chi\varphi^2\} - \frac{\kappa\nu\varphi}{2} \left\{ \left(\varphi\varphi_0^{-1}\, \bar{\lambda}_1\bar{\lambda}_2\bar{\lambda}_3 \right)^2 - 1 \right\} \tag{9}$$

To model thermo-responsive effect, we assumed the temperature dependent Flory-Huggins interaction parameter χ has the following form,[146]

$$\chi = \frac{1}{2}(\chi_{\mathrm{L}} + \chi_{\mathrm{H}}) + \frac{1}{2}(\chi_{\mathrm{H}} - \chi_{\mathrm{L}}) \tanh\left(\frac{T - T_{tran}}{\Delta T} \right) \tag{10}$$

where χ_{L} and χ_{H} is the Flory-Huggins interaction parameters at low temperature and high temperature, T_{tran} is the transition temperature and ΔT is the width of the transition region. These parameters were obtained by fitting the simulation free swelling data to the experimental results as shown in **Figure 3.6.** The parameters used in the model are listed in **Table 3.1.**

The constitutive model was implemented into TAHOE (Sandia National Laboratories) to simulate the self-folding pyramidal and cubic structures. **Figure 3.7.**

shows the finite element model of the pyramidal specimen (the finite element model of cubic specimen is not shown). The mesh was discretized using trilinear hexahedral elements and a higher mesh density was chosen at the hinge. For simplicity, we modeled the gradient in the hinges as a two-layer structure where the top layer of the hydrogel has a higher cross-linker density and corresponding smaller swelling ratio (G = 90 KPa and χ_L = 0.58) compared with the bottom layer with a lower modulus and higher swelling ratio (G = 60 KPa and χ_L = 0.562). The parameters for the model were chosen to reproduce the modulus and swelling ratio measured for the 50 mJ cm^{-2} materials shown in **Table 3.1.** The displacement boundary conditions were set as:

$$u_x\,(x=0,y,z)=0,\ u_y\,(x=0,y=0,z)=0,\ u_z\,(x=0,y=0,z=0)=0. \quad (11)$$

The simulation starts from stress free state at temperature T = 25 °C, at which temperature the structure is unfolded as shown in experiments. The initial polymer fraction φ_0 is obtained by solving equations (8) and (9) with the condition σ = 0 and μ = 0. The temperature is continuously increased to 37 °C. At each temperature, the deformation gradient **f** and polymer concentration φ are updated to satisfy the force balance and chemical potential equilibrium. From the simulation we can obtain the folding angle as a function of temperature (**Figure 3.8. (A)**). To verify the model, we measured the folding angles of cubic structures. We did not measure the folding angle of the pyramid structure because it was difficult to obtain an accurate angle from experiments. As shown in **Figure 3.8. (A)**, the simulation shows good agreement with the experimental data. We also did a parameter study by changing the thickness of

hinge. As expected, a thinner hinge yields a large folding angle as shown in **Figure 3.8. (B)**. In the present study, the thinnest hinge we could reproducibly deposit by spin coating was 1.6 μm which was used. If alternate techniques such as layer by layer, surface initiated polymerization or self-assembly are used, then thinner hinges could possibly be developed for even greater fold angles.

3.4.3. Applications of pNIPAM-AAc Hydrogels

Since, we can create a wide range of structures using this approach we highlight a few applications. In Figure 8, we show self-folding of a cubic container that assembled on heating. **Figure 3.9. (A, B)** indicates the high-throughput nature of the process so that many structures can be patterned and assembled at once. Once assembled, the structures can be loaded with cargo such as the beads shown in **Figure 3.9. (C)**. This example highlights possible utility of this approach to create self-folding capsules or containers. Further, transparency of pNIPAM-AAc faces permits visualization of the encapsulated cargo using optical bright filed or fluorescence microscopy.

In addition to capsules, we also highlight the combined thermally and pH responsive opening and closing of grippers (**Figure 3.10.**). These grippers close in environments of pH 2, T = 60 °C and open in environments of pH 7, T = 25 °C. These grippers were patterned with six symmetrical fingers and three joints in each finger. The reversibility of pNIPAM-AAc gripper was tested over several folding to unfolding cycles and no phenomenological residual plastic deformation was observed under parallel stimuli triggers between (60 °C, pH 2) and (25 °C, pH 7). We did however

observe that the soft digits sometimes adhered to each other or the underlying substrate.

Finally, stimuli responsive micro mirror scanners were designed to demonstrate proof-of-concept applicability in optics (**Figure 3.11.**). Recently, much research has been directed at the design and fabrication of smart material based optomechanical micro-mirrors.[147] Additionally, micro-mirror elements have been widely used in optical systems such as flat panel displays, optical interconnects, adaptive optical arrays and laser beam scanners.[148,149] They benefit from low weight, low operating optical power, compact design and sizes, which are potentially applicable to a variety of optoelectronic devices. We created five-faced pNIPAM-AAc structures with (500 μm x 500 μm) square Au mirrors that were attached using an epoxy. In order to highlight applicability of a thermally responsive micro-mirror steering system, we directed a beam of light at these structures. As depicted in **Figure 3.10. (A)**, a 650 nm red laser beam was expanded and collimated by a beam-expander and the collimated beam was coupled into 50 μm diameter multimode fiber core by a microscope objective lens (Plan 10x/0.25, Olympus). The distal end of the fiber was directed toward the gold mirror on the surface of hydrogel devices in **Figure 3.11. (B)**, thus incident light reflected by the micro-mirror through the 200 μm multimode fiber could be detected using an avalanche photodetector (APD110A, Thorlabs). When the structures self-fold in different environments, the beam of light changes from reflection from a single mirror to two mirrors separated by different distances as can be seen in **Figure 3.11. (C, D)**. In the present design, the distance between incident

and reflected beam vary from d= 0 mm to 2 mm. Hence, both the intensity and direction of the reflected beam thus varies with the environment and can be utilized for steering in optical beams or to decipher positional information. The advantages are that this approach is contactless and does not require an electrical or wired connections or external power sources.

3.5. Conclusion

In conclusion, we have developed a new approach to enable self-folding stimuli responsive microstructures. Photolithographic patterning of thin gradient cross-linked hinges and thick fully cross-linked panels have enabled advanced functionalities such as capsules, grippers and stimuli responsive micro-mirrors. We anticipate widespread applicability in optics, electronics, and robotics. A predictive finite element model was used to rationalize fold angles and its variation with hinge thickness and swelling ratio. Our study also highlights several important challenges. Notably increasing the speed of actuation to the sub-second time scales remains challenging. Additionally, increasing the resolution of lithographic patterning such as by imprint techniques could enable smaller structures. Finally due to the low modulus of hydrogels, such actuators are floppy and additionally work primarily in aqueous environments. The inclusion of more rigid elements[30] and microfluidic interfaces could be used to further expand their capabilities.

Table 3.1. Parameters determined for the pNIPAM-AAc materials synthesized with different UV intensities.

Parameters	G	χ_L	χ_H	T_{tran}	ΔT
500 mJ cm^{-2}	125 KPa	0.595	0.98	34 °C	5 °C
50 mJ cm^{-2}	74 KPa	0.570	0.98	34 °C	5 °C

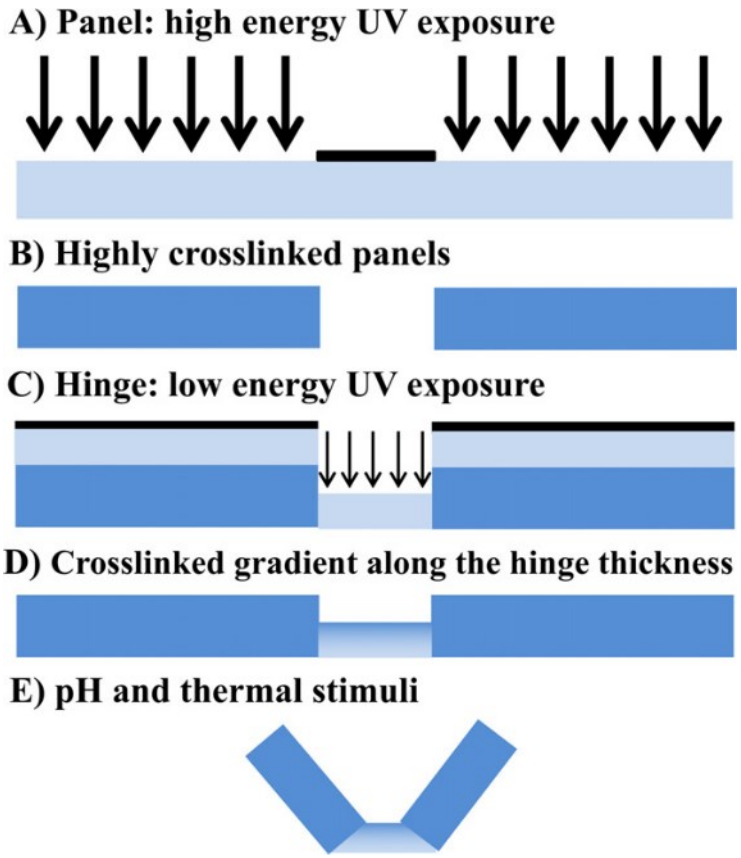

Figure 3.1. Illustration of the key steps utilized in creating 3D self- folding structures using thin, gradient cross-linked hinges and thick, fully cross-linked panels. (A)–(B) High energy UV exposed thick panels are fully crosslinked, while **(C)–(D)** low energy UV exposed thin hinges have crosslink gradients along their thickness. **(E)** On release from the substrate, and only when triggered by external thermal and pH stimuli, the patterns self-fold due to differential swelling and bending of the thin gradient cross-linked hinges.

Reprinted with permission from C. K. Yoon, R. Xiao, J. H. Park, J. Cha, T. D. Nguyen and D. H. Gracias, "Functional Stimuli Responsive Hydrogel Devices by Self-Folding," *Smart Materials & Structures*, vol. 23, pp. 094008, 2014.

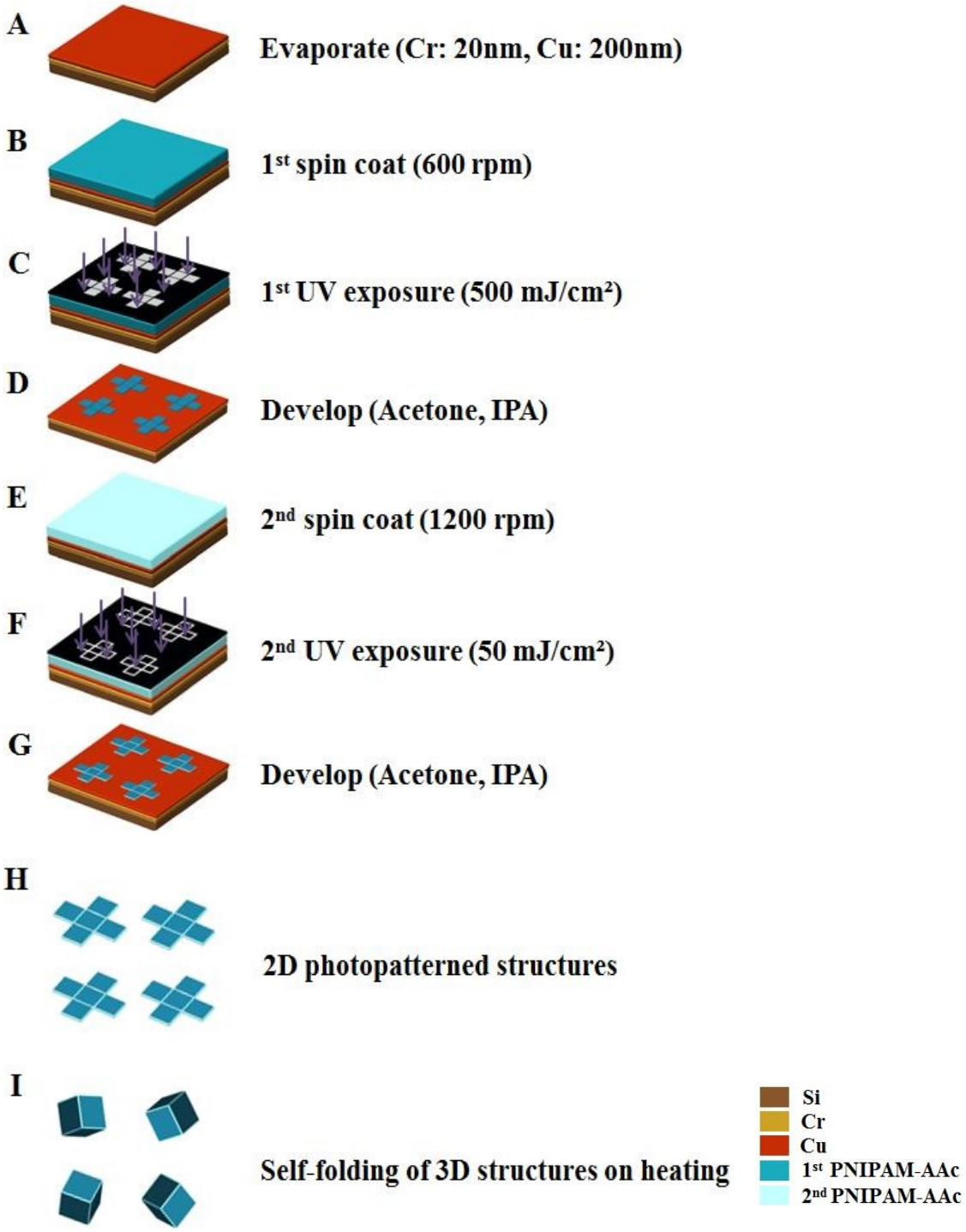

Figure 3.2. Detailed schematic of the fabrication process to photopattern and actuation of pNIPAM-AAc thin monolayer.

Reprinted with permission from C. K. Yoon, R. Xiao, J. H. Park, J. Cha, T. D. Nguyen and D. H. Gracias, "Functional Stimuli Responsive Hydrogel Devices by Self-Folding," *Smart Materials & Structures*, vol. 23, pp. 094008, 2014.

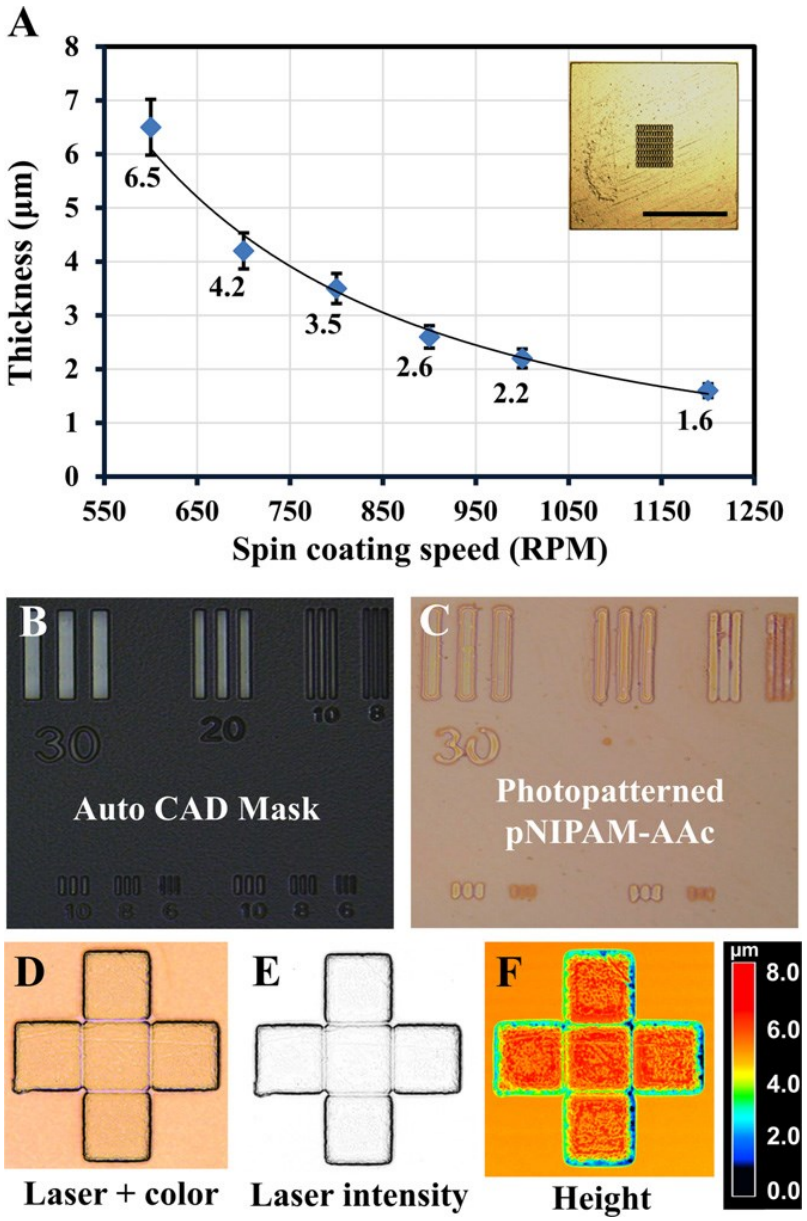

Figure 3.3. Characterization of the pNIPAM-AAc hydrogel deposition and patterning process. (A) Thickness versus spin speed. The inset shows the test structure, and the scale bar is 1 mm. Images depicting the **(B, C)** resolution and **(D–F)** uniformity of photocrosslinking.

Reprinted with permission from C. K. Yoon, R. Xiao, J. H. Park, J. Cha, T. D. Nguyen and D. H. Gracias, "Functional Stimuli Responsive Hydrogel Devices by Self-Folding," *Smart Materials & Structures*, vol. 23, pp. 094008, 2014.

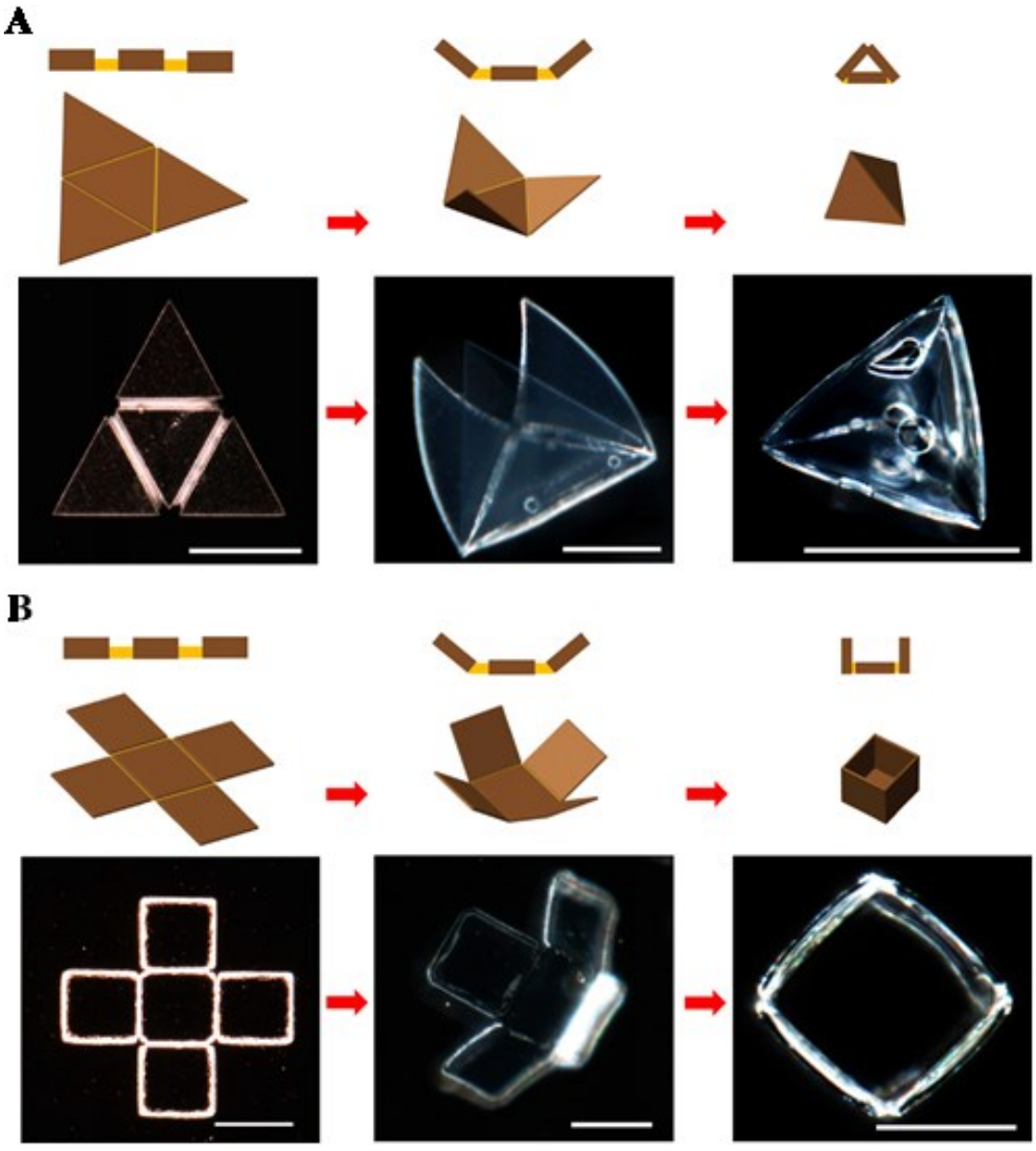

Figure 3.4. Schematic and optical microscopy images showing thermally responsive self-folding pNIPAM-AAc structures of different shapes such as a, **(A)** pyramidal, and **(B)** cubic shaped capsule. The optical images were taken using a NIKON AZ 100 microscope at pH 2 in APS 100 solution with increasing temperature from 25 °C to 60 °C. All scale bars are 300 μm.

Reprinted with permission from C. K. Yoon, R. Xiao, J. H. Park, J. Cha, T. D. Nguyen and D. H. Gracias, "Functional Stimuli Responsive Hydrogel Devices by Self-Folding," *Smart Materials & Structures*, vol. 23, pp. 094008, 2014.

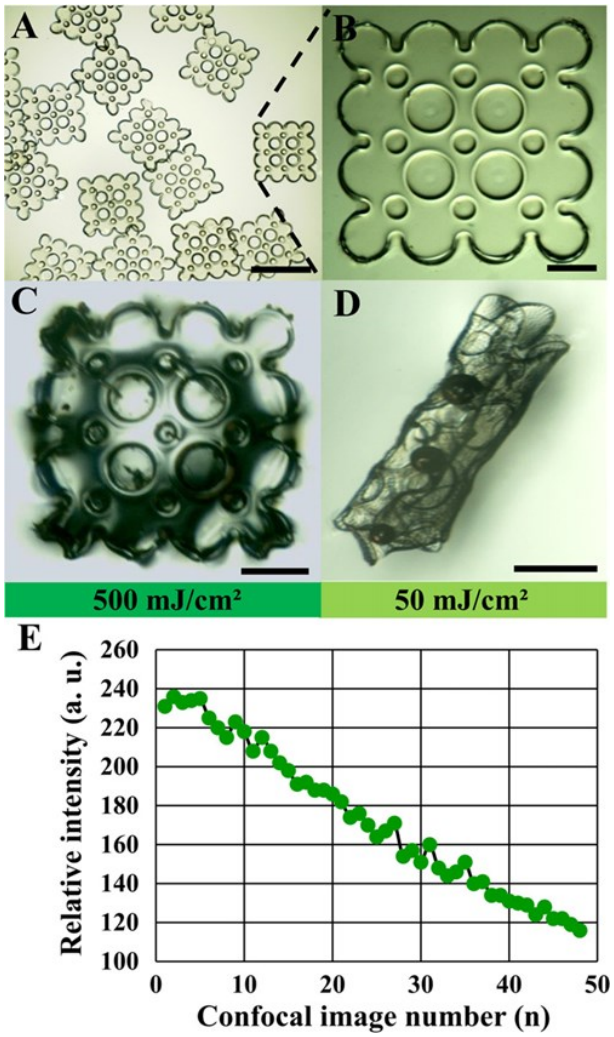

Figure 3.5. Characterization of the effect of UV energy exposure. (A) – (B) Optical and zoomed image of the holey test structure composed of a single pNIPAM-AAc panel. **(C)** Test structures exposed to high energy of 500 mJ cm^{-2} only buckled but did not roll up which is attributed to high crosslinking and absence of a crosslink gradient. **(D)** In contrast, test structures exposed to low energy of 50 mJ cm^{-2} rolled up indicating presence of a cross-link gradient. **(E)** Visualization of a cross-link gradient using confocal microscopy imaging of dyed low-UV exposed samples. Data shows a plot of the relative fluorescence intensity as a function of Z-section image stack. Larger confocal image numbers correspond to sections taken deeper into the sample. The low relative fluorescence intensity from these sections indicate a less-dense film (lower cross-linking). Scale bars are (A) 1.5 and (B–D) 300 μm.

Reprinted with permission from C. K. Yoon, R. Xiao, J. H. Park, J. Cha, T. D. Nguyen and D. H. Gracias, "Functional Stimuli Responsive Hydrogel Devices by Self-Folding," *Smart Materials & Structures*, vol. 23, pp. 094008, 2014.

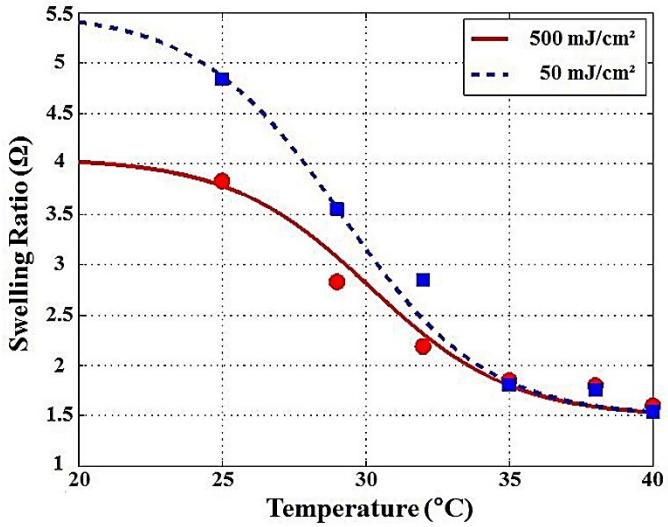

Figure 3.6. Swelling ratio versus temperature. Experimental (points) and simulation (lines) swelling ratios plotted as a function of temperature for low UV exposure (red circle, solid line: 50 mJ cm^{-2}) and high UV exposure (blue square, dotted line: 500 mJ cm^{-2}) energies.

Reprinted with permission from C. K. Yoon, R. Xiao, J. H. Park, J. Cha, T. D. Nguyen and D. H. Gracias, "Functional Stimuli Responsive Hydrogel Devices by Self-Folding," *Smart Materials & Structures*, vol. 23, pp. 094008, 2014.

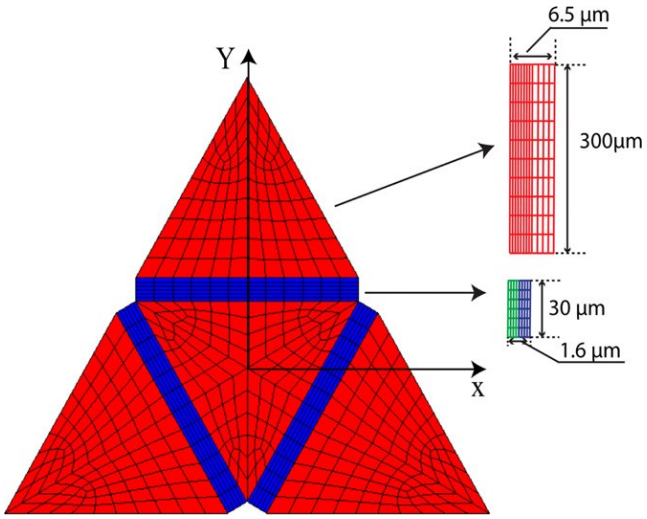

Figure 3.7. Finite element model of the pyramid specimen.

Reprinted with permission from C. K. Yoon, R. Xiao, J. H. Park, J. Cha, T. D. Nguyen and D. H. Gracias, "Functional Stimuli Responsive Hydrogel Devices by Self-Folding," *Smart Materials & Structures*, vol. 23, pp. 094008, 2014.

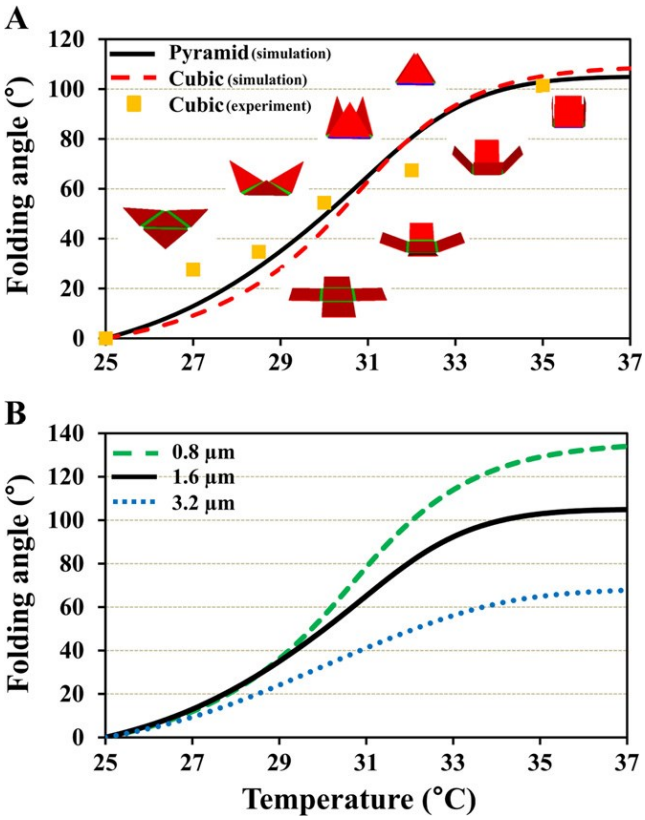

Figure 3.8. Experiments and simulation results of folding angles of pNIPAM-AAc structures according to temperature. (A) Experimental and simulation results of the folding angle of pyramidal and cubic structures having 1.6 μm thickness as a function of temperature. **(B)** Simulation results of folding angles of the pyramidal structure having different hinge thickness of 0.8, 1.6, and 3.2 μm as a function of temperature. Thinner films show larger fold angles.

Reprinted with permission from C. K. Yoon, R. Xiao, J. H. Park, J. Cha, T. D. Nguyen and D. H. Gracias, "Functional Stimuli Responsive Hydrogel Devices by Self-Folding," *Smart Materials & Structures*, vol. 23, pp. 094008, 2014.

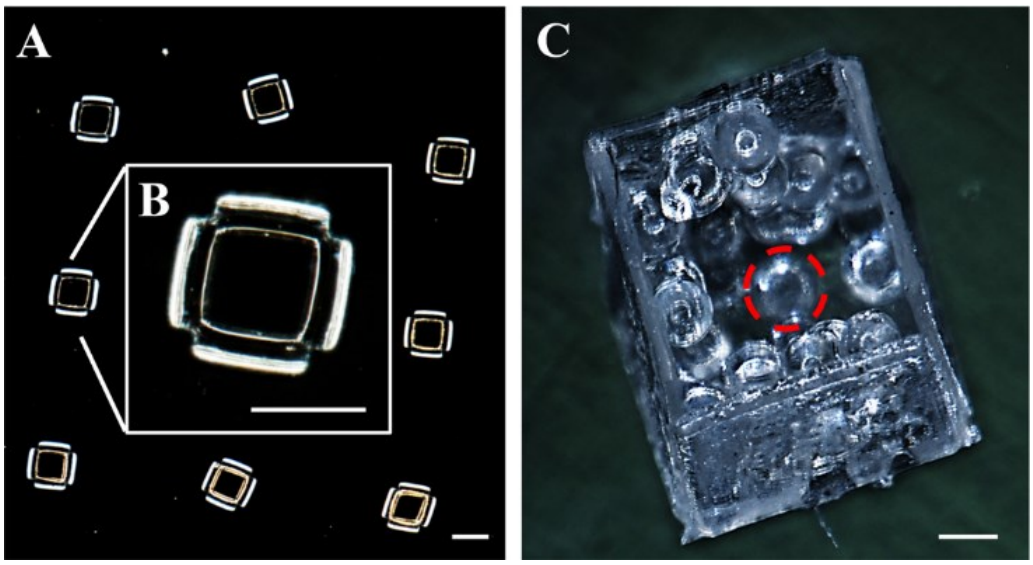

Figure 3.9. Parallel self-folding of cubic capsules with thick highly cross-linked panels and thin gradient cross-linked hinges. (A) Top view optical image of the self-folded capsules, **(B)** zoomed inset of a cubic capsule, and **(C)** image of a cubic capsule loaded with beads. One of the transparent beads is outlined with a red dotted circle to aid visualization. All scale bars are 350 μm.

Reprinted with permission from C. K. Yoon, R. Xiao, J. H. Park, J. Cha, T. D. Nguyen and D. H. Gracias, "Functional Stimuli Responsive Hydrogel Devices by Self-Folding," *Smart Materials & Structures*, vol. 23, pp. 094008, 2014.

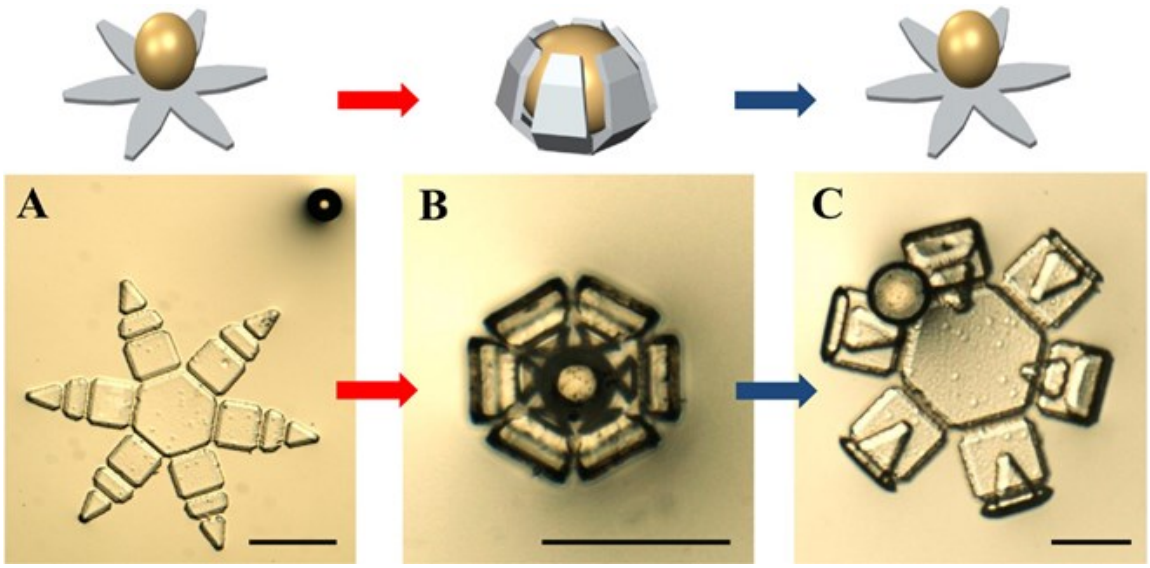

Figure 3.10. pNIPAM-AAc hydrogel grippers. (A)–(C) Sequential snapshots showing closing (60 °C in pH 2) and opening (25 °C in pH 7) of a gripper around a 250 μm bead. Scale bars are, **(A)** 550 μm, **(B)** 650 μm, and **(C)** 400 μm.

Reprinted with permission from C. K. Yoon, R. Xiao, J. H. Park, J. Cha, T. D. Nguyen and D. H. Gracias, "Functional Stimuli Responsive Hydrogel Devices by Self-Folding," *Smart Materials & Structures*, vol. 23, pp. 094008, 2014.

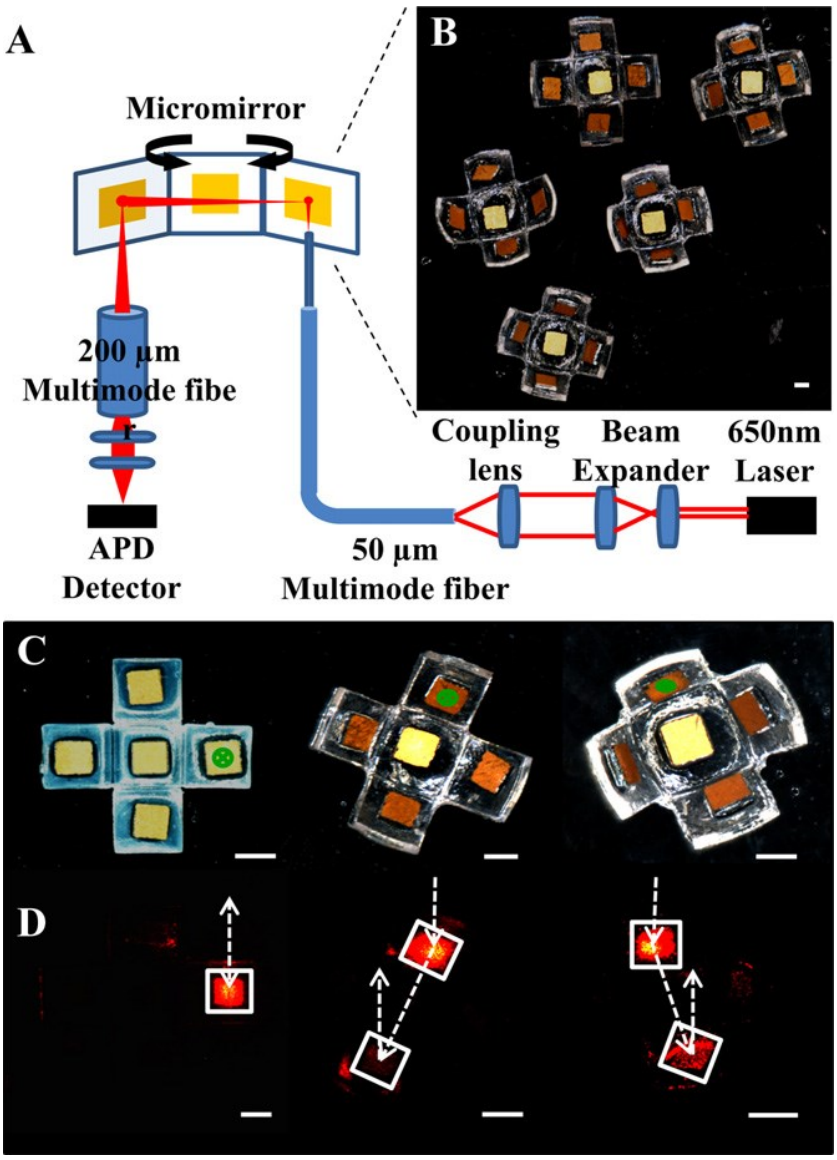

Figure 3.11. Stimuli responsive thermally steered optoelectronic micro-mirror system. (A) Schematic of micro-mirror system that utilizes a 650 nm laser and fiber optics. **(B)** Samples of 3D self- actuating systems composed of pNIPAM-AAc hydrogel actuators with gold micro mirrors. **(C)** Sequence of thermally responsive self- folding and **(D)** corresponding light incidence and reflection as depicted by the white lines and arrows. The white squares depict the Au mirrors. All scale bars are 500 µm.

Reprinted with permission from C. K. Yoon, R. Xiao, J. H. Park, J. Cha, T. D. Nguyen and D. H. Gracias, "Functional Stimuli Responsive Hydrogel Devices by Self-Folding," *Smart Materials & Structures*, vol. 23, pp. 094008, 2014.

4. Programmable, High-degree Expansion of Micropatterned DNA Copolymer Hydrogels*

4.1. Overview

Stimuli-responsive self-folding devices have important applications in the design of therapeutics, soft actuators, and the low-cost assembly of three dimensional materials. Chemomechanical self-folding systems are of particular interest because they do not require the inclusion of wires or batteries and can operate untethered and at smaller size scales. Current chemomechanical systems can respond to a small number of extrinsic stimuli, such as light or pH, by folding into one or two possible final structures. Here we report the micropatterning and self-folding of chemomechanical devices that fold in different ways in response to different DNA sequence inputs. These devices consist of an arrangement of different hydrogel domains and are micropatterned using a high-throughput lithography process; swelling of some domains but not others drives folding. Because folding is induced by DNA hybridization, it is straightforward to design a combinatorial variety of material domains that each swell in response to a DNA input of particular sequence. The hybridization process can drive very high-degree swelling of individual hydrogel domains.

---

* Reprinted with permission from

1. A. Cangialosi[#], C. K. Yoon[#], J. Liu, Q. Huang, T. D. Nguyen, D. H. Gracias, and R. Schulman, "Macroscale Sequence-Selective Shape-Change driven by Photopatterned DNA hydrogels with High Swelling," *In Preparation*, 2017. [#]: Equal contributions.

Furthermore, the degree of swelling of individual domains can be controlled by the nature of the biomolecular inputs, enabling the design of versatile but well-controlled folding processes. We demonstrate that multi-domain devices can fold into many different forms depending on the DNA sequence inputs presented. Because DNA sequences can serve as inputs and outputs of synthetic sensors, logic circuits and signaling cascades, folding driven by DNA sequence introduces the possibility of designing complex programs that direct autonomous folding, i.e. motion programs, that are triggered in response to a particular stimulus or combinations of stimuli. Such devices therefore could serve as a basis for the development of metamorphic materials and autonomous soft robots.

4.2. Introduction

Materials and devices that leverage the large variability, specificity and programmability of biomolecular interactions to drive macroscale shape change are important in the design of soft robots, programmable matter, smart medicine and autonomous systems. Among biomolecules, DNA sequences when integrated within structures can offer significant advantages due to their binary, predictable, base pairing. Indeed, DNA hybridization process can drive changes in the shape of nanostructures,[150,151] thin films[152] or colloidal crystals[153,154] but the creation of macroscale devices have been limited by the relatively modest changes in hybridization size induced by simple DNA hybridization processes. The design of shape-changed based DNA devices has further been hindered by limited patterning and scalable integration processes. Here, we demonstrate how DNA hybridization

cascades can induce up to 64-fold volumetric expansion of DNA co-polymer hydrogels in a sequence-selective fashion, such that control over swelling degree and rate may be further tuned using sequence design. We developed a new class of millimeter to centimeter scale shape-change devices, by photopatterning and scalable integration of architectured DNA co-polymer hydrogels with as many as three different DNA-sequence domains. The resulting macroscale structures can change shape dramatically in multiple different ways in response to DNA sequence inputs. We characterize the mechanical properties and swelling rates using a combination of experiments and finite element simulations and realize selectively shape changeable microstructures such as flowers and a crab. Since DNA sequences can serve as inputs and outputs of synthetic sensors, amplifiers, logic circuits and controllers, patterned shape change structures driven by the DNA sequence introduces the possibility for soft materials and functional devices that respond to a diverse array of chemical inputs by autonomously implementing adaptive chemical control programs.

A common design for smart materials and devices is a heterogeneous, patterned architecture in which a specific chemical or physical stimulus results in swelling or shrinking of one or more regions of the material.[108,130,155] For example, selective swelling or shrinking of domains have been used to create a wide range of self-folding, shape change and bioinspired devices. However, in previous demonstrations, response has been limited to stimuli such as temperature, light, electromagnetic signals or pH.[134,156] Indeed versatility and programmability can be significantly enhanced by wiring the material to locally control material properties and enable

multi-state shape change, but wires add physical bulk and require batteries or tethering, limiting the scope of their operation. Due to the variability of vast libraries of chemicals, the exquisite specificity of molecular interactions and the fact that molecules can diffuse over large distances and through small sub-nanometer sized spaces, chemomechanically responsive materials present obvious advantages in programmability, device integration and miniaturization. In addition, chemicals and especially biomolecules provide a route to enable complex feedback processes and interaction networks as seen in biological cells, tissues and organs.

We asked whether we might bring the specificity and multi-state behavior attainable within wired systems to a chemomechanical system by patterning materials consisting of a combinatorial variety of domains that each responded to a unique chemical trigger, such that a large number of domains could be swollen addressibly. To enable biomolecular interactions to drive shape change, we focused on hydrogels, where structural changes within cross-link segments can drive expansion or contraction in aqueous media. In particular we utilized DNA molecules that can hybridize in a sequence dependent fashion such that large numbers of these molecules can act independently in a single environment.[157,158]

An initial challenge to designing a system in which different DNA sequences, or more generally heteropolymers induce swelling is that a large amount of swelling is needed to produce interesting motion driven by chemomechanical interactions. Most polymer materials achieve this shape change through a change in pH or temperature that triggers a dramatic change in solvent uptake,[159] while other materials swell when

hydrated or dehydrated.[52,160] While biomolecules can significantly stiffen or soften hydrogels,[161,162] these changes cannot direct folding or motion without pre-stressing the original device, which makes fabrication difficult and also limits the range of motion.[163]

We began by considering DNA crosslinked polyacrylamide hydrogels in which DNA duplexes crosslink polyacrylamide chains into a hydrogel network (**Figure 4.1. (a)**).[164] These hydrogels have been studied extensively as substrates for molecular sensing,[165–170] dynamically controlled gelation or stiffening,[171,172] or as materials that can swell or shrink in response to pH or specific reagents.[37,156] Specific DNA molecules can induce a change in the crosslinks that can stiffen and/or swell materials through hybridization and assembles new crosslinks or stiffens existing ones, although this swelling has been limited to 10-15 %. We postulated that a greater degree of swelling could be achieved using a DNA hybridization cascade in which DNA hairpins are inserted into crosslinks via strand displacement, lengthening them (**Figure 4.1. (b)**). Such a mechanism has been used as a hybridization-driven motor that can push nanoscale objects away from one another.[173] Because double stranded DNA, with a persistence length of 50 nm[174] is significantly stiffer than polyacrylamide chains, such an extension could effectively push the network by pushing the flexible chains, leading to significant swelling.

To test this theory, we first developed a method to pattern hydrogels into precisely defined, thin shapes and architectures using photolithography. DNA molecules could diffuse into a thin material readily, while precise control over shapes

and the ability to assemble many structures in parallel would allow the precise characterization of swelling behavior of many identical hydrogels. Such a technique, through multistage fabrication, could also readily be extended to the assembly of architectured materials in which different DNA crosslinks swell in response to different DNA sequences that extend them.

4.3. Fabrication of DNA Crosslinked Hydrogels

The overall protocol for preparing DNA copolymer hydrogels involves preparation of the DNA pregel solution and photolithographic fabrication of the gel structures.

4.3.1. DNA-co-Am and BIS-co-Am Solutions Preparation

All oligonucleotide sequences are listed in **Table 4.1.** The sequences for strands A_1, R_1, H_1, and H_2 are the reverse of those used in Venkataraman *et al*.[173] DNA samples were supplied by Integrated DNA Technologies (IDT) in their lyophilized form. Oligonucleotide stock solutions were prepared by resuspending samples in 1x TAE buffer (12.5 mM Mg^{2+}) to a final concentration of approximately 25 mM. Oligonucleotide concentrations were verified by absorbance spectroscopy at 260 nm. The final hydrogel solution consisted of 1.154 mM of each ssDNA species, 1x TAE buffer (50x stock, Life Technologies, Catalog #24710-030), 12.5 mM magnesium acetate tetrahydrate (Sigma M5661), 11.1 mM of calcium chloride, 1.41 M acrylamide (Bio-Rad Catalog #161-0100), and 3 % (v/v) of Irgacure 2100 (Ciba). To prepare the DNA copolymer gel, the acrydite-modified strands were added to a solution of 1x TAE, magnesium acetate tetrahydrate, and MilliQ water and incubated at 90 °C for five

minutes, then annealed from 90 °C to 20 °C at 1 °C per minute. Immediately before photopolymerization, acrylamide and photoiniator Irgacure 2100 were added to the solution, followed by degassing for 5 minutes under vacuum. All designed DNA base sequences are described in **Table 4.1.**

Oligonucleotides SA_3 and SA_4, each 20 nucleotides long and of random sequence, were modified at the 5' end with Acrydite. The 50 base pair crosslinking oligonucleotide (designated L_2) contained domains complementary to SA_3 and SA_4 along with a 10 base pair toehold domain at the 3' end to allow for removal of the crosslinking strand. The final hydrogel solution consisted of 1.154 mM of each ssDNA species, 1x TAE buffer (50x stock, Life Technologies, Catalog #24710-030), 12.5 mM magnesium acetate tetrahydrate (Sigma M5661), 1.41 M acrylamide (Bio-Rad Catalog #161-0100), and 3 % (v/v) of Irgacure 2100 (Ciba). First, DNA strands SA_3, SA_4, and L_2 were added to a solution of 1x TAE, magnesium acetate tetrahydrate, and MilliQ water and allowed to hybridize for 30 minutes at room temperature. To this solution was added acrylamide (from a stock solution of roughly 11 M), and Irgacure 2100. The hydrogel solution was then mixed thoroughly by pipet to minimize the incorporation of air bubbles. The solutions were then degassed under vacuum for 5 minutes to minimize the O_2 (g) concentration in solution.

4.3.2. Photolithography Chambers Preparation

Top slide of the photolithography chambers which served as a chromium (Cr) photomask, was prepared by spin coating SC 1827 (Microposit) on a clean glass slide at 3500 rpm and baking at 115 °C for 60 seconds. The glass slides were UV exposed

at 360 mJ/cm^2 through different film masks designed by AutoCAD. After UV exposure, the glass slides were developed with a 1:10 (w/w) solution of 351 (Shipley) and DI water, after which they were rinsed with DI water and dried with N_2 gas. Next, a 200 nm layer of Cr was deposited on the glass slide by physical vapor deposition (PVD), after which the slides were rinsed with acetone, IPA, and dried under N_2 gas to remove the non UV light reacted regions of 1827 photo resist. Once prepared, Cr mask was spin-coated with CYTOP (Type M, Bellex International Corp.) at 4000 rpm and subsequently baked at 90 °C for 2 hours to ensure evaporation of the organic solvent.

Bottom slide of the photolithography chambers were prepared by sonicating glass slides (Catalog #16004-424, VWR) for 30 minutes in 10 % (w/w) NaOH, rinsed with MilliQ water, and dried under N_2 gas. The slides were then treated with O_2 plasma for 5 minutes to fully oxidize the glass surface. Next, a single layer of polyimide tape (~30 μm thick) was placed along the width of the glass slide to act as a spacer. Then, the sacrificial layer was covered with PAA. The PAA sacrificial layer was prepared by 25% PAA (w/v) stock solution was mixed with 10 % NaOH (w/v) to make pH ~7.5. MilliQ water was added in the neutralized 25 % PAA stock solution to prepare 5 % (w/v) solution of PAA and then filtered using 0.5 μm pore size filter. The 5 % (w/v) PAA solution was spin coated onto O_2 plasma treated clean glass slide at 3000 rpm for 15 seconds. The PAA coated glass slides were baked on hot plate at 150 °C for 3 minutes and then soaked the dried PAA coated glass slides were soaked

in 1M $CaCl_2$ for 1 minutes, DI water for 3 minutes. Then, the slides were baked again on hot plate at 150 °C for 5 minutes.

4.3.3. Self-folding DNA Crosslinked Hydrogel and Imaging

As illustrated in **Figure 4.2. (a)**, the Poly(DNA-co-Am) and Poly(BIS-co-Am) hydrogels were photopatterned using easily assembled photolithography chambers that were constructed from glass slides separated by tape spacers. The glass bottom slide served as a substrate onto which the hydrogel samples adhered after photopatterning, while the top slide served as a photomask to selectively expose the pre-gel solution to ultraviolet (UV) light and initiate photopolymerization. Specifically, the DNA hydrogel solution was aliquoted onto a PAA (sacrificial layer) spin-coated clean glass slide with polyimide tape spacers. The Cr mask (coated with CYTOP) was then placed on top of the hydrogel solution and glass substrate. The photolithography chamber was then clipped with metal binders (Office Depot) and first BIS-co-Am solution was injected between the top and bottom chambers by using syringe. The chambers were then exposed to UV light (280 mJ/cm^2) (Neutronix Quintel aligner). A UV exposure energy of 280 mJ/cm^2 was calculated by multiplying the measured UV intensity (Vari-Wave II, 365 nm sensor; Quintel) by the exposure time. After photopatterning, the chamber was disassembled and washed with 200µL of 1x TAE buffer (12.5 mM Mg^{2+}) + $CaCl_2$ to the hydrogel samples, which were preferentially adhered to the bottom slide and dried. To make the second layer of poly (DNA-co-Am), another spacer was added and the Cr masks were then aligned with poly(BIS-co-Am) photopatterns under microscope. After getting precise aligning with

first photopatterned BIS-co-Am thin layer, second solution of DNA-co-Am solution was injected into the chambers again. Then, 250 mJ/cm^2 UV light was exposed through the top Cr mask to the bottom. Then, the chambers were apart and the photopatterned bilayer thin structures were released from the PAA sacrificial layer by dipping in the 1ml NaCl solution. The free standing bilayer structures were transferred to the PDMS coated petri dishes and 1ml 1x TAE buffer was gently put in the petri dish. In more detail, to make the non-sticky surface with photopatterned thin DNA/BIS bilayers, 1:10 curing agent mixed PDMS (Dow Corning) were spin coated on the petri dishes at 4000 rpm and baked at 60 °C for 12 hours and O_2 plasma (100 W, 240 s) was exposed to treat the PDMS surface making them hydrophilic. The photopatterned samples in the PDMS coated petri dish with 1ml NaCl and 1ml 1X TAE were added another 1ml 10x SYBR Green (Catalog #S-11494; Life Technologies) or/and rhodamine to get fluorescence staining. The hydrogel samples were kept in the fridge over 18 hours to allow to stain SYBR Green or/and rhodamine in the DNA or BIS crosslinked hydrogel layers and get fully swollen hydrogels. The samples were stayed on the station for two hours at room temperature before actuation test under microscope.

All fluorescence optical images were taken using a Nikon AZ100 multi-zoom microscope at 0.5x objective with the intensilight UV lamp and Nikon DS-Fi1 camera. Specifically, fluorescent images were captured using a Nikon B-2E/C blue excitation filter (420-495 nm) for DNA crosslinked hydrogel (Green color images) and green excitation filter (510-560 nm) for BIS crosslinked hydrogel (Red color images)

visualization. In addition, to check the programmability of swelling power of DNA crosslinked hydrogel, gel imager (MODEL) was used to take sequential snap shots at each swelling states of DNA hydrogels.

4.4. Results and Discussions

4.4.1. Fabrication of DNA Crosslinked Hydrogel System

We photopatterned DNA-crosslinked hydrogels using free radical initiation and UV irradiation through CAD designed photomasks. Unlike silicon based devices for which many photolithographic processes have been developed, photopatterning of DNA hydrogels present unique challenges. DNA-crosslinked hydrogels have orders of magnitude lower moduli as compared to silicon or even conventional photoresists and also tended to stick to the substrate and photomask, potentially because of charge mediated interactions involving the DNA. Furthermore, UV light damages DNA and the intensity of UV light needs to be optimized.[175] To address these concerns, we developed a process in which a precise amount of light exposure drives fabrication, and structure thickness is controlled by solid spacers and sandwiched glass slides that presented a chrome mask. Cytop, a hydrophobic fluoropolymer was found to reduce sticking of the DNA hydrogels to the chrome mask, and a calcium sensitive sacrificial layer enabled benign and damage-free release of the structures after patterning. Structures on the millimeter scale with thickness ranging from 15 to 100 μm were using this process, and multiple domains could be patterned serially using mask alignment with registry to underlying layers. Incorporation of fluorescent dyes into the polyacrylamide chains enabled multiple domains to be distinguished using

fluorescence microscopy (**Figure 4.2. (b)**). Multiple structures could be fabricated in parallel, and after fabrication, structures were stable in buffer at room temperature or at 4 °C for up to 6 months,

4.4.2. Characterization of DNA Crosslinked Hydrogels: Swelling

To determine whether the crosslink lengthening using hybridization cascades that we envisioned could induce significant swelling of a DNA-crosslinked hydrogel, we fabricated 32 μm thick hydrogel squares 1 mm on a side and added them to a buffer solution containing 20 μM of each hairpin (H_1 and H_2). The hydrogels expanded at least 200 % in both the X and Y directions but maintained a square shape, suggesting that growth occurred through swelling, as designed.

Time-lapse imaging of the structures in the presence of an excess of H_1 and H_2 solution showed that swelling occurred at a roughly linear rate until they had expanded at least 4-fold in each direction (**Figure 4.3. (a, b)**). The expansion of the gels continued unabated at least until the gels were so faint as to be no longer visible, with gel corners and edges generally receding from view fist. Because the gels presumably grew more than 100-fold in volume but incorporated a relatively small amounts of material other than solvent, one possibility is the polyacrylamide, while still part of a connected network, effectively de-gelled due to its reduced concentration.

While these initial experiments suggested that while the DNA polymerization cascade that extended crosslinks could indeed drive high-degree swelling, this swelling was difficult to control. We next asked whether it was possible to tune

swelling so that a hydrogel domain would swell to a certain extent and then remain stable at its new size. To build a system in which crosslink polymerization, and thus swelling, would finish after some period of time, we introduced modified DNA hairpins, which we called "terminator hairpins" that could insert into a crosslink and extend it, but after insert presented no further sites for crosslink extension (**Figure 4.3. (c)**). Gels swollen by a mix of regular and "terminator" hairpins swelled but then reached a fixed final size. By tuning the ratio of the regular and terminator hairpins, we were able to tune the degree of swelling over a broad range.

These experiments also suggested that a significant degree of polymerization occurred during the expansion process. Samples swollen with 1% terminator, where average polymer-length would be up to 100 pairs of hairpins expanded more than samples with 2 % terminator, where average crosslink length would be expected to be about 50 pairs of hairpins. Interestingly, such chains are significantly longer than the 50 nm persistence length of double-stranded DNA, suggesting that the crosslinks need not be perfectly rigid to induce expansion. In addition, this swelling behavior was verified by introducing random DNA reaction solution of PolyT as a control. When comparing **Figure 4.3. (d)** and **(e)**, only H_1 and H_2 hairpins were reacted with square shaped DNA crosslinked hydrogels.

4.4.3. Characterization of DNA and BIS Bilayer Bars

To test whether swelling of DNA crosslinked hydrogels could induce shape change, we photopatterned a hydrogel bilayers in the shape of a beam with a 32 μm-thick BIS-crosslinked polyacrylamide layer on the bottom and a 32 μm thick DNA-

crosslinked hydrogel that responded to the first hairpin system described at **Figure 4.4.** The beams were immersed in buffer in order to equilibrate in buffer and curved during this process, probably because the DNA-crosslinked hydrogels swell due to solvent uptake after fabrication to a different degree than BIS-crosslinked hydrogels do. Afterwards, the bilayers were placed either in a solution containing a hairpin with a unreactive "control" DNA sequence or in a solution containing the 98% polymerizing / 2% terminating hairpin mixture that induced swelling in previous experiments. The bilayers in the polymerizing hairpin solution curved tightly (**Figure 4.5. (a)**). This bilayer in the polymerizing hairpins H_1 and H_2 solution curved significantly driven by the swelling of the DNA crosslinked layer. However, the BIS crosslinked layer did not swell in response to any of those hairpins so that interrupting swelling at the DNA/BIS interface caused mechanical bending. The next **Figure 4.5. (b)** shows the sequential folding steps of DNA/BIS bilayer bar after introducing H_1 and H_2 solutions.

4.4.4. Finite Element Analysis: Radius Change of DNA/BIS Bars

To understand how DNA polymerization-driven swelling can drive folding of architected hydrogels, we developed a finite element model of the folding process. We used the measured bulk modulus of the DNA- and BIS-crosslinked hydrogels and the degree of swelling observed in DNA-crosslinked hydrogels as parameters to constrain the system. We tested how folding was predicted to occur within the model for various values of the modulus and swelling ratio of the fully swollen DNA crosslinked hydrogel (**Figure 4.5. (c,d)**). We found that the model predicted several

qualitatively distinct folding pathways for different values of this modulus but that the folding behavior of the system matched our experiments best for a final modulus of 229 Pa. We used this modulus value in models that predicted the folding of more complex structures in relatively good agreement with experiment.

4.4.5. Multi-state Fabrications of Complex Shaped DNA and BIS Hydrogels

The multistage fabrication technique can ensemble complex shaped multi domain DNA crosslinked hydrogel systems that demonstrate programmable selective chemomechanical actuations in response to different DNA inputs. In order to illustrate expansion of complex shaped multi domain DNA and BIS hydrogel systems, one BIS crosslinked and two 98 % polymerizing / 2 % terminating hairpin mixtures of DNA crosslinked solutions were prepared with corresponding external reactant hairpin solutions. In more detailed fabrication steps, biomimetic flower shaped 1st six fingers BIS crosslinked layer was photopatterned and then 2nd four fingers and 3rd two figures DNA crosslinked hydrogel layers were aligned and photopatterned on top of 1st six fingers BIS crosslinked hydrogel layer (**Figure 4.6. and 4.7 (a)**). The fully swollen flower-shaped DNA crosslink hydrogel samples were allowed to stain SYBR Green or rhodamine in the DNA or BIS crosslinked hydrogel layers to get fluorescence images. When all reactant DNA solutions were introduced simultaneously, all fingers were bent due to the DNA reaction driven swelling from the each domains of DNA hydrogel finger patterns (**Figure 4.7. (b)**). Furthermore, the selective lock-and-key type reactions were verified by two different combinations of DNA reaction orders (**Figure 4.7. (c)**). It emphasize clearly that 2D photopatterned combinational

DNA/BIS bilayers including multiple domains could be folded selectively driven by lock-and-key type DNA hybridization. These photolithographically patterned DNA crosslinked flower shaped hydrogels show the programmability of selective chemomechanical actuation systems in response to particular sequences of external DNA inputs with large swelling power.

Finally, more complex shaped multi-domain and selective chemomechanical actuation systems were tested by multi-step fabrications of complex geometry such as biomimetic crab shape. **Figure 4.8.** shows fabrication steps to create a crab shaped hydrogel that are composed of different parts such as hexagonal shaped body, eight legs, two grippers, and two antennas (**Figure 4.9 (a)**). Experimentally, all different sections of a crab were photopatterned by using one BIS and three different DNA sequences solutions. We found that it was possible to swell individual domains, by presenting DNA sequences that inserted specifically into that domain's crosslinks, and to swell multiple domains simultaneously. Swelling could proceed sequentially through a process of buffer exchange, in which structures were removed from a solution containing one combination of DNA sequences and placed into another. Selective actuation enabled the folding of all together or the selective curling of the antennas, grippers and legs of a crab (**Figure 4.9 (b, c)**). It clearly indicates that VLSI based photolithographic strategy, through multistage fabrication steps, could readily be envisioned to integrate high selective DNA chemomechanical reaction driven hydrogel actuators.

4.5. Conclusion

Biological tissues demonstrate the versatility and functionality of shape change driven by biomolecular signals. Different types of cues can direct different responses and signal transduction cascades can amplify signals or integrate information about multiple different cues. Variations in chemical concentrations or ratio can direct how shape change occurs, and mechanochemical sensors can regular and modulate shape change through chemical feedback loops. Collectively such processes enable multistage, goal directed behavior that is impossible to achieve using existing mechanisms of soft material actuation.

Here, we have shown how synthetic biomolecules, DNA oligonucleotides, can act as easy-to-design signals for combinatorial actuation within synthetic systems. Molecular sequence, concentration ratios and other free parameters can rationally tune not only what is swollen, but swelling extent. Complex architectures and multi-domain devices can be readily fabricated and a virtually limitless array of devices can conceivably be created via a simple process of photomask design. The DNA-based signals used to induce swelling can be integrated with a range of DNA-based sensors and strand-displacement circuits, potentially allowing shape change processes to be directed by different chemical inputs or chemical controllers. The use of conventional photolithographic approaches also allows for hybrid integration with electronic and optical layer, to build devices that use biomolecular sensors and actuators to execute a range of tasks.

Table 4.1. DNA Sequences.

All DNA strands were synthesized by Integrated DNA Technologies, Inc. The A, R, H_1, and H_2 strands are the reverse of the strands used by Venkataraman *et al.*[173] Terminator hairpins of H_{1T} and H_{2T} were designed such that the loop domain of each hairpin was orthogonal to the respective binding site on the other hairpin, i.e. H_1 loop domain is orthogonal to binding site on H_2 and vice versa. This was verified by simulating equilibrium concentrations of all species present after in NUPACK.

DNA Strand	Sequence
A	**TAAGTTCGCTGTGGCACCTGCACG**
R	**CAACGTGCAGGTGCCACAGCGTGG**
H_1	**CCACGCTGTGGCACCTGCACGCACCCACGTGCAGGTGCCACAGCGAACTTA**
H_2	**TGGGTGCGTGCAGGTGCCACAGCGTAAGTTCGCTGTGGCACCTGCACGTTG**
H_{1T}	**CCACGCTGTGGCACCTGCACGTAGACTCGTGCAGGTGCCACAGCGAACTTA**
H_{2T}	**TGGGTGCGTGCAGGTGCCACAGCGGCCTAGCGCTGTGGCACCTGCACGTTG**

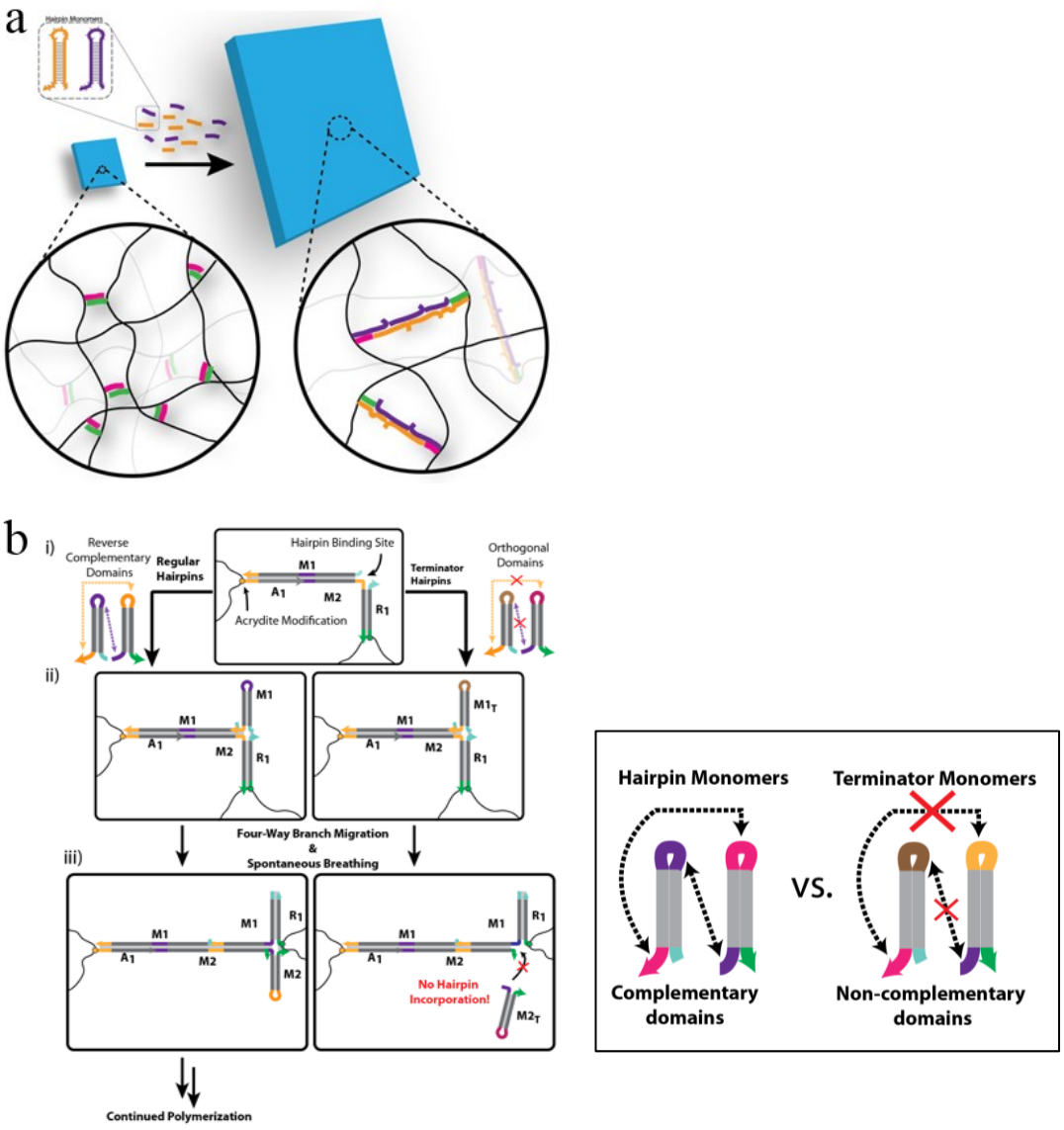

Figure 4.1. Chemomechanical actuation of DNA-crosslinked hydrogels and detailed DNA coupling mechanism in hydrogel net. (a) Concept of intelligent chemomechanical actuation of DNA crosslinked thin monolayer film tuned by architected DNA inputs. **(b)** Detailed coupling mechanism of chemical DNA binding/unbinding to mechanical pushing of nets in hydrogel system.

Reprinted with permission from A. Cangialosi, C. K. Yoon, J. Liu, Q. Huang, T. D. Nguyen, D. H. Gracias, and R. Schulman, "Macroscale Sequence-Selective Shape-Change driven by Photopatterned DNA hydrogels with High Swelling," *In Preparation*, 2017

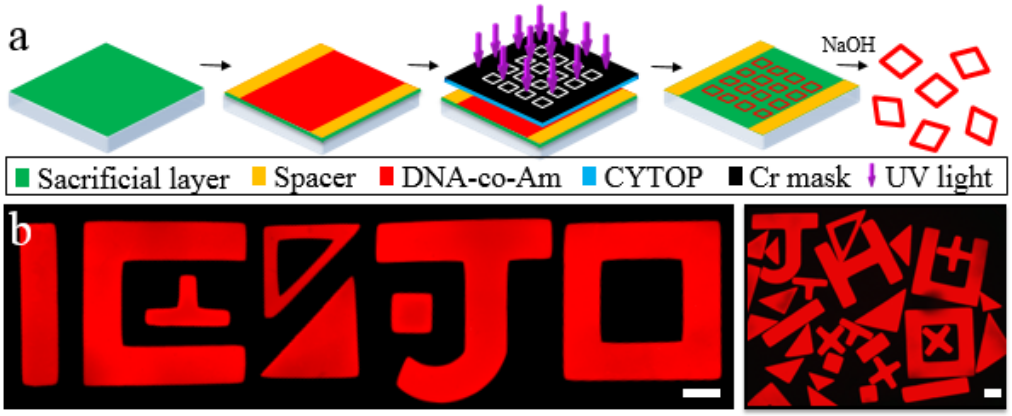

Figure 4.2. Photopatterning of DNA-crosslinked hydrogels. (a) Schematic illustration of photolithographic fabrication steps. **(b)** Experimental observations of photopatternable and mass producible DNA-co-Am hydrogels with several different shapes and sizes stained by Rhodamine 6G to obtain clear fluorescence images. All scales are 500 μm.

Reprinted with permission from A. Cangialosi, C. K. Yoon, J. Liu, Q. Huang, T. D. Nguyen, D. H. Gracias, and R. Schulman, "Macroscale Sequence-Selective Shape-Change driven by Photopatterned DNA hydrogels with High Swelling," *In Preparation*, 2017

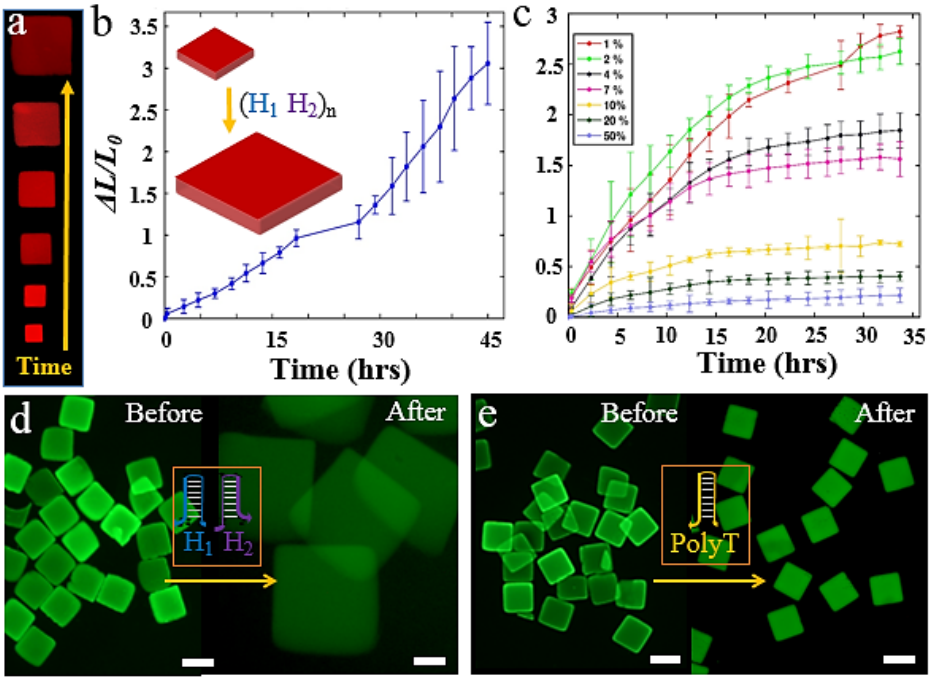

Figure 4.3. Swelling of DNA-co-Am hydrogels. **(a)** Sequential illustration of swelling of square shaped DNA-co-Am hydrogels when time goes by. **(b)** Experimental observations of uniaxial expansion of DNA-co-Am Hydrogels with no terminator hairpins. **(c)** Tunable swelling of DNA-co-Am hydrogels via terminator hairpin DNAs compositions. **(d)** Reconfigurable swelling of mass produced DNA-co-Am hydrogels when introduced reactant DNA hairpins. **(e)** Control experiment to verify lock-and-key type swelling of DNA-co-Am hydrogels. Random PolyT hairpin did not react with photopatterned DNA-co-Am hydrogels. All scales are 2mm.

Reprinted with permission from A. Cangialosi, C. K. Yoon, J. Liu, Q. Huang, T. D. Nguyen, D. H. Gracias, and R. Schulman, "Macroscale Sequence-Selective Shape-Change driven by Photopatterned DNA hydrogels with High Swelling," *In Preparation*, 2017

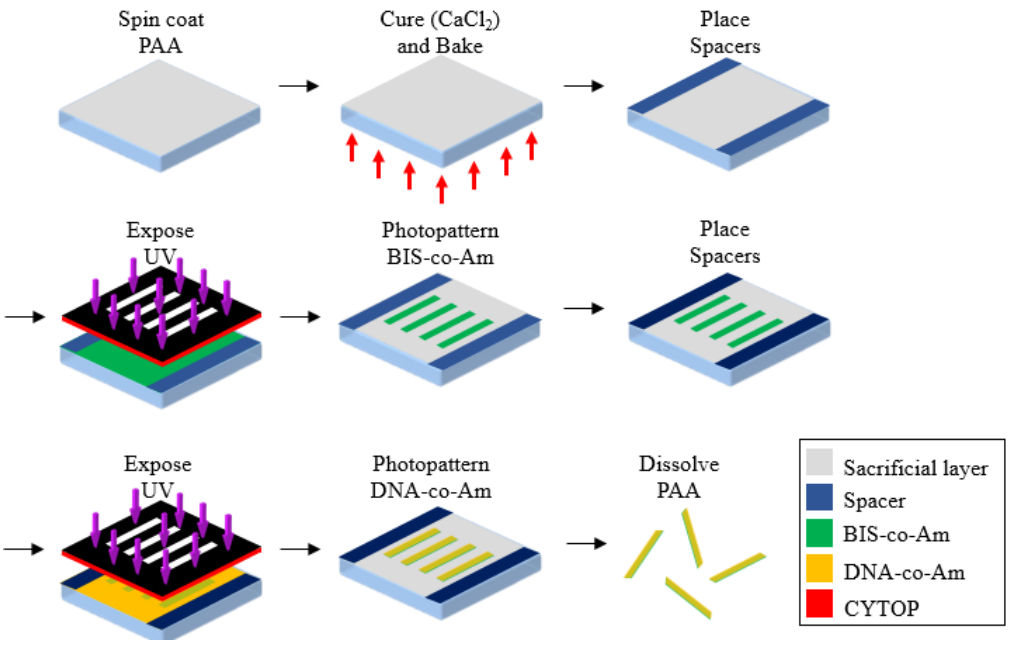

Figure 4.4. Schematic illustration of photolithographic fabrication steps of DNA/BIS bars.

Reprinted with permission from A. Cangialosi, C. K. Yoon, J. Liu, Q. Huang, T. D. Nguyen, D. H. Gracias, and R. Schulman, "Macroscale Sequence-Selective Shape-Change driven by Photopatterned DNA hydrogels with High Swelling," *In Preparation*, 2017

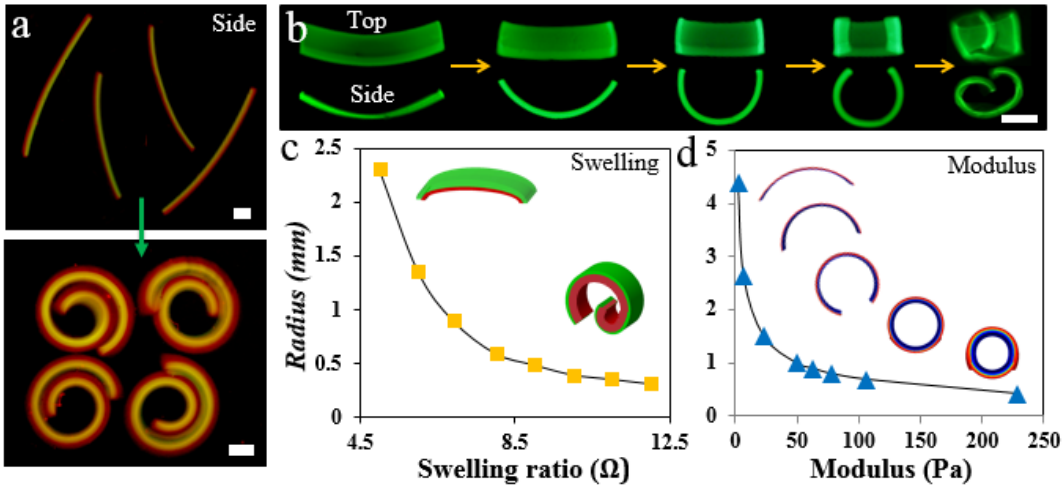

Figure 4.5. Actuation of DNA/BIS bilayer bars and computational estimation of radius changes according to swelling ratio and Young's modulus. (a) Experimental observation of folding of DNA/BIS bars when introducing reactant specific DNA solutions into DNA crosslinked hydrogels. **(b)** Example of sequential top and side snap shots of self-folding DNA/BIS bilayer during reactant DNAs diffusion into the photopatterned hydrogel bar systems. **(c, d)** FEM estimation of radius change of DNA/BIS bars according to swelling ratio and Young's modulus parameters. Scales are (a) 250 μm and (b) 1.5 mm.

Reprinted with permission from A. Cangialosi, C. K. Yoon, J. Liu, Q. Huang, T. D. Nguyen, D. H. Gracias, and R. Schulman, "Macroscale Sequence-Selective Shape-Change driven by Photopatterned DNA hydrogels with High Swelling," *In Preparation*, 2017

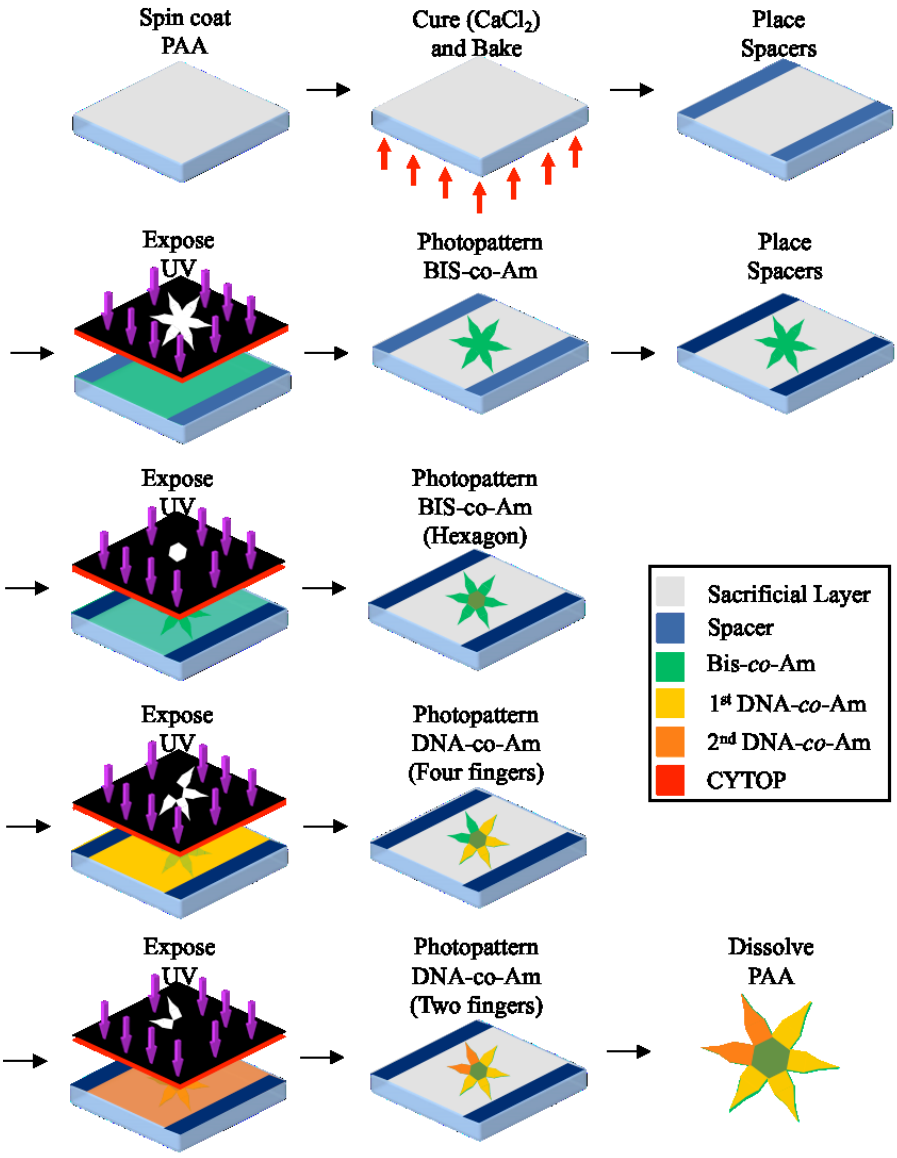

Figure 4.6. Schematic illustration of multi-step fabrications of flower shaped DNA/BIS hydrogel system.

Reprinted with permission from A. Cangialosi, C. K. Yoon, J. Liu, Q. Huang, T. D. Nguyen, D. H. Gracias, and R. Schulman, "Macroscale Sequence-Selective Shape-Change driven by Photopatterned DNA hydrogels with High Swelling," *In Preparation*, 2017

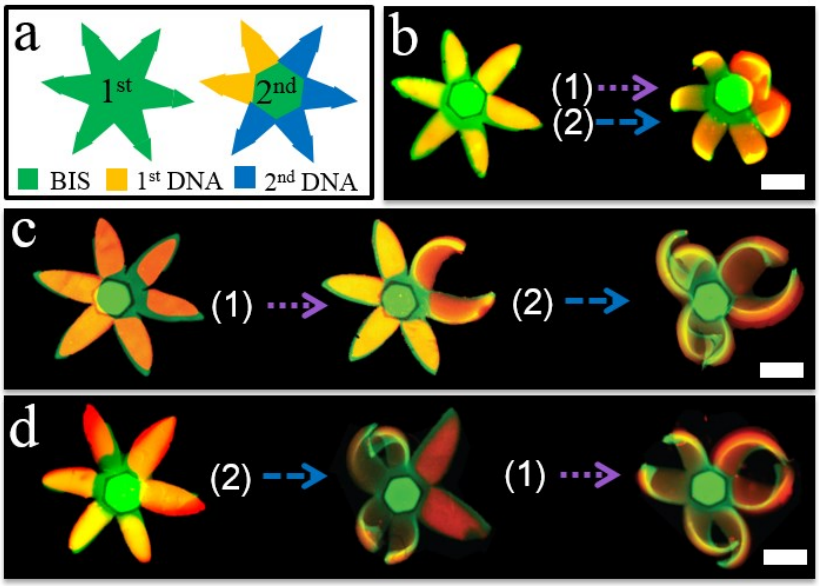

Figure 4.7. Selective actuation of flower shaped DNA/BIS hydrogel. (a) Brief schematic description of parts of bilayer composed of one BIS and two DNA crosslinked hydrogel systems. **(b)** Optical images of experimentally photopatterned flower shaped hydrogels. When introduced two DNA reaction solutions, flat flower shaped hydrogels turned into 3D folded structure. **(c)** Furthermore, two different selective sequential folding of flowers were observed when introducing two different reactants of DNAs in orders. All scales are 1mm.

Reprinted with permission from A. Cangialosi, C. K. Yoon, J. Liu, Q. Huang, T. D. Nguyen, D. H. Gracias, and R. Schulman, "Macroscale Sequence-Selective Shape-Change driven by Photopatterned DNA hydrogels with High Swelling," *In Preparation*, 2017

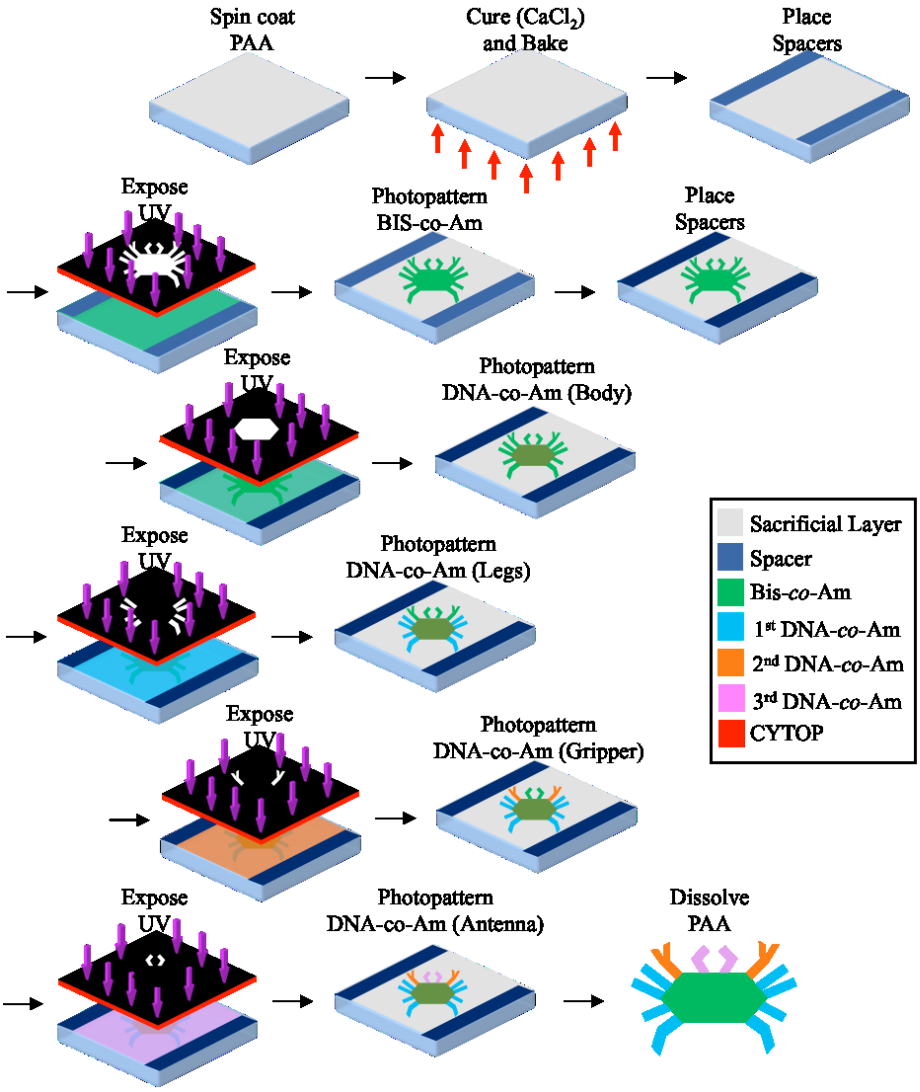

Figure 4.8. Schematic illustration of multi-domain fabrication steps of a crab shaped DNA/BIS hydrogel system.

Reprinted with permission from A. Cangialosi, C. K. Yoon, J. Liu, Q. Huang, T. D. Nguyen, D. H. Gracias, and R. Schulman, "Macroscale Sequence-Selective Shape-Change driven by Photopatterned DNA hydrogels with High Swelling," *In Preparation*, 2017

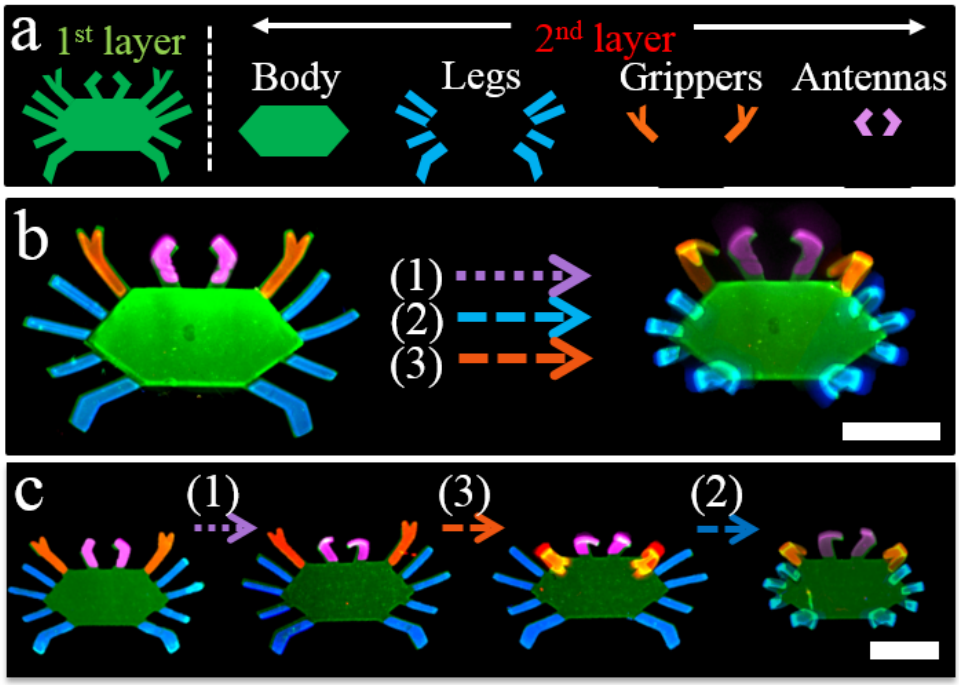

Figure 4.9. Selective chemomechanical folding of a crab. (a) Mask designs of a crab including multi-domain parts such as a body, legs, grippers, and antennas **(b)** Optical images of photopatterned crab and its actuation test of legs, grippers, and antenna parts. **(c)** Furthermore, selective sequential folding of a crab when introduced three different reactants of DNAs in orders. All scales are 1.5 mm.

Reprinted with permission from A. Cangialosi, C. K. Yoon, J. Liu, Q. Huang, T. D. Nguyen, D. H. Gracias, and R. Schulman, "Macroscale Sequence-Selective Shape-Change driven by Photopatterned DNA hydrogels with High Swelling," *In Preparation*, 2017

5. Programmable Magnetically and Thermally Responsive Self-folding Soft Microgrippers*

5.1. Overview

Hydrogels such as poly(*N*-isopropylacrylamide-co-acrylic acid) (pNIPAM-AAc) can be photopatterned to create a wide range of actuatable and self-folding microstructures. Mechanical motion is derived from the large and reversible swelling response of this cross-linked hydrogel in varying thermal or pH environments. This action is facilitated by their network structure and capacity for large strain. However, due to the low modulus of such hydrogels, they have limited gripping ability of relevance to surgical excision or robotic tasks such as pick-and-place. Using experiments and modeling, we design, fabricate, and characterize photopatterned, self-folding functional microgrippers that combine a swellable, photo-cross-linked pNIPAM-AAc soft-hydrogel with a nonswellable and stiff segmented polymer (polypropylene fumarate, PPF). We also show that we can embed iron oxide (Fe_2O_3) nanoparticles into the porous hydrogel layer, allowing the microgrippers to be responsive and remotely guided using magnetic fields. Using finite element models, we investigate the influence of the thickness and the modulus of both the hydrogel and stiff polymer layers on the self-folding characteristics of the microgrippers. Finally, we illustrate operation and functionality of these polymeric microgrippers for soft robotic and surgical applications.

---

* Reprinted with permission from

1. J. C. Breger, C. K. Yoon, R. Xiao, H. R. Kwag, M. Wang, J. Fisher, T. D. Nguyen and D. H. Gracias, "Self-Folding Thermo-Magnetically Responsive Soft-Microgrippers," *ACS Applied Materials & Interfaces*, vol. 7, pp. 3398-3405, 2015.

5.2. Introduction

The ability to grip and securely hold onto objects is a vital task in robotics, manufacturing, and surgery. Conventional robots are composed of stiff materials such as metals (aluminum, steel) and ceramics (silicon, silicon oxide) with their joints being actuated using electrical, pneumatic, or hydraulic signals. Soft robotics is an emerging, bioinspired field that promises to augment the capabilities of traditional hard robotics with polymeric modules that mimic biological actuators.[105] As compared to their hard robotic counterparts, soft robotic structures have distinct advantages: they can be constructed using simple designs; be made lighter and inexpensively; be processed at low temperatures and in aqueous environments; and offer the possibility to mimic human functionality through their robotic functions.

Many previously described soft robotic actuators including those developed in the MEMS community are electrically or pneumatically driven.[105,176–181] For example, the reversible electrochemical swelling of polypyrrole in a variety of bilayer, trilayer, and sandwiched configurations has been used to create a number of folding and actuating structures.[179] More recently, a variety of pneumatically actuated robotic devices have been developed including a microhand for surgery,[178] networks capable of intricate motion,[105] and a universal gripper based on granular materials.[181] While these devices offer significant advantages in terms of the control, speed, universality, and momentum, their need for tethers as well as electrical power or gas sources can increase their weight and complexity. This limits their applicability in small or confined spaces or during repetitive actuation over long time periods.

The use of stimuli responsive mechanisms provides an alternative to tethered actuation and offers the possibility for smart behaviors such as autonomous responses in specific environments.[28,108,116,182,183] Many of these schemes employ hydrogels since these materials are able to swell significantly in response to a variety of stimuli such as temperature, light, or chemical reactions generating the energy and force to perform mechanical tasks.[124,184] Hydrogel actuators can also be created using bigel strips composed of partially interpenetrated hydrogel networks with differing swelling properties. This concept was first demonstrated using bilayers of pNIPAM and acrylamide that had drastically different swelling behavior in response to temperature or aqueous environments.[118] The use of stimuli responsive bilayers has recently been combined with photo-cross-linking approaches to create a range of microstructured actuators and self-folding devices.[17,28,108,132,185,186]

In our previous work on self-folding microactuators, we have demonstrated a range of self-assembled, origami-inspired structures that spontaneously fold-up and actuate from two-dimensional patterns without the need for any wires or external controls.[28,30,38,72,134,182] These structures utilized a variety of actuation forces derived by the minimization of surface tension; the release of residual stress triggered by light, enzymes, biochemicals, or temperature; and differential swelling based on pH or temperature changes. It is particularly noteworthy that previously created metallic microgrippers were autonomously actuated on introduction into the gastrointestinal tract of live pigs and used to biopsy tissue.[72] In order to enhance biocompatibility and possibly endow biodegradability in such surgical applications and for robotics, we

believe there is a pressing need to develop polymeric, origami-inspired, and stimuli responsive microgripper structures.[30,134,182,187]

We have observed that one of the significant limitations of stimuli responsive hydrogel actuators is their low stiffness. For example, when we previously designed microgrippers composed of cross-linked pNIPAM-AAc alone, we observed that these grippers were very floppy and unable to securely grip onto beads which would often fall out of their grasp.[187] In order to address this limitation, we previously introduced the concept of combining rigid polymer segments of a nonswellable polymer to increase the overall stiffness of the pNIPAM-AAc polymer.[30] In this chapter, we build on these earlier results to design, fabricate, and characterize mass-producible microgrippers capable of cell excision. We have incorporated nanoparticle doping and a sequential photolithographic approach to create large numbers of autonomous, polymer-hydrogel bilayer grippers. These grippers have numerous advantageous properties including the capability for magnetic direction, simultaneous actuation based on temperature, independent function, optical transparency, and gripping onto and isolating tissue. Over numerous cycles, the resulting grippers can fold completely in either direction on the basis of temperature and fold reversibly. We use finite element analysis to model the folding behavior of these soft robotic grippers to gain insight into the influence of important material and design considerations such as polymer thickness and modulus.

The characteristics, thermal responsiveness, and stiffness were chosen for the polymer materials of the grippers based on their relevance for biological applications.

pNIPAM is a thermo-responsive hydrogel that undergoes a low critical solution temperature (LCST) above physiological temperature where the polymer becomes hydrophobic expelling water and losing 90 % of its mass while below its LCST, the polymer is hydrophilic and absorbs water.[80] The absorption and desorption of water in response to temperature serves as the actuation mechanism, and pNIPAM has been used extensively in drug delivery applications, cell culture, and tissue engineering applications.[188–192]

Biocompatibility of pNIPAM has to be addressed in order to utilize in biomedical applications.[30] Essentially, the backbone of pNIPAM hydrogels is not degradable although specific cross-linkers used to network the hydrogel can provide biodegredability.[188,190] Therefore, a networked pNIPAM hydrogel can be created with tunable degradation rates based on cross-linker density and type. PPF, a material originally designed for filling bone defects and similar in tensile strength to trabecular bone,[193,194] serves as a stiff and restrictive construct, mimicking phalanges in the human hand around which pNIPAM-AAc can contract or expand. The biodegradation products of PPF are propylene glycol and fumaric acid which are naturally expelled through the Krebs's cycle.[195]

Both PPF and pNIPAM are photopatternable and have been used previously in lithographic applications as well as to create therapeutic grippers or "theragrippers" in our own laboratory. By cross-linking, one can tune the physical and mechanical properties of the polymers without chemical modifications to the polymer backbone which can affect its biocompatibility.[196] The main advantage of photo-crosslinking

over other crosslinking techniques is the ability to spatially and temporally control polymerization using photomasks and by varying the intensity of light. Further, a wide range of portable UV sources are available, and fast curing rates are achievable at room temperature. Photopatterned hydrogels can also be created over a wide range of sizes: we have previously created metallic microgrippers as small as a few hundred microns from tip to tip so that they can grip onto small sized cargo or pass through conventional catheters used in surgery.[72] All that is needed is the optimization of spacing between grippers, spacing of the rigid segments, and thickness of the hydrogel and stiff segment layers.

Magnetic fields are biocompatible even at clinically relevant but high field strengths; therefore, they offer many attractive advantages over other propulsion and guidance schemes.[197] Numerous examples of magnetically directed robotic devices have been developed for in vivo applications including metallic microgrippers, microdrillers, modified bacteria, and microswimmers.[11,134,197–199] Polymer microstructures can be made responsive to an electromagnetic field by incorporating magnetic nanoparticles within their network.[132,200] In this work, we have directly incorporated magnetic nanoparticles into the pNIPAM-AAc trigger layer, allowing for remote direction while keeping the arms free to grip onto and/or isolate tissue at a desired location.

5.3. Materials and Methods

5.3.1. Materials

N-Isopropylacrylamide monomer (NIPAM, Scientific Polymer Products Inc.), poly-N-isopropylacrylamide (pNIPAM, MW 300 000, Scientific Polymer Products Inc.), N,N-methylenebisacrylamide (BIS, Sigma-Aldrich), n-butanol (Sigma-Aldrich), acrylic acid (AAc, Sigma-Aldrich), diethyl fumarate (DEF, Sigma-Aldrich), 80% hydrolyzed poly(vinyl alcohol) (PVA, MW 9−10 kDa, Sigma- Aldrich), iron(III) oxide (Sigma-Aldrich), Irgacure 2100 (Ciba), 1827 photoresist (Microchem), 351 developer (Microchem), and three inch silicon (Si) wafers (WRS) were used as is without further modification.

5.3.2. Synthesis of Polypropylene Fumarate (PPF)

PPF was synthesized by a previously published method[193] and determined to have a MW of 804 Da and a polydispersity of 1.21.

5.3.3. Synthesis of pNIPAM-AAc

A NIPAM-AAc solution was prepared as described previously.[134] Briefly, 3 g of NIPAM monomer, 0.4 g pNIPAM, and 0.18 g BIS were dissolved overnight in 7.5 mL of n-butanol under constant stirring at room temperature. To this solution, 0.3 mL of AAc was added followed by 0.1 g of Irgacure 2100. The resultant mixture was stirred until the additives had been completely incorporated.

5.3.4. Thickness Measurement: Profilometry

Glass slides were repeatedly washed with acetone, methanol (MeOH), and isopropyl alcohol (IPA) after which they were dried with compressed air. A strip of

cellophane tape was fixed to the middle of the glass slide making sure the edges were pressed down. A 3:1 w/w mixture of PPF/DEF with approximately 1 % of Irgacure 2100 was added to the top of each glass slide. The PPF/DEF solutions were spin coated at varying speeds (500 − 3000 rpm) following which the tape was carefully removed. The polymer was UV crosslinked by varying amounts of UV (650 − 2600 mJ/cm^2) flood exposure through a glass mount with a mask aligner. The slide was then incubated and washed with ethanol (EtOH) followed by deionized (DI) H_2O to remove any unreacted components and dried under compressed air. Crosslinked polymer thickness was measured utilizing a profilometer. Measurements were taken in four different spatial locations of the glass slide and averaged for each thickness.

5.4. Experiments

5.4.1. Fabrication of Thermo-magnetically Responsive Soft Grippers

Alignment markers were photopatterned onto Si wafers utilizing negative photoresist, a dark field mask, and mask aligner. Cr (20 nm) and Cu (100 nm) were evaporated on the Si wafers, after which excess Cr, Cu, and photoresist were removed by sonication of the wafer in acetone. The wafers were rinsed with copious amounts of acetone, EtOH, MeOH, and IPA followed by drying with compressed air. A sacrificial, transparent PVA layer was deposited onto a Si wafer as described previously. These wafers were subsequently used for photopatterning polymeric structures.

To fabricate polymeric grippers, warm (~70 °C) PPF solution (3:1 PPF/DEF with approximately 1 % w/w Irgacure 2100) was deposited onto the wafer, spread utilizing a spatula then spin coated at 3000 rpm to achieve a film approximately 10

μm thick. PPF segments were photopatterned utilizing a dark field mask and a mask aligner in noncontact mode and exposed to 650 mJ/cm^2 UV light to initiate cross-linking. A solution of NIPAM-AAc (1 mL) was deposited on top of the wafer, and the wafer was slowly rotated by hand to spread out the NIPAM-AAc evenly, and allowed to sit for 1 min to achieve uniform thickness before being exposed to 100 mJ/cm^2 UV light through a dark field mask that was the outline of the structure in noncontact mode as described previously. Unreacted PPF/DEF and NIPAM-AAc were removed by repeated EtOH and MeOH washes followed by a single final DI H_2O wash. The wafer was then immersed in DI H_2O to completely dissolve the PVA sacrificial layer. Grippers were collected into a 20 mL scintillation vial, rinsed with DI H_2O, and then stored in DI H_2O at 4 °C until use. Structures were made ferromagnetic by incorporating 5 % w/w Fe_2O_3 into the NIPAM-AAc solution before spin coating and photopatterning.

5.4.2. Modeling of Swelling/Deswelling of Soft Microgrippers

In order to determine the swelling ratio, pNIPAM-AAc films were placed in fresh DI H_2O and incubated at 4 °C for 1 h to reach their equilibrium swollen state. Specimens were then removed from DI H_2O, blotted with a tissue, and weighed (n = 8). Specimens were placed back in DI H_2O and incubated at 27, 31, 33, 35, 37, and 40 °C. Afterward, the specimens were weighed again in the same manner as described previously. The swelling ratio (SR) or its inverse function, $1/\varphi$, was then calculated. We use the following definition for these quantities: $SR = 1/\varphi = W_{swollen}/W_{dry}$.

The Young's moduli of swollen PPF and pNIPAM-AAc were measured using a dynamic mechanical analyzer Q800 (TA Instruments). The specimens were tested at room temperature in the dynamic mode with a frequency sweep from 0.1 to 10 Hz under a 0.2 % applied strain for PPF and a 1 % applied strain for pNIPAM-AAc. The storage modulus at 0.1 Hz was used to represent the Young's modulus for low strain rates since the storage modulus was an order of magnitude larger than the loss modulus at this low frequency.

5.4.3. Cell Culture

L929 (ATCC CCL-1; American Type Culture Collection, Manassas, VA), a fibroblast murine cell line, was stored at − 80 °C. Aliquots were rapidly thawed and cultured in 5 % CO_2/95 % air, 70 % humidity, at 37 °C in complete media (RPMI supplemented with 10 % fetal bovine serum) until they adhered to the culture flask and reached 80 − 90 % confluence (usually 2 − 3 days). The monolayer was harvested by washing the flask 3 times with 5mL phosphate buffered saline (PBS) and then incubated in the presence of 0.25 % (w/v) Trypsin until the cells became rounded and detached from the bottom of the flask (usually 3 − 5 min). The cells were centrifuged at 1000 rpm for 3 min to remove trypsin and resuspended in cold PBS. The cells were incubated on ice for 45 min in the presence of 2 mM calcein AM to stain the cells. Afterward the cells were centrifuged again at 1000 rpm for 5 min to remove excess dye and to create a L929 tissue-like pellet.

5.4.4. Gripping of Tissue

Grippers were incubated at 4 °C or on ice to achieve a closed formation and were carefully dripped on top of each tissue pellet in warm PBS (~37 °C). The grippers immediately opened and were allowed to close around the tissue pellet (usually within 5 min). After closure, tissue filled grippers were retrieved with a transfer pipet and visualized. The gripper process of closing around the tissue pellet was monitored with an AZ-100 fluorescent microscope. Time lapse images were taken every 2 s until the gripper closed completely.

5.5. Results and Discussion

5.5.1. Design of Soft Grippers

Our design is based on the combined use of stimuli responsive polymers such as pNIPAM-AAc with a degradable yet stiff polymer like PPF to increase rigidity of the actuator. Polymeric grippers were fabricated using sequential photolithography and fold into 3-D structures based on the swelling/deswelling through water absorption/desorption in response to temperature (**Figure 5.1.**). The pNIPAM-AAc layer serves as a thermally responsive swelling hydrogel layer with a low shear modulus (G_h = 162 KPa) while the PPF layer serves as the nonswelling, restrictive layer with a much higher shear modulus (G_p = 16 MPa). Similar moduli values were previously reported for PPF mixed with ceramic materials showing compressive strengths ranging from 2 to 30 MPa.[201]

We used a serial photolithographic method to pattern the PPF/pNIPAM-AAc microgrippers (**Figure 5.2.**). It is noteworthy that PPF is typically used in gram

quantities for filling bone defects and photopatterning of this material is relatively new. Hence, it was necessary to develop methods to precisely control the thickness and lateral resolution of photopatterned PPF films. Specifically, we varied the spin coat speed, the UV intensity, and the spacing between PPF patterns to reliably mass produce well-structured microgrippers (**Figure 5. 3.**) We also note that since the PPF/DEF solution is much more viscous than the NIPAM-AAc solution, it is preferable to pattern the PPF/DEF solution first followed by NIPAM-AAc photopatterning. We observed that when patterned second, the PPF/DEF solution can dislodge the underlying patterned pNIPAM-AAc structures during spin coating. We also intentionally did not develop the PPF patterns before the addition of the NIPAM-AAc solution. It is noteworthy that delamination of bilayer actuators is a concern during reversible swelling and deswelling cycles. In our case, due to the material properties and processing, we observed sufficient adhesion between the two films, and we attribute it to two factors. First, the n-butanol in the NIPAM-AAc solution could partially develop the underlying PPF leading to polymer chain entanglement. Second, the reaction between the alkene functional groups of NIPAM, acrylic acid, DEF, and PPF could lead to improved adhesion at the interface.

5.5.2. Characterization of Gripper Folding

Once released from the wafer and equilibrated in solution, the polymeric structures were thermally responsive and could fold in both directions as shown in **Figure 5. 4. (A)**. The literature LCST value for pNIPAM lies between 30 to 35 °C;[80] however, it is known that the LCST can be altered by copolymerization of NIPAM with

other monomers as in pNIPAM-AAc.[190,202] We observed the self-folding transition temperature to be approximately 36 °C. We rationalize self-folding by noting that above this temperature pNIPAM-AAc is hydrophobic, the polymer collapses causing the gripper to close with the PPF segments on the outside of a closed gripper. Since the pNIPAM-AAc layer is opaque during polymer chain collapse, the transition can be readily observed under a microscope. As the temperature cools below 36 °C, the pNIPAM-AAc layer becomes clear and swells as it absorbs water causing it to open and then close in the opposite direction, now with the PPF segments on the inside of the gripper, as verified over 50 cycles.

We also applied the model to investigate the effect of the gap between PPF segments, thickness, and modulus on the temperature-dependent folding configuration. Specifically, we varied the spacing between adjacent PPF segments on the gripper arms from 20 to 90 μm and found that this had a negligible effect. A smaller spacing between the rigid segments led to only slightly more folding. In contrast, both the thickness and modulus of the layers had a pronounced effect. In order to quantify the extent of folding as a function of these parameters, we plotted the ratio of the overall diameter of the grippers in the folded state (D) to the unfolded, flat diameter (D_o) while varying these parameters (**Figure 5.5.**). A smaller value of (D/D_o) signifies greater folding. The thickness of PPF and pNIPAM-AAc was varied between half to twice the experimental thickness used, i.e., from 5 to 20 μm for PPF and 10 to 100 μm for pNIPAM-AAc (**Figure 5.5. (A)**). The thickness of PPF (t_p) used in experiments was approximately 10 μm while the thickness of pNIPAM-AAc (t_n)

used was approximately 34 μm when swollen. Increasing the PPF layer thickness results in a higher (D/D_o) ratio signifying lower folding which we attribute to a higher bending rigidity of the PPF. However, the effect of varying the thickness of the pNIPAM-AAc layer is more complicated. For example, when the thickness of pNIPAM-AAc is increased from 34 to 100 μm, the folding decreased only slightly, but when the thickness of pNIPAM-AAc is decreased from 34 to 10 μm, the folding also decreased but in a significantly more pronounced manner. We rationalize this result by noting that thin pNIPAM-AAc layers could not exert enough force to compress the stiffer PPF layers and bend the gripper arm while very thick pNIPAM-AAc layers were negligibly affected by the PPF layer. In order to find the optimum thickness of the pNIPAM-AAc layer, we ran an additional set of parameter studies by changing the thickness of pNIPAM-AAc layer while keeping the PPF layer thickness 10 μm. Our results suggest that the optimum thickness for the pNIPAM-AAc is around 45 μm.

One of the important advances in this study is the validation of the hypothesis that bilayers composed of a high modulus layer with a hydrogel could increase the overall stiffness of the soft robotic tool. Hence, we simulated and compared self-folding ratios for a bilayer microgripper composed of a fixed pNIPAM-AAc modulus (=162 KPa) as a function of varying modulus of the stiff polymer layer ranging from the experimentally used PPF polymer modulus (Gp) of 16 MPa to hypothetical layers with 0.1 and 10 times this modulus, 1.6 and 160 MPa, respectively (**Figure 5.5 (B)**). We observed that decreasing the modulus of the PPF by a factor of 10 led to tighter folding but also resulted in inhomogeneous folding and warping. Increasing the

modulus of the stiff layer to 10 times that of the PPF resulted in decreased folding due to increased bending rigidity. Our simulations indicate that a modulus of about 16 MPa for PPF or any other stiff polymer would work best. Currently, we are working on a contact model to investigate the force between the gripper and tissue using the finite element method. We are also trying to develop experimental methods to characterize the contact force for verification of the numerical model.

5.5.3. Finite Element Analysis of Gripper Folding

We developed constitutive models for finite element simulation of the pNIPAM-AAc and PPF bilayer grippers to study the influence of various design parameters on gripper folding and unfolding. The model was implemented into the open-source finite element code TAHOE (Sandia National Laboratories). As shown in Supporting Information **Figure 5. 6.**, the mesh was discretized using trilinear hexahedral elements, and a mesh convergence study was also performed to decide the mesh density. Self-folding results from the model are shown in **Figure 5. 4. (B)** as a function of temperature and the ratio of dry to swollen hydrogel weight (φ): the ratio φ increases with increasing temperatures as water is expelled. The simulation model is based on the thermodynamic framework for equilibrium mechanics coupled with hydrogel swelling[187] to describe the thermo-responsive behavior of the pNIPAM-AAc layer. The free energy of the hydrogel is assumed to be the sum of a mechanical part, represented by a Neo-Hookean model for the entropy elasticity of the polymer network with Gaussian chain statistics and a component for the energy of mixing represented by the Flory–Huggins model.[41] The Flory − Huggins parameter increases

sigmoidally with temperature. The low-temperature and high-temperature values along with the transition temperature range were determined from the temperature-dependent swelling experiments described in the Materials and Methods section (5.3). The effect of diffusion through the micrometer-scale thick hydrogel layer was neglected, and we assumed the hydrogel was at equilibrium for each test temperature. A Neo-Hookean model was also applied to describe the mechanical behavior of the PPF layer. The shear modulus of the two layers was determined by dynamic mechanical analysis (DMA) described in the Materials and Methods section (5.3). Simulation snapshots in **Figure 5.4. (B)** capture the opening and closing behavior of the grippers with the pNIPAM-AAc film on the inside of the grippers at high temperatures, and the trends agree with experimental data.

In detail, the deformation gradient, defined as $\mathbf{F} = \partial\, \phi(\mathbf{X})/\partial\mathbf{X}$, describes the mapping of material lines from the reference dry and stress free configuration to the swollen and stressed configuration. We assume that the deformation gradient can be decomposed into a mechanical part $\mathbf{F}_e$ and a swelling part $\mathbf{F}_s$ as:

$$\mathbf{F} = (\varphi)^{-1/3}\, \mathbf{F}_e = (\varphi_0)^{-1/3}\, \mathbf{f} \qquad (1)$$

where φ and φ_0 are the polymer volume fraction defined from the dry and initially swollen stress-free state respectively, and $\mathbf{f}$ is the deformation gradient mapping between the initially swollen and existing configuration. The polymer volume fraction is represented as $\varphi = 1/(1 + vc)$ where v is the volume per solute molecule and c is the number of solute molecules per volume.

We first define the left and right Cauchy-Green tensor as $\mathbf{b} = \mathbf{F}\mathbf{F}^{\mathbf{T}}$ and $\mathbf{C} = \mathbf{F}^{\mathbf{T}}\mathbf{F}$ and the first invariant as I_1 = trace(**b**) = trace(**C**). We also define Θ = det [**F**] and Θ_e = det [$\mathbf{F}_e$] as the total volume change ratio and the component caused by the elastic deformation. The corresponding deformation tensors relative to the initially swollen intermediate configuration are defined as $\boldsymbol{b}^* = \mathbf{f}\mathbf{f}^{\mathrm{T}}$ and $\boldsymbol{\Theta}^* =$ det [**f**]. The free energy of the system is assumed to be a combination of the mixing and the entropic change of stretching polymer chains by swelling and mechanical deformation as:

$$\Psi = \Psi_{mixing}(\varphi) + \Psi_{mechanical}(\mathbf{F}, \Theta_e) \tag{2}$$

The Flory-Huggins model[41] is adopted to represent the free energy change from the mixing of polymers and solvents:

$$\Psi_{mixing}(\varphi) = \frac{RT}{v\varphi}((1-\varphi)\ln(1-\varphi) + \chi\varphi(1-\varphi)) \tag{3}$$

where R is gas constant and χ is Flory-Huggins interaction parameter. We assumed a Gaussian distribution for the polymer chains and a volumetric quasi-incompressible model for mechanical deformation. Thus, the free energy change associated with the stretching polymer chains[203] is:

$$\Psi_{mecahnical} = \left(\frac{G_h}{2}\right)\left(I_1 - 3 - 2\ln(\Theta)\right) + \left(\frac{\kappa_h}{4}\right)\left(\Theta_e^2 - 2\ln\Theta_e - 1\right) \tag{4}$$

where G_h is shear modulus and K_h is bulk modulus. We assumed that the bulk modulus is 1000 times that of the shear modulus to achieve the volumetric

incompressible of mechanical deformation. The Cauchy-Green stress is calculated as $\sigma = (1/\Theta)\ \mathbf{F}\ (\partial\Psi/\partial\mathbf{C})\ \mathbf{F}^{T}$ and the chemical potential is obtained as $\mu = \partial\Psi/\partial c$.[143] Substituting equations (2)-(4) into the previous two equations yields:

$$\sigma = \frac{G_h}{\Theta}\left(\boldsymbol{b} - I\right) + \frac{\kappa_h}{2\Theta}\left(\Theta_e^2 - 1\right)I \tag{5}$$

$$\mu = RT\left(\ln\left(1-\varphi\right) + \varphi + \chi\varphi^2\right) - \frac{\kappa_h v\varphi}{2}\left(\Theta_e^2 - 1\right) \tag{6}$$

Applying the decomposition in equation 1 of **F** into **f** and φ_0 as the stress response can be expressed as,

$$\sigma = \frac{G_h}{\Theta^*}\varphi_0\left(\varphi_0^{-2/3}\boldsymbol{b}^* - I\right) + \frac{\kappa_h}{2\Theta^*}\varphi_0\left(\Theta_e^2 - 1\right)I \tag{7}$$

To model thermo-responsive effect, we assumed the following temperature-dependent function for the Flory-Huggins interaction parameter χ,[146]

$$\chi = \frac{1}{2}\left(\chi_L + \chi_H\right) + \frac{1}{2}\left(\chi_H - \chi_L\right)\tanh\left(\frac{T - T_{tran}}{\Delta T}\right) \tag{8}$$

where χ_L and χ_H is the Flory-Huggins interaction parameters at low temperature and high temperature, T_{tran} is the transition temperature and ΔT is the width of the transition region. We adopted a generalized Neo-Hookean model for PPF. The Cauchy stress is represented as a combination of the deviatoric part and volumetric part,

$$\sigma = \frac{G_p}{\Theta}\left(\bar{\boldsymbol{b}} - \frac{1}{3} I_1\left(\bar{\boldsymbol{b}}\right)\right) + \frac{\kappa_p}{2\Theta}\left(\Theta^2 - 1\right)I \tag{9}$$

where $\bar{\boldsymbol{b}}$ is the deviatoric part of left Cauchy-Green tensor, defined as $\bar{\boldsymbol{b}} = \Theta^{-2/3}\boldsymbol{b}$, and $I_1(\bar{\boldsymbol{b}})$ is trace of $\bar{\boldsymbol{b}}$. The material parameters for the two materials listed in **Table 5.1.** are obtained from the swelling test and mechanical test described in the experimental section and the detailed information about the procedures can be found.[155]

The constitutive model was implemented in an open-source finite element code TAHOE (Sandia National Laboratories). **Figure 5.6.** shows the finite element model of gripper specimen. The mesh was discretized by trilinear hexahedral elements. The displacement boundary condition were set as follows,

$$\begin{aligned} &u_x(x=0,y,z)=0, \\ &u_y(x=0,y=0,z)=0, \\ &u_z(x=0,y=0,z=0)=0. \end{aligned} \tag{10}$$

The simulation starts from the intermediate swollen, stress free state at temperature T = 35 °C. The equilibrium polymer fraction φ_0 is obtained by solving equations (5) and (6) with condition σ = 0 and μ = 0. During every time step, the temperature is changed and the deformation gradient **f** and polymer concentration φ are updated to satisfy the force balance and chemical potential equilibrium.

5.5.4. Applications of Soft Grippers

The soft microgrippers can be made magnetic through the incorporation of iron oxide (Fe_2O_3) into one of the polymeric layers. Here, 5 % w/w Fe_2O_3 was incorporated into the pNIPAM-AAc layer to achieve better dispersion of the Fe_2O_3 throughout the

layer as compared to incorporation into the PPF layer. These polymeric grippers open in unison in response to temperature. The Fe_2O_3 particles provide contrast in visualizing the polymeric grippers which orient themselves in a magnetic field. The incorporation of Fe_2O_3 into the pNIPAM-AAc layer did not affect folding or photopatterning. By placing an external magnet near the desired location, the gripper can be guided toward that location (**Figure 5.7. (A)**). Hence, they could potentially be directed or retrieved using a magnetic guide wire in a clinical setting as was done previously with ferromagnetic metallic grippers.[72]

Importantly, due to increased stiffness of the grippers, we observed that they were able to grip and excise cells from a fibroblast cell clump (**Figure 5.7. (B)**). Fibroblasts are cells found in connective tissue. In these experiments, the grippers were stored at 4 °C so that they folded completely due to maximal absorption of water by the pNIPAM-AAc layer. The grippers were pipetted on top of a fibroblast clump and allowed to open up and then close in warm PBS (~37 °C) around the tissue, gripping it. The gripper is outlined with a dotted white line to aid in visualization of the gripper. The cells were stained with the Calcein AM, a commonly used stain to indicate live cells, and fluoresced bright green. A pipet was used to retrieve the grippers, and they were visualized with microscopy. After retrieval, we observed cells within the arms of the grippers. The fluorescent green live cells can be visualized through the transparent gripper arms (**Figure 5.7. (C)**).

5.6. Conclusion

The goal of this study was to create and model stimuli responsive self-folding soft microgrippers composed of a continuous low modulus actuator layer of pNIPAM-AAc and stiff segments composed of PPF. pNIPAM-AAc was chosen as an appropriate actuator material based on its stimuli responsive properties and its method of actuation by swelling and deswelling in aqueous environments. We have validated the hypothesis that when this swellable soft hydrogel is combined with a nonswellable stiff polymer, it endows sufficient strength such that microgrippers structured in this manner are strong enough to excise cells from a tissue clump. On the basis of the stiffness, biocompatibility, biodegradability, and photo-crosslinking of PPF we believe that this is an attractive material for photopatternable soft robotic actuators especially for medical applications. As we have shown, very thin but robust films of PPF can be created in any desired shape by spin coating and photopatterning.

Our results suggest that these thermally responsive soft microgrippers actuate around physiological temperatures. The grippers could be stored in a cold solution, allowed to fold completely in one direction, and then deployed with a catheter to a desired location in the body. In the body, this self-folding transition would occur autonomously as the grippers equilibrate from a cold state to physiological temperatures as we achieved previously with metallic microgrippers.

The incorporation of magnetic particles into one or both of the polymeric layers allows the grippers to be remotely directed or retrieved. Since the grippers fold up compactly at both high and low temperatures, they are small enough to be deployed

and retrieved using conventional catheters. Further, the compact initial shape would also reduce shear forces in the catheter during deployment. PPF is naturally hydrophobic as is pNIPAM-AAc when the temperature is above 36 °C, suggesting that cells could be grown onto the PPF for other biomedical applications. In cartilage engineering projects, PPF has been incubated in the presence of fetal calf serum to allow the adsorption of proteins onto the surface of PPF to promote cell adherence.[204,205] In addition to cell excision, these magnetic polymeric grippers could be directed and allowed to latch onto specific tissue locations to deliver therapeutics. This can be done by incorporating drugs into either the trigger layer or the stiff segment layer as demonstrated previously.[30]

Finally, we have validated an important design approach for the enabling of relatively stiff stimuli responsive soft-tools by pairing a rigid polymer with a thermo-responsive hydrogel. From a bilayer design perspective, our modeling study shows that there is an optimal thickness ratio and modulus ratio of the active hydrogel layer and the stiff structural layer for the folding angle. Self-folding allows such actuators to respond to stimuli without the need for any wires, tethers, batteries, or power/gas sources. We envision that this approach could also be utilized with other photopatternable or printable biomaterials.[206]

Table 5.1. Parameters of the constitutive model for pNIPAM-AAc and PPF.

Parameters	G_h (pNIPAM-AAc)	χ_L	χ_H	T_{tran}	ΔT	G_p (PPF)
Values	162 KPa	0.556	0.710	36 ^oC	4 ^oC	16 MPa

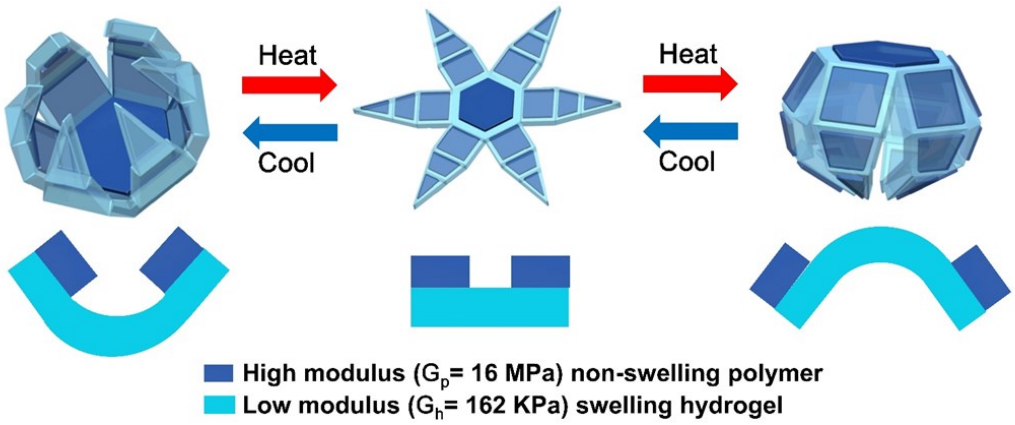

Figure 5.1. Schematic diagram illustrating the reversible self-folding of soft microgrippers in response to temperature. The photopatterned microgrippers are composed of stiff PPF segments atop a pNIPAM-AAc layer. Above 36 °C, the pNIPAM-AAc layer excludes water and contracts which causes the grippers to first open and then close such that the PPF segments face outward. Below 36 °C, the pNIPAM-AAc absorbs water and swells which causes the microggripper to open and then close in the opposite direction such that the pNIPAM-AAc layer faces outward.

Reprinted with permission from J. C. Breger, C. K. Yoon, R. Xiao, H. R. Kwag, M. Wang, J. Fisher, T. D. Nguyen and D. H. Gracias, "Self-Folding Thermo-Magnetically Responsive Soft-Microgrippers," *ACS Applied Materials & Interfaces*, vol. 7, pp. 3398-3405, 2015.

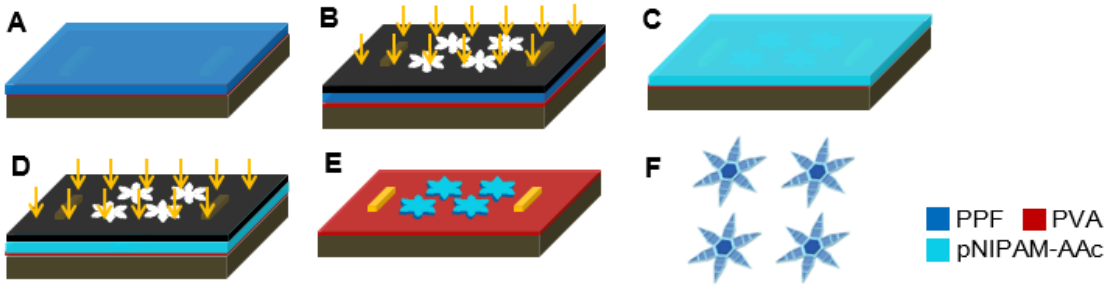

Figure 5.2. Schematic diagram of the PPF/pNIPAM-AAc microgripper fabrication process flow. (A) Metal alignment markers were evaporated onto a silicon wafer and a polyvinyl alcohol (PVA) sacrificial layer and PPF/DEF solution was deposited by spin coating. **(B)** Using a conventional mask aligner UV light was irradiated onto the PPF solution through a dark field mask to cross-link the PPF segments. **(C)** A layer of pNIPAM-AAc was added on top of the wafer and leveled by hand. **(D)** A second UV exposure through a dark field mask was used to photopattern the pNIPAM-AAc layer. **(E)** The uncrosslinked PPF, DEF, NIPAM-AAc was removed by developing the wafer in alcohol (EtOH and/or MeOH) and DI H_2O. **(F)** The microgrippers were released from the wafer by placing the wafer in DI H_2O to dissolve the underlying PVA sacrificial layer.

Reprinted with permission from J. C. Breger, C. K. Yoon, R. Xiao, H. R. Kwag, M. Wang, J. Fisher, T. D. Nguyen and D. H. Gracias, "Self-Folding Thermo-Magnetically Responsive Soft-Microgrippers," *ACS Applied Materials & Interfaces*, vol. 7, pp. 3398-3405, 2015.

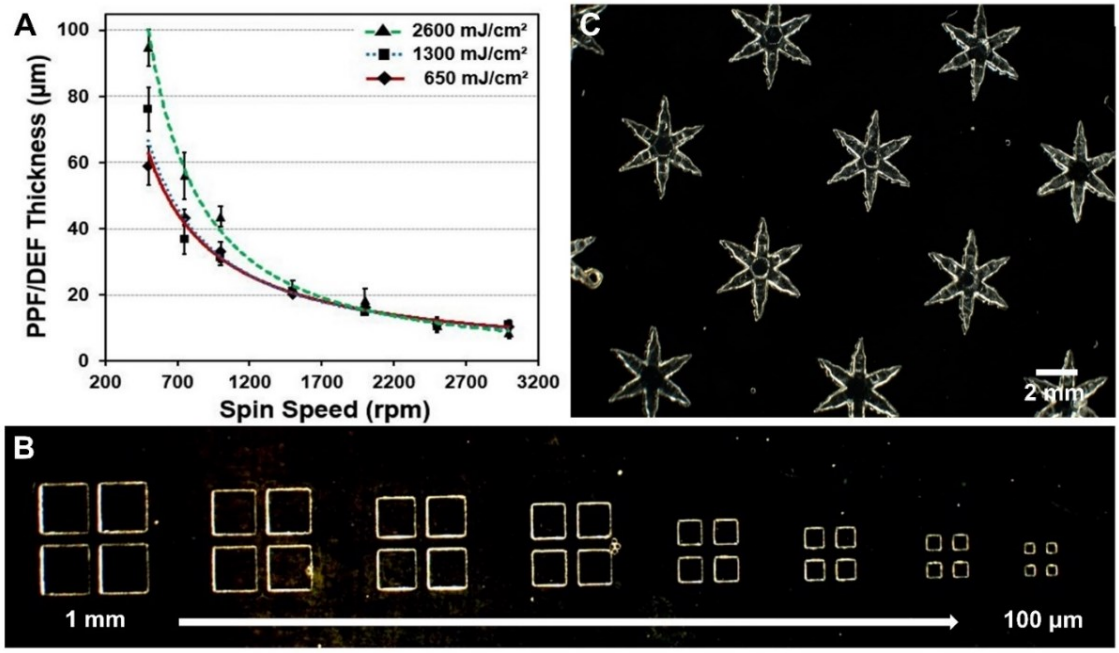

Figure 5.3. Optimization of the photopatterning of the microgrippers. (A) Films of different PPF thickness ranging from 10 to 100 µm were created by controlling the spin coat speed and the UV exposure intensity. Each point in the plot represents the average of four measurements along with the standard deviation. **(B)** Optical images showing the resolution of photopatterning. The smallest squares that could be reproducibly patterned were 100 x 100 µm squares (the smallest size on the dark field mask) spaced approximately 130 µm apart. **(C)** Optical images of developed PPF/pNIPAM-AAc microgrippers on the substrate prior to release from the wafer. The image highlights the parallel and mass-producible features of the microgripper photopatterning process.

Reprinted with permission from J. C. Breger, C. K. Yoon, R. Xiao, H. R. Kwag, M. Wang, J. Fisher, T. D. Nguyen and D. H. Gracias, "Self-Folding Thermo-Magnetically Responsive Soft-Microgrippers," *ACS Applied Materials & Interfaces*, vol. 7, pp. 3398-3405, 2015.

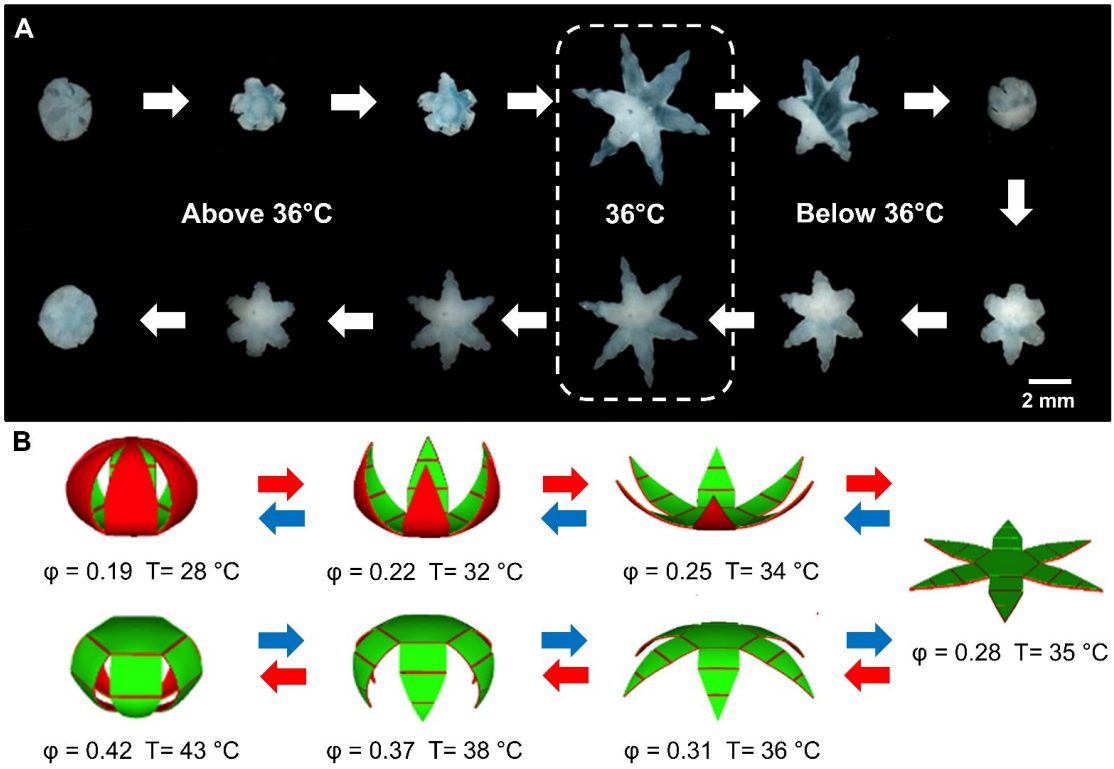

Figure 5.4. Experimental and simulation image illustrate reversible thermally responsive self-folding of a representative microgrippers in DI H_20. (A) Images of a closed gripper with PPF segments on the outside opening as the temperature is decreased below 36 °C and then folding back on itself to become a closed gripper but with the PPF segments on the inside. On heating the self-folding process reverses, and reversibility was verified over 50 cycles (data not shown). In the absence of any thermal gradients associated with heating the grippers, we estimate the experimental time scale for actuation on the order of minutes. **(B)** Simulation snapshots are in agreement with the experimental trends and suggest that the extent of gripper folding depends on the temperature and the swelling function φ.

Reprinted with permission from J. C. Breger, C. K. Yoon, R. Xiao, H. R. Kwag, M. Wang, J. Fisher, T. D. Nguyen and D. H. Gracias, "Self-Folding Thermo-Magnetically Responsive Soft-Microgrippers," *ACS Applied Materials & Interfaces*, vol. 7, pp. 3398-3405, 2015.

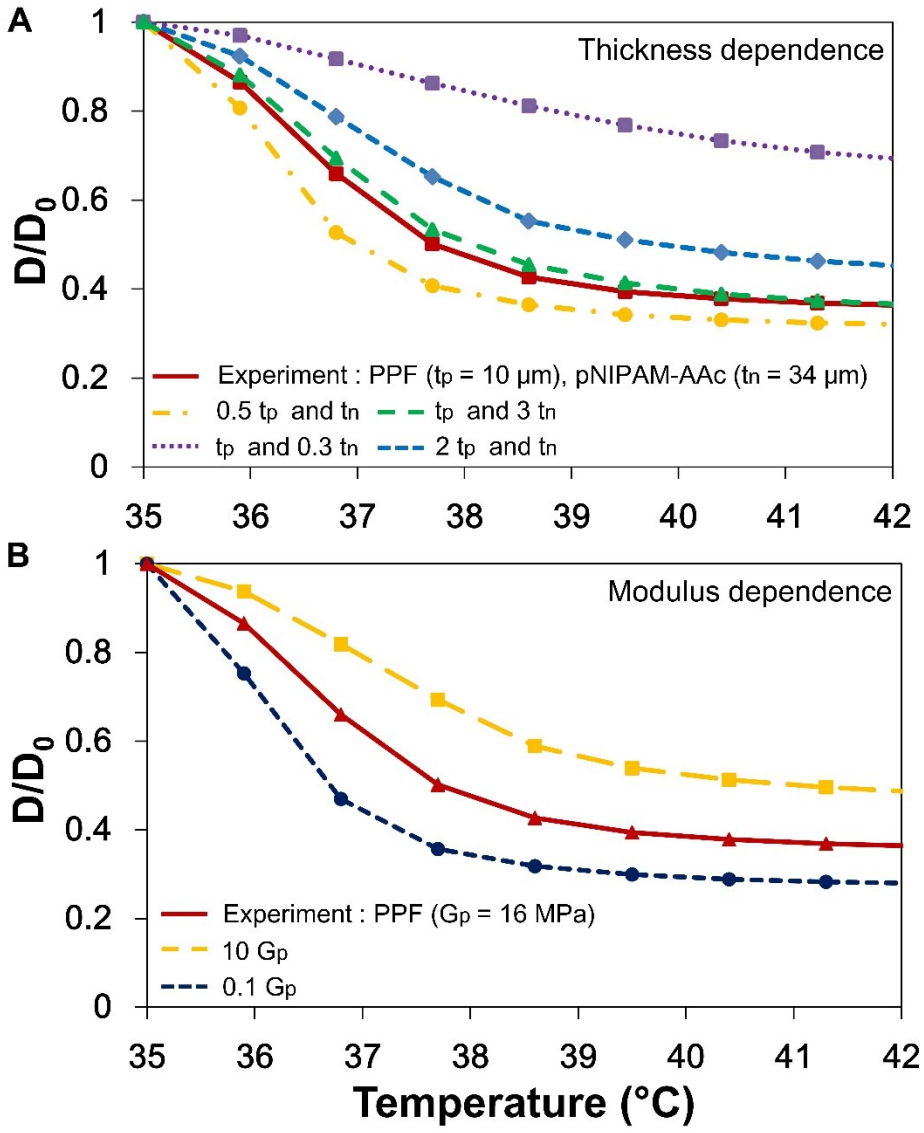

Figure 5.5. FEM sensitivity analysis exploring the dependence of the microgripper diameter reduction ratio (D/Do) on the **(A)** thickness of the pNIPAM-AAc and PPF layers and **(B)** the modulus of the stiff layer.

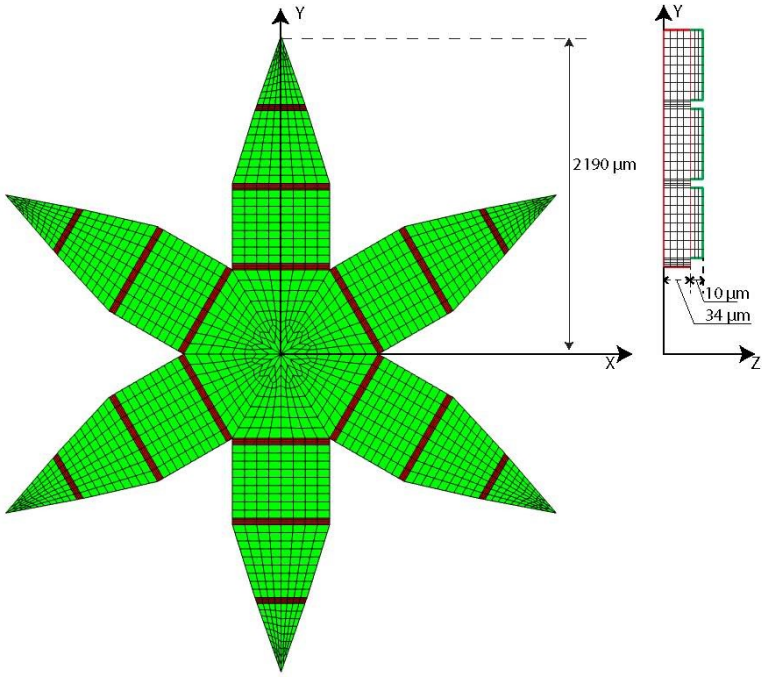

Figure 5.6. Finite element model of gripper specimen

Reprinted with permission from J. C. Breger, C. K. Yoon, R. Xiao, H. R. Kwag, M. Wang, J. Fisher, T. D. Nguyen and D. H. Gracias, "Self-Folding Thermo-Magnetically Responsive Soft-Microgrippers," *ACS Applied Materials & Interfaces*, vol. 7, pp. 3398-3405, 2015.

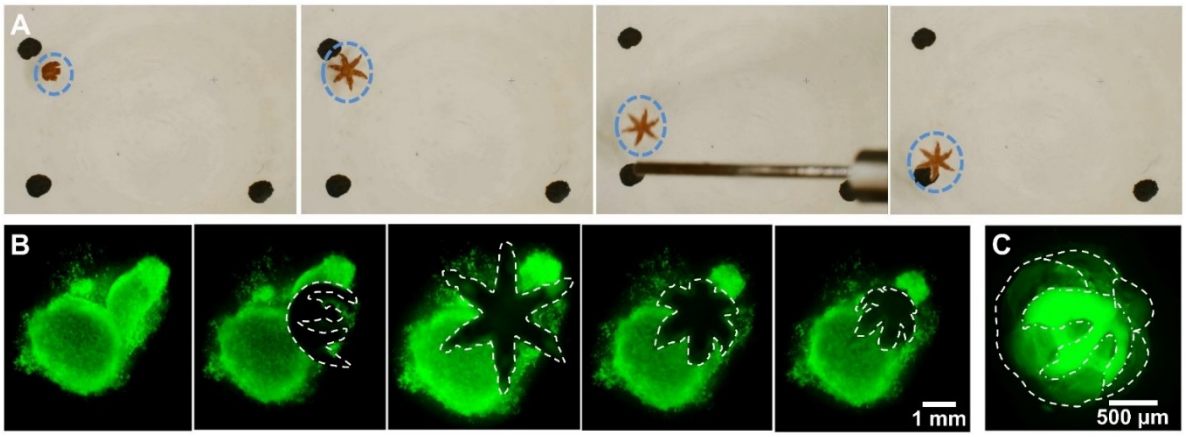

Figure 5.7. Applications of the soft thermoresponsive self-folding grippers. (A) Video snapshots showing guidance of Fe_2O_3 doped polymer grippers between two round black marks using a magnetic probe. **(B)** Capture and excision of cells from a live cell fibroblast clump. **(C)** Gripper with excised cells within its grasp. The dashed lines are added to aid visualization of the gripper and the excised cells.

Reprinted with permission from J. C. Breger, C. K. Yoon, R. Xiao, H. R. Kwag, M. Wang, J. Fisher, T. D. Nguyen and D. H. Gracias, "Self-Folding Thermo-Magnetically Responsive Soft-Microgrippers," *ACS Applied Materials & Interfaces*, vol. 7, pp. 3398-3405, 2015.

6. Control of Untethered Soft Micro Grippers for Pick-and-place Tasks*

6.1. Overview

In order to handle complex tasks in hard-to-reach environments, small-scale robots have to possess suitable dexterous and untethered control capabilities. The fabrication and manipulation of soft, small-scale grippers complying to these requirements is now made possible by advances in material science and robotics. In this paper, we use soft, small-scale grippers to demonstrate pick-and-place tasks. The precise remote control is obtained by altering both the magnetic field gradient and the temperature in the workspace. This allows us to regulate the position and grasping configuration of the soft thermally-responsive hydrogel-nanoparticle composite magnetic grippers. The magnetic closed-loop control achieves precise localization with an average region-of-convergence of the gripper of 0.12±0.05 mm. The micro-sized payload can be placed with a positioning error of 0.57±0.33 mm. The soft grippers move with an average velocity of 0.72±0.13 mm/s without a micro-sized payload, and at 1.09±0.07 mm/s with a micro-sized payload.

---

* Reprinted with permission from

1. F. Ongaro, C. K. Yoon, F. van den Brink, M. Abayazid, S. H. Oh, D. H. Gracias, and S. Misra, "Control of Soft Untethered Grippers for Pick-and-Place Tasks," *Proceedings of the IEEE RAS/EMBS International Conference on Biomedical Robotics and Biomechatronics (BioRob) (IEEE BioRob)*, pp. 299-304, 2016.

6.2. Introduction

The ability of untethered, small-scale robots to handle nontrivial tasks has been demonstrated in a broad variety of applications, such as manipulation, assembly and microactuation.[71,207,208] However, traditional small robots are often passive with no shape-changing capabilities. This results in limited dexterity that restricts the complexity of achievable tasks. In contrast, robots with gripping capabilities provide significant advantages in achieving complex tasks. Small-scale grippers have enabled a wide set of applications, like precise micro-assembly, minimally invasive surgery, genetics, cell manipulation and mechanical characterization.[209–212] For instance, Gultepe *et al.* demonstrated the feasibility of an in vivo biopsy of the porcine bile duct using thermally responsive grippers.[72] Ichikawa *et al.* demonstrated the enucleation of bovine oocytes using untethered millimeter scale grippers.[211]

In the aforementioned studies, the small size of the grippers has been exploited to perform tasks that would otherwise be unfeasible with traditional techniques. Nonetheless, at least four main challenges need to be overcome before untethered grippers can be broadly used in biomedical applications; (1) Further miniaturization of the grippers combined with untethered operation has to be achieved. (2) Precise closed-loop control of motion and grasping of the grippers has to be realized. (3) The grippers have to reliably manipulate micro-sized objects. (4) The grippers have to be fabricated using biocompatible materials and operate in a manner that poses no risk to humans.

Size reduction and untethered actuation are critical to enable maneuverability of small-scale grippers in hard-to-reach environments. Conventional robotic approaches with electrical motors and actuators do not allow for significant miniaturization of the electronic components and on-board batteries. Hence, the use of wirelessly powered self-folding robots have drawn interest and shown promising results.[30,132,182,213–216] A family of prominent self-folding structures are composed of hydrogels. Hydrogels have several attractive properties of relevance to untethered small robots. Many can be constructed with biocompatible and even biodegradable polymer chains or cross-linkers making them attractive for biomedical applications. They can function in aqueous media of relevance to biology and medicine. Their soft and squishy nature allows them to mimic the touch and feel of biological and even human appendages. Finally, they can be photopatterned into definite shapes so that they can change their shape on swelling and shrinkage.[28]

In this chapter, self-folding is achieved by constraining the swelling of the hydrogel using a stiff polymer (SU-8). As previously demonstrated this combination of a stiff polymer with a reversibly swelling hydrogel can be used to create microtools with significant strength and applicability for grasping applications. In a related study, Breger et al. doped the polymer with magnetic nanoparticles to demonstrate open-loop control of soft grippers.[74] We utilize similarly designed grippers to realize closed-loop control and obtain levels of precision and reliability that are not achievable in open-loop. Closed-loop control of hydrogel grippers have also been reported by Fusco *et al*.[132,213] The main differences between Fusco *et al*.[132,213] and our

study are: (a) The previously reported grippers[132,213] were not magnetic themselves, so magnetic motion control was only possible when they gripped onto a magnetic object. (b) Previously near-IR radiation was used to heat the grippers whereas here we use a Peltier element. (c) The numerical results and analysis of the closed-loop motion control and pick-and-place tasks were not reported. Consequently, the accuracy of previously reported tasks remains unclear.

In this study, we demonstrate and analyze the performance of loaded and unloaded grippers that can be precisely localized and positioned in two-dimensional space using closed-loop motion control. We exploit the self-folding properties of the hydrogel to provide temperature control and regulate the configuration of the grippers. Finally, through the synergy of magnetic and temperature control, we demonstrate the capability of grippers to execute pick-and-place of micro-sized objects.

6.3. Experiments

In this section, the magnetic and thermal systems are described. Subsequently, we illustrate the fabrication process of the gripper and the techniques applied for their magnetic and thermal characterization.

6.3.1. Magnetic and Thermal Systems

Our magnetic system consists of six orthogonally oriented electromagnets surrounding a Petri dish with an attached Peltier element (**Figure 6.1.**).[217] The electromagnets are controlled using a proportional-integral-derivative (PID) controller.[218] Each electromagnet is powered by an Elmo Whistle 1/60 servo

controller (Elmo Motion Control, PetachTikva, Israel). A color camera (Point Grey Research Inc., Richmond, Canada) and a microscope (Mitutoyo, Kawasaki, Japan) are used to track the grippers. The system can generate magnetic fields with maximum magnitude of 15 mT with 60 mT/m gradients. These magnetic fields are safe in clinical applications, where fields of up to 1.5 T are used daily in magnetic resonance imaging.

A Peltier element is used to regulate the temperature of the water where the soft grippers are floating. The element is attached below the Petri dish with conductive double-sided tape and controls its temperature by conduction. An Arduino Uno (Arduino, Ivrea, Italy) micro-controller powers and controls the Peltier element using Proportional-Derivative (PD) control.[218] The PD temperature controller is able to achieve a steady-state error of about 1°C and can heat the water at an average rate of 10 °C/min. A commercial thermometric probe is used in the PD control loop.

6.3.2. Fabrication of Soft Grippers

In order to fabricate the segmented SU-8/continuous poly (*N*-isopropylacrylamide) (pNIPAM-AAc) bilayer grippers, a 90 % hydrolyzed polyvinyl alcohol (PVA) sacrificial layer is spin coated onto a silicon (Si) wafer and then baked at 115 °C for 5 minutes (**Figure 6.2.**). SU-8 is then spin coated on the PVA at 2000 rpm followed by a pre-bake process at 70 °C for 1 minute, 115 °C for 3 minutes, and 70 °C for 1 minute. The 21 μm-thick SU-8 film is then photopatterned using a photomask and exposed to 180 mJ/cm^2 ultraviolet (UV) light (365 nm) to initiate crosslinking. Further, post baking is carried out at 70 °C for 1 minutes, 115 °C for 3

minutes, and 70 °C for 1 minute. Uncrosslinked portions of the SU-8 are removed using a commercial SU-8 developer for 1 minute and then washed with acetone for 1 second and isopropyl alcohol (IPA) for 10 seconds before being dried with compressed air. In order to make the 34μm thick magnetic second layer of pNIPAM-AAc, 5 % w/w biocompatible iron (III) oxide (Fe_2O_3, Sigma-Aldrich, St. Louis, USA) 50 nm nanoparticles are incorporated into the pNIPAM-AAc stock solution.[74] The obtained pNIPAM-AAc solution including Fe_2O_3 is patterned on the previously photopatterned SU-8 segments using a second dark field mask and aligned in non-contact mode using spacers. Once deposited and aligned, pNIPAM-AAc is exposed to 40 mJ/cm^2 UV light to initiate crosslinking. A wash in acetone and IPA is used to remove uncrosslinked pNIPAM-AAc before drying using compressed air. Finally, the wafer is immersed in DI water overnight to completely dissolve the PVA sacrificial layer. When fully opened, the grippers have a hexagram shape with a tip-to-tip dimension of 4 mm. When fully closed, the grippers have the shape of a sphere with an approximately 0.4 mm radius.

6.3.3. Magnetic Characterization of Soft Grippers

We characterize the grippers resulting from this fabrication process evaluating their magnetic dipole moment and thermal behavior. The magnetic dipole moment of the grippers ($\mathbf{m}_g \in R^{3\times1}$) is required for modeling purposes. In order to evaluate $\mathbf{m}_g$, the grippers are assumed to have a uniform Fe_2O_3 distribution. We divide the six-tip gripper in three pairs of counterposed two-tip dipoles. The magnetic dipole moments of the latter ones ($\mathbf{m}_{tips} \in R^{3\times1}$) can be superposed to obtain $\mathbf{m}_g$ (**Figure 6.3.**). The

magnitude of $\mathbf{m}_{tips}$ is experimentally measured using the *U-turn* technique, after removing four tips from the gripper to obtain a two-tips dipole.[219] The two-tip dipole align along the magnetic field lines, reversing the field direction cause them to perform a *U-turn* whose diameter (D) is given by

$$D = \frac{\alpha\pi|\dot{\mathbf{P}}|}{|\mathbf{m}_{tips}||\mathbf{B}|(\mathbf{P})|}, \tag{1}$$

where $\dot{\mathbf{P}} \in R^{3\times1}$ is linear velocity of the dipole, and α is its rotational drag coefficient. We calculate the value of α to be 2.2×10^{-11} Am^2sT approximating the two-tip dipole by a cylinder.[220] In order to determine the magnetic dipole moment, we apply uniform magnetic fields of 3.5 mT. The fields are reversed to initiate the *U-turn*. The experiment is repeated 20 times. The average *U-turn* diameter and velocity are 0.19±0.05 mm and 0.73±0.13 mm/s, respectively. Using (1) we obtain $|\mathbf{m}_{tips}| = 3.5\times10^{-8}$ Am^2. The direction of $\mathbf{m}_{tips}$ is determined using $\mathbf{m}_{tips} = p\mathbf{d} = |\mathbf{m}_{tips}|*d/|\ell|$ where $p \in R$ is the magnetic pole strength and $\mathbf{d} \in R^{3\times1}$ is the vector separating the two poles.[221] Finally, the magnetic dipole moment of the gripper is computed as the superposition of three rotated two-tip dipoles. The magnitude of mg results 7×10^{-8} Am^2 while its orientation with respect to the gripper is represented in **Figure 6.3**. We note that the adopted technique overestimates the magnetic dipole moment of the central overlapping part. However, this section is assumed to have a negligible effect on the overall magnetic dipole moment due to its small **d**.

6.3.4. Thermal Characterization of Soft Grippers

We also characterize the thermal response of the grippers. For this purpose, the temperature of the water was increased until the gripper was fully closed, and then decreased to room temperature. During this procedure, the gripper changes its configuration from star-shaped to spherical, and back (**Figure 6.4.**). Therefore, we use the diameter of the gripper to evaluate its configuration. Five successive opening and closing cycles were analyzed for three different grippers. The results are shown in **Figure 6.4.** The grippers on average completely opened at temperatures below 24 °C and fully closed above 27 °C. However, we noticed a variance of these boundaries depending on the temperature dynamics. Open grippers closed at lower temperatures than the ones at which closed grippers opened. We attribute this behavior to the heating rate being higher than the cooling rate.

6.3.5. Tracking and Control

Magnetic-based wireless control techniques are used for the motion control of grippers. These are based on the ability to map the currents at the electromagnets into the electromagnetic forces exerted on the grippers using,

$$\mathbf{F}(\mathbf{P}) = (\mathbf{m}_{mg} \cdot \nabla)\mathbf{B}(\mathbf{P}) = \mathbf{\Lambda}(\mathbf{m}_{mg}, \mathbf{P})\mathbf{I}\,, \tag{2}$$

where **F** are the electromagnetic forces acting on the soft gripper, $\mathbf{B}(\mathbf{P}) \in \mathrm{R}^{3\times1}$ and $\mathbf{I} \in \mathrm{R}^{6\times1}$ are the magnetic field produced by the electromagnets and their currents, respectively, and $\mathbf{\Lambda}(\mathbf{m}_{mg}, \mathbf{P}) \in \mathrm{R}^{3\times6}$ is the actuation matrix, which maps the input currents into magnetic forces.[222] The forces are then regulated using a two-input,

three-output Multi-Input Multi-Output (MIMO) PID controller. The two inputs of the regulator are the x– and y–coordinates of the gripper. The output **F** is subsequently mapped into **I** using the pseudo-inverse of $\mathbf{\Lambda}(\mathbf{m}_{mg}, \mathbf{P})$.[223]

The computation of the force-current map ($\mathbf{\Lambda}$) requires the knowledge of $\mathbf{B}(\mathbf{P})$ and $\mathbf{m}_{mg}$. The $\mathbf{B}(\mathbf{P})$ of our setup has been evaluated in previous studies, using a finite elements model analysis, and successively verified using a calibrated three-axis Hall magnetometer.[224] The value of $\mathbf{m}_{mg}$ is estimated in Sec. 6.3.3., the tracking procedure to obtain P is presented in Sec. 6.3.5.

The tracking process is composed of two steps. The first step aims at extracting the gripper contour from the input image, and is presented in **Figure 6.5**. The points of this contour are subsequently mapped to the imaginary plane at the beginning of the successive step. The selected equation for this mapping is $z_n = x_n + iy_n$ for n = 0, 1, ..., *N* where *N* is the number of the re-sampled contour points, x_n and y_n are the coordinates of the n-th re-sampled point, and *i* is the imaginary number.[225] We use this uniform sampled complex representation to calculate the Discrete Fourier Transform (DFT) coefficients by,

$$Z_k = \frac{1}{N}\sum_{n=1}^{N-1} z_n \exp\left(\frac{-i2\pi nk}{N}\right) \text{ for } n = 0, 1, ..., N-1, \tag{3}$$

where $k \in \mathbb{Z}$ goes from -15 to 16. The DFT coefficients provide us the position, scale and orientation of the gripper.[225] In order to increase noise rejection, we ignore all

the contours that are not 6-fold symmetric by only tracking objects that satisfy the following conditions:[226]

$$Z_{-5} > \frac{2}{N-2}\left(\sum_{k=-15}^{16} Z_k - Z_1\right), \tag{4}$$

$$Z_7 > \frac{2}{N-2}\left(\sum_{k=-15}^{16} Z_k - Z_1\right), \tag{5}$$

where Z_k are normalized Fourier descriptors. Furthermore, we set a threshold constraint on the ratio between contour and area of the contour. This value must be between 0.5 and 1 in order to avoid erroneous tracking of other 6-fold symmetric objects.

For the purpose of dealing with uncertainties in the tracking, we implemented a standard Kalman filter.[227] The Kalman filter provides a one-step ahead estimation of positions and velocities, using current positions and control input. The process noise is assumed to be a random variable with a Gaussian distribution $N(0, Q)$, $Q \in R^{4\times4}$ being an empirically determined covariance matrix.

6.4. Results and Discussions

In this section, we evaluate the performance and capabilities of the grippers. First motion control experiments are performed. Following these experiments, through the cooperation of motion and temperature closed-loop control, we assess the performance and capabilities of the grippers in pick-and-place tasks.

6.4.1. Motion Control of Micro Grippers

In these experiments, we evaluate the closed-loop control of soft grippers during point-to-point control and tracking of circular and square paths (**Figure 6.6.**). The experiments are performed both when the grippers are unloaded, and loaded with a 500 μm diameter polystyrene bead (Polysciences, Warrington, USA) (micro-sized non-magnetic payload). The circular path has a radius of 3mm. The square path has sides of 6 mm. In order to verify the statistical reliability of the results, we perform 50 experimental trials for each task, using 10 different grippers without the micro-sized payload. The experimental results are tabulated in **Table 6.1.** The grippers without micro-sized payload move with an average velocity and positioning error of 0.72±0.13 mm/s and 0.11±0.1 mm, respectively.

The average positioning error for the 150 experimental trials is 3 % of the body length of the gripper. The error never reaches values above 5.5 % of the gripper body length and such errors only occur during sharp turns, when the magnetic dipole moment of the gripper and the magnetic field are the least aligned, resulting in a weaker magnetic force from equation (2).

In order to determine whether the performance difference among different grippers can be considered statistically negligible, we performed a Two One-Sided T-test (TOST).[228] The tests revealed statistical equivalence, with 90 % interval confidence, suggesting that all soft grippers behave similarly. Consequently, the number of experimental trials of motion control experiments of grippers with the micro-sized payload was reduced to 15 trials. These experiments followed the

previously presented methodology and the results are tabulated in **Table 6.1**. The grippers with the micro-sized payload moved 52 % faster than grippers without the micro-sized payload, with an average velocity and positioning error of 1.09±0.07 mm/s and 0.17±0.23 mm, respectively. We attribute this increase in speed to the compact folded spherical-shape of the closed cargo loaded gripper which reduces the shear forces with the water and the side-walls of the dish.

6.4.2. Pick-and-place Tasks

In this section, we highlight the ability of grippers to perform pick-and-place tasks. A gripper is positioned above a 500 μm spherical plastic bead. Once the position is reached, the temperature is raised to 40 °C. This causes the gripper to close, and grasp the bead. Therefore, the micro-sized payload is captured within the gripper and can be dragged to the desired dropping location. The releasing procedure is activated by decreasing the temperature below 25 °C. The experiment is repeated five times with an average positioning error of the bead of 0.57±0.33 mm. The micro-sized payload is transported for 1.5 cm with an average velocity of 1.09±0.07 mm/s.

6.5. Conclusions

In this chapter, we characterize soft, self-folding grippers and analyze their capabilities and performance. Moreover, we demonstrate their ability to pick-and-place micro-scale objects. The gripper can be localized and follow trajectories with average positioning errors of 0.03 body lengths and speeds of 0.2 body lengths per second. Pick-and-place tasks are completed at average velocity of 1.09±0.07 mm/s and positioning error of the micro-sized object of 0.57 mm.

The experiments are enabled via two significant advances in materials science and robotics which include, (1) The fabrication of reversible soft-actuating grippers that harness mechanical energy and shape change from swelling; hence, they do not need wires, batteries or external power sources for actuation. (2) The ability to control the local temperature and magnetic field in a closed-loop with high accuracy.

As part of future work, grippers will be controlled in three-dimensional space. Furthermore, fully-autonomous pick-and-place of irregularly shaped objects will be studied. Moreover, advanced control techniques (e.g., cascade control) will be used to optimize the tracking of more intricate paths. Also, the Fe_2O_3 pattern of the grippers will be exploited in order to utilize the presented system in clinically-relevant applications using medical imaging systems.

Table 6.1. Experimental motion control results of soft grippers for point-to-point, circular and square trajectories.
The average speeds and Euclidean-norm of average positioning error are reported with the respective standard deviation (150 and 15 experimental trials are conducted for grippers without and with the micro-sized non-magnetic payload, respectively).

	Micro-grippers without payload		Micro-grippers with payload	
Experiment	Average speed	Error	Average speed	Error
Point to point	804±107 μm/s	129±56 μm	1104±60 μm/s	236±44 μm
Circular	629±132 μm/s	123±95 μm	1081 ±42 μm/s	171±120 μm
Square	731±115 μm/s	93±104 μm	1089±49 μm/s	130±126 μm

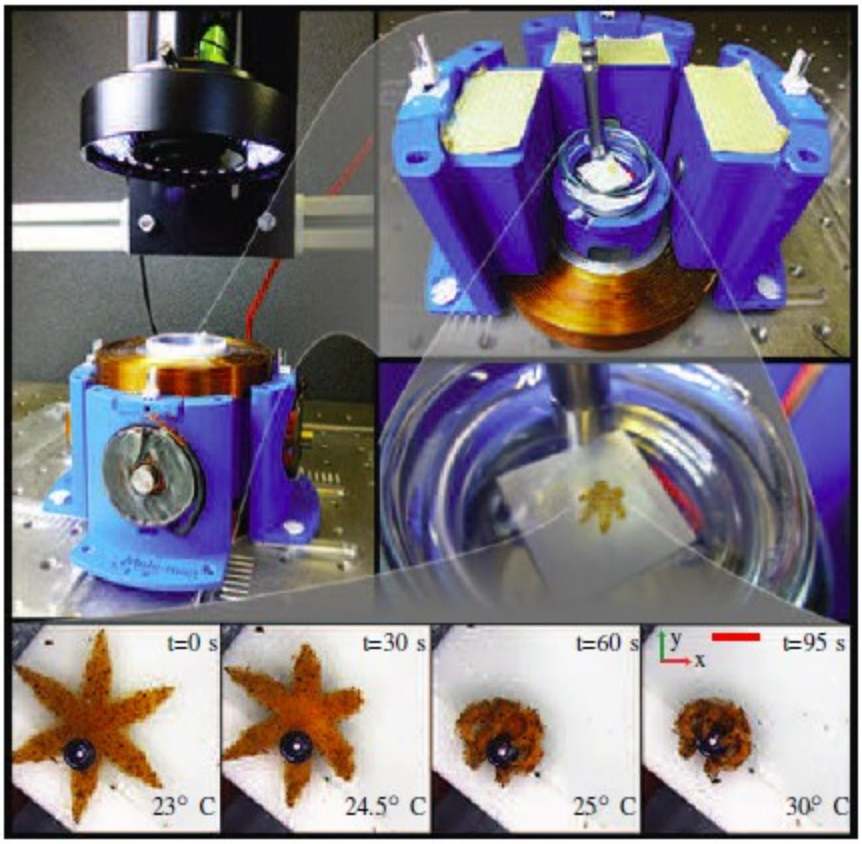

Figure 6.1. Photographs of the electromagnetic and thermal systems used to control the soft grippers. The system consists of 6 orthogonally configured coils, and a Peltier element. The electromagnetic coils have a cutoff frequency of 70 Hz and a maximum current rating of 1 A. The system generates a maximum magnetic field and magnetic field gradient of 15 mT and 60 mT/m, respectively. Bottom: Snapshots showing the gripper grasping a micro-sized bead. The scale bar is 0.8 mm.

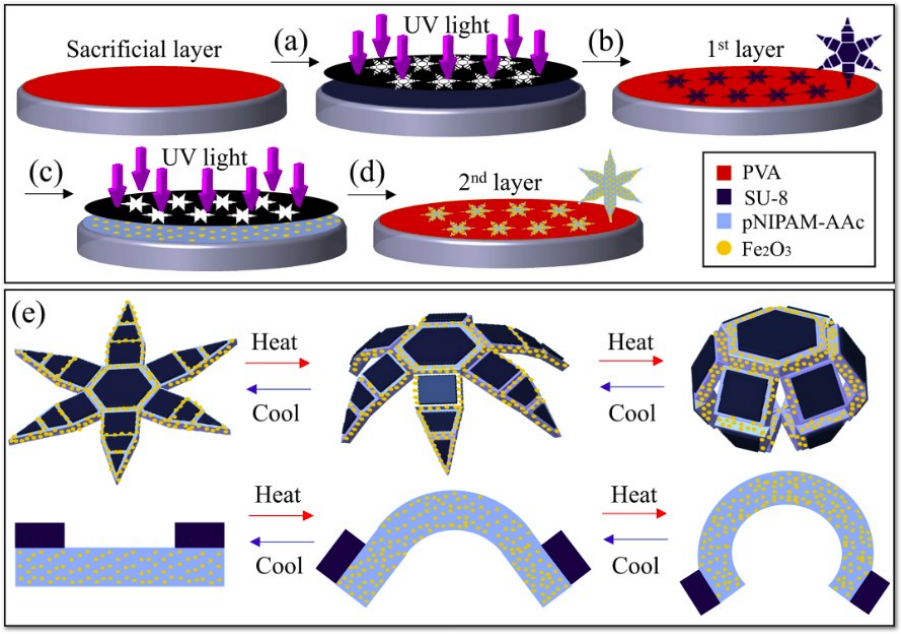

Figure 6.2. A schematic of the fabrication process of the soft grippers: **(a)** SU-8 is spin-coated on a polyvinyl alcohol (PVA) sacrificial layer. **(b)** The SU-8 film is photopatterned and exposed to ultraviolet (UV) light. **(c)** A 95% poly *N*-isopropylacrylamide (pNIPAM-AAc) and 5 % biocompatible Fe_2O_3 layer is deposited on the SU-8 layer. **(d)** The coated surface is photopatterned and exposed to UV light to obtain segmented, multi-fingered, bilayer grippers with rigid phalanges and flexible joints. **(e)** Schematic images of the untethered grippers in open and closed (grasping) configurations. Also shown is a side-view of a single hinge.

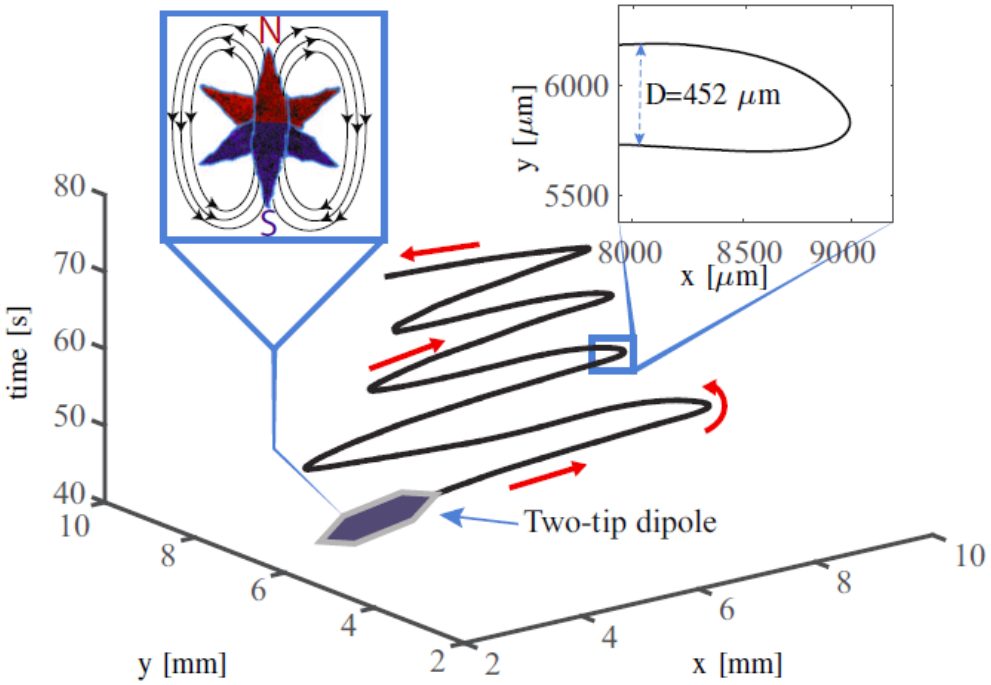

Figure 6.3. Schematic of the trajectory of the two-tip dipole during the U-turn experiments for magnetic characterization. *Left inset:* A graphical representation of the magnetic dipole moment of the soft gripper as a superposition of the magnetic dipole moments of its two-tip dipoles.

Reprinted with permission from F. Ongaro, C. K. Yoon, F. van den Brink, M. Abayazid, S. H. Oh, D. H. Gracias, and S. Misra, "Control of Soft Untethered Grippers for Pick-and-Place Tasks," *Proceedings of the IEEE RAS/EMBS International Conference on Biomedical Robotics and Biomechatronics (BioRob) (IEEE BioRob)*, pp. 299-304, 2016.

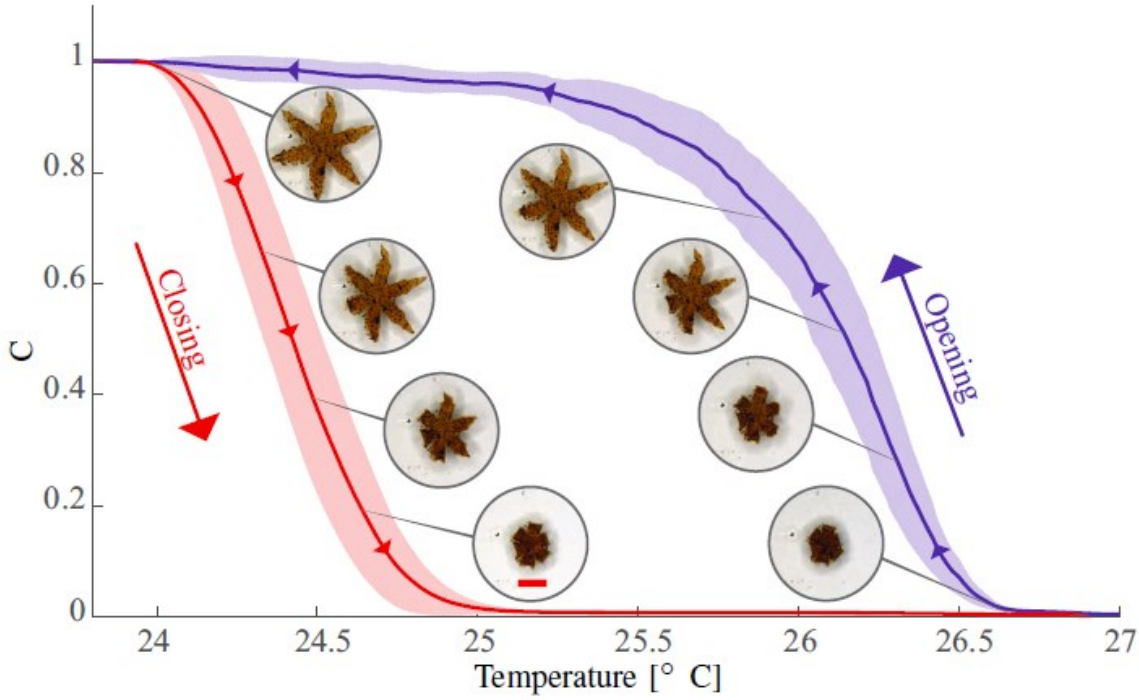

Figure 6.4. Results of the opening and closing characterization of the soft grippers (15 experimental trials): The red and blue lines show the average configuration of the grippers when they are heated and cooled, respectively. The corresponding shaded areas depict the standard deviations. The coefficient C is an indicator of the configuration of the grippers and varies from 1 (for an open configuration) to 0 (for a closed configuration). The value is computed as $C = (D(T)-D_{closed})/(D_{open}-D_{closed})$, where D(T) is the diameter of the contour of the gripper at temperature T, D_{closed} and D_{open} are the diameter values for the completely closed and open gripper, respectively. The scale bar is 0.8 mm.

Reprinted with permission from F. Ongaro, C. K. Yoon, F. van den Brink, M. Abayazid, S. H. Oh, D. H. Gracias, and S. Misra, "Control of Soft Untethered Grippers for Pick-and-Place Tasks," *Proceedings of the IEEE RAS/EMBS International Conference on Biomedical Robotics and Biomechatronics (BioRob) (IEEE BioRob)*, pp. 299-304, 2016.

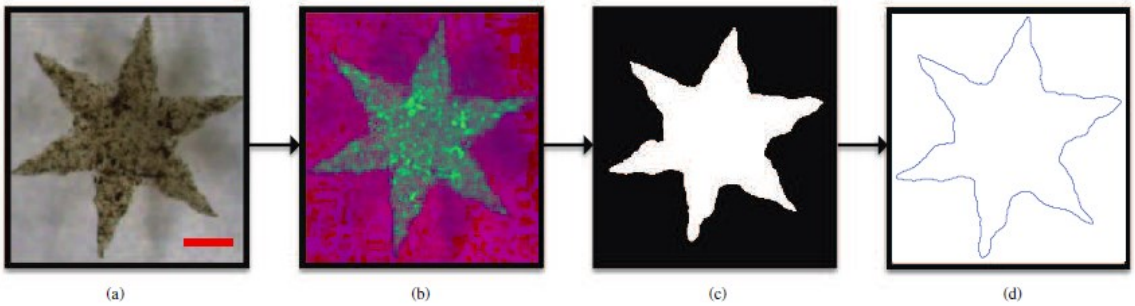

Figure 6.5. Flowchart illustrating the steps in the contour-extraction process for the soft grippers. **(a)** Input image from the microscope in Red-Green-Blue (RGB) colorspace. **(b)** The input is converted to Hue-Saturation-Value (HSV) color representation to separate chrominance from luminance and achieve glare robustness. **(c)** The image binarized using a Gaussian-window threshold after the application of a median filter. **(d)** The extracted contour of the gripper. The scale bar is 0.8 mm.

Reprinted with permission from F. Ongaro, C. K. Yoon, F. van den Brink, M. Abayazid, S. H. Oh, D. H. Gracias, and S. Misra, "Control of Soft Untethered Grippers for Pick-and-Place Tasks," *Proceedings of the IEEE RAS/EMBS International Conference on Biomedical Robotics and Biomechatronics (BioRob) (IEEE BioRob)*, pp. 299-304, 2016.

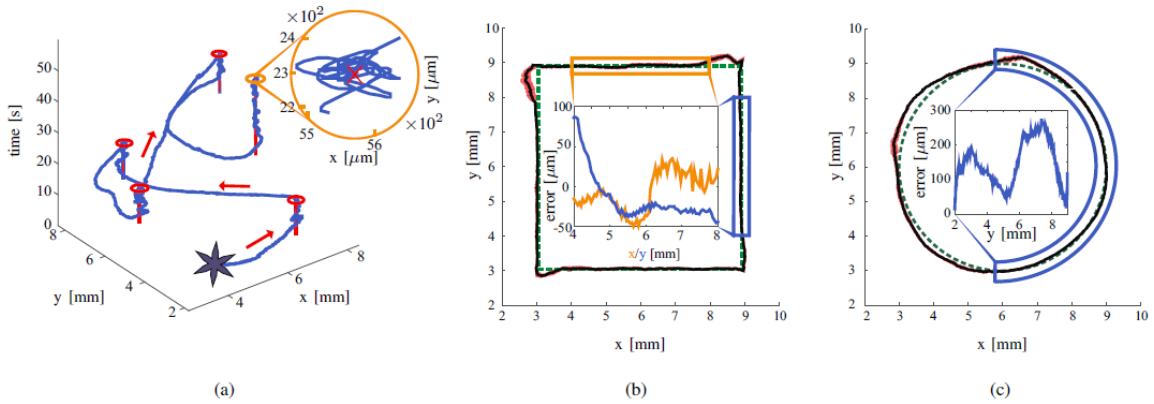

Figure 6.6. Representative closed-loop motion control experimental results of a gripper. (a) An example of point-to-point motion control experiments. The red lines represents the setpoint, the blue line the trajectory of the gripper, and the red circles the Region of Convergence (ROC). **(b)** and **(c)** depict the trajectory following experiments. The green dashed path represents the reference trajectory, the black line shows the path of the gripper, and the red area represents the standard deviation for the corresponding point among all the experiments. The insets show the positioning error in the highlighted parts of the trajectories.

7. Autonomous Panning and Control of Soft Untethered Grippers in Unstructured Environments*

7.1. Overview

The use of small, maneuverable, untethered and reconfigurable robots could provide numerous advantages in various micromanipulation tasks. Examples include microassembly, pick-and-place of fragile micro-objects for lab-on-a-chip applications, assisted hatching for in-vitro fertilization and minimally invasive surgery. This study assesses the potential of soft untethered magnetic grippers as alternatives or complements to conventional tethered or rigid micromanipulators. We demonstrate closed-loop control of untethered grippers and automated pick-and-place of biological material on porcine tissue in an unstructured environment. We also demonstrate the ability of the soft grippers to recognize and sort non-biological micro-scale objects. The fully autonomous nature of the experiments is made possible by the integration of planning and decision-making algorithms, as well as by closed-loop temperature and electromagnetic motion control.

---

* Reprinted with permission from

1. F. Ongaro[#], S. Scheggi[#], C. K. Yoon[#], F. van den Brink, S. H. Oh, D. H. Gracias, and S. Misra, "Autonomous Planning and Control of Soft Untethered Grippers in Unstructured Environments," *Journal of Micro-Bio Robotics, In press*, 2016.
DOI 10.1007/s12213-016-0091-1
[#]: Equal contributions.

These grippers are capable of completing pick-and-place tasks of biological material at an average velocity of 1.8±0.71 mm/s and a drop-off error of 0.62±0.22 mm. Color-sensitive sorting of three microscale objects is completed at a velocity of 1.21±0.68 mm/s and a drop-off error of 0.85±0.41 mm. Our findings suggest that improved autonomous untethered grippers could augment the capabilities of current soft-robotic instruments especially in advanced tasks involving manipulation.

7.2. Introduction

Small-scale robots have shown promising results in a variety of tasks, ranging from micromanipulation[214,229–231] and microassembly[232,233] to minimally invasive surgical (MIS) interventions, such as biopsies[72] and targeted drug delivery.[71,197,234,235] In many of these tasks there is a need to move and transport objects with high precision in unstructured environments. Examples include pick-and-place of fragile objects for lab-on-a-chip applications, assisted hatching for in-vitro fertilization, assembly and repair of printed circuit boards (PCB) and of microelectromechanical systems (MEMS), angioplasty and embolization.[236–240] Untethered small-scale robots with soft, maneuverable and reconfigurable components could perform these procedures, improving functionality. For this purpose, the robots would have to possess reliable and robust motion and grasping capabilities. Soft grippers might represent a viable solution. The reliability and robustness of large-scale soft grippers have been heavily demonstrated, as they are a reality in the market for manipulators.[241,242] Additionally, closed-loop control would be necessary to achieve the required high levels of precision and robustness.

However, the implementation of closed-loop control at such scales presents significant challenges. Furthermore, small-scale robots have to satisfy at least four requirements for applicability. They must: #(1) possess an untethered structure that allows them to move in tortuous environments; #(2) allow manipulation along accurate trajectories in unstructured environments; #(3) have sizes that allow them to reach and move within constrained environments; and #(4) be capable of detecting and promptly reacting to variations of their surroundings. Various untethered agents capable of manipulation on small size scales have been described previously.[132,208,210,216] Among these, self-folding hydrogel soft grippers allow the decoupled control of motion and grasp.[243] Their ability to wirelessly harness power from the surrounding environment offers a solution to requirement #(1).[28,72] They can be fabricated in sizes that are compatible with applications such as in-vitro fertilization, PCB and MEMS assembly, and allow access to the major vascular vessels, satisfying requirement #(3).[74,212] Furthermore, requirements #(2) and #(4) can be fulfilled by using accurate decision-making and tracking algorithms, closed-loop control, and fast online trajectory planning that exploits the ferromagnetic properties of the grippers. The synergy of such algorithms can make the system fully-autonomous, greatly increasing performance consistency and success rates.[244]

Although several pathfinding algorithms have been developed in recent years, only few have been applied to magnetic agents in an experimental scenario. Khalil et al. implemented a 2D path planner based on the A* algorithm and the Artificial Potential Field approach for paramagnetic microparticles.[245] A path planner based on

the Rapidly-exploring Random Tree algorithm was developed for biological cell transportation using optical tweezers.[246] Recently, an experimental comparison of six path planning algorithms when applied to the motion control of paramagnetic micro-particles was presented.[247]

In this work, we show the potential of soft, untethered grippers in tasks that involve autonomous manipulation, as well as obstacle recognition and manipulation in unstructured environments (**Figure 7.1.**). Two experiments are performed for this purpose. In the first, soft bilayer grippers are used to perform the pick-and-place of soft irregularly-shaped biological material in the presence of both static and dynamic obstacles. The second experiment demonstrates that soft grippers can autonomously recognize, classify, and manipulate regularly-shaped micro-scale rigid objects. In both experiments, the soft grippers utilize their six tips to grasp a micro-scale object and constrain it in all directions. (**Figure 7.1.**).

It should be noted that soft grippers were previously manipulated using robotic control.[132] However, there are several important differences between our work and this previously reported study. Firstly, previously utilized grippers had a homogeneous mechanical composition, whereas our soft grippers are designed with rigid segments and flexible joints. This design feature seeks to mimic biological appendages such as hands, and ensures a robust grasp of the transported microscale objects, even in the case of abrupt jerks. Secondly, as compared to previous work in which the gripper itself was not magnetic but rather was moved by a magnetic object, we have succeeded in doping the grippers themselves with magnetic nanoparticles to

allow motion control even when the grippers are not grasping a magnetic object. Furthermore, bulk magnetic doping was chosen instead of a surface coating to preserve the soft material characteristics of the gripper and prevent the corrosion or delamination of the magnetic cladding in media such as acid fluids or blood. Additionally, in this work the grippers are fully autonomous; i.e., they are able to interact with the environment and automatically adapt their behavior in real-time to changes in the scenario. Consequently, the aforementioned tasks can be autonomously performed in a faster, safer, and more robust way. Finally, a novel high sampling rate technique that makes use of an XYZ Cartesian robot is used in order to model and validate the electromagnetic system. Such validation at high density and resolution not only ensures the reliability of the model, but also enables the reliable computation of the magnetic field gradient.

7.3. Experiments

The detailed gripper fabrication process has been described previously[74] with one design change in that we replaced the stiff polymer with SU-8, a widely available photopatternable polymer. Briefly, bilayer grippers (**Figure 7.2. (a)**) were composed of lithographically photopatterned segmented SU-8 (**Figure 7.2. (b)**) and continuous poly (*N*-isopropylacrylamide-co-acrylic acid) (pNIPAM-AAc) (**Figure 7.2. (c)**). Furthermore, in order to make magnetically responsive soft grippers, 5 % (w/w) biocompatible iron (III) oxide (Fe_2O_3, Sigma-Aldrich, St. Louis, USA) 50nm nanoparticle powder was mixed with the pNIPAM-AAc solution prior to crosslinking. The soft grippers open and close reversibly due to a phase transition and associated

swelling or shrinkage in the pNIPAM-AAc layer in response to temperature changes (**Figure 7.2. (d–f)**). When fully opened, the grippers have a tip-to-tip distance of 4 mm and a 0.4 mm radius of overall sphere when fully closed.

The F_2O_3 nanoparticle patterning and the magnetic field gradient generated by an array of six orthogonal iron-core electromagnets (**Figure 7.1.**) can be used for closed-loop motion control of the grippers. To perform autonomous, accurate and robust pick-and-place of biological material in unstructured environments, the following modules are necessary: (1) an accurate image-guided tracking algorithm; (2) a reactive motion planner which uses the information from the tracker to compute suitable motion control inputs for the gripper. In the next section, we describe the tracking algorithm used to estimate the pose of the gripper.

7.4. Results and Discussions

7.4.1 Detection and Tracking of Grippers

Let $\mathbf{p} = [x, y]^T \in R^{2\times1}$ be the position of a gripper in 2D space. The state of the gripper is defined as $\mathbf{x} = [x, y, v_x, v_y]^T \in R^{4\times1}$ where v_x, v_y represent its velocities. Let us consider the miniaturized gripper as a second order system controlled by applying suitable force inputs.

The tracking algorithm is shown in **Figure 7.3.** and estimates the state $\hat{\mathbf{x}}$ and the configuration (open/close) of the gripper at runtime. In the initial phase, it determines the position $\hat{\mathbf{p}}$ of the gripper. This phase is composed of two steps. The first step extracts the contour of the gripper from the binarized color-saturation level of the image. The input to the proposed method is a 1024×1024 Red-Green-Blue

(RGB) color image acquired using a Charge-Coupled Device (CCD) connected to a microscopic lens. In the presented work, the Hue-Saturation-Value (HSV) color space is selected. Then, the coordinates of the selected color space are bounded; i.e., specific values of the axis of the color space are selected in order to detect a particular color. The bounds are chosen empirically; i.e., by examining the distribution of colors in a preselected set of images. Morphological filtering and opening are used in order to segment the image. Finally, small blobs are removed and the remaining, adjacent blobs are merged and kept for further consideration.

In the second step, normalized Fourier Descriptors (FDs) Z_k, $k \in [-15,..., 16]$ are obtained by applying the one-dimensional Discrete Fourier Transform (DFT) to the complex-valued representation of the 2D contour points. FDs provide us with the position and scale of the gripper.[225] To increase noise rejection, we ignore all the contours that are not 6-fold symmetric by only tracking objects that satisfy the conditions described at 6.3.5. Tracking and Control chapter. Furthermore, we set a threshold constraint on the ratio between the number of pixels of the perimeter and of the area of the contour. This value must be between 0.5 and 1 in order to avoid erroneous tracking of other 6-fold symmetric objects.

To compute the estimated state $\hat{\mathbf{x}}$ from position measurements $\hat{\mathbf{p}}$, we implement a standard Kalman filter[248] to consider the second order model of the gripper and control-inputs. Assuming a constant sampling Δt of the system, the Kalman filter provides an estimation of the current state $\hat{\mathbf{x}}$ as well as a one-step ahead prediction of $\hat{\mathbf{x}}$. The process and measurement noises are obtained from zero mean multivariate

Gaussian distributions N (0, **Q**) and N (0, **R**), respectively, where $\mathbf{Q} \in R^{4\times4}$ is the process noise covariance matrix and $\mathbf{R} \in R^{2\times2}$ is the measurement noise covariance matrix. **Q** is determined by empirically tuning its parameters, while **R** is computed by analyzing offline the tracked positions of the gripper using a zero-phase filter.

To speed up the detection procedure, temporal continuity is exploited to track the grippers in a sequence of frames. Given the estimated state $\hat{\mathbf{x}}$ of the tracked gripper from the previous frame, the image pixels that are within a preset range from that estimation are kept, whereas the remaining pixels are discarded. The proposed tracker runs at an average frame rate of 50 frame per second on a PC that has an Intel Xeon CPU 3.2 GHz processor and 8 GB of RAM.

7.4.2. Motion Planning

The estimated state $\hat{\mathbf{x}}$ of the gripper is then provided to a motion planner for the computation of a collision-free trajectory. Among possible motion planners, a Rapidly exploring Random Tree (RRT) is used. The RRT outputs forces that are mapped to currents at the electromagnets. For this purpose, a force-current map is developed using Finite Element Model (FEM) analysis.

The RRT is able to deal with real-valued spaces of extremely high dimension while handling the dynamics of the system. The planner is rooted at the gripper's initial state $\mathbf{x}_{start} = \hat{\mathbf{x}}$. At each iteration, the algorithm samples a collision-free state $\mathbf{x}_{sample}$ in the environment, finds its nearest neighbors $\mathbf{x}_{nn}$ in the tree, and computes feasible control forces ($F \in R^{3\times1}$) that grow $\mathbf{x}_{nn}$ toward $\mathbf{x}_{sample}$. The output of the RRT is a motion plan Γ;

$$\Gamma = [(\mathbf{x}_{start},\ \mathbf{F}_{start}),\ \ldots, (\mathbf{x}_S,\ \mathbf{F}_S)],$$

where S is the number of steps (Algorithm 1). Each entry of the motion plan represents a control input that is applied to the agent after every time interval Δt. Unlike path planning algorithms, which provide waypoints to the robot, RRTs directly provide feasible control inputs **F**.

Algorithm 1 The Rapidly-exploring Random Tree (RRT) $\mathcal{T}$ is rooted at the initial state $\mathbf{x}_{start}$ of the gripper. At each iteration, a new state $\mathbf{x}_{sample}$ is sampled, and the node $\mathbf{x}_{nn}$ of $\mathcal{T}$ closest to $\mathbf{x}_{sample}$ is computed. A feasible control $\mathbf{F}_{new}$ that grows $\mathbf{x}_{nn}$ toward the sampled state is applied. The output of the RRT is a motion plan Γ. The planner is executed every time interval T.

```
1: function BUILD_RRT
2:     T ← x_start;
3:     while k < T do
4:         x_sample ← RANDOM_STATE_GOALZOOM();
5:         x_nn ← NEAREST_NEIGHBOUR(T, x_sample);
6:         (x_new, F_new) ← CONNECT(x_nn, x_sample);
7:         if COLLISION_FREE(x_new, F_new) then
8:             T ← ADD(x_new, F_new);
9:         end if
10:    end while
11:    Γ ← COMPUTE_PLAN(T);
12:    return Γ;
13: end function
```

In the experimental validation, an RRT-GoalZoom policy is used to generate a new random state based on a biased coin toss.[249] The algorithm relies on this state to choose a random sample from either a region around the goal or from the whole space. During the planning procedure, instead of extending the RRT by an incremental step, the algorithm iterates until the random state or an obstacle is reached. Finally, a fixed planning time interval of T = 0.1 s is selected. At the beginning of the task, the RRT computes the motion plan. Successively for each period of duration T, the system

updates the planned trajectory that will be ready for the next planning time interval T. The proposed motion planner allows the system to run autonomously without any need for human intervention during standard operations. This not only reduces the system response time below the average human reaction time (400 ms)[250] to an average of 100 ms, but also lessens – if not eliminates – the need for human supervision. This, combined with the higher repeatability of fully-autonomous systems, greatly increases performance consistency and success rates.

7.4.3. FEM Modeling and Validation

Once the RRT planner has computed the obstacle-free motion plan Γ, suitable currents have to be applied to the magnetic coils in order to exert the desired forces $\mathbf{F}_i$, $i = 1,...,S$ on the agent. For this purpose, we use FEM analysis (COMSOL Multiphysics, COMSOL, Stockholm, Sweden) to develop a map between the current at the electromagnets and the magnetic flux density in the workspace. The FEM analysis is successively compared with the measurements of a 3-axis 3MH3 Teslameter (SENIS AG, Baar, Switzerland). To obtain high-density measurements an XYZ Cartesian robot moves the probe through the entire workspace at a velocity of 0.5 mm/s.[251,252] This technique allows us to compare the results at a resolution of 6.8×10^6 dots/m^2 using a total of 1523 samples in the 1.2×1.2 cm workspace. The average mismatch and its standard deviation between FEM and measurements – when the electromagnets are fed the maximum current of 1 A – are $7.4\times10^{-3} \pm 2.2$ mT and 0.073 ± 0.045 radians for field magnitude and orientation, respectively. The x– and y–components of the field are then fitted to a quadratic Lowess (LOcally WEighted Scatter plot Smooth) function

using MATLAB (MathWorks Inc., Natick, United States). The quality indices of such functions are reported in **Table 7.1.** The quadratic Lowess functions are then used to compute the force-current map as described.[223,253]

7.4.4 Temperature Control

The configuration control is provided by a Peltier element. This element controls the temperature of the environment and, consequently, the configuration (open/close) of the gripper. The configuration, determined using FD, is used as feedback for the closed-loop grasp control. In the next section, an experimental validation is performed in order to demonstrate the ability of the grippers to manipulate both biological and non-biological materials in unstructured environments.

7.4.5 Experimental Validation

An extensive evaluation is performed to assess the capabilities of the systems and demonstrate the ability of grippers to manipulate biological material in unstructured environments, and to detect and sort micro-scale objects. In the first experiment, one static and two dynamic virtual obstacles are avoided by the gripper that is at the same time performing pick-and-place of a piece of egg yolk (**Figure 7.4.**). The dynamic obstacles are two circles of 0.5 mm diameter, while the static obstacle is a wall with length of 4 mm. The dynamic obstacles are modeled as first order linear holonomic systems. Their initial motion directions and speeds are reported in **Figure 7.4. (b)**. To simulate the tracking errors, we add zero-mean white Gaussian noise at a standard deviation $\sigma = 0.5$ mm to the x− and y− coordinates of the dynamic obstacles.

The noisy measured positions of the obstacles are provided to the motion planner in order to compute obstacle free paths. Egg yolk was chosen due to its high content of cholesterol and fat content (58 % of its dry weight), representative of materials that are often manipulated in MIS interventions. To increase the resemblance between the experimental scenario and operations in biological environments, the tasks are performed on a base of porcine tissue. Based on a total of five trials, this experiment is completed with an average error on the drop-off of the object of 0.62 ± 0.22 mm. The results were achieved at an average velocity of 1.81 ± 0.71 mm/s for loaded grippers and 2.08 ± 0.39 mm/s for unloaded grippers.

The second experiment tests if the grippers can autonomously recognize various objects and sort them. We perform an experiment in which the grippers recognize colored micro-scale objects and, one by one, pick-and-place them in the area marked with the corresponding color (**Figure 7.5.**). The manipulated objects are three spherical polyester beads of 0.5mm diameter and 0.6 ± 0.1 mg weight. A color segmentation algorithm similar to that described in **Section 7.4.1.** is used to extract the position of the three objects. Please refer to the accompanying video showing an example of the experiments. A total of five trials are conducted with a velocity and error on the drop-off of the microscale object error of 1.21 ± 0.68 mm/s and 0.85 ± 0.41 mm respectively. The average error of the micro-scale object always lays within the bounds of the radius of the drop-off location (1.5 mm).

7.5. Conclusion

This study has demonstrated the capabilities of soft grippers to autonomously perform micromanipulation tasks. To further validate the proposed approach, we have performed tests on animal tissue in unstructured environments that contain time-varying obstacles. All the experiments were directed by the decision-making, path-planning, and closed loop control algorithms with no human intervention. Results show the ability of grippers to autonomously detect and adapt their behavior in response to changes in the surrounding environment. The demonstrated capabilities suggest that such grippers have the potential to enable delicate and precise manipulation in a broad variety of tasks, including microassembly, assisted fertilization and MIS. Moreover, due to their fully autonomous capabilities, they could find future applications in highly automatized processes as the population of PCB or the assembly of MEMS.

Future work will investigate the use of smaller scale grippers to offer more maneuverability and access to smaller environments. Also, 3D motion as well as operation in presence of fluid flow will be investigated. Operation in swarms will be studied to allow the parallelization of the micromanipulation tasks. Finally, we will exploit the metallic doped nature of these grippers in order to investigate the use of ultrasound or other clinically compatible imaging systems.[224,254]

Table 7.1. Quality indices for the x- (B*x*) and y- (B*y*) components of the magnetic field for the obtained fitting function.
The table reports Sum Squared Error (SSE), R-square (R^2), Adjusted R-square ($\bar{R}^2$), and Root Mean Square Error (RMSE).

	SSE (T^2)	R^2	$\bar{R}^2$	RMSE (T)
B_x	4.7×10^{-7}	1.0000	1.000	6.7×10^{-6}
B_y	2.9×10^{-7}	1.0000	1.000	5.3×10^{-6}

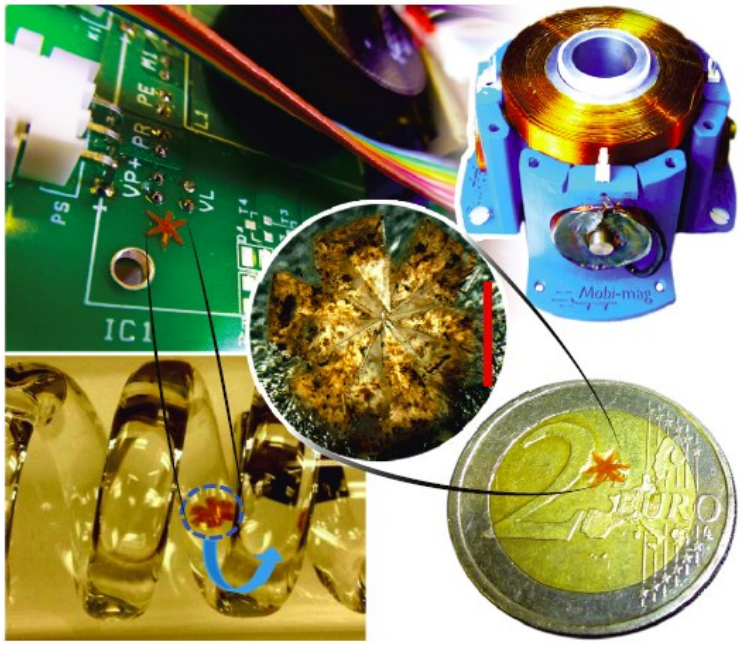

Figure 7.1. Soft grippers. *Top Left:* Image of a soft untethered gripper on a printed circuit board. *Top Right:* The electromagnetic setup consisting of six orthogonally-oriented electromagnetic coils. *Center:* Image of the closed gripper. *Bottom Left:* Video snapshot images of the gripper navigating through a tube with an inner diameter of 3.2 mm, a size smaller than most of the major vessels in the human body. *Bottom Right:* Image of the gripper on a 2€ coin. The scale bar is 0.4 mm.

Reprinted with permission from F. Ongaro, S. Scheggi, C. K. Yoon, F. van den Brink, S. H. Oh, D. H. Gracias, and S. Misra, "Autonomous Planning and Control of Soft Untethered Grippers in Unstructured Environments," *Journal of Micro-Bio Robotics, In press*, 2016.
DOI 10.1007/s12213-016-0091-1

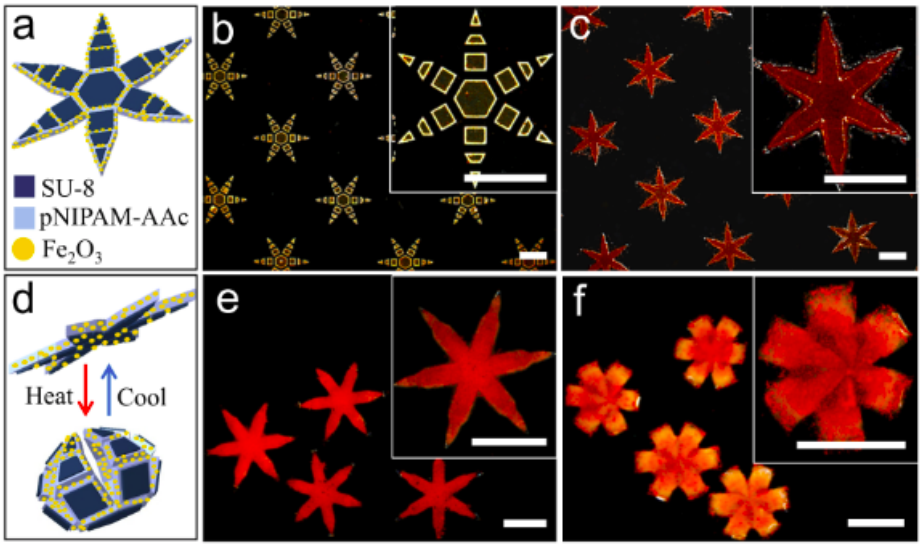

Figure 7.2. Schematic and experimental images of the fabrication and operation of the soft bilayer grippers. (a) Schematic showing the bilayer composed of a stiff, segmented, SU-8 polymer coupled with a 5 % (w/w) magnetic nanoparticle (Fe_2O_3) doped thermally stimuli responsive poly(*N*-isopropylacrylamide-co-acrylic acid) (pNIPAM-AAc) layer **(b-c)**. Experimental images after wafer scale patterning of the two layers. **(d)** Schematic and **(e-f)** experimental images showing operation of the grippers with reconfiguration from, **(e)** a flat state at room temperature to, **(f)** a closed state in which the temperature is raised to 25.3 °C.

Reprinted with permission from F. Ongaro, S. Scheggi, C. K. Yoon, F. van den Brink, S. H. Oh, D. H. Gracias, and S. Misra, "Autonomous Planning and Control of Soft Untethered Grippers in Unstructured Environments," *Journal of Micro-Bio Robotics, In press*, 2016.
DOI 10.1007/s12213-016-0091-1

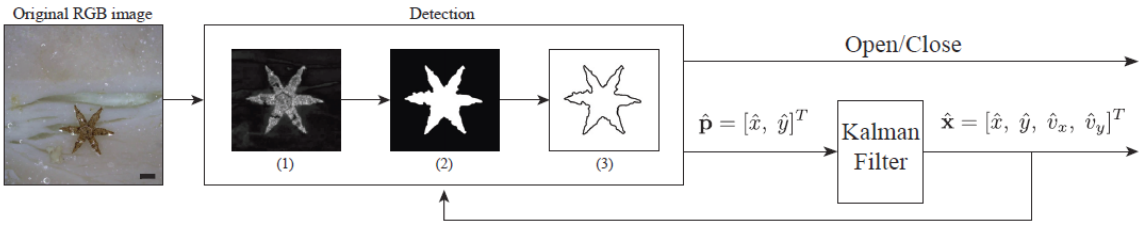

Figure 7.3. Flowchart showing the tracking process: From left to right, a Red-Green-Blue (RGB) image is taken from the microscope. In the detection phase, the image is converted to Hue-Saturation-Value (HSV) color space. (1) Bounds on the coordinates of the selected color space are employed in order to accurately detect the gripper. (2) Adaptive threshold, morphological filtering, and opening are used. Then, the adjacent blobs are merged and kept for further consideration. (3) A Discrete Fourier Transform is applied on the contour of the segmented area in order to detect the pose $\hat{\mathbf{p}} = [\hat{x}, \hat{y}]^T$ and the configuration (open/close) of the gripper. Finally, a Kalman filter is used to estimate the state $\hat{\mathbf{x}}$ of the gripper, where $\hat{v}_x$, $\hat{v}_y$ represent the estimated velocities of the agent. The estimated state of the gripper is used in the next frame to speed up the detection procedure. The scale bar is 1 mm.

Reprinted with permission from F. Ongaro, S. Scheggi, C. K. Yoon, F. van den Brink, S. H. Oh, D. H. Gracias, and S. Misra, "Autonomous Planning and Control of Soft Untethered Grippers in Unstructured Environments," *Journal of Micro-Bio Robotics, In press*, 2016.
DOI 10.1007/s12213-016-0091-1

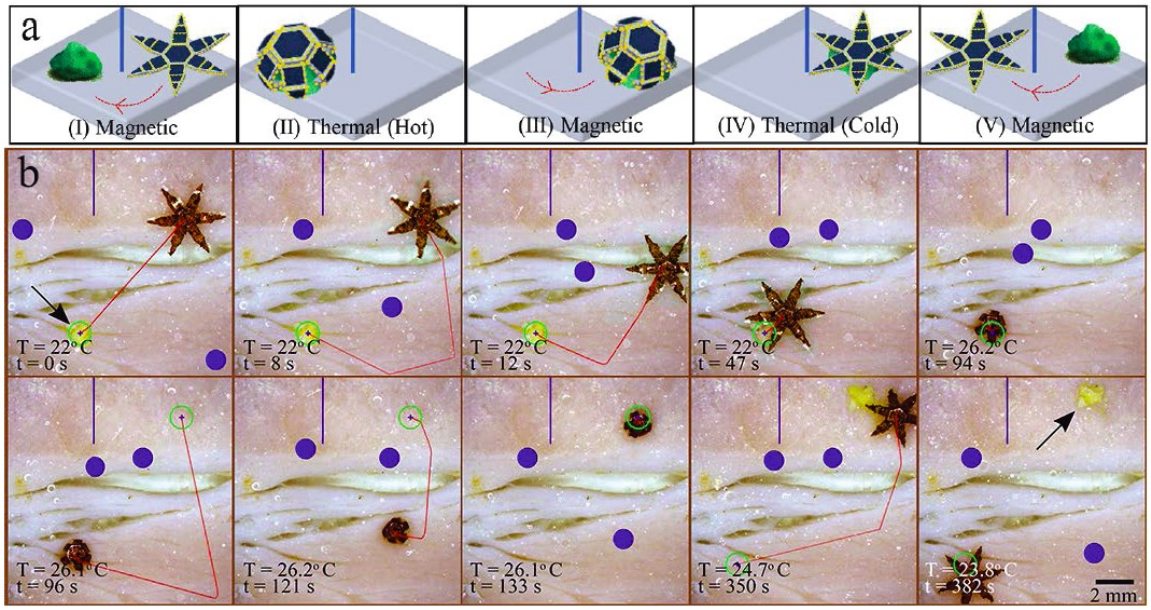

Figure 7.4. Biological manipulation of soft grippers. (a) Schematic of a representative obstacle avoidance and biological manipulation experiment. **(b)** Video snapshots of the gripper during pick-and-place of biological material in an unstructured environment on porcine tissue. The virtual obstacles are shown in blue; the circular ones are dynamic, while the wall on top of the workspace is static. The targeted position is represented the blue cross inside the green circle. The planned obstacle-free trajectory to reach the reference is represented as a red line. The gripper autonomously detects the yolk while a Rapidly-exploring Random Tree motion planner computes, and continuously updates, an obstacle-free trajectory in order to reach it. Once the target is reached, the temperature is increased until the system classifies the gripper as closed. An obstacle-free trajectory then guides the gripper to the target where the temperature is decreased until the gripper is marked as open. Finally, the gripper is moved away from the drop-off area. Times (t) and temperatures (T) are shown on the bottom-left corner of each snapshot.

Reprinted with permission from F. Ongaro, S. Scheggi, C. K. Yoon, F. van den Brink, S. H. Oh, D. H. Gracias, and S. Misra, "Autonomous Planning and Control of Soft Untethered Grippers in Unstructured Environments," *Journal of Micro-Bio Robotics, In press*, 2016.
DOI 10.1007/s12213-016-0091-1

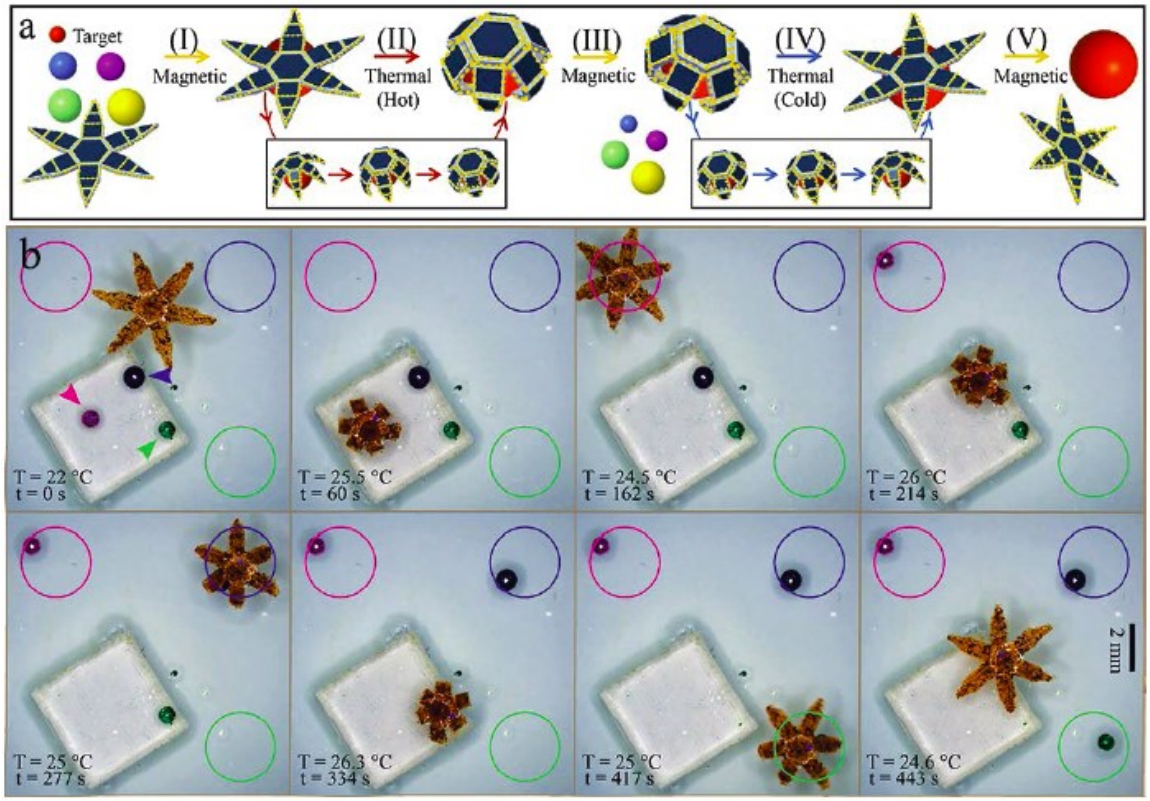

Figure 7.5. Autonomous sorting of soft grippers. (a) Schematic of a representative autonomous sorting experiment. **(b)** Video snapshots that show the gripper autonomously detecting and sorting differently colored beads, pick-and-placing them in the respectively colored drop areas. The gripper autonomously classifies the micro-scale objects, and estimates the configuration of the grippers from Fourier descriptors to determine if the desired configuration is reached. Times (t) and temperatures (T) are shown on the bottom-left corner of each snapshot.

Reprinted with permission from F. Ongaro, S. Scheggi, C. K. Yoon, F. van den Brink, S. H. Oh, D. H. Gracias, and S. Misra, "Autonomous Planning and Control of Soft Untethered Grippers in Unstructured Environments," *Journal of Micro-Bio Robotics, In press*, 2016.
DOI 10.1007/s12213-016-0091-1

8. Stimuli Responsive Self-folding 2D Layered Materials (2DLMs)/Polymer Bilayers*

8.1. Overview

Graphene has attracted significant interest for composites, sensing, electronics and optics due to a variety of attractive properties such as ballistic room temperature transport at sub-micron scales, ambipolar electrical field effect with high mobilities, very high thermal conductivity, extremely high modulus and tensile strength. In sensing applications, the extremely high surface area to volume ratio of such inherently 2D layered materials (2DLMs) translates to significant sensitivity. However, in order to utilize these features in practical devices such as macroscale flexible sensors and actuators with small form factors, there is a need to develop mass producible approaches to package, manipulate and reconfigure graphene in 3D curved and folded geometries. Self-folding is a mass producible self-assembly approach that allows the transformation of planar films to curved and folded geometries by the manipulation of forces associated with thin film stress, minimization of surface tension or swelling. In this letter, we discuss the reversible folding and unfolding of few layer graphene (FLG)/polymer (SU-8) bilayers based on differential swelling in a gradient engineered SU-8 layer.

---

* Reprinted with permission from

1. T. Deng[#], C. K. Yoon[#], Q. Jin, M. Li, Z. Liu, and D. H. Gracias, "Self-Folding Graphene-Polymer Bilayers," *Applied Physics Letters,* vol. 106, pp. 203108, 2015.
2. C. K. Yoon[#], T. Deng[#], Q. Jin, J. P. Cha, M. Li, J. Kang, Z. Liu, and D. H. Gracias, "Self-Assembly of Integrated Curved and Folded Graphene-Polymer Optoelectrical Sensor", *In Preparation*, 2017.

[#]: Equal contributions.

We first discuss micropatterning and reversible actuation of micropatterned FLG/SU-8 films in a variety of geometries such as rectangular strips, discs, crosses and flower shaped structures. We rationalize spontaneous curving using a finite element model and compare theoretically observed radii to experimentally observed radii. We investigate electrical and optical detection using rolled-up bilayers and discuss advantageous features of rolled up geometries as compared to 2D (flat) control samples. We believe that this self-folding approach could be utilized to create a variety of reconfigurable 3D curved and folded graphene based sensors and actuators for a range of applications.

8.2. Introduction

Monolayer and few layer graphene (FLG) have extraordinary intrinsic thermal, electrical, mechanical and optical properties;[255–257] consequently a wide range of multi-functional graphene based materials and devices have been proposed.[258–273] In addition to planar graphene, wrinkled, rippled, suspended, twisted and crumpled morphologies have also been realized.[257,258,262,263,265,268,270,272–276] Such 3D structures are pursued for several reasons. Firstly, strain and geometry can alter the band structure of graphene and consequently alter its properties. Secondly, for generating mass producible composites, there is a need to integrate significant volume fractions of graphene with materials such as polymers which necessitates mass production of graphene often incorporating significant quantities of crumpled architectures. Thirdly, for practical applications it is important to develop strategies to incorporate graphene into macro-scale devices, materials and structures, many of which are three

dimensional. Finally, 3D curved and folded geometries can enable relatively convenient platforms for microelectronic and optical devices such as sensors or photodetectors in a small form factor.

Curving and folding of graphene can be enabled with or without a substrate. In the absence of a thicker substrate, several groups have suggested the use of capillary forces such as with droplets of water or ultrathin polymer films to curve graphene.[277–279] Mechanical effects such as ultrasound forcing of graphene[280] or ultrasound aerosolization of graphene oxide[281] have been used to create rolled up and sack like structures. Also, laser-induced shock straining[282] has been used to generate 3D nanostructures. Curved graphene has been grown on patterned substrates such as by using CVD growth on lithographically patterned catalytic copper substrates[275,276] or by deposition in three dimensional templates such as nickel foams.[262,263] Gelation of graphene oxide using polymers such as polyvinyl alcohol, DNA or metal ions has been utilized to create 3D macrostructures.[283] For applications in flexible electronics, graphene foams have been infiltrated in PDMS[8] allowing such devices to be bent and twisted without breakage. Graphene transferred on PDMS substrates have been widely studied including the development strain and tactile sensors and fabrics.[260–262,268,270–272] In applications as actuators, graphene based systems have been utilized to develop a number of electrically and optically stimuli responsive systems.[284]

In particular, since graphene is inherently a surface, with an extremely high surface area to volume ratio, it is especially attractive for sensing applications. In addition, adsorbed molecular electron donors or acceptors can dramatically alter the

electrical conductivity of graphene which provides a convenient mechanism for sensing using electrical measurements. Indeed, a number of sensors have been realized using graphene**,** including those that were capable of detecting single adsorption and desorption events of gas molecules such as nitrogen dioxide.[285–288] However, previous graphene sensors feature inherently planar geometries such as on rigid substrates (e.g. silicon wafers) or flexible substrates (e.g. polydimethyl siloxane, PDMS).[289] Indeed, planar substrates allow facile integration with other components required for electrical sensing such as electrodes, bond pads and dielectrics as well as electrical measurements using four point probes. But, the large form factor of planar sensors can hinder applicability in small spaces such as in capillaries. Moreover, the integration of graphene with stimuli responsive substrates could facilitate the development of environmentally responsive sensors and actuators.

In the present study, the concept of a self-rolling graphene-polymer bilayers is introduced and demonstrated actuation and the operation of rolled-up 3D sensors. The research builds on prior polymeric folding approaches that have been used to assemble 3D materials and functional devices from patterned thin films.[28,118,290–294] Importantly, these approaches can be used to transform 2D polymeric thin film patterns to 3D geometries either spontaneously or in response to external stimuli such as temperature, pH, solvent exchange, electric field or light. Here, a hypothesis is tested that if graphene is adhered to self-folding polymeric substrate that it should be able to transform planar graphene into a variety of 3D shapes. Consequently, the graphene would behave as a kind of high sensitivity skin atop of the flexible self-

folding substrate. This graphene skin would be attractive for sensing while the polymeric substrate would enable self-folding and function as a flexible mechanical support. It is noteworthy that this hypothesis would also apply to alternate 2D layered materials (2DLM) as well as other flexible and stimuli responsive supports such as fabrics or alternate polymers or hydrogels; hence, the study is relevant to a broad range of 3D curved or folded sensors and actuators composed of 2DLMs.

In testing this hypothesis, one of the first challenges was to find a polymeric substrate that adhered well to graphene to avoid delamination during folding. We independently discovered and later confirmed from the literature[16] that graphene has good adhesion to SU-8 which can be explained by its hydrophobic surface. Hence, by utilizing this good adhesion, the SU-8 film can be engineered to self-fold and "carry" the graphene layer without delamination. SU-8 is a negative photoresist that is widely utilized in the microfluidics and MEMS industry,[295] and hence there are minimal barriers to adoption in sensor or microelectronic fabrication. Additionally, SU-8 films can be processed to enable stimuli responsive self-folding behaviors on solvent exchange.[27] This is realized by forming a density gradient across the film by exposure to low UV dose followed by conditioning in acetone.

In this study, a strategy to pattern stimuli responsive SU-8 directly on CVD grown few layer graphene (FLG) was developed. Reversibly actuating FLG/SU-8 patterned bilayers were investigated that fold and unfold on solvent exchange (**Figure. 8.1.**). Also, we created and tested a tubular graphene-SU-8 device with integrated metal electrodes for demonstrating applicability as a curved functional device.

8.3. Experiments

8.3.1. Fabrication Flow of FLG/SU-8 Bilayer Thin Films

The fabrication process is as follows (**Figure 8.2. (a)**). We first spin coated SU-8 2025 (MicroChem) at 2000 rpm on commercial FLG wafers (SKU-CVD-TP, Graphene Supermarket) which were used as received. According to vendor specifications, these are one to seven layers graphene films with an average of four layers grown by CVD on a nickel catalyst/silicon dioxide/silicon substrate. A crosslink gradient was developed along the thickness of the SU-8 by low energy exposure (120 mJ/cm^2) of the SU-8 film to UV light. In contrast, a regular UV light exposure (around 150 - 215 mJ/cm^2 for 45 – 80 μm thickness, MicroChem) creates a fully crosslinked SU-8 and this film does not self-fold. The creation of a gradient crosslink in the SU-8 film is critical to enable bending and folding of the bilayer. After insufficient UV light exposure, the samples were baked using a ramp sequence of 75 °C for 1min, 100 °C for 6 min and then 75 °C for 1 min. Then the wafer was developed in SU-8 Developer (MicroChem) while stirring at 200 rpm and the exposed graphene was etched away using a low power (75 W) oxygen plasma (20 sccm O_2, 90 sec). The fabrication and self-folding process is versatile and a number of CAD designed FLG/SU-8 patterns such as rectangular strips, crosses, flowers and discs could be fabricated by varying the geometrical parameters such as the width and length of the patterns. After patterning, we released the FLG/SU-8 structures from the substrate by dissolution of the underlying nickel film in an aqueous etchant composed of 40 % ferric chloride and 5 % hydrochloric acid. The structures were then conditioned by immersion in acetone for 10 hours which completely dissolves the partially or uncrosslinked

portion and additives in the SU-8 film after which the material becomes stimuli responsive having stress gradients in thin film. After conditioning, the photopatterned FLG/SU-8 bilayer were flat in acetone (**Figure 8.2. (b)**) due to solvation of the hydrophobic SU-8 and spontaneously curved on de-solvation in water (**Figure 8.2. (c)**).

8.3.2. Mass Producible FLG/SU-8 Bilayer Thin Films

In addition, the microfabrication process is highly parallel and large numbers of self-folding structures can be formed (**Figure 8.3 (a-c)**). The several different sizes, shapes FLG/SU-8 thin bilayers were also designed by conventional photolithography and reversibly self-folding and unfolding mechanism were tested by solvent exchanges. The FLG/SU-8 thin bilayer structures could be manipulated from μm to mm scales with several different shapes. In addition, the FLG/SU-8 thin bilayer structures were tested their reversible actuations through re- and de-solvation of SU-8 when exchanging solvent between acetone and DI water. The process of spontaneous curving and flattening is reversible as verified over 50 cycles of acetone and DI water exchange. It shows that the self-folding approach can be utilized to pattern FLG simply and directly on SU-8 patterns without any other manual transferring process steps. Further, we observed that when the FLG/SU-8 thin film patterns were tuned under low UV dose and conditioned in acetone, totally flat FLG/SU-8 structures in acetone and curved, crumpled or rolled shapes in DI water could keep both their geometries when dehydrated in air.

8.4. Results and Discussion

8.4.1. Self-folding Mechanism of FLG/SU-8 Thin Films

The self-folding mechanism of flexible FLG/SU-8 thin films is illustrated in **Figure 8.4. (a)**. In order to drive self-folding, firstly, the free standing FLG/SU-8 structures were conditioned by immersion in acetone for 10 hours. This conditioning step serves to dissolve uncrosslinked SU-8 which creates a density gradient in the film as was visualized previously using fluorescence microscopy of microtomed sections.[27] On removal from the acetone and immersion in water, spontaneous curving of the bilayer films were observed and attributed this curving to de-solvation of the gradient crosslinked hydrophobic SU-8 films by water. It is noteworthy that this is a reversible process and the thin FLG/SU-8 bilayer structures show spontaneous curving and flattening based on reversible swelling and de-swelling of a gradient cross-linked SU-8 film in acetone and water respectively. Using the CAD mask design, a number of spatially patterned geometries can be formed, representative FLG/SU-8 bilayer thin flower shaped structures on the Ni substrate of which are shown in **Figure 8.4. (b)** with zoom-in imaged (**Figure 8.4. (c)**). After conditioning in general, the freestanding photopatterned FLG/SU-8 bilayer were flat in acetone (**Figure 8.4. (d)**) due to solvation of the hydrophobic SU-8 and spontaneously curved on de-solvation in water **(Figure 8.4. (d))**. For the flower shaped structures shown in **Figure 8.4**., typical folding time scales were on the order of 1-2 minutes.

The self-rolling behavior of the FLG/SU-8 bilayers are rationalized as follows. The experiments show that the SU-8 layer folds up when placed into water, and flattens out on immersion in acetone. We attribute this phenomenon to different swelling ratios in different solvents. The low UV dose during lithography generates a crosslink gradient in SU-8. Due to optical absorption along the thickness of the SU-8, the bottom region of the SU-8 film that is closer to the FLG layer is exposed to a very low UV light dose. Hence, this region is less crosslinked and subject to a mass loss during conditioning in acetone which serves to dissolve any residual uncrosslinked material. In contrast, the top region of the SU-8 film which is completely crosslinked in acetone undergoes a minimal mass change during conditioning. In essence, conditioning takes a crosslink gradient and converts it into a density gradient across the SU-8 film thickness. It is the density gradient that leads to heterogeneous shrinking when the film is submerged in water. The region in the SU-8 film with lower density shrinks more and becomes concave while that with the higher density region shrinks less and becomes convex. Since the FLG is attached to the bottom surface of the SU-8 film (lower density region) the SU-8/FLG structures formed in this paper have the graphene layer on the concave (inside). On immersion in acetone, the entire film is solvated and flattened out.

8.4.2. Characterization of FLG/SU-8 Thin Films: Raman Spectroscopy

The FLG/SU-8 structures were characterized by Raman spectroscopy that confirmed the presence of both FLG and SU-8 layers in the folded state comparing to 2D flat control sample of FLG. We compared the spectra of FLG/SU-8 structures to a 2D flat control sample of FLG by analyzing optical microscopy images with Raman spectra (**Figure 8.5. (a)**). The control FLG Raman spectra shows the characteristic G band around 1580, and 2D band 2720 cm^{-1}. The Raman spectrum is representative of 4-5 layer graphene based on the intensity, shape and position of the G and 2D bands.[256,260,296,297] The 3D self-fold FLG/SU-8 bilayer structures were characterized using the same power and scan parameters. The Raman spectrum was obtained on four samples with over 10 different spots on the curved surface. The averaged Raman peak positions of the G band was 1580 cm^{-1} and the 2D band 2700 cm^{-1} indicating the presence of FLG. Due to the variability of layers in FLG, we cannot comment on any significant differences from the control 2D FLG sample. We also observed peaks which can be assigned to the SU-8 layer. These include peak positions around 800 cm^{-1} of ether, 1120 cm^{-1} of epoxide groups, 1250 cm^{-1} for C-C stretch in the aromatic ring, and 1460 cm^{-1} for CH_3, CH_2 stretches respectively.[27,298,299] These Raman spectral characterization was intended to confirm the presence of FLG after transfer, patterning, fabrication and conditioning on the curved bilayer.

8.4.3. Characterization of FLG/SU-8 Thin Films: Radius of Curvature

We found that the radius of curvature of the self-fold FLG/SU-8 bilayer could be tuned by varying the ultraviolet exposure energy. **Figure 8.5. (b)** illustrates the results of experimental analysis on the radius of curvature changing with UV exposure energy. Experimentally, rectangular strip shape was designed with 7700 μm long and 800 μm wide. The thickness of thin film was determined by the spin coating condition and is set to be 39 μm in this case. It can be seen that extra sufficient UV exposure energy will crosslink the entire film with little gradient, giving less rolling and larger radius. Interestingly, the curved SU-8 film had different radii with and without graphene layer under the same UV exposure energy. The single layer of SU-8 had smaller radius as compared to the FLG/SU-8 bilayer. We also observed the smaller radius at lower ultraviolet exposure energy. We rationalize this difference by noting that the graphene coating on the SU-8 can decrease the removal of uncrosslinked SU-8 into acetone during conditioning. Consequently a lower mass decrease caused by this graphene covering will generate a lower volume change, resulting in smaller gradient and larger radius.

In order to understand the variation of radius of curvature with ultraviolet exposure energy we adopted finite element method (FEM) by using the commercial software ABAQUS as a 3D deformable shell unit. The mass decrease percentage was measured from previous work.[27] 9.6 % is used as the shrinking ratio at the lower exposed region exposed to low UV energy as 90 mJ/cm^2, and 1 % mass decrease was taken from the high exposure condition of 360 mJ/cm^2. The SU-8 thin film was modeled according to

the experimental parameters as 7700 μm long, 800 μm wide and 39 μm thickness. The Young's modulus of the SU-8 film was assumed as 2 GPa based on the data sheet from vendor (MicroChem). In the software model, the swelling ratio gradient was approximated by a linear temperature gradient across the thickness. The top region of the SU-8 which is more exposed towards UV light will be highly crosslinked and subject to a lower volume change on swelling. In contrast, the bottom part of the SU-8 film which experiences a lower UV dose will be less crosslinked and tend to have a significant mass decrease upon conditioning in acetone due to removal of uncrosslinked material. We assume that the percentage of mass decrease is related to the volume shrinking ratio of the thin film. The hydrophobic SU-8 film is solvated in acetone and remains flat. However, when the film is de-solvated in water, the contraction in the bottom region renders a bending moment on the top region and thus the film will roll up towards the less exposed region, and the radius of curvature will be determined from the mass decrease percentage and material modulus as well as the thickness of layers. Further, structured quadratic elements were used for the geometry and Simpson's rule with 9 integral points was used for the thickness. A further increase of mesh density showed no significant difference in results. We performed a sensitivity analysis and our simulation results suggest that the exposure dose and SU-8 thickness play an important role in determining the extent of rolling of SU-8 film. **Table 8.1.** indicates simulation parameters and **Figure 8.5. (c)** shows simulation snapshots of the curvatures corresponding to the four conditions (rows) in the table.

Our simulation results reveal the importance of a parameter referred to as the shrinkage gradient (G). Given the same SU-8 thickness of 39 μm, a larger shrinkage gradient results in a smaller radius of curvature or a tighter roll (numerical values in rows (a) and (b) in **Table 8.1.**). Alternatively, if the gradient G is the same, the radius of curvature is similar even though the films may have different thicknesses (numerical values in rows (a) and (c) in **Table 8.1.**). Given the same top and bottom layer shrinking ratio of 0 % and 9.6 % as boundary conditions, the thicker film folds with a larger radius of curvature which we attribute to a larger bending rigidity (numerical values in rows (a) and (d) in **Table 8.1.**).

8.4.4. Characterization of FLG/SU-8 Thin Films: Current vs Voltage

As a proof-of-concept for a functional electronic device, a rolled-up sensor was fabricated by integrating electrodes and contact pads into the folded FLG/SU-8 structures so that electrical measurements could be performed using standard electrical probes (**Figure 8.6.**). Briefly, metal (gold, Au) electrodes were photopatterned and Au contact pads on top of the graphene prior to SU-8 spin coating (**Figure 8. 6. (a, b)**). Prior to SU-8 spin coating, SC 1827 photoresist (MicroChem) was spin coated at 3000 rpm on the FLG films. The photoresist was baked at 115 °C for 60 sec and then exposed to UV (360 mJ/cm^2) the samples through an Au electrode pattern mask designed by AutoCAD. Then, the panels were developed by immersion in 351 diluted developer (1:5 = 351: DI water) (Shipley) for around 30 sec, rinsed the samples with DI water and then dried them using nitrogen gas. Then, chromium (Cr, 5 nm, adhesion promoter) and Au (10 nm) were thermally evaporated which defined the electrode wiring. In addition, to fabricate the thicker electrode probe pads, an

additional 3 μm of Au was deposited using electroplating. After electroplating, the resist was dissolved with acetone and IPA then dried the samples using nitrogen gas. Then, the process described earlier for SU-8 photopatterning and conditioning was used.

A nice feature of our assembly approach is that only the portion of FLG/SU-8 bilayer that is immersed in water will roll up. This phenomenon is also limited only to the FLG/SU-8 bilayer samples photopatterned under low UV dose and conditioned in acetone. Hence, part of the sensor can be rolled up to enable a curved sensor while the portion in air can be processed to stay flat which is important for testing using conventional electrical probes (**Figure 8.6. (c-f)**). It was also observed that the incorporation of Au electrodes did not inhibit self-folding and insignificant changes in radii of curvature differences with and without the electrodes. We attribute this insensitivity to the small dimensions of our electrode designs. Typically, the area covered by the Au electrodes such as for the structure shown in **Figure 8.6 (c-e)** was 23 % that of the FLG/SU8 area and the combined Cr/Au electrode thickness was only 15 nm. These thin and small dimensions minimize the contribution of the Cr/Au electrodes to the overall bending rigidity.

Current (I) - voltage (V) characteristics were measured by using a programmable current source (Keithley Model 220) and voltmeter (Keithley 2000 Digital Multimeter) using a probe station (Cascade Microtech Probes) and a four probe configuration. Probes were placed on the flat contact pads and we obtained I-V curves of 3D rolled FLG/SU-8/Au sensors in air and on exposure to acetone (**Figure 8.6. (g)**).

Acetone was chosen because it is a common chemical used for sensor validation and is also an important breath biomarker for diabetic ketoacidosis.[298,299] The IV curves indicate an increase in resistivity on exposure of the FLG/SU-8 sensors to acetone as compared to air. This increase is in agreement with prior studies on flat graphene sensors on exposure to acetone and has been attributed to the orientation of the dipole moment of acetone with its electropositive cloud closer to the graphene surface.[300]

8.4.5. Characterization of FLG/SU-8 Thin Films: Photovoltage vs Power

One of the advantages of integration of graphene in curved microstructured environments is that they can be used to create sensitive 3D sensors and optical devices with small form factors. Graphene based devices can be utilized as optical sensors due to its absorption spectrum covers the entire ultraviolet to far-infrared range.[301,302] and graphene has been previously used as a ultrafast photodetector.[303] **Figure 8.7. (a)** shows how the optical sensing properties were measured with probe station (Cascade Microtech Probes) combined with four probes, a programmable current source (Keithley Model 220), a voltmeter (Keithley 2000 Multimeter), several different laser sources and microscope. Specifically, the probes were used to electrically connect the electrodes of the FLG/SU-8 samples to the outside electrical circuits like the current source and the voltmeter. The programmable current source could apply a constant current to the FLG/SU-8 sample through its electrodes. For all experiments shown in **Figure 8.7. (a)**, the current was set to 0 μA, which means that the programmable current source was not used in these experiments. The voltmeter

was used to detect the open-circuit photovoltages between the two electrodes of the FLG/SU-8 sample triggered by the illumination of laser sources. The laser instruments were used to generate lasers with different wavelengths and intensities (power), and to control the laser on and off autonomously. The microscope was used to localize the FLG/SU-8 sample and to align it with the laser spot. The folded FLG/SU-8 sample has two Cr/Au (with the thickness of 5 nm/ 10 nm, where Cr layer acts as the adhesive layer) electrodes, the gap between the two electrodes is 10 μm.

Initially, three different wavelengths of 488, 532 and 600 nm (CW Solid-State Lasers, Coherent Inc.) were used to check the photoresponse of 3D rolled FLG/SU-8 sensors to verify the spectral ranges of photodetection (**Figure 8.7. (b)**) with inset of conceptual schematic of 3D self-rolled up optical sensor. The current applied to the electrodes of the sample by the programmable current source was 0 μA. In addition, the laser power (1.5 mW) and laser-on and -off interval were digitally controlled using analog modulations and set as 10 seconds with large variations of power changing from 10 to 50 mW (**Figure 8.7. (c)**) and more small variations of power changing from 0 to 4 mW were tested with more dynamic auto setting of light on and off intervals from 1 to 8 seconds (**Figure 8.7. (d)**). Specifically, only two probes were used to measure the open-circuit photovoltage between the two electrodes of the FLG/SU-8 photodetector in all of the photo-related experiments. Simultaneously, Labview software was used to record the photovoltage-time data. The variations of open-circuit photovoltage were detected from 0 to 720 μV in first 10 to 50 mW power variations and observed 0 to 90 μV in 0 to 4 mW power states by using blue laser

source (488 nm) (OBIS 488 LX, Coherent Inc.). Especially, the detected maximum and minimum variations of open-circuit photovoltage (μV) at each power (mW) state has less than 2 % so that the error bars were not added on this graph. It also indicates that 3D FLG/SU-8 self-folded sensor were able to detect stably when the 488 nm laser (OBIS 488 LX, Coherent Inc.) was used. Furthermore, the 2D flatted FLG/SU-8 thin bilayer condition was also analyzed under the same optical detection stage.

As plotted on graph at **Figure 8.7. (e)**, we observed that the open-circuit photovoltage variations of 2D sample have 0 to 28 μV in 1 to 5 mW power states. Both 3D and 2D FLG/SU-8 sensors have the linear relations between power and open-circuit photovoltage shown in **Figure 8.7. (f)**, which are formerly observed in graphene photodetectors,[304,305] clearly showing that the 3D rolled one has 3-4 times higher values than 2D flat one at each power states. We tested more self-folded FLG/SU-8 sensors under the same experimental steps with several different power (mW) and current (μA) parameters. As described at a graph, higher incident power (mW) produced higher open-circuit photovoltages (mV) in a feasible way. Currently, He *et al.* suggests the nanotube terahertz detector[306] and we observed a linear variation of voltage with increasing laser power indicating applicability as a photodetector. These characteristics have a huge potential to be used in the optical light communication of 3D self- rolled FLG/SU-8 sensor. As compared to a 2D sensor, a distinct advantage of the 3D rolled structure is that light approaching from different angles can be detected. The self-folding mechanism can be utilized as a smart photo-detector having more

homogeneous light communication from omnidirectional incident light with minimum area taken in a system.

8.5. Conclusion

In summary, a new approach have been demonstrated to create self-folded solvent responsive FLG/SU-8 bilayers. The approach leverages, (a) good adhesion of graphene to hydrophobic SU-8, (b) stimuli responsive engineering of FLG/SU-8, and (c) the ability to pattern and incorporate electrodes via planar lithography prior to release from the substrate. All these traits are essential to create functional 3D self-folding sensors and stimuli responsive actuators. For example, while one may be tempted to create stimuli responsive bilayer sensors by pairing graphene with a popular stimuli responsive material poly (*N*-isopropylacrylamide-co-acrylic acid), our preliminary studies with such hydrogels reveal relatively poor adhesion and delamination of graphene during folding. However, provided the three conditions can be met, the approach can be applied to other 2DLMs and polymers to create a range of electronic and optical sensing devices, wearables and stimuli responsive tools. Due to the small size of such rolled up devices, they could be inserted into small spaces and the multiple rolls could increase sensitivity. For example, several groups have previously demonstrated a range of rolled-up and folded devices including energy storage, microfluidic, electromagnetic and single cell devices that highlight these advantageous characteristics.[266,272,278–280] Additionally, this FLG/SU-8 bilayer is flexible and optically transparent hence it is of relevance to applications such as wearables, metamaterials and imaging. Finally,

it is important to note that the SU-8 self-folding mechanism is such that when the FLG/SU-8 bilayer is transferred from either acetone or water to air, it maintains its previous configuration. That is if folded FLG/SU-8 structures are taken out of water to air they stay folded and if flat structures are taken out of acetone and moved to air they stay flat. Consequently, the process can deliver devices that remain folded in both aqueous environments of relevance to biological applications or air which is of relevance to integrated circuits and gas sensors.

Table 8.1. Simulation parameters and computed radius of curvature for gradient crosslinked and conditioned SU-8.
The symbols represent, T=Total bilayer thickness, S1=Top layer volume decrease, S2=Bottom layer volume decrease, G=Gradient or ratio of the percentage volume change to thickness, and R=Radius of curvature.

	T (μm)	S1 (%)	S2 (%)	G (%/μm)	R (μm)
(a)	39	0	9.6	0.246	377
(b)	39	0	0.96	0.0246	3267
(c)	10	0	2.46	0.246	338
(d)	100	0	9.6	0.096	860

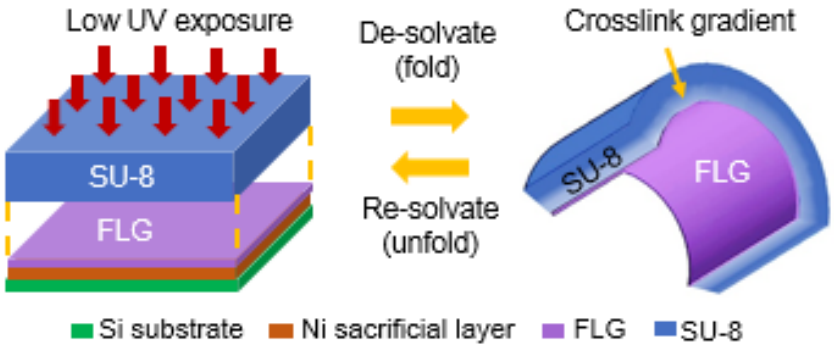

Figure 8.1. Schematic of the fabrication and reversible self-folding of FLG/SU-8 bilayers.

Reprinted with permission from T. Deng, C. K. Yoon, Q. Jin, M. Li, Z. Liu, and D. H. Gracias, "Self-Folding Graphene-Polymer Bilayers," *Applied Physics Letters,* vol. 106, pp. 203108, 2015.

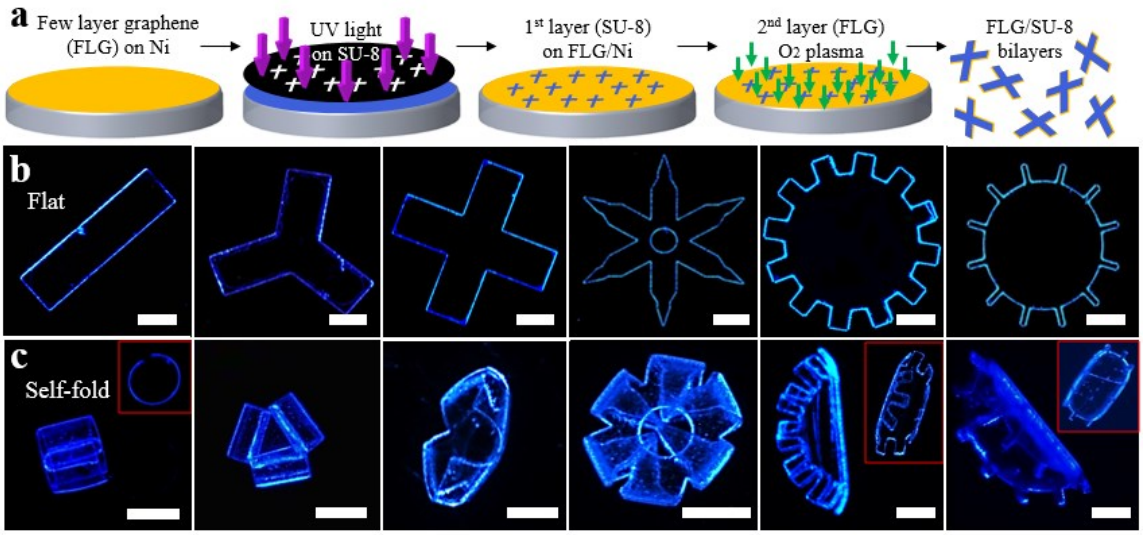

Figure 8.2. Mass-producible reversibly actuating FLG/SU-8 microstructures in a variety of shapes including rectangular strips, crosses, flowers, and discs. **(a)**Schematic description of fabrication flow of FLG/SU-8 microstructures. Images of **(b)** flat FLG/SU-8 structures in acetone and **(c)** corresponding self-folded microstructures in water. Insets indicate images taken from different directions. The blue color results from the auto-fluorescence of SU-8 during optical imaging and all scale bars represent 200 μm.

Reprinted with permission from C. K. Yoon, T. Deng, Q. Jin, J. P. Cha, M. Li, J. Kang, Z. Liu, and D. H. Gracias, "Self-Assembly of Integrated Curved and Folded Graphene-Polymer Optoelectrical Sensor", *In Preparation*, 2017.

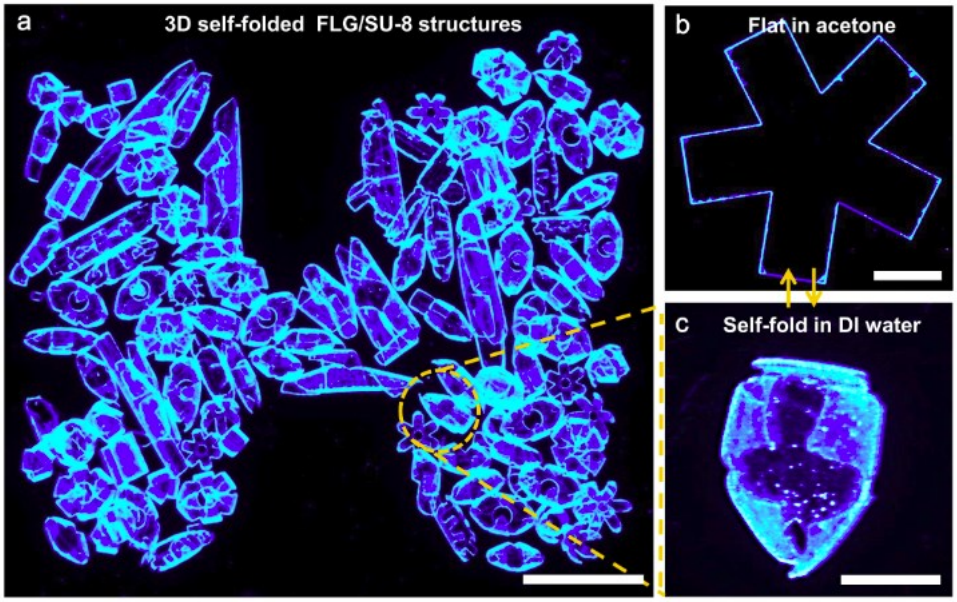

Figure 8.3. Mass production of 3D FLG/SU-8 microstructures. (a) Mass production of photopatterned 3D curved, folded or rolled FLG/SU-8 structures in DI water with several different shapes and sizes from micron to millimeter scales and **(b, c)** reversibility when exchanging solvents. The scale bar indicates (a) 1mm, (b, c) 200 μm.

Reprinted with permission from C. K. Yoon, T. Deng, Q. Jin, J. P. Cha, M. Li, J. Kang, Z. Liu, and D. H. Gracias, "Self-Assembly of Integrated Curved and Folded Graphene-Polymer Optoelectrical Sensor", *In Preparation*, 2017.

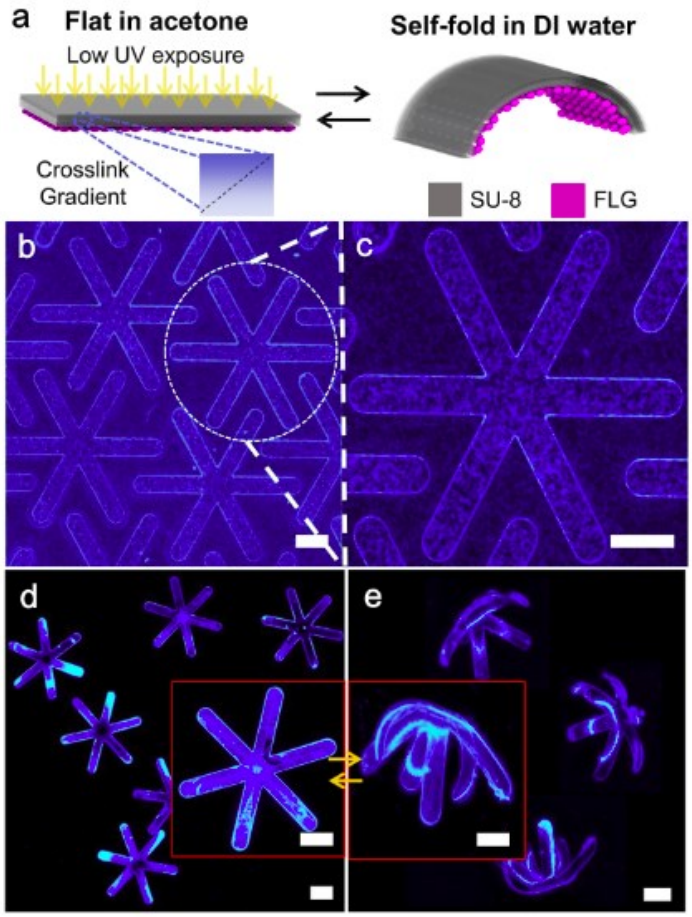

Figure 8.4. Self-folding and reversibly actuating FLG/SU-8 photopatterned bilayer. (a) Schematic diagram illustrating the mechanism of self-folding of a FLG/SU-8 bilayer based on reversible swelling and de-swelling of a gradient cross-linked SU-8 film in acetone and water respectively. **(b)** Optical and **(c)** zoomed-in images of flower-shaped photopatterned FLG/SU-8 microstructures. **(d-e)** Optical image of reversible actuation of a free-standing flower shaped microsctructure. **(d)** Image of a flat FLG/SU-8 flower shaped microstructure on solvation in acetone and **(e)** corresponding image of a spontaneous self-folded microstructure formed on de-solvation of the hydrophobic SU-8 in DI water. The blue color results from the auto-fluorescence of SU-8 during optical imaging and all scale bars represent 200 μm.

Reprinted with permission from C. K. Yoon, T. Deng, Q. Jin, J. P. Cha, M. Li, J. Kang, Z. Liu, and D. H. Gracias, "Self-Assembly of Integrated Curved and Folded Graphene-Polymer Optoelectrical Sensor", *In Preparation*, 2017.

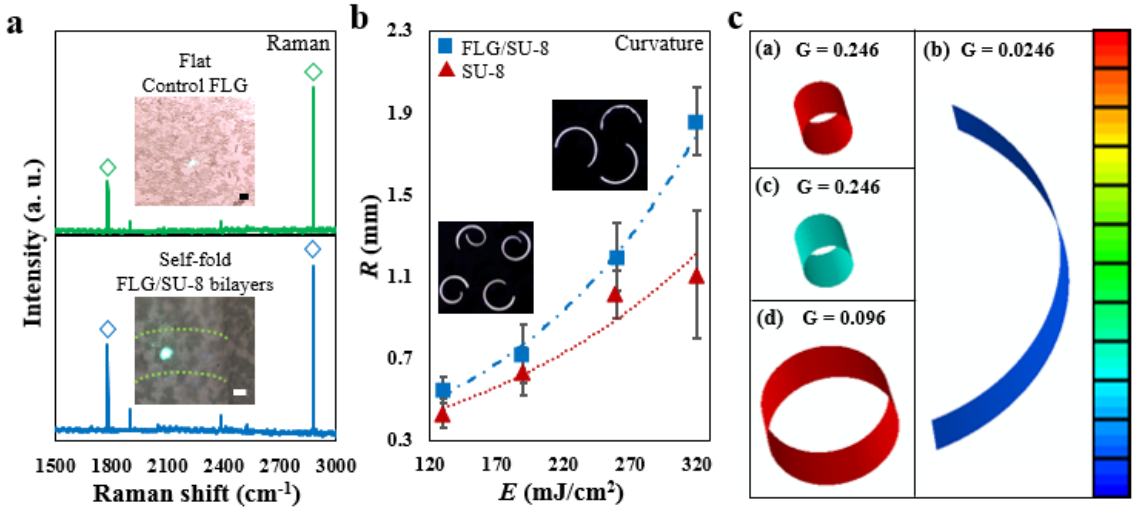

Figure 8.5. Characterization of thin FLG/SU-8 bilayers and experimental and computational folding degree observation according to UV light exposure energy and strain. (a) Microscopic images of flat control FLG and self-folding FLG/SU-8 bilayers with Raman spectra. Raman spectra of the self-folded FLG/SU-8 bilayers have blue line and green line taken on the flat FLG samples as received from the vendor. All scales indicate 8μm. **(b)** Experimental analysis of the radius of curvature as a function of UV exposure for self-folding graphene/SU-8 thin bilayers. **(c)** FEM snapshots of self-folded SU-8 highlighting that the radius of curvature depends on the value of G. (a)-(d) FEM images depicting the extent of curvature of SU-8 films corresponding to the simulation parameters listed in rows (a)–(d) in **Table 8.1.** The colors indicate the magnitude of stress at the inner SU-8 layer which is equivalent to the shrinkage percent S2, with red colors representing high and blue colors representing low stress values. The images pictorially depict that the radius of curvature depends on the value of G. Hence, rolls in panels (a) and (c) with the similar values of G have the similar radius of curvature even they have different thicknesses and different stresses.

Reprinted with permission from

1. T. Deng, C. K. Yoon, Q. Jin, M. Li, Z. Liu, and D. H. Gracias, "Self-Folding Graphene-Polymer Bilayers," *Applied Physics Letters,* vol. 106, pp. 203108, 2015.
2. C. K. Yoon, T. Deng, Q. Jin, J. P. Cha, M. Li, J. Kang, Z. Liu, and D. H. Gracias, "Self-Assembly of Integrated Curved and Folded Graphene-Polymer Optoelectrical Sensor", *In Preparation*, 2017.

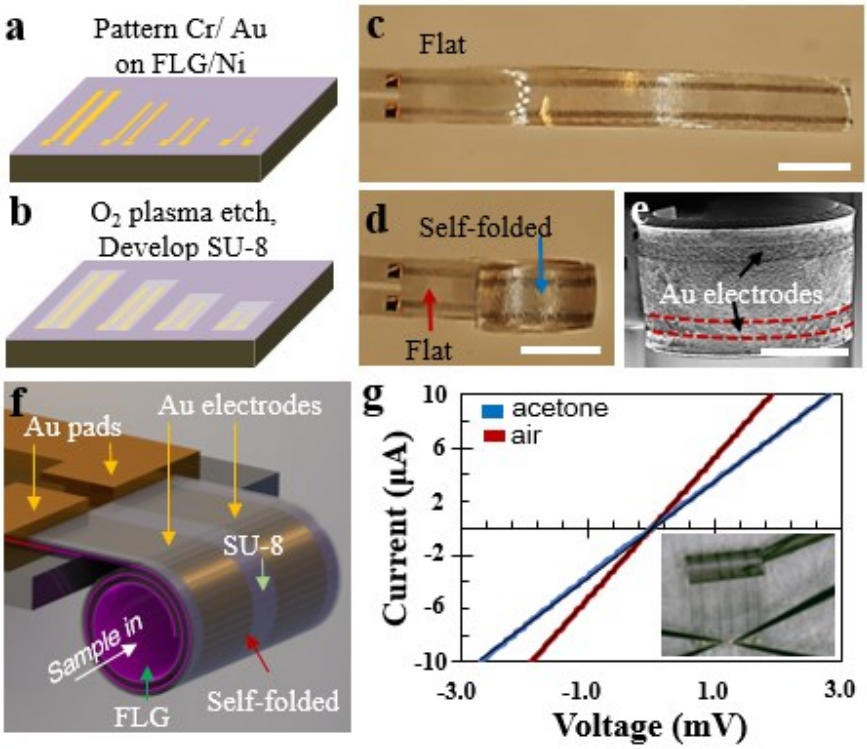

Figure 8.6. Schematic and experimental results of a functional self-folded FLG/SU-8 device. (a) and **(b)** Au electrodes were electroplated and encapsulated prior to roll-up. **(c)** and **(d)** a reversible self-folding FLG/SU-8 bilayer with integrated Au electrodes that functions as a chemical sensor. A portion of the sensor is processed to be flat to enable e-test probing, while a portion is processed to self-fold to enable 3D electrical sensing. **(e)** Scanning electron microscopy (SEM) image of the rolled-up FLG/SU-8/Au sensor with one of the two electrodes highlighted by the red dotted line. **(f)** Schematic of the integrated FLG/SU-8/Au device being used as a sensor. **(g)** I-V curves of the self-folded FLG/SU-8 sensor on exposure to air (control) and acetone. The inset represents the experimental set up with four electrical probes (bottom of the inset) on gold contact pads that were used to measure the resistance across the rolled-up graphene and a capillary (top right of the inset) that was used to introduce the acetone into the rolled up FLG/SU-8 sensor. The scale bars represent 700μm in panels (c) and (d) and 350 μm in panel (e).

Reprinted with permission from T. Deng, C. K. Yoon, Q. Jin, M. Li, Z. Liu, and D. H. Gracias, "Self-Folding Graphene-Polymer Bilayers," *Applied Physics Letters,* vol. 106, pp. 203108, 2015.

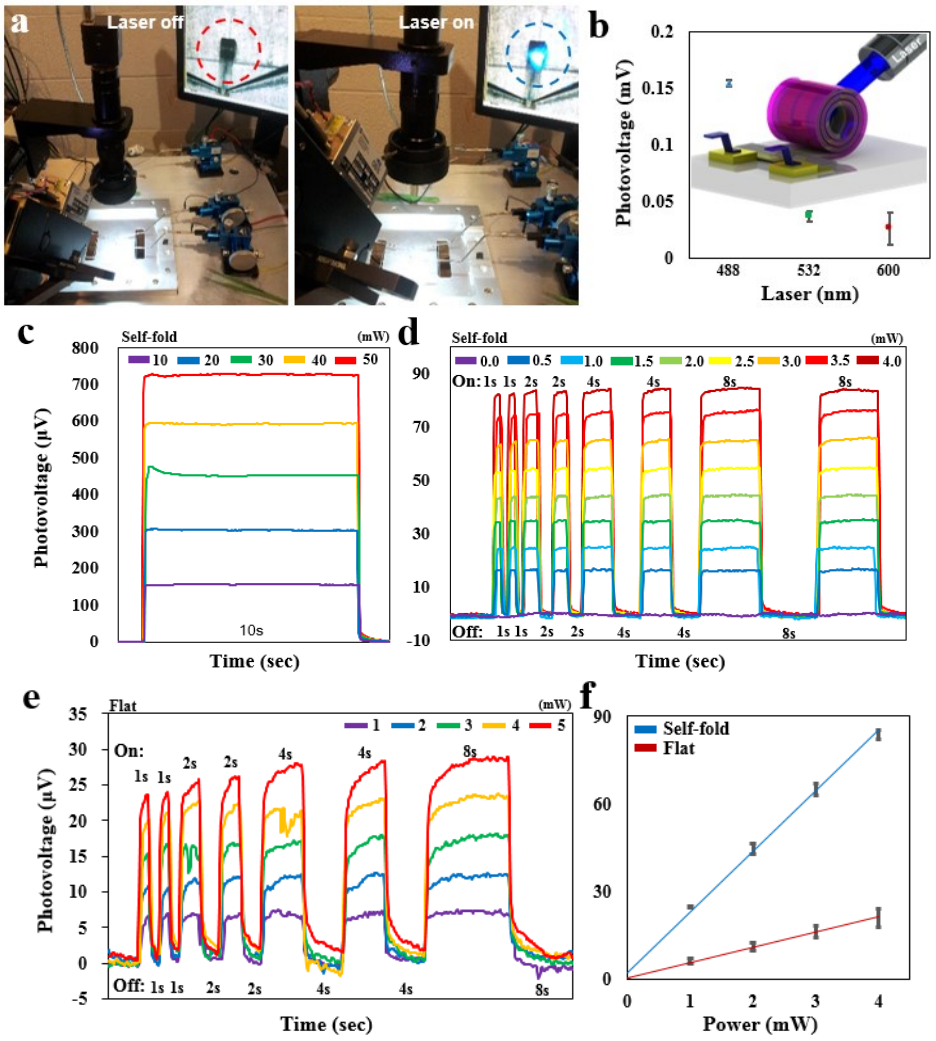

Figure 8.7. Sensitivity and selectivity of integrated self-folding FLG/SU-8 tubular optical sensor. (a) Images of the optical test set-up in laser-on and -off modes. **(b)** Open-circuit photovoltage (mV) using three different lasers (nm). **(c)** Open-circuit photovoltage (μV) curve according to Power (mW) from 0 to 50 mW and **(d)** Power (mW) from 0 to 4 mW using targeted blue laser source (488 nm) on 3D self-fold FLG/SU-8 tubular bilayer structure. **(e)** Open-circuit photovoltage (μV) curve according to Power (mW) from 1 to 5 mW on 2D flat FLG/SU-8 bilayer structure. **(f)** Linear relations of photoelectric effects between open-circuit photovoltage (μV) and power (mW).

Reprinted with permission from C. K. Yoon, T. Deng, Q. Jin, J. P. Cha, M. Li, J. Kang, Z. Liu, and D. H. Gracias, "Self-Assembly of Integrated Curved and Folded Graphene-Polymer Optoelectrical Sensor", *In Preparation*, 2017.

9. Patterned Soft Micropolyhedra by Self-folding and Molding*

9.1. Overview

It is extremely challenging to mass-produce polymeric microstructures with patterns in all three dimensions (3D). In this paper, we describe a highly parallel strategy to create such patterned soft-micropolyhedra with a range of polymers and even live mammalian cell-laden hydrogels. Specifically, we first patterned metallic micropolyhedra using photolithography and capillary force assisted self-folding. Inverse molds were created in the elastomer polydimethylsiloxane (PDMS); interestingly, the patterns were imprinted on the side walls of the molds. The molds were then filled with pre-polymers such as NOA73, PEGDA, and pNIPAM-AAc and cell-laden hydrogel solutions and cross-linked to form soft patterned micropolyhedra. Our results suggest that the combination of self-folding and molding could be used to create a variety of smart particles and building blocks with precisely patterned surfaces for applications in colloidal science, self-assembly, drug delivery and tissue engineering.

---

* Reprinted with permission from

1. S. Pandey[#], C. K. Yoon[#], Z. Zhang, H. R. Kwag, J. Hong, and D. H. Gracias, "Patterned Soft-Micropolyhedra by Self-Folding and Molding," *IEEE 29th International Conference on Micro Electro Mechanical Systems (IEEE MEMS),* pp. 203-206, 2016.
[#]: Equal contributions.

9.2. Introduction

Polymeric microparticles are important for a variety of applications including directed assembly, drug delivery, tissue engineering, microfluidics and colloidal science.[307–310] Methods such as micromolding in capillaries, microinjection molding, and microfluidic methods can be used to mass-produce polymeric microparticles.[311–313] However, the particles formed by these methods are limited to a few geometries such as spheres, cylinders, pancake, and ellipsoidal shapes with limited surface patterns as illustrated in **Figure 9.1. (a, b)** respectively. Other techniques such as 3D printing can be used to form a wide range of shapes but are inherently serial in nature.

Self-folding is an emerging methodology that can combine top-down lithographic patterning with origami inspired engineering to mass-produce polyhedra with a wide range of sizes demonstrated between 100 nm and 2 cm.[139] Sealed polyhedra are formed using capillary forces which cause both folding of panels and fusing of hinges. However, the requirement for capillary folding is that a hinge material must be identified that can be liquefied typically by heating at a reasonably low temperature. Hence, the number of soft-materials that can be utilized to form such polyhedra is limited. In this paper, we overcome this challenge by first self-folding metal micropolyhedra with patterns and then utilizing them to mold soft-polymeric micropolyhedra. Notably, we observed that during molding, the surface patterns on the metal polyhedra could be transferred to the polymer micropolyhedra. Hence, in principle patterns can be defined on the surface of the polyhedra with high resolution (**Figure 9.1. (c, d)**).

9.3. Experiments

9.3.1. Fabrication Step: Photolithography, PVD, and Self-folding

The process flow schematic is highlighted in **Figure 9.2.** First, a variety of gold (Au) designs were patterned *via* photolithography, physical vapor deposition (PVD) and lift-off-metallization. Then, each net composed of nickel (Ni) panels interconnected by solder (Pb-Sn) hinges was fabricated. The side of a panel measured 300 microns, with two adjacent panels spaced apart by a width equal to 10% of the panel edge length.[138,139,314] We used two layers of optical lithography to pattern features on a silicon wafer and electrodeposited nickel panels and Pb-Sn solder hinges respectively. We then released the nets with nickel panels connected with solder hinges from the substrate and heated the free standing structures in a high boiling point organic solvent N-Methylpyrrolidone. At ~183 °C, solder hinges melt and 2D nets begin to fold into a 3D polyhedron. All the planar precursors for a polyhedron were folded in close proximity in order to minimize any effect from variation in processing parameters. After etching the chromium and copper layers, the particles were stored in an ethanol solution until further use as master particles to prepare the polydimethylsiloxane (PDMS) molds (**Figure 9.2. (a)**).

9.3.2 Fabrication Step: Molding

PDMS molds were made using these metal polyhedra and these molds were used to mass-produce soft-polyhedra (**Figure 9.2. (b)**). We used the PDMS elastomer kit (Dow Corning) for making PDMS and mixed the base part and the curing agent in a 10:1 (w/w) ratio and mixed vigorously using a plastic spatula. To remove the bubbles,

we placed the mixture in a desiccator for 30 minutes. We attached the metallic polyhedra onto a double sided tape that was secured to the bottom of a petri dish. The scotch tape prevents premature floating of the structures when PDMS is poured into the Petri dish. We poured the elastomer solution gently into the Petri dish until it completely covered the master polyhedra and placed the Petri dish in a desiccator again for 30 minutes to remove any bubbles present and cured the elastomer solution at 50 °C for 4 hours. The solidified PDMS was gently peeled off the substrate where the metallic polyhedra remain attached on the tape thus creating molds with the shape of the structure. We used both simple shapes (tetrahedra, cubes) as well as the complex shapes (dodecahedra, truncated octahedra) with and without precise patterns on the panel surfaces. In the case of metallic polyhedra with gold patches, the patches created an impression on the side walls of the molds which transferred onto the surfaces of the molded polymeric polyhedra.

9.4. Results and Discussions

9.4.1. Self-folding and Molding

Experimental results of molded polyhedra with imprinted patterns are shown in **Figure 9.3.** Specifically, a variety of Au patches such as circles, crosses, triangles, and squares (1st column) were precisely aligned with Ni panels (2nd column) and solder hinges (3rd column) and then self-folded (4th column). Scanning electron microscopic (SEM) images (4th column) highlight the high resolution of the patterned Au patches on Ni panels of 3D metallic tetrahedra, octahedra, and dodecahedra shaped microparticles. The self-folded metallic microparticles were also precisely soft-

molded and then replicas of polymeric microparticles (5th column) with precise pattern transfer (insets in the 5th column) were fabricated.

Briefly, to mold polyhedra, pre-polymer solutions were spread on the molds and placed in a desiccator under vacuum for 2 hours to overcome the strong interfacial forces that prevents the liquid from filling the small mold cavities and to remove any bubbles present in the solution. Once the molds were completely filled with the photosensitive polymer solution, we removed the excess and exposed the sample to UV light for 2 minutes to crosslink the polymer. After photocrosslinking, we separated the molded particles from the molds. To remove any flakes on the edges of microparticles, we glued a sand paper on the bottom of a Petri dish, placed the molded microparticles, covered the dish and placed it on a vortexer at 500 rpm for 3 hours. We further sonicated the molded soft-polyhedra for 10 minutes to remove any remnants of flakes.

9.4.2. Mass-producing

We utilized this process to mass-produce polyhedra with a variety of epoxy polymers and hydrogel materials such as Norland Optical Adhesive 73 (NOA-73), polyethylene (glycol) diacrylate (PEGDA), poly *N*-isopropylacrylamide-acrylic acid (pNIPAM-AAc), and iron oxide doped magnetically responsive polymers (**Figure 9.4. (a-c)**). Additionally, we highlight potential applications of these polyhedra in drug delivery and lab-on-a-chip applications by filling molds with multi-colored dyes arranging them in 1x3 and 3x3 assembled arrays and visualizing chemical release (**Figure 9.4. (d, e)**).

Further, we anticipate use of these micropolyhedra as building blocks for aggregative assembly. Previously, most studies on colloidal assemblies have been carried out with spherical particles.[315,316] It is important to note that two non deformable spheres touch each other only at a single point and aggregates are isotropic, whereas polyhedral shapes such as cubes, dodecahedra and octahedra touch at planar surfaces and can lead to highly anisotropic assemblies. Further, if loaded with cells, these cell-laden hydrogels can be used for tissue engineering applications. We illustrate this idea by utilizing cell laden hydrogel molded polyhedra (**Figure 9.5. (a, b)**). Specifically, we used mouse pancreatic cell *β*-TC-6 cultured in complete growth medium containing Dulbecco's Modified Eagle Medium with 10 % fetal bovine serum. In the photo-encapsulation process, we first stained the cells with a live stain Calcein AM (0.7 μg/mL) in PBS solutions for 30 minutes in the incubator (37 °C, 5.0 % CO_2), trypsinized and centrifuged at 1200 rpm to form a pellet. We suspended the pellet in 1mL of PBS and 4 mL of PEGDA (700 MW), and added Irgacure 2100. The cell-PEDGA solution was spread on a sterilized PDMS mold and exposed to UV light for 2 minutes. We verified that our molding process which requires only simple photocrosslinking does not kill the cells and live cell laden blocks visualized by the green color of the Calcein stain can be formed. Consequently, we were able to mold *ß*-TC-6 mouse insulinoma cell-laden hydrogels to form polyhedra and then assemble them in the shape of a pancreas (**Figure 9.5. (c, d)**) highlighting applications of these patterned building blocks in bottom-up assembly of tissues.[317]

9.5. Conclusion

In summary, we have combined self-folding and molding to create soft polyhedra such as tetrahedra, octahedra and dodecahedra. The process is scalable and can be applied to a range of soft-materials and hydrogels including those loaded with chemicals or live cells or organisms. We anticipate use of these polyhedra in colloidal science, self-assembly, tissue engineering and lab-on-a-chip applications.

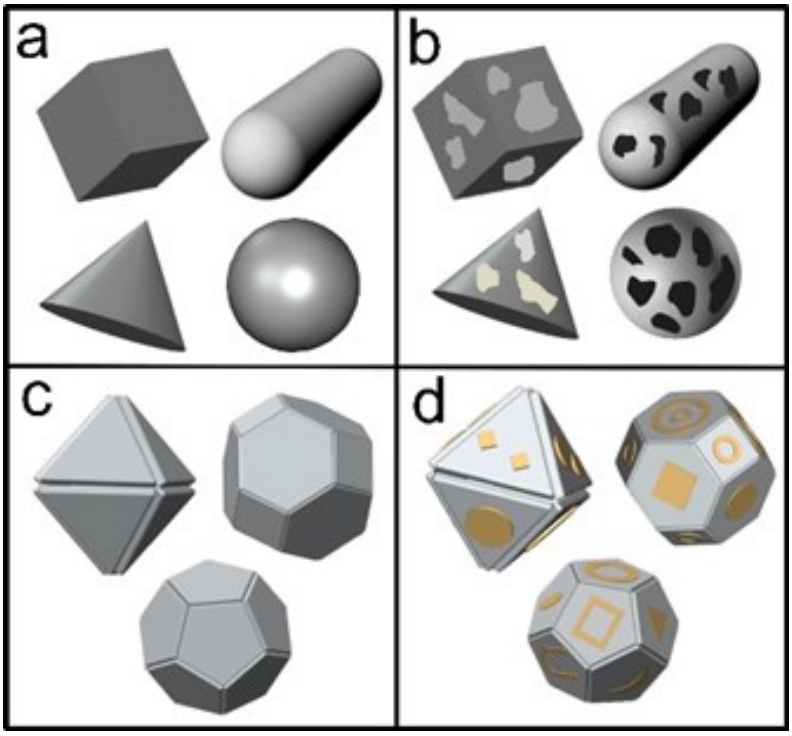

Figure 9.1. Schematic showing the comparison of our patterned micropolyhedra as compared toexisting microparticles. (a, b) Presently, soft-microparticles can be mass-produced but only withsimple shapes and patterns. **(c, d)** Our approach allows the mass-fabrication of polyhedra shapes with precise side-wall patterning in all three dimensions limited only by the resolution of planar lithography.

Reprinted with permission from S. Pandey, C. K. Yoon, Z. Zhang, H. R. Kwag, J. Hong, and D. H. Gracias, "Patterned Soft-Micropolyhedra by Self-Folding and Molding," *IEEE 29th International Conference on Micro Electro Mechanical Systems (IEEE MEMS),* pp. 203-206, 2016.

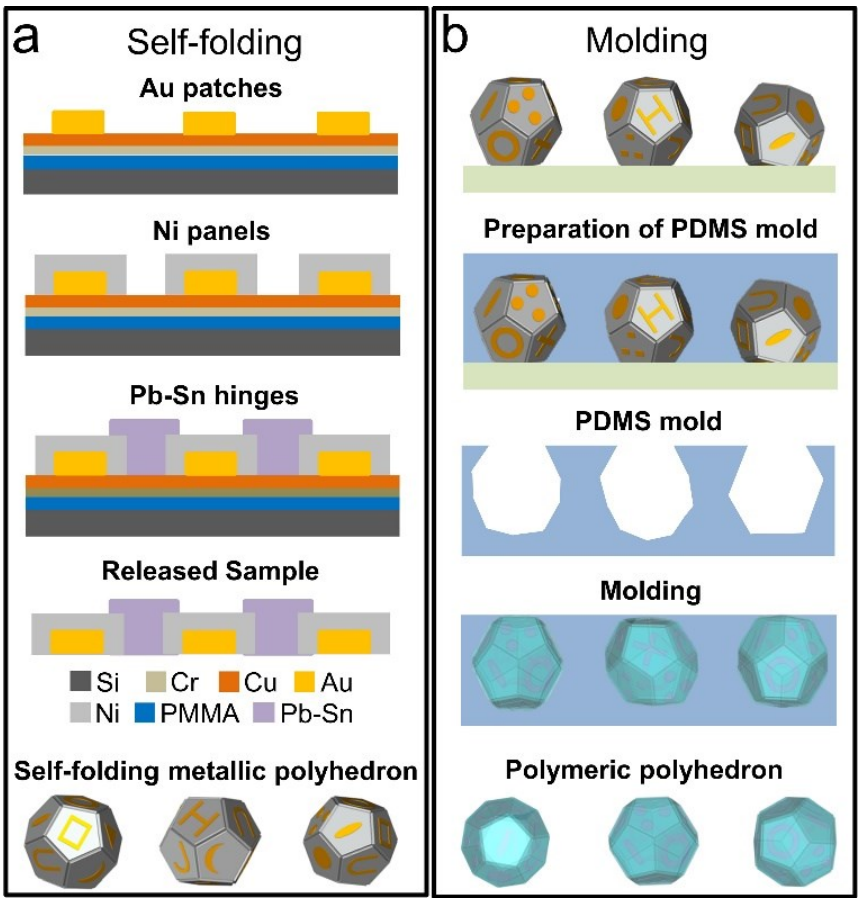

Figure 9.2. Schematic of the self-folding and molding process flow (a) Patterning and self-folding of metallic polyhedra as master particles for molding. **(b)** Preparation of PDMS molds and mass-fabrication of patterned polymeric micropolyhedra.

Reprinted with permission from S. Pandey, C. K. Yoon, Z. Zhang, H. R. Kwag, J. Hong, and D. H. Gracias, "Patterned Soft-Micropolyhedra by Self-Folding and Molding," *IEEE 29th International Conference on Micro Electro Mechanical Systems (IEEE MEMS),* pp. 203-206, 2016.

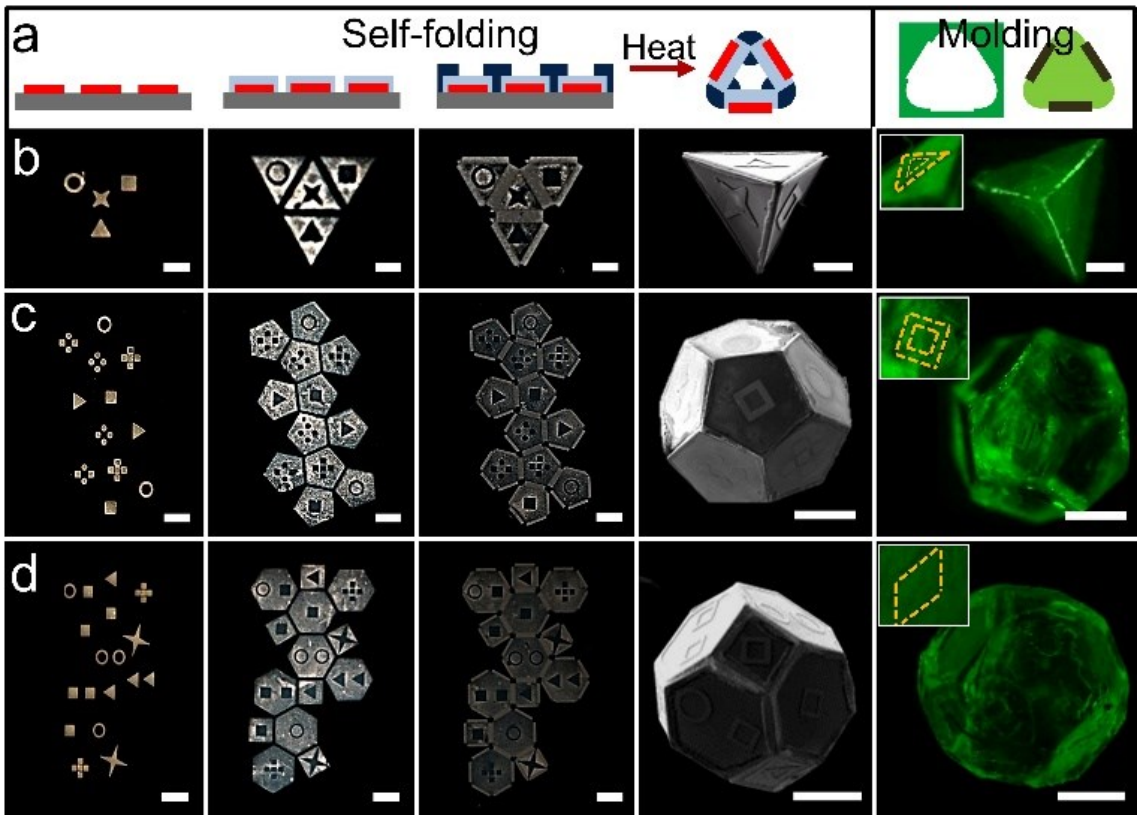

Figure 9.3. Experimental results showing 3D pattern transfer during molding. **(a)** Schematic, and **(b-d)** optical images from left to right showing fabrication of a nickel tetrahedron, octahedron and dodecahedron with gold patterns and their transfer to form patterned epoxy polyhedra with the same shape and pattern. All scale bars represent 300 μm.

Reprinted with permission from S. Pandey, C. K. Yoon, Z. Zhang, H. R. Kwag, J. Hong, and D. H. Gracias, "Patterned Soft-Micropolyhedra by Self-Folding and Molding," *IEEE 29th International Conference on Micro Electro Mechanical Systems (IEEE MEMS),* pp. 203-206, 2016.

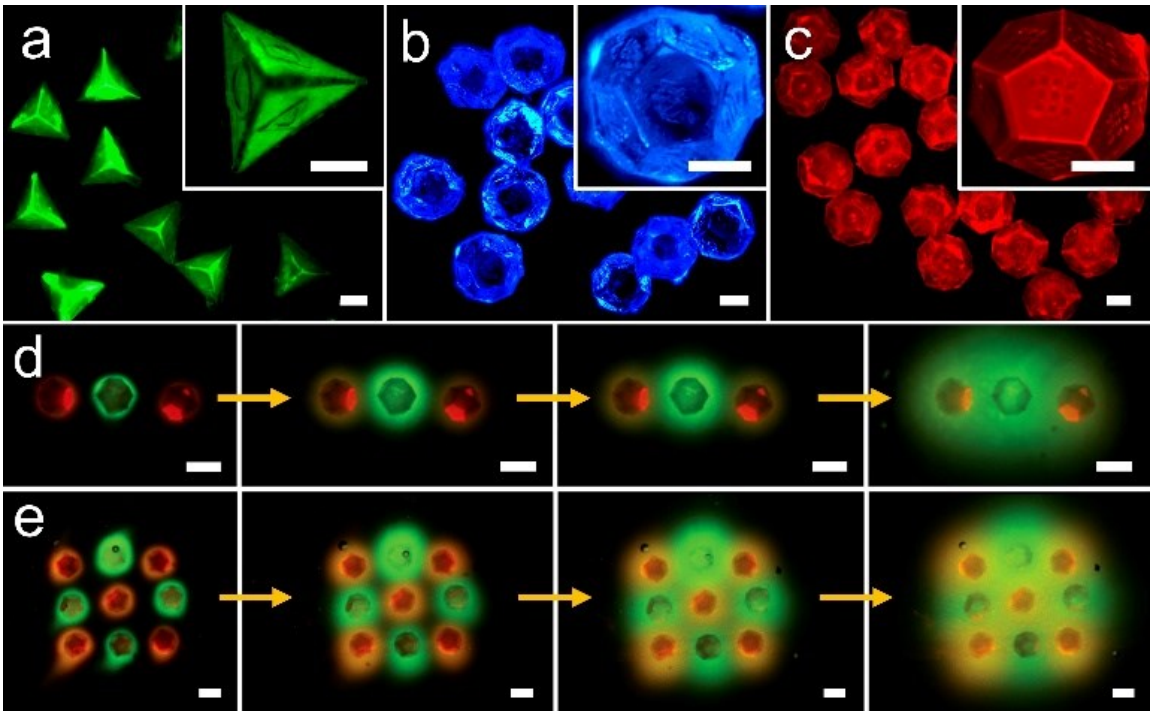

Figure 9.4. Soft-polyhedra with different polymers and hydrogels with and without loaded chemical dyes. (a) Fluorescent image of fluorescein loaded molded pNIPAM-AAc tetrahedra with surface patterns. **(b)** Image of molded NOA73 truncated octahedra. **(c)** Fluorescent image of rhodamine loaded PEGDA dodecahedra. **(d-e)** Optical images visualizing chemical release from arrays of two-color dye loaded PEGDA polyhedra. Scale bars represent (a-c) 300 μm, (d, e) 700 μm.

Reprinted with permission from S. Pandey, C. K. Yoon, Z. Zhang, H. R. Kwag, J. Hong, and D. H. Gracias, "Patterned Soft-Micropolyhedra by Self-Folding and Molding," *IEEE 29th International Conference on Micro Electro Mechanical Systems (IEEE MEMS),* pp. 203-206, 2016.

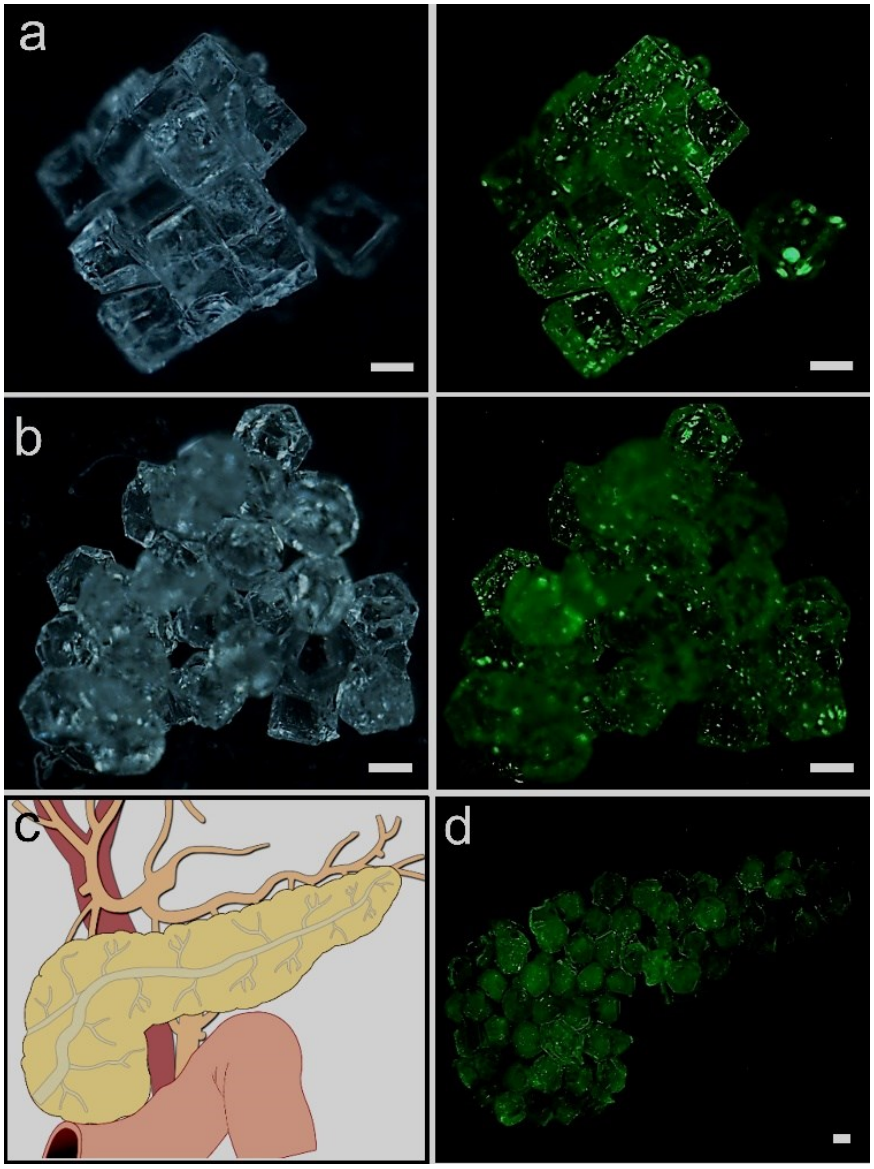

Figure 9.5. Assembly of cell-laden bioblocks for tissue engineering applications. Optical and fluorescent images of *ß*-TC-6 mouse insulinoma cell-laden PEGDA **(a)** cubes, and **(b)** dodecahedra, **(c)** schematic diagram of the human pancreas and **(d)** the assembly of *ß*-TC-6 cell-laden bioblocks in the shape of the pancreas. All scale bars are 300 μm and green fluorescence indicates viability of the cells stained with a Calcein AM live stain.

Reprinted with permission from S. Pandey, C. K. Yoon, Z. Zhang, H. R. Kwag, J. Hong, and D. H. Gracias, "Patterned Soft-Micropolyhedra by Self-Folding and Molding," *IEEE 29th International Conference on Micro Electro Mechanical Systems (IEEE MEMS),* pp. 203-206, 2016.

10. Rolled-up Nanoporous Membranes by Nanoimprint Lithography and Strain Engineering*

10.1. Overview

It is extremely challenging to enable nanoscale patterning in three dimensional (3D) curved geometries using conventional nanolithographic approaches. In this paper, we describe a highly parallel approach that combines nanoimprint lithography (NIL) and thin film bilayer strain engineering to spontaneously roll-up nanopatterned membranes into curved geometries. Specifically, we first patterned a silicon nitride (Si_3N_4) / silicon (Si) bilayer using nanoimprint lithography followed by plasma etching to create well defined pores. The diameter of the pores was further reduced by physical vapor deposition of platinum to sizes as small as 50 nm. After patterning, the bilayers were released from the substrate by etching an underlying SiO_2 sacrificial layer. Based on the high deposition stress values for low pressure chemical vapor deposition (LPCVD) deposited Si_3N_4 and Si, we varied the thickness of the bilayer to realize rolled-up tubes with different radii of curvature; these curvature values were in good agreement with a finite element analysis model (FEM). The assembled nanoporous tubes had well defined pores along their curved interface and can be applied for drug delivery, separations and ion-sensing devices.

---

* Reprinted with permission from

1. J. H. Park, C. K. Yoon, Q. Jin, L. Chen, and D. H. Gracias, "Rolled-up Nanoporous Membranes by Nanoimprint Lithography and Strain Engineering," *IEEE International Conference on Nano/Micro Engineered and Molecular Systems (IEEE NEMS),* pp. 233-237, 2015.

We highlight biocompatibility of the devices by encapsulating β-TC-6 islet cells of relevance to cell encapsulation therapy for diabetes. More broadly, we believe that this approach of combining NIL with strain engineering processes could be utilized to create a range of precisely nanopatterned curved structures in a highly parallel manner.

10.2. Introduction

Nanoscale patterning approaches based on electron beam or nanoimprint lithography (NIL) have revolutionized science and engineering.[318] However, these approaches are typically implemented on flat planar substrates; hence it can be very challenging to realize precise nanoscale patterns in curved geometries. In order to address this challenge, focused ion beam approaches have been developed but they are inherently serial and expensive for nanomanufacturing.[319] Parallel approaches such as roll-to-roll nanoimprint lithography have been used to pattern nanoscale gratings and polarizers.[320] However, these can be challenging to implement when patterning the entire circumferential surface area of cylinders or tubes, as achieved in our present demonstration. Moreover, in many applications multiple layers of patterning are needed with registry and these patterns can be extremely challenging to implement in a roll- to-roll manner.

An emerging approach for 3D nanomanufacturing is based on the utilization of stress to curve previously lithographically nanopatterned thin films.[321–326] In one embodiment of this approach, bilayers are deposited with differential stress and then subsequently patterned using conventional planar lithographic approaches. On

release from the substrate, the films relax and the strain mismatch causes them to curve spontaneously. As we demonstrate, when combined with NIL, the attractive feature of our approach is that both patterning and assembly can be realized in a highly parallel manner which is important for cost-effective nanomanufacturing.

High stresses can develop in thin films during or after deposition due to a variety of reasons such as epitaxial mismatch, thermal coefficient mismatch or defects during film growth.[327] Si_3N_4 is a silicon-based material compatible with conventional semiconductor nanofabrication technology, and is also generally considered biocompatible.[328] Therefore, Si_3N_4 is widely utilized in conventional MEMS and NEMS processing for a range of applications including electronics, sensors and biomedical engineering. Due to these attractive material properties, the nanoporous Si_3N_4 based devices that we describe are relevant for selective separations, biosensors and immunoisolation.[329] Stoichiometric LPCVD of Si_3N_4 is known to deposit films with high stress (~1 GPa), which is required for our assembly approach, even if the high stress is avoided in many other conventional thin film applications. As the second component of the bilayer, we utilize the monocrystalline silicon (Si) device layer on commercial Silicon on Insulator (SOI) wafers.

Si is also a widely utilized material in electronics and biomedical devices and has a significantly lower stress as compared to Si_3N_4;[330] consequently, due to this difference in stress between the two layers a strain mismatch occurs on release from the substrate. In addition, release of the bilayer can be achieved by etching the

underlying buried oxide (SiO_2) layer in hydrofluoric acid with sufficiently high etch selectivity so as not to damage the patterned Si_3N_4 and Si layers.

10.3. Experiments: Nanoporous Si_3N_4/Si Bilayers

Nanoporous Si_3N_4/Si bilayers were first patterned on planar substrates (**Figure 10.1.**). The Si_3N_4 layer was deposited using LPCVD on an SOI wafer with a 500 nm top Si device layer. The advantage of using SOI wafers is the presence of a high quality electrically tunable Si device layer and the buried oxide layer which can serve as a sacrificial layer and be dissolved to release high quality silicon devices.[137] Hence, in principle even electronic devices patterned in the high quality tunable, semiconducting Si device layer on an SOI wafer could be formed. The LPCVD deposited Si_3N_4 and Si device layer form the mismatched strain bilayer in our experiments.

We patterned the nanopores by first spin coating a 400 nm thick thermal resist (NXR-1020, Nanonex, **Figure 10.1. (a)**). Periodic circular patterns were imprinted using commercial Si master flat stamps (LightSmyth) and the Nanonex Advanced Nanoimprint Tool NX-2000 (**Figure 10.1. (b)**). After NIL, we performed an O_2 plasma etch (Unaxis 790 RIE) to remove the resist residue (**Figure 10.1. (c)**). Then a 50 nm thick chromium (Cr) film was deposited by thermal evaporation (**Figure 10.1. (d)**); the Cr serves as a dry etch mask. We dissolved the resist by sonication in acetone (**Figure 10.1. (e)**) and then dry etched the exposed Si_3N_4/Si using a Unaxis 790 RIE tool to form the nanopores. We used an etch gas composition of 1:16 of SF_6:CF_4 to etch

the pores through the bilayer. Finally the Cr was stripped using a commercial Cr etchant (CRE-473, Transene) (**Figure 10.1. (f)**).

10.4. Results and Discussions

10.4.1. Characterization of Nanoporous Surface

The NIL patterned and dry etched pores were characterized using SEM (**Figure 10.2**). As seen, pores are well defined and have an average diameter ranging from 200 to 400 nm along the height of the pore (**Figure 10.2. (a, b)**) compared to a 200 to 290 nm diameter of the posts in the NIL stamp, as specified by the vendor; hence, the pattern was transferred with good accuracy by NIL. In case of **Figure 10.2. (c)**, we did observe some etch related widening of the pores in the Si layer; we attribute this widening to etch rate differences for the two different materials (Si_3N_4 and Si) of the bilayer. If needed, the undercut can be reduced by adjusting the etch parameters as seen in the SEM image of narrow pores in **Figure 10.2. (d)**.

10.4.2. Characterization of Nanopores Sizes

We could further decrease the pore sizes by additive deposition. Platinum (Pt) is highly biocompatible material and widely used in MEMS and NEMS fabrication especially of relevance to electrodes, electrochemical devices and biosensors.[331–334] The diameter of nanopores could be further reduced by controlling the amount of sputtered Pt. The sequence of panels in **Figure 10.3. (a)** to **(f)** show decreasing nanopore sizes ranging from the initial patterned nanopores (~ 300 nm) down to 60 nm when Pt was deposited for 100 minutes using power settings of 5 mA and 15 kV.

10.4.3. Characterization of Self-rolled Tubes

The schematic flow in **Figure 10.4. (a)** shows the process for generating 3D self-rolled tubes. The tubes are formed by releasing the strain mismatched bilayer while keeping one side attached using a patterned strip of photoresist. If needed, this strip can be dissolved to completely release the tubes from the substrate or alternatively left behind if the nanoporous tubes need to be integrated with other on-chip components such as in conventional microfluidic devices. Importantly, the assembly process is parallel (**Figure 10.4. (b)**) and the zoomed in image shows well-formed tubes with NIL patterned nanoporous surfaces (**Figure 10.4. (c, e)**).

We also investigated the tunability of curvature in the roll-up process by varying several geometric parameters such as the lateral dimensions and thickness of Si_3N_4/Si bilayer. For example, by controlling the width of the bilayer we can control the circumference of the tube. Hence, it is possible to assemble semi-cylinders, cylinders, and rolls with overlapping seams as shown in **Figure 10.5. (a-c)**. Further, by controlling the thickness of Si_3N_4 thin layer from 50 to 140 nm, the roll diameter could be varied from 200 to 500 μm.

In order to understand the mechanics of self-rolling and rationalize the variation in the diameter of the cylinders, we performed finite element analysis. The Si_3N_4/Si bilayer was constructed using a 3D deformable shell model in ABAQUS (Dassault Systemes), considering the large length/thickness ratio. The dimensions were selected directly from the experimental design parameters. The elastic properties and

stress in LPCVD Si_3N_4 films were obtained from the literature[330] and are listed in **Table 10.1.**

Since in the experiments, one edge of the thin film was fixed on the wafer using the photoresist strip, the plane strain condition was considered for this case. Therefore, for boundary conditions, we fixed one edge displacement as zero in all translational and rotational directions. We modeled the stress in Si_3N_4 by assigning a thermal expansion coefficient only in Si_3N_4 layer, and applying a temperature field to simulate the folding process. The shell is meshed by structured quadratic elements. The shell layer uses the Simpson's integration rule and each layer was assigned with nine integral points. Further, we verified that an increase in the mesh element density and integral points did not make a significant difference to the results. The model predicts similar trends to that observed in experiments. Essentially, an increased $Si3N_4$ thickness from 50 to 140 nm improves the folding and yields smaller diameter tubes in agreement with experimental results (**Figure 10.5. (d)**). We rationalize this result by noting that the stress-thickness product is important in causing rolling and if either the stress or the thickness of the driving layer is too low, then the bending moment of the bilayer is small so the tubes formed would have large radii. However, this moment is balanced by the bending rigidity which also depends on thickness so increasing the thickness of the Si_3N_4 will eventually cause reduced bending and larger radii. Based on our simulations for the values in **Table 10.1.** and a fixed thickness of the Si layer = 500 nm, our model suggests that the maximum bending (rolling) with

an associated diameter of 322 μm in diameter (inflection point) would occur at a Si_3N_4 thickness of 205 nm.

10.4.4. Applications of Nanoporous Membranes

One of the applications of nanoporous membranes is in the encapsulation and delivery of xenotrasplanted islet cells for diabetes therapy.[335] It has been suggested that nanoporous embranes could protect encapsulated cells from various components of the immune system while enabling adequate transport of nutrients, waste and therapeutic insulin from transplanted cells. A variety of nanoporous hydrogel materials such as alginate have been utilized but it has been suggested that nanofabricated pores with well-defined chemistry and straight pore geometries could enhance immunoisolation and reduce biofouling.[336] However, it can be challenging to create such 3D nanoporous capsules using conventional fabrication approaches due to the inherent planarity of parallel lithographic approaches. We explored the use of our rolled-up tubes as nanoporous encapsulants for cells and devised an experimental set-up to load *β*-TC-6 (beta) cells (ATCC, CRL-11506) into the tubes using a syringe pump (**Figure 10.6. (a, b)**). After loading, cells were cultured in the tubes and cell viability was verified after five days by staining with a Calcein stain. This stain fluoresces green in live cells due to acetoxymethyl ester hydrolysis by esterases that are present within cells. We observed that cells fluoresced green indicating cell viability in the nanoporous tubes (**Figure 10.6. (c, d)**). Further studies are needed to develop approaches to effectively seal the two ends of the tubes and measure glucose release and applicability for immunoisolation. It is

noteworthy that elsewhere we have demonstrated how self-aligning surface tension driven seams can be used to seal self-folding structures[139] and these approaches along with polymer plugs could be utilized.

10.5. Conclusion

In conclusion, we have described the use of NIL and strain engineering to create precisely nanopatterned curved nanostructures. The highlight of the approach is that it is scalable and highly parallel. As opposed to expensive serial planar patterning techniques such as e-beam lithography, NIL allows highly parallel patterning. One limitation is that registry between multiple layers in NIL patterning can be challenging, but the approach is highly relevant for periodic single layer patterns such as pores, crosses or resonators. The latter patterns are relevant for optical waveguides and metamaterials. Our studies also provide further evidence that strain engineering can be used to transform flat films into curved geometries and the highly parallel nature of the approach should be contrasted with serial 3D patterning approaches such as two-photon or ion beam machining. Hence, this approach could be applied to mass-produce curved nanopatterned electronic, optical and biomedical devices in a cost-effective manner.

Table 10.1. Elastic properties of each layer.

	Simulation parameters			
	Thickness (nm)	***Young's modulus (GPa)***	***Poisson Ratio***	***Stress (MPa)***
Si_3N_4	50 to 140	290	0.253	1000
Si	500	190	0.220	0

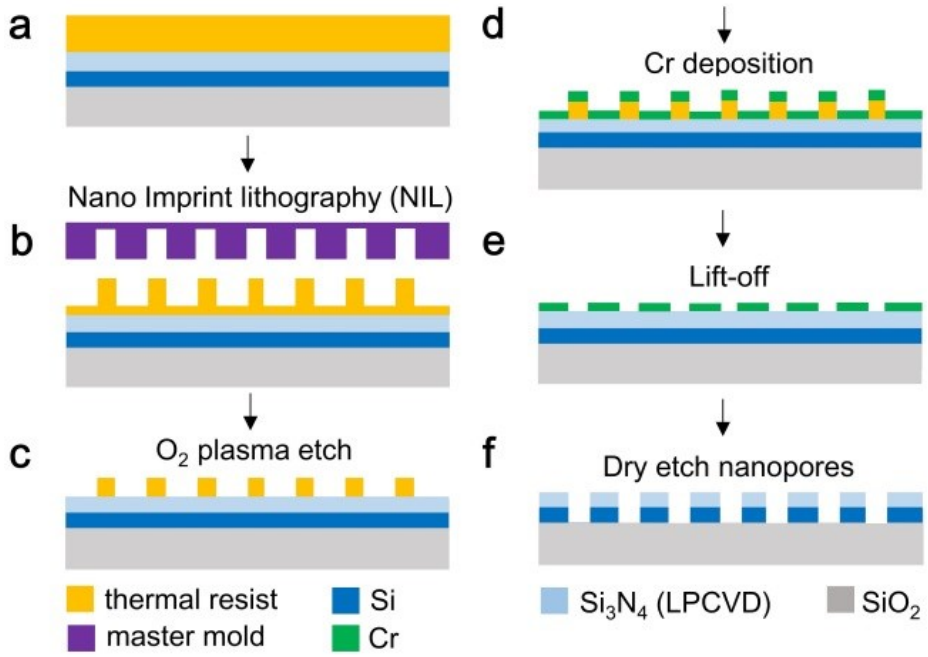

Figure 10.1. Schematic of the process flow that was used to pattern the nanopores in the Si_3N_4/Si bilayer.

Reprinted with permission from J. H. Park, C. K. Yoon, Q. Jin, L. Chen, and D. H. Gracias, "Rolled-up Nanoporous Membranes by Nanoimprint Lithography and Strain Engineering," *IEEE International Conference on Nano/Micro Engineered and Molecular Systems (IEEE NEMS),* pp. 233-237, 2015.

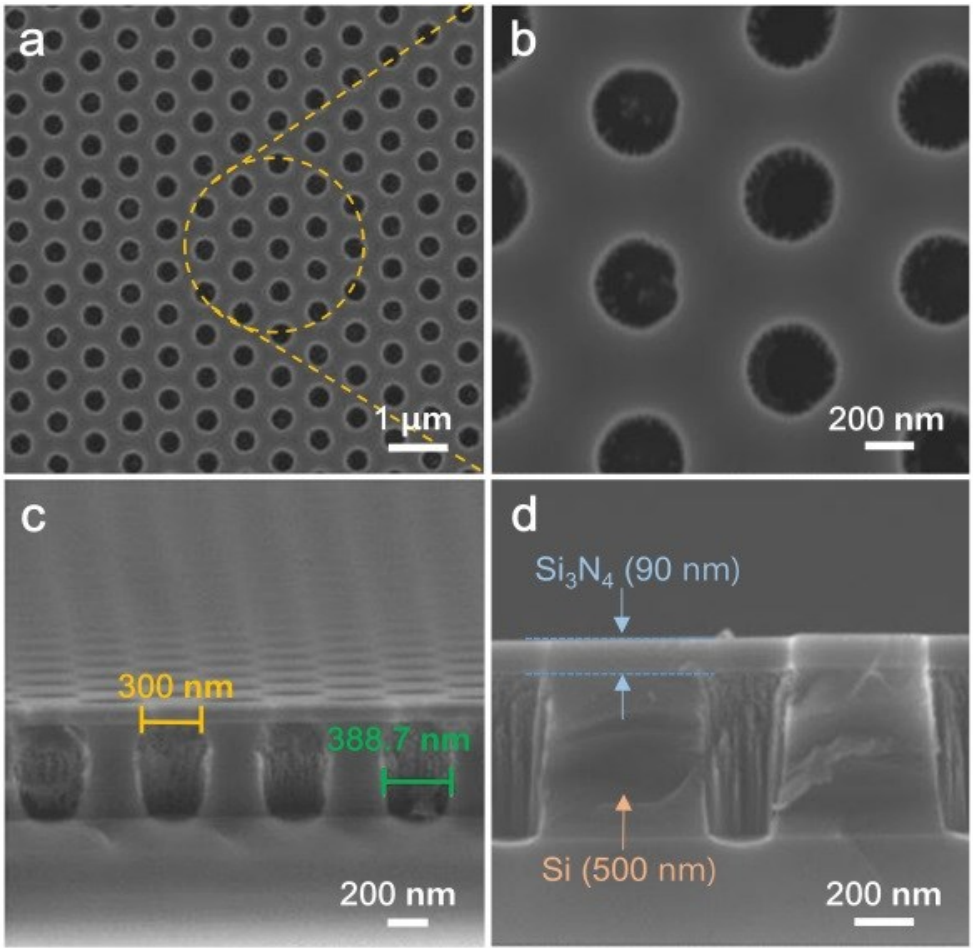

Figure 10.2. SEM images of nanopores in the Si_3N_4/Si bilayer. (a) Array and **(b)** zoomed-in image showing well-formed pores. **(c)** Typical cross-section view of the nanopores, and **(d)** zoomed in image of pores in Si_3N_4 (t= 90 nm) /Si (t= 500 nm) thin films. By varying etch parameters, the pore widths could be tuned between 400-200 nm as illustrated in the images in panels (c) and (d).

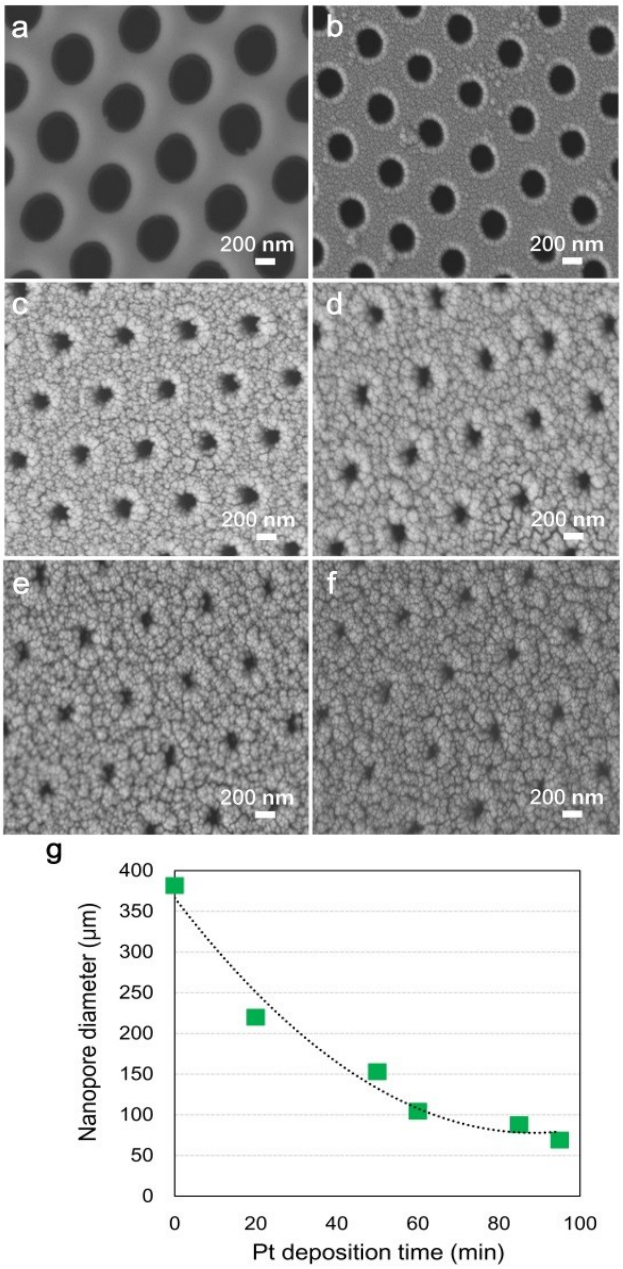

Figure 10.3. Reduction in nanopore size by platinum deposition. (a-f) Pores on the rolled-up tubes with sizes ranging from an initial nanopore diameter approximately 300 nm which was decreased down to 60 nm. **(g)** Plot of the nanopore diameter (nm) vs Pt deposition time (min).

Reprinted with permission from J. H. Park, C. K. Yoon, Q. Jin, L. Chen, and D. H. Gracias, "Rolled-up Nanoporous Membranes by Nanoimprint Lithography and Strain Engineering," *IEEE International Conference on Nano/Micro Engineered and Molecular Systems (IEEE NEMS),* pp. 233-237, 2015.

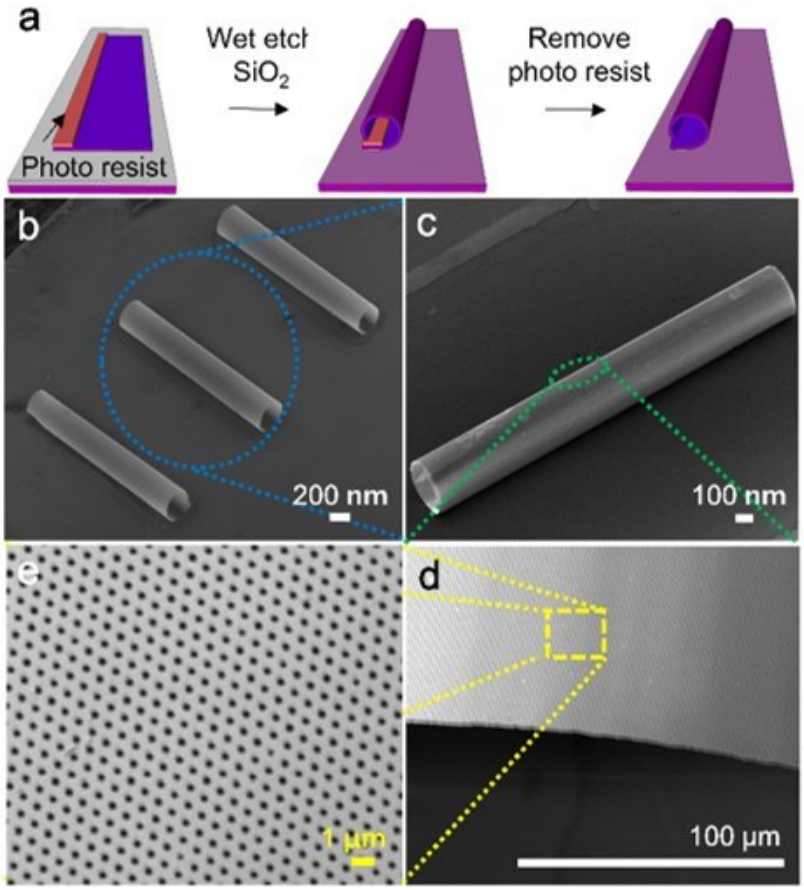

Figure 10.4. Self-rolling nanoporous films. Schematic and experimental images showing the **(a)** process flow and **(b-e)** SEM images of self-rolling nanoporous films. (b) Multiple and (c) single rolled-up film (d, e) Array of well-formed nanopores by NIL.

Reprinted with permission from J. H. Park, C. K. Yoon, Q. Jin, L. Chen, and D. H. Gracias, "Rolled-up Nanoporous Membranes by Nanoimprint Lithography and Strain Engineering," *IEEE International Conference on Nano/Micro Engineered and Molecular Systems (IEEE NEMS),* pp. 233-237, 2015.

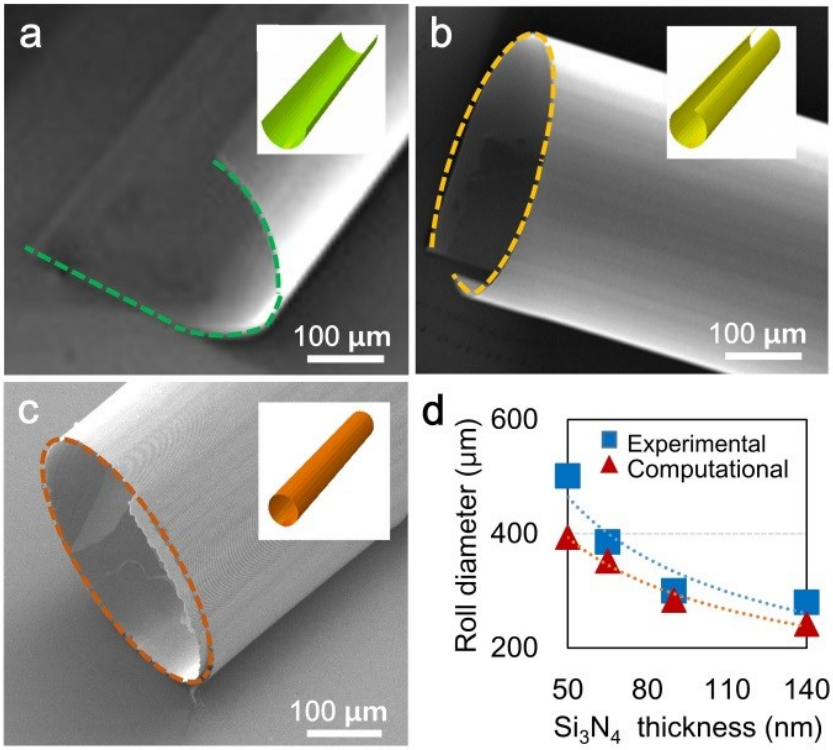

Figure 10.5. Experiments and FEM results of rolled-up nanoporous membranes with different characteristics. (a-c) SEM images of semi-cylinders, cylinders and rolls with overlapping seams. **(d)** Plot comparing experimental and FEM curvature as a function of Si_3N_4 thickness.

Reprinted with permission from J. H. Park, C. K. Yoon, Q. Jin, L. Chen, and D. H. Gracias, "Rolled-up Nanoporous Membranes by Nanoimprint Lithography and Strain Engineering," *IEEE International Conference on Nano/Micro Engineered and Molecular Systems (IEEE NEMS),* pp. 233-237, 2015.

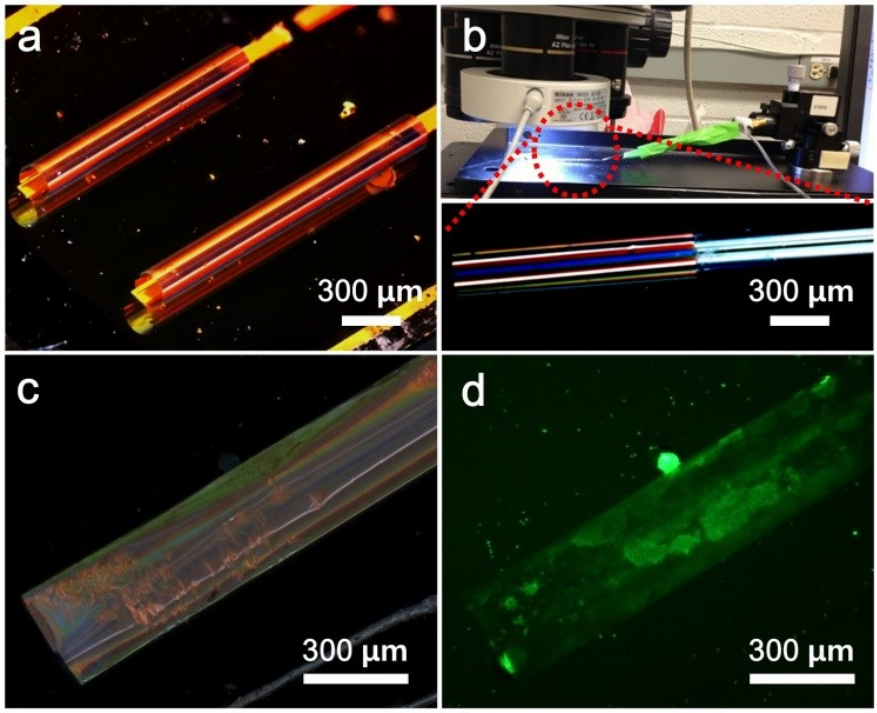

Figure 10.6. Cell culture in nanoporous tubes. (a) Optical image of the rolled-up nanoporous Si_3N_4/Si bilayers and **(b)** experimental set-up for loading the cells into the tubes. The set-up consists of a hollow glass-tube inserted into the nanoporous tube and attached to a syringe pump for controlled loading of a high-density cell suspension **(c-d)** Optical and fluorescence image of calcein (viability stain) stained cells indicating cell viability.

Reprinted with permission from J. H. Park, C. K. Yoon, Q. Jin, L. Chen, and D. H. Gracias, "Rolled-up Nanoporous Membranes by Nanoimprint Lithography and Strain Engineering," *IEEE International Conference on Nano/Micro Engineered and Molecular Systems (IEEE NEMS),* pp. 233-237, 2015.

11. Summary and Future Studies

The main contribution of this dissertation is to mimic elements of natural systems capable of showing environmentally adaptive shape changing behaviors by using naturally self-assembled, -curved, or –folded structures. In order to realize biomimetic reconfigurable engineered devices, photolithographic methodology, and self-folding mechanism can be adapted to create multi-functional stimuli responsive soft microsystems. Especially, self-folding strategies have been developed due to their simplicity in creating multi-functional three dimensional (3D) microsystems that are required for the development of biomimetic microscale devices applicable in medicine, electronics, optics etc. These self-folding strategies can generate reliable and reproducible high-throughput transformation of 3D patterns from those of two dimensional (2D) by utilizing many materials (metallic or/and polymeric), size ranges (cm to nm), and geometries (simple to complex) in a cost-effective and highly parallel manner. In addition, to design biomimetic materials and devices at small scales, stimuli responsive materials and devices have received considerable technological attentions as intelligent materials due to their stimuli responding mechanism when exposed to external stimuli. These stimuli responsive shapes and structures can be manufactured by methods such as photolithography, 3D printing, molding, or layer by layer assembly. In addition, the reconfigurable and spontaneous shape changes of stimuli responsive microsystems can be generated by simple control of volume changes in hydrogels or polymers. These stimuli responsive soft microsystems can be autonomously navigated and controlled by using different external environmental triggers such as heat, pH, light, magnetic fields etc. without

the usage of any complex sensors, tethers, or batteries. Amongst many stimuli responsive materials, poly (*N*-isopropylacrylamide-co-acrylic acid) (pNIPAM-AAc) based hydrogels have been selected as one of the stimuli responding hydrogels because of their high reversibility of phase transition around physiological body temperature.

In order to implement the concept of self-folding stimuli responsive microsystems, we proposed a simple programmable MEMS-inspired lithographic approach in order to design stimuli responsive 3D polymeric structures made of PNIPAM-AAc in Chapter 3. The pNIPAM-AAc based hydrogel was chosen as one of the appropriate materials to generate shape changes based on dual thermal and pH responsive properties controlled by simple swelling and deswelling in aqueous environments. In photolithographic approaches, we have refined the programmability of crosslinking degree of pNIPAM-AAc hydrogel systems so as to generate self-folding stimuli responsive microsystems by utilizing different UV exposure levels on panels and hinges. Especially, less UV exposed domains could generate crosslinking gradients along a thickness resulting in spontaneous diverse origami-like 3D curving, rolling, or folding structures when they are exposed to external stimuli such as heat and pH. First, we characterized the chemical and mechanical properties of pNIPAM-AAc experimentally and computationally in order to understand the stimuli responsive folding mechanism of thin pNIPAM-AAc monolayer composed of fully crosslinked panels and crosslinked gradient hinges. Further, these self-folding and stimulus responding mechanisms of pNIPAM-AAc

hydrogel were identified with their practical potentials such as hydrogel capsules for drug delivery, multifunctional pH steered optoelectronic micro mirror systems for code reading, imaging, and motion detecting by a simple programmable photolithographic approach. It was demonstrated that the use of pNIPAM-AAc based hydrogel microsystem could cover different possibilities towards the design of biomimetic soft actuator at small scales. However, these stimuli responsive hydrogel devices have limitations. For example, most complex 3D shapes of nano-scale stimuli responsive materials and devices are hard to be structured. In addition, the most of the shape deformation in stimuli responsive materials is quite simple and is limited to aqueous solutions. Among many technical limitations, one of the big challenges of stimuli responsive materials and devices is that the shape changing orders are hard to be determined by conventional external triggers and there are none or very few ways of programming the desired pathway of shape changing. In order to overcome these limitations in stimuli responsive hydrogel systems, we utilized DNA-hybridization driven swelling and developed highly selective shape changing soft matter.

Stimuli responsive shape changing chemomechanical self-folding devices are important in the design of soft robots, smart therapeutics, laboratories on chips and assembly of 3D devices. However, most of them can fold or actuate into one or two possible final structures by a small number of limited programmability. In order to solve this challenge, we adopted a high throughput photolithographic approach to fabricate multi-domain DNA crosslinked hydrogel systems to elucidate large

specificity and programmability of biomolecular interactions to drive macroscale shape change by DNA hybridization. A new class of chemomechanical soft actuators could be developed by photopatterning and scalable integration of DNA-co-polymer hydrogels with dramatic shape changes in multiple different ways in response to DNA sequence inputs. We demonstrated the possibility of soft materials and functional devices responding to a diverse array of chemical inputs has been demonstrated by autonomously implementing adaptive chemical control programs. Especially, lock-and-key type sequence-specific DNA hybridization could allow achieving the combinatorial variety of material domains that have different swelling in different micro-patterned hydrogel domain arrangements, in response to a DNA input of particular sequence. In addition, we discussed the implementation of an FEM model to understand the actuation of DNA responsive hydrogel systems by using bilayer bar shapes.

In Chapter 4, we discussed the possibilities of highly selective intelligent chemomechanical actuators by demonstrating selective and sequential actuation of micropatterned shapes. This study has proposed an innovative multi-step fabrication strategies to pattern complex shaped multi-domain DNA crosslinked hydrogel systems and also their highly selective shape-changes by adopting DNA engineering. However, DNA hybridization reactions in order to fold micro and millimeter scale hydrogel systems were quite slow on the order of an hour. To mimic sub-mille seconds folding and unfolding actuation such as Venus flytrap or bunchberry dogwood, new DNA materials and geometric design parameters have to be

considered in order to amplify bi-stable systems as snap-buckling deformation having quick motion. In addition, our understanding of shape deformation of DNA crosslinked hydrogel systems is limited to a simple model of bilayer bending based on Flory-Huggins polymeric and Neo-Hookean spring models with experimental mechanical moduli and swelling ratio parameters. However, a more in-depth understanding of DNA programming in crosslinked hydrogel systems needs to be acquired based on theoretical thermodynamics and kinetics.

In addition, most of the conventional stimuli responsive soft microsystems have a low mechanical stiffness including our previously described pNIPAM-AAc (162 KPa) and crosslinked DNA (229 to 667 Pa) actuators. This can limit the grip-functionality of soft actuators in a biopsy, for instance. To overcome one of these limitations of soft stimuli responsive microsystems, we have adapted poly propylene fumarate (PPF) which has higher mechanical modulus (16 MPa) compared to pNIPAM-AAc and crosslinked DNA hydrogels. In specific, we further designed bio-friendly and soft stimuli responsive micro scale grippers having rigid PPF panels atop a continuous stimuli responsive pNIPAM-AAc hydrogel layer to demonstrate biopsy as one of the alternative materials to enable low-power functional, adaptive and autonomous systems. We have demonstrated that these untethered soft micro scale grippers are attractive candidates to substitute metallic grippers for bio-inspired microscale biopsy tools that reversibly fold and unfold based on the swelling/deswelling when the temperature changes. These grippers could activate an anisotropic swelling response between the top and bottom layers when triggered by

an external thermal stimulus so that spontaneous 3D folding occurs. In order to implement this self-folding mechanism, we further modified Flory-Huggins model to describe the bi-folding and reversible thermal actuation of pNIPAM-AAc/PPF soft gripper mechanism. We have validated an important design strategy to create stimuli responsive soft microsystems by pairing a rigid polymer such as PPF or SU-8 with thermo-responsive pNIPAM-AAc hydrogel. In theoretical viewpoints, a finite element model (FEM) could rationalize folding angles and their variations in stimuli responsive microsystems based on swelling ratio and mechanical moduli. From a bilayer design perspective, our modeling study has suggested an optimal thickness and modulus ratio for the stimuli responsive hydrogel and stiff structural bilayers in order to obtain the targeted folding angles. This FEM study highlights some important challenges such as the materials and geometric design strategies to increase the speed of actuation to the order of sub-second time scales while increasing the resolution of lithography to get smaller structures. Finally, we showed that when the pNIPAM-AAc layer was combined with the non-swellable stiff polymer such as PPF or SU-8, the soft grippers could provide enough strength to extract cells from a tissue clump. Further, we have shown the possibilities of these stimuli responsive materials and systems which possess widespread advanced functionalities in soft robotic non-invasive biopsy tools in surgeries by incorporating ferromagnetic iron oxide (Fe_2O_3) into the gripper so that they can be potentially guided using a magnetic wire in a clinical setting.

Additionally, in order to broadly implement the concept of precisely guided thermo- and magneto- responsive soft micro gripper systems for pick-and-place and smart manipulation applications, point-to-point and autonomously controllable electromagnetic and thermal systems have been developed (Chapters 6 and 7). As described in the Chapters 6 and 7, the materials design of stiff polymers (PPF or SU-8) and stimuli responsive pNIPAM-AAc based bilayer structures that are functioning together with Fe_2O_3, could allow autonomous pick-and-place targets in unstructured environments that contain time varying obstacles. These soft grippers could be directed by the decision-making, path-planning, and closed loop control algorithms with no human intervention. Experimentally, we designed autonomous micro soft grippers and performed pick-and-place tasks. Furthermore, these soft grippers were less destructive while picking and placing soft biological organisms. This suggested the ability of soft grippers to autonomously detect and adapt precise manipulation in a broad variety of tasks such as micro assembly and assisted fertilization in response to external environmental changes. In addition, we have envisioned that these thermo- and magneto- responsive soft gripping systems could enlarge the schemes of non-invasive diagnostics and therapeutics by one step closer to reality. This wireless magnetic-based motion control of soft untethered grippers can be developed by using feedback from ultrasound or other clinically compatible imaging system as well. Currently, these autonomously controlled magnetic and thermal responsive soft gripper systems have to face further challenges in finding alternate solution or materials to increase the magnetic response because they do not have enough magnetic response to be guided to a place where friction is high or in mucus

membranes, for example. In addition, in order to broadly utilizing the untethered tools for surgery, there is need to construct devices that are biocompatible and possibly biodegradable so that any tools left behind are completely cleared away by the body. Finally, a systematic controller for precise heating or/and cooling delivery at a target area is also one of the critical parts to be developed in soft-robotics and surgery.

Stimuli responsive engineering also can be validated through several different materials and methodological strategies so as to create functional 3D self-folding microsystems. We developed solvent responsive flexible 3D optical and chemical sensors composed of few layers graphene (FLG) and SU-8 bilayers (Chapter 8). Highly sensitive, with low power miniaturized sensors have promoted MEMS-inspired fabrication technologies in a single analytical device. The development of the ultra-dense small 2D or 3D detectors composed of metallic and semi metallic materials have resulted in improved sensitivity, thereby delivering better performance in sensor applications. However, most 2D or 3D metallic and semi metallic sensors are brittle, opaque, and have low flexible to control the shapes as compared to the soft polymeric devices. We have demonstrated that the photolithographic self-folding mechanism could be replaced with metallic and semi metallic sensors on soft matters. Especially, we also discovered that a low level UV light exposure on the SU-8 polymer can make photo-crosslink gradient along a thickness direction to change shapes spontaneously and reversibly. We proposed these unique characteristics of SU-8 combined with 2D layers of graphene in order to make soft sensors with better

performance due to the extreme sensitivity of graphene to the external environment and reversible shape control of SU-8 by the self-folding mechanism. We also developed an alternative approach to pattern and design the transparent free-standing, and untethered reversibly rolling and flattening graphene/SU-8 sensors. We demonstrated first good adhesion of FLG to hydrophobic SU-8, then second, the capability to pattern and incorporate gold electrodes using planar lithography prior to release from the substrate and finally stimuli responsive engineering of SU-8. Finally, we highlighted these FLG/SU-8 sensors that can control the electrical and optical properties through programming the structures from 2D to 3D by self-rolling, in order to prove the ultimate dual functional opto-electrical sensing abilities through several ionic media, cell lines, and laser sources.

Furthermore, one of the significant challenges in soft matter engineering is the mass fabrication of precisely patterned 3D soft micro and nanoscale materials and devices. An attractive strategy to overcome this challenge is to leverage the existing infrastructure and precision of planar photo, e-beam, and nanoimprint lithography approaches, and to fold up the previously patterned thin films to form precisely patterned 3D materials and devices. However, due to the small size and stiction, it is difficult to design complex shapes of soft micro structures or particles with conventional probes. In order to overcome this methodological limitation, in Chapter 9, we identified the method that combines self-folding and conventional soft molding techniques in order to create complex shaped microscale polymeric particles. Especially, these approaches not only enable us to synthesize complex shaped 3D

polymeric microstructures but also make it possible to transfer arbitrary patterns precisely onto the surfaces of the molded soft particles with microscale resolution in a highly parallel and mass-producible manner.

In addition, nanoscale patterning in 3D curved geometries is extremely challenging. In chapter 10, we described an innovative technique that combines nanoimprint lithography (NIL) and strain engineering to obtain spontaneous rolled-up nanopatterned membranes into 3D curved geometries. Self-folding refers to processes wherein planar structures fold up spontaneously, typically when released from a substrate or when exposed to specific stimuli. The driving forces for self-folding result from material heterogeneities that are either stimulated or engineered during thin film deposition or fabrication and can be varied. Especially, in this chapter, we described that self-folding of uniformly strained structures resulted in curved or rolled-up structures with different radii of curvature. Technically, the curvature of silicon nitride (Si_3N_4)/ silicon (Si) bilayer could be controlled by varying its thickness during low pressure chemical vapor deposition (LPCVD). We could assemble nanoporous tubes via combining NIL with strain engineering processes in a cost effective and parallel assembly manner. Finally, we proposed that 3D rolled up tubes having arrays of nanopores along their curved surface could be applied for drug delivery, separations, and ion-sensing devices.

As contribution to future work, fully biodegradable stimuli responsive self-folding microsystems have to be considered for biopsy or/and drug delivery applications in biomedical engineering. Recently, untethered soft robotic devices

have been introduced for biopsy or drug delivery but the materials utilized to make these devices are often non-biodegradable, thus increasing the risk for utilization in humans, especially, if they are lost or are left inside the body. Particularly, these devices have to be non-cytotoxic, including both before and after degradation processes. In order to obtain fully biodegradable and biocompatible stimuli soft materials, poly (acrylamide-*N*, *N*-Bis(acryloyl)cystamine) p(AAm-BAC) and poly (oligo ethylene glycol methyl ether methacrylate-co- bis(2-methacryloyl) oxyethyl disulfide) p(OEGMA-DSDMA) can be considered. We can utilize wafer scale patterning to design a variety of shape changing stimuli responsive micro devices including grippers by using p(AAm-BAC) and p(OEGMA-DSDMA). These structures are also expected to fold and bend due to anisotropic differential swelling similar to previous bilayer structures such as pNIPAM-AAc/PPF or pNIPAM-AAc/SU-8. Furthermore, it is anticipated that the stimuli responsive devices composed of p(AAm-BAC)/p(OEGMA-DSDMA) bilayers can be fully degraded in the presence of glutathione or similar reducing agents at physiological body temperature. We expect the development of a wide range of such thermally and magnetically responsive soft drug delivery devices that can move to the desired area, grab targets, release drugs, which can be fully biodegraded. Moreover, 3D printing strategy combined with self-folding mechanism can also envision further high applicability of stimuli responsive self-folding macroscale systems. Photolithographic and self-folding methodologies are appropriate for sub-millimeter scales devices and 3D printing can enlarge the size scopes to macroscales in order to develop 3D printed stimuli responsive materials and devices which are applicable in a variety of applications such as alternatives of

biological organs, minimally or non-invasive surgical tools, and high sensitive and selective configurable sensors and actuators. Furthermore, these biodegradable and biocompatible materials and newly innovative methodological approach of 3D printing will make the stimuli responsive self-folding systems obtain distinct less-invasive and bio-friendly operating systems in a body compared to traditional electrically or pneumatically driven motion of conventional tethered robots. Finally, the rapid development of stimuli responsive systems in recent years has increased the necessity of micro- and macro-scale devices in soft robotics, smart therapeutic drug delivery capsules, less-invasive and precisely controllable biopsy tools, highly selective programmable intelligent actuators, and flexible chemical and optical sensors etc. We have expected that the photolithographic methodology combined with self-folding mechanism can realize those reconfigurable stimuli responsive microsystems in mass-producible and cost-effective parallel operation manners. In addition, we also believe that these stimuli responsive self-folding microsystems have addressed a new platform to study microscale physics and dynamics.

References

1. Binauld, S. & Stenzel, M. H. Acid-degradable polymers for drug delivery: a decade of innovation. *Chem. Commun.* **49,** 2082–102 (2013).

2. Gong, C. *et al.* Thermosensitive polymeric hydrogels as drug delivery systems. *Current medicinal chemistry* **20,** 79–94 (2013).

3. Murdan, S. Electro-responsive drug delivery from hydrogels. *Journal of Controlled Release* **92,** 1–17 (2003).

4. Miyata, T., Asami, N. & Uragami, T. Preparation of an antigen-sensitive hydrogel using antigen-antibody bindings. *Macromolecules* **32,** 2082–2084 (1999).

5. Takashi, M., Asami, N. & Uragami, T. Structural design of stimuli-responsive bioconjugated hydrogels that respond to a target antigen. *J. Polym. Sci. Part B Polym. Phys.* **47,** 2144–2157 (2009).

6. Leong, T. G. *et al.* Tetherless thermobiochemically actuated microgrippers. *Proc. Natl. Acad. Sci. U. S. A.* **106,** 703–708 (2009).

7. Bassik, N. *et al.* Enzymatically triggered actuation of miniaturized tools. *J. Am. Chem. Soc.* **132,** 16314–16317 (2010).

8. Hu, J., Zhang, G. & Liu, S. Enzyme-responsive polymeric assemblies, nanoparticles and hydrogels. *Chem. Soc. Rev.* **41,** 5933 (2012).

9. Sershen, S. R., Westcott, S. L., Halas, N. J. & West, J. L. Temperature-sensitive polymer-nanoshell composites for photothermally modulated drug delivery. *J. Biomed. Mater. Res.* **51,** 293–298 (2000).

10. Zhang, X., Wu, D. & Chu, C. C. Synthesis and characterization of partially biodegradable, temperature and pH sensitive Dex-MA/PNIPAAm hydrogels. *Biomaterials* **25,** 4719–4730 (2004).

11. Fusco, S. *et al.* Shape-switching microrobots for medical applications: The influence of shape in drug delivery and locomotion. *ACS Appl. Mater. Interfaces* **7,** 6803–6811 (2015).

12. Meng, H. & Jinlian Hu. A brief review of stimulus-active polymers responsive to thermal, light, magnetic, electric, and water/solvent stimuli. *J. Intell. Mater. Syst. Struct.* **21,** 859–885 (2010).

13. Hirokawa, Y. & Tanaka, T. Volume phase transition in a nonionic gel. *J. Chem. Phys.* **81,** 6379 (1984).

14. Oh, J. K., Drumright, R., Siegwart, D. J. & Matyjaszewski, K. The development of microgels/nanogels for drug delivery applications. *Progress in Polymer Science* **33,** 448–477 (2008).

15. Shah, R. K., Kim, J.-W., Agresti, J. J., Weitz, D. a. & Chu, L.-Y. Fabrication of monodisperse thermosensitive microgels and gel capsules in microfluidic devices. *Soft Matter* **4,** 2303–2309 (2008).

16. Hoffman, A. S. *et al.* Really smart bioconjugates of smart polymers and receptor proteins. in *Journal of Biomedical Materials Research* **52,** 577–586 (2000).

17. Guan, J., He, H., Hansford, D. J. & Lee, L. J. Self-folding of three-dimensional hydrogel microstructures. *J. Phys. Chem. B* **109,** 23134–23137 (2005).

18. Shim, T. S., Kim, S. H., Heo, C. J., Jeon, H. C. & Yang, S. M. Controlled origami folding of hydrogel bilayers with sustained reversibility for robust microcarriers. *Angew. Chemie - Int. Ed.* **51,** 1420–1423 (2012).

19. Kameda, M., Sumaru, K., Kanamori, T. & Shinbo, T. Probing the dielectric environment surrounding poly(N-isopropylacrylamide) in aqueous solution with covalently attached spirobenzopyran. *Langmuir* **20,** 9315–9319 (2004).

20. Sumaru, K., Kameda, M., Kanamori, T. & Shinbo, T. Characteristic phase transition of aqueous solution of poly(N-isopropylacrylamide) functionalized with spirobenzopyran. *Macromolecules* **37,** 4949–4955 (2004).

21. Mano, J. F. Stimuli-responsive polymeric systems for biomedical applications. *Advanced Engineering Materials* **10,** 515–527 (2008).

22. Zhang, X. *et al.* Optically- and thermally-responsive programmable materials based on carbon nanotube-hydrogel polymer composites. *Nano Lett.* **11,** 3239–3244 (2011).

23. Cho, K. J. *et al.* Review of manufacturing processes for soft biomimetic robots. *International Journal of Precision Engineering and Manufacturing* **10,** 171–181 (2009).

24. Bartlett, N. W. *et al.* A 3D-printed, functionally graded soft robot powered by combustion. *Science* **349,** 161–165 (2015).

25. Wehner, M. *et al.* An integrated design and fabrication strategy for entirely soft, autonomous robots. *Nature* **536,** 451–455 (2016).

26. Mannoor, M. S. *et al.* 3D printed bionic ears. *Nano Lett.* **13,** 2634–2639 (2013).

27. Jamal, M., Zarafshar, A. M. & Gracias, D. H. Differentially photo-crosslinked polymers enable self-assembling microfluidics. *Nat. Commun.* **2,** 527 (2011).

28. Gracias, D. H. Stimuli responsive self-folding using thin polymer films. *Curr. Opin. Chem. Eng.* **2,** 112–119 (2013).

29. Kwag, H. R. *et al.* A self-folding hydrogel in vitro model for ductal carcinoma. *Tissue Eng. Part C. Methods* **22,** 398–407 (2016).

30. Malachowski, K. *et al.* Stimuli-responsive theragrippers for chemomechanical controlled release. *Angew. Chemie - Int. Ed.* **53,** 8045–8049 (2014).

31. Yoo, J. W., Doshi, N. & Mitragotri, S. Adaptive micro and nanoparticles: Temporal control over carrier properties to facilitate drug delivery. *Advanced Drug Delivery Reviews* **63,** 1247–1256 (2011).

32. Qiu, Y. & Park, K. Environment-sensitive hydrogels for drug delivery. *Advanced Drug Delivery Reviews* **64,** 49–60 (2012).

33. Wischke, C., Behl, M. & Lendlein, A. Drug-releasing shape-memory polymers - the role of morphology, processing effects, and matrix degradation. *Expert Opin. Drug Deliv.* **10,** 1193–205 (2013).

34. Chang, C., Duan, B., Cai, J. & Zhang, L. Superabsorbent hydrogels based on cellulose for smart swelling and controllable delivery. *Eur. Polym. J.* **46,** 92–100 (2010).

35. Okay, O. General Properties of Hydrogels. *Hydrogel Sensors and Actuators* **6,** 1–15 (2009).

36. Patenaude, M. & Hoare, T. Injectable, degradable thermoresponsive poly(N-isopropylacrylamide) hydrogels. *ACS Macro Lett.* **1,** 409–413 (2012).

37. Stoychev, G., Puretskiy, N. & Ionov, L. Self-folding all-polymer thermoresponsive microcapsules. *Soft Matter* **7,** 3277 (2011).

38. Fernandes, R. & Gracias, D. H. Self-folding polymeric containers for encapsulation and delivery of drugs. *Advanced Drug Delivery Reviews* **64,** 1579–1589 (2012).

39. Gruhn, T. & Emmerich, H. Simulation of stimuli-responsive polymer networks. *Chemosensors* **1,** 43–67 (2013).

40. Flory, P. J. & Rehner, J. J. Statistical mechanics of cross-linked polymer networks. *J. Chem. Phys.* **11,** 512–520 (1943).

41. Flory, P. J. & Rehner, J. Statistical mechanics of cross-linked polymer networks II. swelling. *J. Chem. Phys.* **11,** 521 (1943).

42. Flory, P. J. & Erman, B. Critical phenomena and transitions in swollen polymer networks and in linear macromolecules. in *American Chemical Society, Polymer Preprints, Division of Polymer Chemistry* **26,** 34 (1985).

43. English, A. E. *et al.* Equilibrium swelling properties of polyampholytic hydrogels. *J. Chem. Phys.* **104,** 8713–8720 (1996).

44. Okay, O. & Sariisik, S. B. Swelling behavior of poly(acrylamide-co-sodium acrylate) hydrogels in aqueous salt solutions: theory versus experiments. *Eur. Polym. J.* **36,** 393–399 (2000).

45. Sun, D., Gu, W. & Guo, X. A mixed finite element formulation of triphasic mechano-electrochemical theory for charged, hydrated biological soft tissues. *Int. J. Numer. Methods Eng.* **45,** 1375–1402 (1999).

46. Zhou, X., Hon, Y. C., Sun, S. & Mak, a F. T. Numerical simulation of the steady-state deformation of a smart hydrogel under an external electric field. *Smart Mater. Struct.* **11,** 459–467 (2002).

47. Chen, J. & Ma, G. Modelling deformation behaviour of polyelectrolyte gels under chemo-electro-mechanical coupling effects. *Int. J. Numer. Methods Eng.* **68,** 1052–1071 (2006).

48. Yue, P., Feng, J. J., Liu, C. & Shen, J. Diffuse-interface simulations of drop coalescence and retraction in viscoelastic fluids. *J. Nonnewton. Fluid Mech.* **129,** 163–176 (2005).

49. Boffetta, G., Mazzino, A., Musacchio, S. & Vozella, L. Rayleigh–Taylor instability in a viscoelastic binary fluid. *J. Fluid Mech.* **643,** 127 (2010).

50. Tian, H., Shao, J., Ding, Y., Li, X. & Li, X. Numerical studies of electrically induced pattern formation by coupling liquid dielectrophoresis and two-phase flow. *Electrophoresis* **32,** 2245–2252 (2011).

51. Tanaka, T., Hocker, L. O. & Benedek, G. B. Spectrum of light scattered from a viscoelastic gel. *J. Chem. Phys.* **59,** 5151–5159 (1973).

52. Tanaka, T. & Fillmore, D. J. Kinetics of swelling of gels. *J.Chem. Phys.* **70,** 1214–1218 (1979).

53. Tanaka, T. *et al.* Phase transitions in ionic gels. *Phys. Rev. Lett.* **45,** 1636–1639 (1980).

54. Tanaka, T. *et al.* Mechanical instability of gels at the phase transition. *Nature* **325,** 796–798 (1987).

55. Cai, S. & Suo, Z. Mechanics and chemical thermodynamics of phase transition in temperature-sensitive hydrogels. *J. Mech. Phys. Solids* **59,** 2259–2278 (2011).

56. Toh, W., Ng, T. Y., Hu, J. & Liu, Z. Mechanics of inhomogeneous large deformation of photo-thermal sensitive hydrogels. *Int. J. Solids Struct.* **51,** 4440–4451 (2014).

57. De, K. S. *et al.* Equilibrium swelling and kinetics of pH-responsive hydrogels: Models, experiments, and simulations. *J. Microelectromechanical Syst.* **11,** 544–555 (2002).

58. De, S. K. & Aluru, N. R. A chemo-electro-mechanical mathematical model for simulation of pH sensitive hydrogels. *Mech. Mater.* **36,** 395–410 (2004).

59. Chen, J., Li, H. & Lam, K. Y. Transient simulation for kinetic responsive behaviors of electric-sensitive hydrogels subject to applied electric field. *Materials Science and Engineering C* **25,** 710–712 (2005).

60. Li, H. Kinetics of smart hydrogels responding to electric field: A transient deformation analysis. *Int. J. Solids Struct.* **46,** 1326–1333 (2009).

61. Lai, F. & Li, H. Transient modeling of the reversible response of the hydrogel to the change in the ionic strength of solutions. *Mech. Mater.* **43,** 287–298 (2011).

62. Li, H., Luo, R., Birgersson, E. & Lam, K. Y. Modeling of multiphase smart hydrogels responding to pH and electric voltage coupled stimuli. *J. Appl. Phys.* **101,** 4905 (2007).

63. Luo, R., Li, H. & Lam, K. Y. Modeling and analysis of pH-electric-stimuli-responsive hydrogels. *J. Biomater. Sci. Polym. Ed.* **19,** 1597–610 (2008).

64. Quesada-Pérez, M., Ramos, J., Forcada, J. & Martín-Molina, A. Computer simulations of thermo-sensitive microgels: Quantitative comparison with experimental swelling data. *J. Chem. Phys.* **136,** 244903 (2012).

65. Jaramillo-Botero, A., Blanco, M., Li, Y., McGuinness, G. & Goddard, W. A. First-principles based approaches to nano-mechanical and biomimetic characterization of polymer-based hydrogel networks for cartilage scaffold-supported therapies. *J. Comput. Theor. Nanosci.* **7,** 1238–1256 (2010).

66. Fuchs, K. H. Minimally invasive surgery. *Endoscopy* **34,** 154–159 (2002).

67. Traverso, G. & Langer, R. Perspective: Special delivery for the gut. *Nature* **519,** S19 (2015).

68. Dogangil, G., Davies, B. L. & Rodriguez y Baena, F. A review of medical robotics for minimally invasive soft tissue surgery. *Proc. Inst. Mech. Eng. H.* **224,** 653–679 (2010).

69. Lazzaro, M. a & Chen, M. Interventional management of intracranial stenosis. *Atherosclerosis* **3,** 24–34 (2010).

70. Nelson, B. J., Kaliakatsos, I. K. & Abbott, J. J. Microrobots for minimally invasive medicine. *Annu. Rev. Biomed. Eng.* **12,** 55–85 (2010).

71. Sitti, M. *et al.* Biomedical applications of untethered mobile milli/microrobots. *Proceedings of the IEEE* **103,** 205–224 (2015).

72. Gultepe, E. *et al.* Biopsy with thermally-responsive untethered microtools. *Adv. Mater.* **25,** 514–519 (2013).

73. Hawks, J. A., Kunowski, J. & Platt, S. R. In vivo demonstration of surgical task assistance using miniature robots. *IEEE Trans. Biomed. Eng.* **59,** 2866–2873 (2012).

74. Breger, J. C. *et al.* Self-folding thermo-magnetically responsive soft microgrippers. *ACS Appl. Mater. Interfaces* **7,** 3398–3405 (2015).

75. Rus, D. & Tolley, M. T. Design, fabrication and control of soft robots. *Nature* **521,** 467–475 (2015).

76. Peer, D. *et al.* Nanocarriers as an emerging platform for cancer therapy. *Nat. Nanotechnol.* **2,** 751–760 (2007).

77. Yoshida, T., Lai, T. C., Kwon, G. S. & Sako, K. pH- and ion-sensitive polymers for drug delivery. *Expert Opin. Drug Deliv.* **10,** 1497–513 (2013).

78. Andersen, E. S. *et al.* Self-assembly of a nanoscale DNA box with a controllable lid. *Nature* **459,** 73–76 (2009).

79. Vihola, H., Laukkanen, A., Valtola, L., Tenhu, H. & Hirvonen, J. Cytotoxicity of thermosensitive polymers poly(N-isopropylacrylamide), poly(N-vinylcaprolactam) and amphiphilically modified poly(N-vinylcaprolactam). *Biomaterials* **26,** 3055–3064 (2005).

80. Schild, H. G. Poly(N-isopropylacrylamide): Experiment, theory and application. *Progress in Polymer Science* **17,** 163–249 (1992).

81. Kavanagh, C. A. *et al.* Poly(N-isopropylacrylamide) copolymer films as vehicles for the sustained delivery of proteins to vascular endothelial cells. *J. Biomed. Mater. Res. - Part A* **72,** 25–35 (2005).

82. Naha, P. C. *et al.* Intracellular localisation, geno- and cytotoxic response of poly N-isopropylacrylamide (PNIPAM) nanoparticles to human keratinocyte (HaCaT) and colon cells (SW 480). *Toxicol. Lett.* **198,** 134–143 (2010).

83. Hsiue, G. H., Hsu, S. H., Yang, C. C., Lee, S. H. & Yang, I. K. Preparation of controlled release ophthalmic drops, for glaucoma therapy using thermosensitive poly-N-isopropylacrylamide. *Biomaterials* **23,** 457–462 (2002).

84. Bhattarai, N., Gunn, J. & Zhang, M. Chitosan-based hydrogels for controlled, localized drug delivery. *Advanced Drug Delivery Reviews* **62,** 83–99 (2010).

85. Kurisawa, M. & Yui, N. Gelatin/dextran intelligent hydrogels for drug delivery: Dual-stimuli-responsive degradation in relation to miscibility in interpenetrating polymer networks. *Macromol. Chem. Phys.* **199,** 1547–1554 (1998).

86. Kulkarni, R. V & Sa, B. Evaluation of pH-sensitivity and drug release characteristics of (polyacrylamide-grafted-xanthan)-carboxymethyl cellulose-based pH-sensitive interpenetrating network hydrogel beads. *Drug Dev Ind Pharm* **34,** 1406–1414 (2008).

87. Matricardi, P., Di Meo, C., Coviello, T., Hennink, W. E. & Alhaique, F. Interpenetrating polymer networks polysaccharide hydrogels for drug delivery and tissue engineering. *Adv. Drug Deliv. Rev.* **65,** 1172–1187 (2013).

88. Kim, D. H. & Martin, D. C. Sustained release of dexamethasone from hydrophilic matrices using PLGA nanoparticles for neural drug delivery. *Biomaterials* **27,** 3031–3037 (2006).

89. Pérennès, F. *et al.* Sharp beveled tip hollow microneedle arrays fabricated by LIGA and 3D soft lithography with polyvinyl alcohol. *J. Micromechanics Microengineering* **16,** 473 (2006).

90. Pillai, O. & Panchagnula, R. Polymers in drug delivery. *Current Opinion in Chemical Biology* **5,** 447–451 (2001).

91. He, C., Kim, S. W. & Lee, D. S. In situ gelling stimuli-sensitive block copolymer hydrogels for drug delivery. *Journal of Controlled Release* **127,** 189–207 (2008).

92. Polygerinos, P., Wang, Z., Galloway, K. C., Wood, R. J. & Walsh, C. J. Soft robotic glove for combined assistance and at-home rehabilitation. in *Robotics and Autonomous Systems* **73,** 135–143 (2015).

93. Nemat-Nasser, Sia, and C. T. Electroactive polymer (EAP) actuators as artificial muscles. Reality, potential and challenges. *Bellingham, WA SPIE* 139–191 (2001).

94. Shahinpoor, M., Bar-Cohen, Y., Simpson, J. O. & Smith, J. Ionic polymer-metal composites (IPMCs) as biomimetic sensors, actuators and artificial muscles - a review. *Smart Mater. Struct.* **7,** R15–R30 (1998).

95. Smela, E. Conjugated polymer actuators for biomedical applications. *Adv. Mater.* **15,** 481–494 (2003).

96. Ching-Ping Chou & Hannaford, B. Measurement and modeling of McKibben pneumatic artificial muscles. *IEEE Trans. Robot. Autom.* **12,** 90–102 (1996).

97. Deimel, R. & Brock, O. A novel type of compliant , underactuated robotic hand for dexterous grasping. *Int. J. Rob. Res.* (2014). doi:10.1177/0278364915592961

98. Martinez, R. V. *et al.* Robotic tentacles with three-dimensional mobility based on flexible elastomers. *Adv. Mater.* **25,** 205–212 (2013).

99. Mazzolai, B., Margheri, L., Cianchetti, M., Dario, P. & Laschi, C. Soft-robotic arm inspired by the octopus: II. From artificial requirements to innovative technological solutions. *Bioinspir. Biomim.* **7,** 25005 (2012).

100. Cianchetti, M. *et al.* Soft robotics technologies to address shortcomings in today's minimally invasive surgery: The STIFF-FLOP approach. *Soft Robot.* **1,** 122–131 (2014).

101. Adam Bilodeau, R., White, E. L. & Kramer, R. K. Monolithic fabrication of sensors and actuators in a soft robotic gripper. *Intell. Robot. Syst. (IROS), 2015 IEEE/RSJ Int. Conf.* 2324–2329 (2015). doi:10.1109/IROS.2015.7353690

102. Park, Y.-L. *et al.* Design and control of a bio-inspired soft wearable robotic device for ankle-foot rehabilitation. *Bioinspir. Biomim.* **9,** 16007 (2014).

103. Mosadegh, B. *et al.* Pneumatic networks for soft robotics that actuate rapidly. *Adv. Funct. Mater.* **24,** 2163–2170 (2014).

104. Hirotsu, S., Hirokawa, Y. & Tanaka, T. Volume-phase transitions of ionized N-isopropylacrylamide gels. *J. Chem. Phys.* **87,** 1392–1395 (1987).

105. Ilievski, F., Mazzeo, A. D., Shepherd, R. F., Chen, X. & Whitesides, G. M. Soft robotics for chemists. *Angew. Chemie - Int. Ed.* **50,** 1890–1895 (2011).

106. Lipomi, D. J. & Bao, Z. Stretchable, elastic materials and devices for solar energy conversion. *Energy Environ. Sci.* **4,** 3314–3328 (2011).

107. Tee, B. C.-K., Wang, C., Allen, R. & Bao, Z. An electrically and mechanically self-healing composite with pressure- and flexion-sensitive properties for electronic skin applications. *Nat. Nanotechnol.* **7,** 825–832 (2012).

108. Ionov, L. Biomimetic hydrogel-based actuating systems. *Adv. Funct. Mater.* **23,** 4555–4570 (2013).

109. Stokes, A. a, Shepherd, R. F., Morin, S. a, Ilievski, F. & Whitesides, G. M. A hybrid combining hard and soft robots. *Soft Robot.* **1,** 70–74 (2014).

110. Nilsen, E. T. Thermonastic leaf movements: A synthesis of research with Rhododendron. *Bot. J. Linn. Soc.* **110,** 205–233 (1992).

111. Williams, S. E. and Bennett, A. B. Leaf closure in the Venus Flytrap : An acid growth response. *Science* **218,** 1120–1122 (1982).

112. Forterre, Y., Skotheim, J. M., Dumais, J. & Mahadevan, L. How the Venus flytrap snaps. *Nature* **433,** 421–425 (2005).

113. Gil, E. S. & Hudson, S. M. Stimuli-reponsive polymers and their bioconjugates. *Progress in Polymer Science* **29,** 1173–1222 (2004).

114. C. de Las Heras Alarcon, C., Pennadam, S. & Alexander, C. Stimuli responsive polymers for biomedical applications. *Chem. Soc. Rev.* **34,** 276–285 (2005).

115. Ahn, S., Kasi, R. M., Kim, S.-C., Sharma, N. & Zhou, Y. Stimuli-responsive polymer gels. *Soft Matter* **4,** 1151–1157 (2008).

116. Stuart, M. a C. *et al.* Emerging applications of stimuli-responsive polymer materials. *Nat. Mater.* **9,** 101–113 (2010).

117. Suzuki, A. & Tanaka, T. Phase transition in polymer gels induced by visible light. *Nature* **346,** 345–347 (1990).

118. Hu, Z., Zhang, X. & Li, Y. Synthesis and application of modulated polymer gels. *Science* **269,** 525–527 (1995).

119. Juodkazis, S. *et al.* Reversible phase transitions in polymer gels induced by radiation forces. *Nature* **408,** 178–181 (2000).

120. Tsutsui, H., Mikami, M. & Akashi, R. All-polymer-gel light modulator consisting of a 'gel-in-gel' system. *Adv. Mater.* **16,** 1925–1929 (2004).

121. Yoshida, R. *et al.* Maskless microfabrication of thermosensitive gels using a microscope and application to a controlled release microchip. *Lab Chip* **6,** 1384–1386 (2006).

122. Chu, L. Y., Kim, J. W., Shah, R. K. & Weitz, D. A. Monodisperse thermoresponsive microgels with tunable volume-phase transition kinetics. *Adv. Funct. Mater.* **17,** 3499–3504 (2007).

123. Klein, Y., Efrati, E. & Sharon, E. Shaping of elastic sheets by prescription of non-Euclidean metrics. *Science* **315,** 1116–1120 (2007).

124. Maeda, S., Hara, Y., Sakai, T., Yoshida, R. & Hashimoto, S. Self-walking gel. *Adv. Mater.* **19,** 3480–3484 (2007).

125. Fujigaya, T., Morimoto, T., Niidome, Y. & Nakashima, N. NIR laser-driven reversible volume phase transition of single-walled carbon nanotube/ poly(N-isopropylacrylamide) composite gels. *Adv. Mater.* **20,** 3610–3614 (2008).

126. Fujimoto, K. L. *et al.* Synthesis, characterization and therapeutic efficacy of a biodegradable, thermoresponsive hydrogel designed for application in chronic infarcted myocardium. *Biomaterials* **30,** 4357–4368 (2009).

127. Pelah, A., Bharde, A. & Jovin, T. M. Protein manipulation by stimuli-responsive polymers encapsulated in erythrocyte ghosts. *Soft Matter* **5,** 1006–1010 (2009).

128. Kim, J., Yoon, J. & Hayward, R. C. Dynamic display of biomolecular patterns through an elastic creasing instability of stimuli-responsive hydrogels. *Nat. Mater.* **9,** 159–164 (2010).

129. Zakharchenko, S., Puretskiy, N., Stoychev, G., Stamm, M. & Ionov, L. Temperature controlled encapsulation and release using partially biodegradable thermo-magneto-sensitive self-rolling tubes. *Eur. Cells Mater.* **20,** 279 (2010).

130. Kim, J., Hanna, J. a., Byun, M., Santangelo, C. D. & Hayward, R. C. Designing responsive buckled surfaces by halftone gel lithography. *Science (80-.).* **335,** 1201–1205 (2012).

131. Kim, J., Hanna, J. a., Hayward, R. C. & Santangelo, C. D. Thermally responsive rolling of thin gel strips with discrete variations in swelling. *Soft Matter* **8,** 2375–2381 (2012).

132. Fusco, S. *et al.* An integrated microrobotic platform for on-demand, targeted therapeutic interventions. *Adv. Mater.* **26,** 952–957 (2014).

133. Zhang, Y. & Yarin, A. L. Stimuli-responsive copolymers of n-isopropyl acrylamide with enhanced longevity in water for micro- and nanofluidics, drug delivery and non-woven applications. *J. Mater. Chem.* **19,** 4732–4739 (2009).

134. Bassik, N., Abebe, B. T., Laflin, K. E. & Gracias, D. H. Photolithographically patterned smart hydrogel based bilayer actuators. *Polymer* **51,** 6093–6098 (2010).

135. Bassik, N., Abebe, B. T. & Gracias, D. H. Solvent driven motion of lithographically fabricated gels. *Langmuir* **24,** 12158–12163 (2008).

136. Cai, S. G. and T. Controlled actuation of alternating magnetic field-sensitive tunable hydrogels. *J. Phys. D. Appl. Phys.* **43,** 415504 (2010).

137. Gracias, D. H., Kavthekar, V., Love, J. C., Paul, K. E. & Whitesides, G. M. Fabrication of micrometer-scale, patterned polyhedra by self-assembly. *Adv. Mater.* **14,** 235–238 (2002).

138. Leong, T. G., Lester, P. A., Koh, T. L., Call, E. K. & Gracias, D. H. Surface tension-driven self-folding polyhedra. *Langmuir* **23,** 8747–8751 (2007).

139. Azam, A., Laflin, K. E., Jamal, M., Fernandes, R. & Gracias, D. H. Self-folding micropatterned polymeric containers. *Biomed. Microdevices* **13,** 51–58 (2011).

140. Chen, G. & Hoffman, A. S. Graft copolymers that exhibit temperature-induced phase transitions over a wide range of pH. *Nature* **373,** 49–52 (1995).

141. Shibayama, M. & Nagai, K. Shrinking kinetics of poly (N-isopropylacrylamide) gels T-jumped across their volume phase transition temperatures. *Macromolecules* **32,** 7461–7468 (1999).

142. Zhang, J., Chu, L. Y., Li, Y. K. & Lee, Y. M. Dual thermo- and pH-sensitive poly(N-isopropylacrylamide-co-acrylic acid) hydrogels with rapid response behaviors. *Polymer* **48,** 1718–1728 (2007).

143. Hong, W., Zhao, X., Zhou, J. & Suo, Z. A theory of coupled diffusion and large deformation in polymeric gels. *J. Mech. Phys. Solids* **56,** 1779–1793 (2008).

144. Flory, P. J. Thermodynamics of high polymer solutions. *J. Chem. Phys.* **10,** 51–61 (1942).

145. Huggins, M. L. Solutions of long chain compounds. *J. Chem. Phys.* **9,** 440 (1941).

146. Chester, S. A. & Anand, L. A thermo-mechanically coupled theory for fluid permeation in elastomeric materials: Application to thermally responsive gels. *Journal of the Mechanics and Physics of Solids* **59,** 1978–2006 (2011).

147. Lee, H.-S., Cho, C. & Cho, M.-W. Magnetostrictive micro mirrors for an optical switch matrix. *Sensors* **7,** 2174–2182 (2007).

148. Aksyuk, V. A. *et al.* Beam-steering micromirrors for large optical cross-connects. in *Journal of Lightwave Technology* **21,** 634–642 (2003).

149. Borrelli, N. F. *Microoptics technology*. *CRC Press* (2004). doi:10.1201/9781420030907

150. Yurke, B., Turberfield, A. J., Mills, A. P., Simmel, F. C. & Neumann, J. L. A DNA-fuelled molecular machine made of DNA. *Nature* **406,** 605–608 (2000).

151. Yan, H., Zhang, X., Shen, Z. & Seeman, N. C. A robust DNA mechanical device controlled by hybridization topology. *Nature* **415,** 62–65 (2002).

152. Shim, T. S. *et al.* Shape changing thin films powered by DNA hybridization. *Nat. Nanotechnol.* 1–8 (2016). doi:10.1038/nnano.2016.192

153. Rogers, W. B. & Manoharan, V. N. Programming colloidal phase transitions with DNA strand displacement. *Sci.* **347,** 639–642 (2015).

154. Maye, M. M., Kumara, M. T., Nykypanchuk, D., Sherman, W. B. & Gang, O. Switching binary states of nanoparticle superlattices and dimer clusters by DNA strands. *Nat. Nanotechnol.* **5,** 116–120 (2010).

155. Jamal, M. *et al.* Bio-origami hydrogel scaffolds composed of photocrosslinked PEG bilayers. *Adv. Healthc. Mater.* **2,** 1142–1150 (2013).

156. Therien-Aubin, H., Wu, Z. L., Nie, Z. & Kumacheva, E. Multiple shape transformations of composite hydrogel sheets. *J. Am. Chem. Soc.* **135,** 4834–4839 (2013).

157. Zhang, D. Y. & Seelig, G. Dynamic DNA nanotechnology using strand-displacement reactions. *Nat. Chem.* **3,** 103–113 (2011).

158. Seelig, G., Soloveichik, D., Zhang, D. Y. & Winfree, E. Enzyme-Free Nucleic Acid Logic Circuits. *Science* **314,** 1585–1588 (2006).

159. Tanaka, T., Sato, E., Hirokawa, Y., Hirotsu, S. & Peetermans, J. Critical kinetics of volume phase transition of gels. *Phys. Rev. Lett.* **55,** 2455–2458 (1985).

160. Yoon, J., Cai, S., Suo, Z. & Hayward, R. C. Poroelastic swelling kinetics of thin hydrogel layers: comparison of theory and experiment. *Soft Matter* **6,** 6004–6012 (2010).

161. Murphy, W. L., Dillmore, W. S., Modica, J. & Mrksich, M. Dynamic hydrogels: Translating a protein conformational change into macroscopic motion. *Angew. Chemie - Int. Ed.* **46,** 3066–3069 (2007).

162. Sui, Z., King, W. J. & Murphy, W. L. Protein-based hydrogels with tunable dynamic responses. *Adv. Funct. Mater.* **18,** 1824–1831 (2008).

163. Seffen, K. A. & Guest, S. D. Prestressed morphing bistable and neutrally stable shells. *J. Appl. Mech.* **78,** 11002 (2010).

164. Nagahara, S. & Matsuda, T. Hydrogel formation via hybridization of oligonucleotides derivatized in water-soluble vinyl polymers. *Polym. Gels Networks* **4,** 111–127 (1996).

165. Murakami, Y. & Maeda, M. Hybrid hydrogels to which single-stranded (ss) DNA probe is incorporated can recognize specific ssDNA. *Macromolecules* **38,** 1535–1537 (2005).

166. Liedl, T., Dietz, H., Yurke, B. & Simmel, F. Controlled trapping and release of quantum dots in a DNA-switchable hydrogel. *Small* **3,** 1688–1693 (2007).

167. Yang, H., Liu, H., Kang, H. & Tan, W. Engineering Target-Responsive Hydrogels Based on Aptamer - Target. 6320–6321 (2008).

168. Tierney, S. & Stokke, B. T. Development of an oligonucleotide functionalized hydrogel integrated on a high resolution interferometric readout platform as a label-free macromolecule sensing device. *Biomacromolecules* **10,** 1619–1626 (2009).

169. Dave, N., Chan, M. Y., Huang, P. J. J., Smith, B. D. & Liu, J. Regenerable DNA-functionalized hydrogels for ultrasensitive, instrument-free mercury(II) detection and removal in water. *J. Am. Chem. Soc.* **132,** 12668–12673 (2010).

170. Shastri, A. *et al.* An aptamer-functionalized chemomechanically modulated biomolecule catch-and-release system. *Nat. Chem.* **7,** 447–454 (2015).

171. Yurke, B. Mechanical properties of a reversible, DNA-crosslinked polyacrylamide hydrogel. *J. Biomech. Eng.* **126,** 104–110 (2004).

172. Lin, D. C., Yurke, B. & Langrana, N. a. Inducing reversible stiffness changes in DNA-crosslinked gels. *J. Mater. Res.* **20,** 1456–1464 (2005).

173. Venkataraman, S., Dirks, R. M., Rothemund, P. W. K., Winfree, E. & Pierce, N. a. An autonomous polymerization motor powered by DNA hybridization. *Nat. Nanotechnol.* **2,** 490–494 (2007).

174. Hays, J. B., Magar, M. E. & Zimm, B. H. Persistence length of DNA. *Biopolymers* **8,** 531–536 (1969).

175. Ravanat, J.-L., Douki, T. & Cadet, J. Direct and indirect effects of UV radiation on DNA and its components. *J. Photochem. Photobiol. B.* **63,** 88–102 (2001).

176. Nguyen, N.-T., Ho, S.-S. & Low, C. L.-N. A polymeric microgripper with integrated thermal actuators. *J. Micromechanics Microengineering* **14,** 969–974 (2004).

177. Chronis, N. & Lee, L. P. Electrothermally activated SU-8 microgripper for single cell manipulation in solution. *J. Microelectromechanical Syst.* **14,** 857–863 (2005).

178. Lu, Y. W. & Kim, C. J. Microhand for biological applications. *Appl. Phys. Lett.* **89,** 164101 (2006).

179. Carpi, F. & Smela, E. *Biomedical applications of electroactive polymer actuators*. *John Wiley and Sons* (2009). doi:10.1002/9780470744697

180. Mirfakhrai, T., Madden, J. D. W. & Baughman, R. H. Polymer artificial muscles. *Mater. Today* **10,** 30–38 (2007).

181. Brown, E. *et al.* From the Cover: Universal robotic gripper based on the jamming of granular material. *Proc. Natl. Acad. Sci.* **107,** 18809–18814 (2010).

182. Randhawa, J. S., Laflin, K. E., Seelam, N. & Gracias, D. H. Microchemomechanical systems. *Adv. Funct. Mater.* **21,** 2395–2410 (2011).

183. Peraza-Hernandez, E. A., Hartl, D. J., Malak Jr, R. J. & Lagoudas, D. C. Origami-inspired active structures: a synthesis and review. *Smart Mater. Struct.* **23,** 94001 (2014).

184. Wang, E., Desai, M. S. & Lee, S. W. Light-controlled graphene-elastin composite hydrogel actuators. *Nano Lett.* **13,** 2826–2830 (2013).

185. Yuan, B. *et al.* A strategy for depositing different types of cells in three dimensions to mimic tubular structures in tissues. *Adv. Mater.* **24,** 890–896 (2012).

186. Thérien-Aubin, H., Wu, Z. L., Nie, Z. & Kumacheva, E. Multiple shape transformations of composite hydrogel sheets. *J. Am. Chem. Soc.* **135,** 4834–4839 (2013).

187. Yoon, C. *et al.* Functional stimuli responsive hydrogel devices by self-folding. *Smart Mater. Struct.* **23,** 94008 (2014).

188. Kim, S. & Healy, K. E. Synthesis and characterization of injectable poly(N-isopropylacrylamide-co-acrylic acid) hydrogels with proteolytically degradable cross-links. *Biomacromolecules* **4,** 1214–1223 (2003).

189. Schmaljohann, D. Thermo- and pH-responsive polymers in drug delivery. *Advanced Drug Delivery Reviews* **58,** 1655–1670 (2006).

190. Siegwart, D. J., Bencherif, S. A., Srinivasan, A., Hollinger, J. O. & Matyjaszewski, K. Synthesis, characterization, and in vitro cell culture viability of degradable poly(N-isopropylacrylamide-co-5,6-benzo-2-methylene-1,3-dioxepane)-based polymers and crosslinked gels. *J. Biomed. Mater. Res. - Part A* **87,** 345–358 (2008).

191. Nistor, M. T., Chiriac, A. P., Vasile, C., Verestiuc, L. & Nita, L. E. Synthesis of hydrogels based on poly(NIPAM) inserted into collagen sponge. *Colloids Surfaces B Biointerfaces* **87,** 382–390 (2011).

192. Guan, Y. & Zhang, Y. PNIPAM microgels for biomedical applications: from dispersed particles to 3D assemblies. *Soft Matter* **7,** 6375–6384 (2011).

193. Kasper, F. K., Tanahashi, K., Fisher, J. P. & Mikos, A. G. Synthesis of poly(propylene fumarate). *Nat. Protoc.* **4,** 518–525 (2009).

194. Fisher, J. P., Dean, D. & Mikos, A. G. Photocrosslinking characteristics and mechanical properties of diethyl fumarate/poly(propylene fumarate) biomaterials. *Biomaterials* **23,** 4333–4343 (2002).

195. He, S. *et al.* Synthesis of biodegradable poly(propylene fumarate) networks with poly(propylene fumarate)–diacrylate macromers as crosslinking agents and characterization of their degradation products. *Polymer (Guildf).* **42,** 1251–1260 (2001).

196. Cooke, M. N., Fisher, J. P., Dean, D., Rimnac, C. & Mikos, A. G. Use of stereolithography to manufacture critical-sized 3D biodegradable scaffolds for bone ingrowth. *J. Biomed. Mater. Res. B. Appl. Biomater.* **64,** 65–69 (2003).

197. Martel, S. *et al.* Automatic navigation of an untethered device in the artery of a living animal using a conventional clinical magnetic resonance imaging system. *Appl. Phys. Lett.* **90,** 114105 (2007).

198. Xi, W. *et al.* Rolled-up magnetic microdrillers: towards remotely controlled minimally invasive surgery. *Nanoscale* **5,** 1294–1297 (2013).

199. Behkam, B. & Sitti, M. Bacterial flagella-based propulsion and on/off motion control of microscale objects. *Appl. Phys. Lett.* **90,** 23902 (2007).

200. Guo, J., Yang, W., Deng, Y., Wang, C. & Fu, S. Organic-dye-coupled magnetic nanoparticles encaged inside thermoresponsive PNIPAM microcapsules. *Small* **1,** 737–741 (2005).

201. Temenoff, J. S. & Mikos, a G. Injectable biodegradable materials for orthopedic tissue engineering. *Biomaterials* **21,** 2405–2412 (2000).

202. Lutz, J. F., Akdemir, Ö. & Hoth, A. Point by point comparison of two thermosensitive polymers exhibiting a similar LCST: Is the age of poly(NIPAM) over? *J. Am. Chem. Soc.* **128,** 13046–13047 (2006).

203. Flory, P. J. *Principles of polymer chemistry*. *Cornell University Press*, (1953).

204. Fisher, J. P. *et al.* Soft and hard tissue response to photocrosslinked poly(propylene fumarate) scaffolds in a rabbit model. *J. Biomed. Mater. Res.* **59,** 547–556 (2002).

205. Kim, K. *et al.* The influence of stereolithographic scaffold architecture and composition on osteogenic signal expression with rat bone marrow stromal cells. *Biomaterials* **32,** 3750–3763 (2011).

206. Lendlein, A. *et al.* Biodegradable, elastic shape-memory polymers for potential biomedical applications. *Science* **296,** 1673–1676 (2002).

207. Martel, S. & Mohammadi, M. Using a swarm of self-propelled natural microrobots in the form of flagellated bacteria to perform complex micro-assembly tasks. in *Proceedings - IEEE International Conference on Robotics and Automation* 500–505 (2010). doi:10.1109/ROBOT.2010.5509752

208. Tottori, S. *et al.* Magnetic helical micromachines: Fabrication, controlled swimming, and cargo transport. *Adv. Mater.* **24,** 811–816 (2012).

209. Randhawa, J. S. *et al.* Pick-and-place using chemically actuated microgrippers. *J. Am. Chem. Soc.* **130,** 17238–17239 (2008).

210. Diller, E. & Sitti, M. Three-dimensional programmable assembly by untethered magnetic robotic micro-grippers. *Adv. Funct. Mater.* **24,** 4397–4404 (2014).

211. Ichikawa, A., Sakuma, S., Arai, F. & Akagi, S. Untethered micro-robot with gripping mechanism for on-chip cell surgery utilizing outer magnetic force. in *Proceedings - IEEE International Conference on Robotics and Automation* 3795–3800 (2014). doi:10.1109/ICRA.2014.6907409

212. Malachowski, K. *et al.* Self-folding single cell grippers. *Nano Lett.* **14,** 4164–4170 (2014).

213. Fusco, S. *et al.* Self-folding mobile microrobots for biomedical applications. in *Proceedings - IEEE International Conference on Robotics and Automation* 3777–3782 (2014). doi:10.1109/ICRA.2014.6907406

214. Miyashita, S., Guitron, S., Ludersdorfer, M., Sung, C. R. & Rus, D. An untethered miniature origami robot that self-folds, walks, swims, and degrades. in *Proceedings - IEEE International Conference on Robotics and Automation* 1490–1496 (2015). doi:10.1109/ICRA.2015.7139386

215. Li, H., Go, G., Ko, S. Y., Park, J.-O. & Park, S. Magnetic actuated pH-responsive hydrogel-based soft micro-robot for targeted drug delivery. *Smart Mater. Struct.* **25,** 27001 (2016).

216. Kuo, J. C., Huang, H. W., Tung, S. W. & Yang, Y. J. A hydrogel-based intravascular microgripper manipulated using magnetic fields. *Sensors Actuators A. Phys.* **211,** 121–130 (2014).

217. Ë, A. S., Sadek, Y. M., Khalil, I. S. M. & Ë, S. M. Mobi-Mag : A compact device for medical research using wireless control of magnetic microrobots Session - Robotic devices Session - Robotic devices. *Proc. Des. Med. Devices Conf.* 100–101 (2014).

218. Franklin, G. F., Powell, J. D. & Emami-Naeini, A. *Feedback Control of Dynamic Systems*. *Addison-Wesley, Reading, MA* (1994).

219. Bahaj, A. S., James, P. A. B. & Moeschler, F. D. An alternative method for the estimation of the magnetic moment of non-spherical magnetotactic bacteria. *IEEE Trans. Magn.* **32,** 5133–5135 (1996).

220. Chemla, Y. R. *et al.* A New Study of Bacterial Motion: Superconducting Quantum Interference Device Microscopy of Magnetotactic Bacteria. *Biophys. J.* **76,** 3323–3330 (1999).

221. Brown, W. F. Magnetostatic Principles. *Ferromagn. North-holl. Amsterdam* 2–5 (1962).

222. Khalil, I. S. M. & Misra, S. Control characteristics of magnetotactic bacteria : MagnetospirillumMagnetotacticum strain MS-1 and MagnetospirillumM agneticum strain AMB-1. *IEEE Trans. Magn.* **50,** 1–11 (2014).

223. Khalil, I. S. M., Abelmann, L. & Misra, S. Magnetic-based motion control of paramagnetic microparticles with disturbance compensation. *IEEE Trans. Magn.* **50,** 1–10 (2014).

224. Sánchez, A., Magdanz, V., Schmidt, O. G. & Misra, S. Magnetic control of self-propelled microjets under ultrasound image guidance. in *Proceedings of the IEEE RAS and EMBS International Conference on Biomedical Robotics and Biomechatronics* 169–174 (2014). doi:10.1109/BIOROB.2014.6913771

225. Heiiden, F. van der. *Image Based Measurement Systems: Object Recognition and Parameter Estimation*. *John Wiley & Sons,* (1994).

226. He, M. The Faber polynomials for m-fold symmetric domains. *J. Comput. Appl. Math.* **54,** 313–324 (1994).

227. Belanger, P. R., Dobrovolny, P., Helmy, A. & Zhang, X. Estimation of angular velocity and acceleration from shaft-encoder measurements. *Int. J. Rob. Res.* **17,** 1225–1233 (1998).

228. Limentani, G. B., Ringo, M. C., Ye, F., Berquist, M. L. & McSorley, E. O. Beyond the t-test: Statistical equivalence testing. *Anal. Chem.* **77,** 221A–226A (2005).

229. Pelrine, R. *et al.* Diamagnetically levitated robots: An approach to massively parallel robotic systems with unusual motion properties. in *Proceedings - IEEE International Conference on Robotics and Automation* 739–744 (2012). doi:10.1109/ICRA.2012.6225089

230. Wang, J. Cargo-towing synthetic nanomachines: towards active transport in microchip devices. *Lab Chip* **12,** 1944–50 (2012).

231. Wong, D., Steager, E. B. & Kumar, V. Independent control of identical magnetic robots in a plane. *IEEE Robot. Autom. Lett.* 1–8 (2016). doi:10.1109/LRA.2016.2522999

232. Hoover, A. M. & Fearing, R. S. Rapidly prototyped orthotweezers for automated microassembly. in *Proceedings - IEEE International Conference on Robotics and Automation* 812–819 (2007). doi:10.1109/ROBOT.2007.363086

233. Solovev, A. A. *et al.* Self-propelled nanotools. *ACS Nano* **6,** 1751–1756 (2012).

234. Arcese, L., Fruchard, M. & Ferreira, A. Endovascular magnetically guided robots: Navigation modeling and optimization. *IEEE Trans. Biomed. Eng.* **59,** 977–987 (2012).

235. Venugopalan, P. L. *et al.* Conformal cytocompatible ferrite coatings facilitate the realization of a nanovoyager in human blood. *Nano Lett.* **14,** 1968–1975 (2014).

236. Cecil, J., Powell, D. & Vasquez, D. Assembly and manipulation of micro devices-A state of the art survey. *Robot. Comput. Integr. Manuf.* **23,** 580–588 (2007).

237. Gauthier, M. & Régnier, S. *Robotic Microassembly*. *John Wiley & Sons*, (2011). doi:10.1002/9780470634417

238. Chaillet, N. & Régnier, S. *Microrobotics for Micromanipulation*. *Microrobotics for Micromanipulation* (2013). doi:10.1002/9781118622810

239. Agnus, J. *et al.* Robotic microassembly and micromanipulation at FEMTO-ST. *J. Micro-Bio Robot.* **8,** 91–106 (2013).

240. Chowdhury, S. Path planning and control for autonomous navigation of single and multiple magnetic mobile microrobots. *Proc. ASME 2015 Int. Des. Eng. Tech. Conf. Comput. Inf. Eng. Conf.* 1–10 (2015).

241. Amend, J. R., Brown, E., Rodenberg, N., Jaeger, H. M. & Lipson, H. A positive pressure universal gripper based on the jamming of granular material. *IEEE Trans. Robot.* **28,** 341–350 (2012).

242. Majidi, C. Soft Robotics: A perspective—current trends and prospects for the future. *Soft Robot.* **1,** 5–11 (2014).

243. Ongaro, F. *et al.* Control of untethered soft grippers for pick-And-place tasks. *Proc. IEEE RAS EMBS Int. Conf. Biomed. Robot. Biomechatronics* 299–304 (2016). doi:10.1109/BIOROB.2016.7523642

244. Wang, W. H., Liu, X. Y. & Sun, Y. Autonomous zebrafish embryo injection using a microrobotic system. in *Proceedings of the 3rd IEEE International Conference on Automation Science and Engineering, IEEE CASE 2007* 363–368 (2007). doi:10.1109/COASE.2007.4341701

245. Khalil, I. S. M., Keuning, J. D., Abelmann, L. & Misra, S. Wireless magnetic-based control of paramagnetic microparticles. in *Proceedings of the IEEE RAS and EMBS International Conference on Biomedical Robotics and Biomechatronics* 460–466 (2012). doi:10.1109/BioRob.2012.6290856

246. Ju, T., Liu, S., Yang, J. & Sun, D. Rapidly exploring random tree algorithm-based path planning for robot-aided optical manipulation of biological cells. *IEEE Trans. Autom. Sci. Eng.* **11,** 649–657 (2014).

247. Scheggi, S. & Misra, S. An experimental comparison of path planning techniques applied to micro-sized magnetic agents. *IEEE Int. Conf. Manip. Autom. Robot. Small Scales* (2016). doi:10.1109/MARSS.2016.7561695

248. Gelb, A. *Applied optimal estimation*. *MIT Press* (1974). doi:10.1109/PROC.1976.10175

249. LaValle, S. M. & Kuffner, J. J. Rapidly-exploring random trees: Progress and prospects. *4th Work. Algorithmic Comput. Robot. New Dir.* 293–308 (2000). doi:10.1017/CBO9781107415324.004

250. Thorpe, S., Fize, D. & Marlot, C. Speed of processing in the human visual system. *Nature* **381,** 520–522 (1996).

251. Vrooijink, G. J., Abayazid, M. & Misra, S. Real-time three-dimensional flexible needle tracking using two-dimensional ultrasound. in *Proceedings - IEEE International Conference on Robotics and Automation* 1688–1693 (2013). doi:10.1109/ICRA.2013.6630797

252. Vrooijink, G. J., Abayazid, M., Patil, S., Alterovitz, R. & Misra, S. Needle path planning and steering in a three-dimensional non-static environment using two-dimensional ultrasound images. *Int. J. Rob. Res.* **33,** 1361–1374 (2014).

253. Kummer, M. P. *et al.* Octomag: An electromagnetic system for 5-DOF wireless micromanipulation. *IEEE Trans. Robot.* **26,** 1006–1017 (2010).

254. Khalil, I. S. M., Ferreira, P., Eleutério, R., De Korte, C. L. & Misra, S. Magnetic-based closed-loop control of paramagnetic microparticles using ultrasound feedback. in *Proceedings - IEEE International Conference on Robotics and Automation* 3807–3812 (2014). doi:10.1109/ICRA.2014.6907411

255. Novoselov, K. S. *et al.* Electric field effect in atomically thin carbon films. *Science* **306,** 666–669 (2004).

256. Geim, A. K. & Novoselov, K. S. The rise of graphene. *Nat. Mater.* **6,** 183–191 (2007).

257. Novoselov, K. S. *et al.* A roadmap for graphene. *Nature* **490,** 192–200 (2012).

258. Meyer, J. C. *et al.* The structure of suspended graphene sheets. *Nature* **446,** 60–63 (2007).

259. Bao, W. *et al.* Controlled ripple texturing of suspended graphene and ultrathin graphite membranes. *Nat. Nanotechnol.* **4,** 562–566 (2009).

260. Kim, K. S. *et al.* Large-scale pattern growth of graphene films for stretchable transparent electrodes. *Nature* **457,** 706–710 (2009).

261. Scharfenberg, S. *et al.* Probing the mechanical properties of graphene using a corrugated elastic substrate. *Appl. Phys. Lett.* **98,** 91908 (2011).

262. Chen, Z. *et al.* Three-dimensional flexible and conductive interconnected graphene networks grown by chemical vapour deposition. *Nat. Mater.* **10,** 424–428 (2011).

263. Niu, Z., Chen, J., Hng, H. H., Ma, J. & Chen, X. A leavening strategy to prepare reduced graphene oxide foams. *Adv. Mater.* **24,** 4144–4150 (2012).

264. Kim, T. *et al.* Large-scale graphene micropatterns via self-assembly-mediated process for flexible device application. *Nano Lett.* **12,** 743–748 (2012).

265. Yan, W. *et al.* Strain and curvature induced evolution of electronic band structures in twisted graphene bilayer. *Nat. Commun.* **4,** 2159 (2013).

266. Yin, S. *et al.* Functional free-standing graphene honeycomb films. *Adv. Funct. Mater.* **23,** 2972–2978 (2013).

267. Wu, C., Huang, X., Wu, X., Qian, R. & Jiang, P. Mechanically flexible and multifunctional polymer-based graphene foams for elastic conductors and oil-water separators. *Adv. Mater.* **25,** 5658–5662 (2013).

268. Zang, J. *et al.* Multifunctionality and control of the crumpling and unfolding of large-area graphene. *Nat. Mater.* **12,** 321–325 (2013).

269. Song, J. *et al.* A general method for transferring graphene onto soft surfaces. *Nat. Nanotechnol.* **8,** 356–362 (2013).

270. Yan, C. *et al.* Highly stretchable piezoresistive graphene-nanocellulose nanopaper for strain sensors. *Adv. Mater.* **26,** 2022–2027 (2014).

271. Zhu, B. *et al.* Microstructured graphene arrays for highly sensitive flexible tactile sensors. *Small* **10,** 3625–3631 (2014).

272. Chun, S., Kim, Y., Jung, H. & Park, W. A flexible graphene touch sensor in the general human touch range. *Appl. Phys. Lett.* **105,** 41907 (2014).

273. Wang, Y. *et al.* Wearable and highly sensitive graphene strain sensors for human motion monitoring. *Adv. Funct. Mater.* **24,** 4666–4670 (2014).

274. Cranford, S. W. & Buehler, M. J. Packing efficiency and accessible surface area of crumpled graphene. *Phys. Rev. B - Condens. Matter Mater. Phys.* **84,** 205451 (2011).

275. Kim, K. *et al.* Multiply folded graphene. *Phys. Rev. B - Condens. Matter Mater. Phys.* **83,** 245433 (2011).

276. Pereira, V. M., Castro Neto, A. H., Liang, H. Y. & Mahadevan, L. Geometry, mechanics, and electronics of singular structures and wrinkles in graphene. *Phys. Rev. Lett.* **105,** 156603 (2010).

277. Patra, N., Wang, B. & Král, P. Nanodroplet activated and guided folding of graphene nanostructures. *Nano Lett.* **9,** 3766–3771 (2009).

278. Guo, F. *et al.* Hydration-responsive folding and unfolding in graphene oxide liquid crystal phases. *ACS Nano* **5,** 8019–8025 (2011).

279. Li, C., Koslowski, M. & Strachan, A. Engineering curvature in graphene ribbons using ultrathin polymer films. *Nano Lett.* **14,** 7085–7089 (2014).

280. Zhang, J. *et al.* Free folding of suspended graphene sheets by random mechanical stimulation. *Phys. Rev. Lett.* **104,** 166805 (2010).

281. Chen, Y. *et al.* Aerosol synthesis of cargo-filled graphene nanosacks. *Nano Lett.* **12,** 1996–2002 (2012).

282. Li, J., Chung, T. F., Chen, Y. P. & Cheng, G. J. Nanoscale strainability of graphene by laser shock-induced three-dimensional shaping. *Nano Lett.* **12,** 4577–4583 (2012).

283. Li, C. & Shi, G. Three-dimensional graphene architectures. *Nanoscale* **4,** 5549–5563 (2012).

284. Zhao, Y., Song, L., Zhang, Z. & Qu, L. Stimulus-responsive graphene systems towards actuator applications. *Energy Environ. Sci.* **6,** 3520–3536 (2013).

285. Schedin, F. *et al.* Detection of individual gas molecules adsorbed on graphene. *Nat. Mater.* **6,** 652–655 (2007).

286. Kuila, T. *et al.* Recent advances in graphene-based biosensors. *Biosensors and Bioelectronics* **26,** 4637–4648 (2011).

287. Liu, Y., Dong, X. & Chen, P. Biological and chemical sensors based on graphene materials. *Chem Soc Rev* **41,** 2283–2307 (2012).

288. He, Q., Wu, S., Yin, Z. & Zhang, H. Graphene-based electronic sensors. *Chem. Sci.* **3,** 1764–1772 (2012).

289. Huang, X., Zeng, Z., Fan, Z., Liu, J. & Zhang, H. Graphene-based electrodes. *Advanced Materials* **24,** 5979–6004 (2012).

290. Smela, E., Inganäs, O. & Lundström, I. Controlled folding of micrometer-size structures. *Science* **268,** 1735–1738 (1995).

291. Cho, J. H., Hu, S. & Gracias, D. H. Self-assembly of orthogonal three-axis sensors. *Appl. Phys. Lett.* **93,** 43505 (2008).

292. Ionov, L. Soft microorigami: self-folding polymer film. *Soft Matter* **7,** 6786–6791 (2011).

293. Smith, E. J. *et al.* Lab-in-a-tube: ultracompact components for on-chip capture and detection of individual micro-/nanoorganisms. *Lab Chip* **12,** 1917–1931 (2012).

294. Xu, S. *et al.* Assembly of micro/nanomaterials into complex, three-dimensional architectures by compressive buckling. *Science (80-.).* **347,** 154–159 (2015).

295. Lorenz, H. *et al.* SU-8: a low-cost negative resist for MEMS. *J. Micromech. Microeng. J. Micromech. Microeng* **7,** 121–121 (1997).

296. Ferrari, A. C. *et al.* Raman spectrum of graphene and graphene layers. *Phys. Rev. Lett.* **97,** 187401 (2006).

297. Li, X. *et al.* Large-area synthesis of high-quality and uniform graphene films on copper foils. *Science (80-.).* **324,** 1312–1314 (2009).

298. Chen, Y.-T. & Lee, D. A bonding technique using hydrophilic SU-8. *J. Micromechanics Microengineering* **17,** 1978–1984 (2007).

299. Keller, S., Blagoi, G., Lillemose, M., Haefliger, D. & Boisen, A. Processing of thin SU-8 films. *J. Micromechanics Microengineering* **18,** 125020 (2008).

300. Owen, O. E. *et al.* Acetone metabolism during diabetic ketoacidosis. *Diabetes* **31,** 242–248 (1982).

301. Nair, R. R. *et al.* Universal dynamic conductivity and quantized visible opacity of suspended graphene. *Science* **320,** 1308 (2008).

302. Mak, K. F., Ju, L., Wang, F. & Heinz, T. F. Optical spectroscopy of graphene: From the far infrared to the ultraviolet. *Solid State Commun.* **152,** 1341–1349 (2012).

303. Xia, F., Mueller, T., Lin, Y., Valdes-Garcia, A. & Avouris, P. Ultrafast graphene photodetector. *Nat. Nanotechnol.* **4,** 839–843 (2009).

304. Mueller, T., Xia, F. & Avouris, P. Graphene photodetectors for high-speed optical communications. *Nat. Photonics* **4,** 297–301 (2010).

305. Koppens, F. H. L. *et al.* Photodetectors based on graphene, other two-dimensional materials and hybrid systems. *Nat. Nanotechnol.* **9,** 780–793 (2014).

306. He, X. *et al.* Carbon nanotube terahertz detector. *Nano Lett.* **14,** 3953–3958 (2014).

307. Freiberg, S. & Zhu, X. X. Polymer microspheres for controlled drug release. *International Journal of Pharmaceutics* **282,** 1–18 (2004).

308. Du, Y., Lo, E., Ali, S. & Khademhosseini, A. Directed assembly of cell-laden microgels for fabrication of 3D tissue constructs. *Proc. Natl. Acad. Sci. U. S. A.* **105,** 9522–9527 (2008).

309. Mason, T. G., Ganesan, K., van Zanten, J., Wirtz, D. & Kuo, S. Particle Tracking Microrheology of Complex Fluids. *Phys. Rev. Lett.* **79,** 3282–3285 (1997).

310. Kim, S. H., Abbaspourrad, A. & Weitz, D. A. Amphiphilic crescent-moon-shaped microparticles formed by selective adsorption of colloids. *J. Am. Chem. Soc.* **133,** 5516–5524 (2011).

311. Kim, E., Xia, Y. N. & Whitesides, G. M. Polymer Microstructures Formed by Molding in Capillaries. *Nature* **376,** 581–584 (1995).

312. Zauner, R. Micro powder injection moulding. *Microelectron. Eng.* **83,** 1442–1444 (2006).

313. Vozzi, G., Flaim, C., Ahluwalia, A. & Bhatia, S. Fabrication of PLGA scaffolds using soft lithography and microsyringe deposition. *Biomaterials* **24,** 2533–2540 (2003).

314. Randhawa, J. S., Kanu, L. N., Singh, G. & Gracias, D. H. Importance of surface patterns for defect mitigation in three-dimensional self-assembly. *Langmuir* **26,** 12534–12539 (2010).

315. Cho, Y. S. *et al.* Self-organization of bidisperse colloids in water droplets. *J. Am. Chem. Soc.* **127,** 15968–15975 (2005).

316. Yethiraj, A. & van Blaaderen, A. A colloidal model system with an interaction tunable from hard sphere to soft and dipolar. *Nature* **421,** 513–517 (2003).

317. Fernandez, J. G. & Khademhosseini, A. Micro-masonry: Construction of 3D structures by microscale self-assembly. *Adv. Mater.* **22,** 2538–2541 (2010).

318. Chou, S. Y., Krauss, P. R., Zhang, W., Guo, L. & Zhuang, L. Sub-10 nm imprint lithography and applications. *J. Vac. Sci. Technol.* **15,** 2897–2904 (1997).

319. Langford, R. M., Nellen, P. M., Gierak, J. & Fu, Y. Focused Ion Beam Micro- and Nanoengineering. *MRS Bull.* **32,** 417–423 (2007).

320. Ahn, S. H. & Guo, L. J. Large-area roll-to-roll and roll-to-plate Nanoimprint Lithography: A step toward high-throughput application of continuous nanoimprinting. *ACS Nano* **3,** 2304–2310 (2009).

321. Stoney, G. G. The tension of metallic films deposited by electrolysis the tension of metallic films deposited by electrolysis . *Proc. R. Soc. London Ser. A Contain. Pap. a Math. Phys. Character* **82,** 172 (1909).

322. Prinz, V. Y. *et al.* Free-standing and overgrown InGaAs/GaAs nanotubes, nanohelices and their arrays. *Phys. E Low-Dimensional Syst. Nanostructures* **6,** 828–831 (2000).

323. Schmidt, O. G. & Eberl, K. Nanotechnology: Thin solid films roll up into nanotubes. *Nature* **410,** 168 (2001).

324. Bell, D. J. *et al.* Fabrication and characterization of three-dimensional InGaAs/GaAs nanosprings. *Nano Lett.* **6,** 725–729 (2006).

325. Wang, J., Patel, M. & Gracias, D. H. Self-Assembly of Three-Dimensional Nanoporous Containers. *Nano* **4,** 1–5 (2009).

326. Grimm, D. *et al.* Rolled-up nanomembranes as compact 3D architectures for field effect transistors and fluidic sensing applications. *Nano Lett.* **13,** 213–218 (2013).

327. Freund, L. B. & Suresh, S. *Thin Film Materials: Stress, Defect Formation and Surface Evolution*. *Cambridge University Press* (2004).

328. Neumann, A. *et al.* Comparative investigation of the biocompatibility of various silicon nitride ceramic qualities in vitro. *J. Mater. Sci. Mater. Med.* **15,** 1135–1140 (2004).

329. Randall, C. L., Kalinin, Y. V., Jamal, M., Shah, A. & Gracias, D. H. Self-folding immunoprotective cell encapsulation devices. *Nanomedicine Nanotechnology, Biol. Med.* **7,** 686–689 (2011).

330. Tabata, O., Kawahata, K., Sugiyama, S. & Igarashi, I. Mechanical property measurements of thin films using load-deflection of composite rectangular membranes. *Sensors and Actuators* **20,** 135–141 (1989).

331. Agnew, W. F., Yuen, T. G. H., McCreery, D. B. & Bullara, L. A. Histopathologic evaluation of prolonged intracortical electrical stimulation. *Exp. Neurol.* **92,** 162–185 (1986).

332. Ekkels, P., Rottenberg, X., Puers, R. & Tilmans, H. a C. Evaluation of platinum as a structural thin film material for RF-MEMS devices. *J. Micromechanics Microengineering* **19,** 65010 (2009).

333. Tyagi, P. *et al.* Patternable nanowire sensors for electrochemical recording of dopamine. *Anal. Chem.* **81,** 9979–9984 (2009).

334. Brummer, S. B. & Turner, M. J. Electrical stimulation with Pt electrodes: II-estimation of maximum surface redox (theoretical non-gassing) limits. *IEEE Trans. Biomed. Eng.* **24,** 440–443 (1977).

335. Orive, G. *et al.* Cell encapsulation: promise and progress. *Nat. Med.* **9,** 104–107 (2003).

336. Desai, T. A. *et al.* Microfabricated immunoisolating biocapsules. *Biotechnol. Bioeng.* **57,** 118–120 (1998).

Curriculum Vitae

Chang-Kyu (CK) Yoon
Department of Materials Science and Engineering, Johns Hopkins University
3400 N. Charles Street, 133 MD Hall, Baltimore, MD 21218 USA
Phone: 410) 982-7906; E-mail: ckyoon@jhu.edu

EDUCATION

Johns Hopkins University
Ph. D. in Materials Science and Engineering
Thesis Title: *Design, Characterization $ Application of Stimuli Responsive Self-folding Soft Microsystems*
Advisor: *Professor **David Gracias***
Date of Graduation – December 2016

Washington State University
Master of Science in Materials Science and Engineering
Thesis Title: *Evolution of Annealing Twins in Sputtered Cu Thin Films*
Advisor: *Professor **David Field***
Date of Graduation – July 2009

Bachelor of Science in Materials Science and Engineering, **Cum Laude**
Senior Project Title: *Mechanical Properties of Hardness and Elasticity in Nickel Based Superalloy, Rene88DT*
Advisor: *Associate Professor **Kip Findley**, currently in Colorado School of Mines*
Date of Graduation – December 2006

PEER-REVIEWED JOURNAL PUBLICATIONS

1. K. Kobayashi, S. H. Oh, W. Gong, C. K. Yoon, and D. H. Gracias, "Multi-state Self-folding Hydrogel Devices," 2017. **[In preparation]**

2. A. Ghosh, C. K. Yoon, F. Ongaro, S. Misra, and D. H. Gracias, "Soft Microgrippers for Biomedical Applications," 2017. [**Review paper**, **In preparation]**

3. K. Kobayashi[1], C. K. Yoon[1], J. Pagaduan, S. H. Oh and D. H. Gracias, "Fully Biodegradable Shape Change Soft-Gripping Devices," 2017. **[In preparation]**

4. C. K. Yoon[1], A. Cangialosi[1], J. Liu, Q. Huang, T. D. Nguyen, D. H. Gracias and R. Schulman "Programmable, High-Degree Expansion of DNA Copolymer Hydrogels," 2017. **[In preparation]**

5. J. Guo, T. Shroff, C. K. Yoon, D. H. Gracias and T. D. Nguyen, "Thermally Responsive Bidirectional Folding Hydrogel System," 2017. **[In preparation]**

6. S. Scheggi, T. C. Krishna Kumar, C. K. Yoon, B. Sawaryn, G. van den Steeg, D. H. Gracias and S. Misra, "Magnetic Motion Control and Planning of Untethered Soft Grippers Using Ultrasound Image Feedback*,"* 2016. **[In review]**

7. C. Pacchierotti, F. Ongaro, F. van den Brink, C. K. Yoon, D. Prattichizzo, D. H. Gracias and S. Misra, "Steering and Control of Magnetic Soft Microgrippers with Haptic Feedback," *IEEE Transactions on Automation Science and Engineering*, 2016. **[Accepted]**

[1]: Contributed equally to the work. [Hyperlinks to a **Bold** and *italic* font]

8. F. Ongaro[1], S. Scheggi[1], C. K. Yoon[1], F. van den Brink, S. H. Oh, D. H. Gracias and S. Misra, "Autonomous Planning and Control of Soft Untethered Grippers in Unstructured Environments," *Journal of Micro-Bio Robotics*, pp. 1-8, 2016.

9. S. Pandey, N. Macias, C. Ciobanu, C. K. Yoon, C. Teuscher and D. H. Gracias, "Assembly of a 3D Cellular Computer Using Folded E-Blocks," *Micromachines*, vol. 7, pp. 78, 2016.

10. J. C. Breger, C. K. Yoon, R. Xiao, H. R. Kwag, M. Wang, J. Fisher, T. D. Nguyen and D. H. Gracias, "Self-Folding Thermo-Magnetically Responsive Soft-Microgrippers," *ACS Applied Materials & Interfaces*, vol. 7, pp. 3398-3405, 2015. **[Highlights in** IEEE Spectrum, ***Medical microbots take a fantastic voyage into reality***, June 2015, Wired (Germany) ***Die Nano- Docs***, April 2015, Gizmag, ***Tiny robotic hand-like grippers dissolve in the body after performing task***, Feb. 2015, ACS Press Release, ***Tiny robotic hands could improve cancer diagnostics, drug delivery***, Feb. 2015, Chemistry World (RSC), ***Soft robots get a grip***, Mar. 2016]

11. T. Deng[1], C. K. Yoon[1], Q. Jin, M. Li, Z. Liu and D. H. Gracias, "Self-Folding Graphene-Polymer Bilayers," *Applied Physics Letters*, vol. 106, pp. 203108, 2015.

12. C. K. Yoon, R. Xiao, J. H. Park, J. Cha, T. D. Nguyen and D. H. Gracias, "Functional Stimuli Responsive Hydrogel Devices by Self-Folding," *Smart Materials and Structures*, vol. 23, pp. 094008, 2014.

13. C. K. Yoon and D.P. Field, "Evolution of Annealing Twins in Thin Film Microstructure," *Journal of Electronic Materials*, vol. 39, pp. 191-199, 2009.

PEER-REVIEWED CONFERENCE PUBLICATIONS

1. S. Scheggi, C. K. Yoon, D. H. Gracias, and S. Misra, "Model-based Tracking of Miniaturized Grippers Using Particle Swarm Optimization," *Proceedings of the IEEE International Conference on Intelligent Robots and Systems (IROS) (IEEE IROS 2016)*, pp. 454-459, 2016.

2. F. Ongaro, C. Pacchierotti, C. K. Yoon, D. Prattichizzo, D. H. Gracias, and S. Misra, "Evaluation of Electromagnetic System with Haptic Feedback for Control of Untethered, Soft Grippers Affected by Disturbances," *Proceedings of the IEEE RAS/EMBS International Conference on Biomedical Robotics and Biomechatronics (BioRob) (IEEE BioRob 2016)*, pp. 908-913, 2016.

3. F. Ongaro, C. K. Yoon, F. van den Brink, M. Abayazid, S. H. Oh, D. H. Gracias, and S. Misra, "Control of Soft Untethered Grippers for Pick-and-Place Tasks," *Proceedings of the IEEE RAS/EMBS International Conference on Biomedical Robotics and Biomechatronics (BioRob) (IEEE BioRob 2016)*, pp. 299-304, 2016.

4. S. Pandey[1], C. K. Yoon[1], Z. Zhang, H. R. Kwag, J. Hong and D. H. Gracias, "Patterned Soft-Micropolyhedra by Self-Folding and Molding," *IEEE 29th International Conference on Micro Electro Mechanical Systems (IEEE MEMS 2016)*, pp. 203-206, 2016.

5. J. H. Park, C. K. Yoon, Q. Jin, L. Chen, and D. H. Gracias, "Rolled-up Nanoporous Membranes by Nanoimprint Lithography and Strain Engineering," *IEEE International Conference on Nano/Micro Engineered and Molecular Systems (IEEE NEMS 2015)*, pp. 233-237, 2015. **[Best paper in IEEE NEMS 2015]**

6. N. Macias, S. Pandey, A. Deswandikar, C. K. Kothapalli, C. K. Yoon, D. H. Gracias and C. Teuscher, "A Cellular Architecture for Self-Assembled 3D Computational Devices," *IEEE/ACM International Symposium on Nanoscale Architecture (NANOARCH 2013)*, pp. 116-121, 2013.

[1]: Contributed equally to the work. [Hyperlinks to a **Bold** and *italic* font]

ORAL PRESENTAIONS in CONFERENCES

1. C. K. Yoon and D. H. Gracias, "Targeted Pick-and-Place Using Untethered Self-Assembled Soft Grippers," Mid-Atlantic Regional Conference 2016 (MARC 2016), Apr. 23, Vienna, VA 2016. **[Invited]**
2. C. K. Yoon, F. van den Brink, R. Xiao, T. D. Nguyen, S. Misra, and D. H. Gracias, "Untethered Thermo-Magnetically Responsive Hydrogel Microgrippers," MRS, Nov. 29 - Dec. 4, Boston, MA 2015.
3. C. K. Yoon, and D. H. Gracias, "Thin Film Origami Inspired 3D Micro and Nanofabrication," Collaborative Conference on 3D and Materials Research (CC3DMR), Jun. 15-19, Busan, South Korea, 2015. **[Invited]**
4. C. K. Yoon, J. Breger, H. R. Kwag, R. Xiao, M. Wang, J. P. Fisher, T. D. Nguyen and D. H. Gracias, "Untethered Stimuli Responsive All Polymeric Grippers," MRS, Dec. 1-6, Boston, MA 2013.
5. C. K. Yoon, R. Xiao, J. H. Park, J. P. Cha, H. Wang, V. Shenoy, T. D. Nguyen and D. H. Gracias, "Functional Stimuli Responsive Hydrogel Devices by Self-Folding," MRS, Dec. 1-6, Boston, MA 2013.
6. C. K. Yoon and D. P. Field, "Evolution of Annealing Twins in Thin Film Microstructures," TMS, Feb. 14-18, San Francisco, CA 2009.

POSTERS in CONFERENCES

1. C. K. Yoon, F. Ongara, S. Scheggi, S. H. Oh, S. Misra, and D. H. Gracias, "Automated Control of Magneto-Thermally Responsive Soft Grippers for Pick-and-Place of Biological Cargo," MRS, Nov. 27- Dec. 2, Boston, MA 2016.
2. F. Ongaro, C. K. Yoon, F. van den Brink, M. Abayazid, S. H. Oh, D. H. Gracias and S. Misra, "Control of Soft Untethered Grippers for Pick-and-Place Tasks," Proceedings of the IEEE RAS/EMBS international conference on Biomedical Robotics and Biomechatronics (BioRob), June 26-29, Singapore, 2016. **[Best Poster Award]**
3. C. K. Yoon, F. Ongaro, S. Scheggi, S. H. Oh, S. Misra, and D. H. Gracias, "Soft, Miniaturized Untethered Grippers for Pick-and-Place Applications," Mid Atlantic Micro/Nano Alliance 2016 Spring Workshop, Mar. 25, JHU Applied Physics Laboratory (APL) Laurel, MD 2016. **[3rd place of Poster Award]**
4. C. K. Yoon, T. Deng, Z. Liu, and D. H. Gracias, "Self-Assembly of Integrated Curved and Folded Graphene-Polymer Sensors," MRS, Nov. 29- Dec. 4, Boston, MA 2015. **[Best Poster Award Nominee]**
5. C. K. Yoon, J. C. Breger, K. Malachowski, R. Xiao, T. D. Nguyen, and D. H. Gracias, "Stimuli Responsive Soft Micro GripBots," Mid Atlantic Micro/Nano Alliance 2015 Spring Workshop, Apr. 6, JHU Applied Physics Laboratory (APL) Laurel, MD 2015.
6. C. K. Yoon, J. C. Breger, K. Malachowski, R. Xiao, T. D. Nguyen, and D. H. Gracias, "Stimuli Responsive Soft Microgrippers for Diagnostics and Therapeutics," INBT Nano-Bio Symposium, May 2, Baltimore, MD 2014.
7. C. K. Yoon and D. P. Field, "Evolution of Annealing Twins in Thin Film Microstructures," WSU Showcase, Mar. 27, Pullman, 2009.

ARTICLES and BOOK CHAPTERS

1. T. Shroff, C. K. Yoon, and D. H. Gracias, "Shape Change Poly (N-isopropylacrylamide) Microstructures for Drug Delivery," Polymeric Drug Delivery Techniques: Translating Polymer Science for Drug Delivery, *Aldrich Materials Science, Sigma-Aldrich*, pages 28-30. 2015.

AWARDS /HONORS

1. **International Student Tuition Supporting Award** in recognition of outstanding achievement at the final semester of master degree program, Washington State University. [2009 Spring]
2. **International Academic Award**, Washington State University. [Spring 2006, Fall 2005, Spring 2005, Fall 2004, Spring 2004, Fall 2003]
3. **Member of President's Honor Roll**, Washington State University. [Fall 2006, Spring 2006, Fall 2005, Spring 2005, Fall 2004, Spring 2004]

PROFESSIONAL SOCIETIES

- **Tau Beta Pi**, national engineering honor society /organization
- Materials Research Society (**MRS**)
- The Minerals, Metals and Materials Society (**TMS**)

SKILLS and EXPERTISE

I. Extensive hands on experience in micro and nanofabrication with polymers, hydrogels, metals and semiconductors.

- **Nano and Microfabrication**: Photolithography, Nanoimprint lithography (NIL), Soft lithography, metallic and polymeric Nanoparticles, Physical vapor deposition (PVD), Electroplating, Thin-Films, Wet and Plasma etching, Molding, MEMS, NEMS, Microfluidics, Self-assembled 3D computers.

II. Experience with a range of micro and nanofabrication skills with cell culture, imaging, characterization techniques, and software programs.

- **Cell culture**: Basic bacterial and mammalian cell culture.
- **Imaging**: Scanning Electron Microscope (SEM), Fluorescence microscopy.
- **Characterization techniques**: Electron Backscatter Diffraction (EBSD), Orientation Imaging Microscopy (OIM^{TM}) data analysis, Energy Dispersive X-ray Spectroscopy (EDS), UV-Vis and fluorescence spectrophotometry. Mechanical tensile and compression test of thin films (metal, hydrogel, polymer, and composites) with digital image correlation (DIC).
- **Simulation and software programs**: Monte-Carlo simulation (FORTRAN), MATLAB.
- **Vector programs**: AutoCAD, Pro/ENGINEER.

RELATED PROFESSIONAL EXPERIENCE

I. Experience with multidisciplinary research with strong record of problem solving and productivity: successfully completed and ongoing collaborative projects on fabrication of 3D self-folding nano- and micro-chips and systems such as;

- Autonomous control of untethered soft grippers projects collaborating with ***Sarthak Misra*** lab, *University of Twente*.
- Mechanics of soft matter (hydrogels, polymers) projects collaborating with ***Thao Nguyen*** lab, *Department of Mechanical Engineering, Johns Hopkins University*.
- Programmable DNA hydrogel actuator projects collaborating with ***Rebecca Schulman*** lab, *Department of Chemical and Biomolecular Engineering*, *Johns Hopkins University*.

- Self-folding graphene-polymer sensors project collaborating with ***Zewen Liu*** lab, *Tsinghua University*.
- Rolled-up nanoporous membranes project collaborating with ***Lei Chen***, *Center for Nanoscale Science and Technology, National Institute of Standard and Technology* (NIST).
- Assembly of 3D cellular computer project collaborating with ***Christof Teuscher*** lab, *Portland State University*.
- Multi-states self-folding and biodegradable gripper projects collaborating with ***Kunihiko Kobayashi***, *JSR Corporation, Japan.*

II. Excellent analytical, organizational and interpersonal skills: Have given several talks, presentations and mentorships in the presence of distinguished audiences;

- Designing and demonstrating an experimental module for junior and high school students under a program of
  A. ***Center for Talented Youth*** (CTY), Johns Hopkins University.
  B. ***Women in Science and Engineering*** (WISE) programs, Johns Hopkins University.
- Mentoring masters, undergraduates and high school students in researches under a program of
  A. ***Research Experience for Undergraduates*** Summer Programs (REU), Institute for NanoBioTechnology (INBT), Johns Hopkins University.
  B. ***Women in Science and Engineering*** (WISE) programs, Johns Hopkins University
  C. ***Gracias*** lab, Johns Hopkins University.
- Teaching assisted undergraduate students of
  A. **Physical Chemistry of Materials (Kinetics)**, Department of Materials Science and Engineering, Johns Hopkins University. [Spring 2014]
  B. **Materials Characterizations**, Department of Materials Science and Engineering, Johns Hopkins University. [Fall 2013]
  C. **Manufacturing Process**, Department of Mechanical Engineering, Johns Hopkins University. [Fall 2010]
  D. **Introduction to Materials Science and Engineering**, Department of Mechanical and Materials Engineering, Washington State University. [Fall 2007, Spring 2008, Fall 2008]